SCUOLA DI DOTTORATO
UNIVERSITÀ DEGLI STUDI DI MILANO-BICOCCA

Department of

Earth and Environmental Sciences

PhD program in Chemical, Geological and Environmental Sciences, Cycle XXXV

Curriculum in Terrestrial and Marine Environmental Sciences

Geochemical and mineralogical studies to assess the significance of temperate coralline algae as paleoclimate archives

TESI IN COTUTELA

Piazza Giulia

821923

Tutors: Prof. Daniela Basso, Prof. Isabel Cacho

Coordinator: Prof. Marco Giovanni Malusà

ACADEMIC YEAR 2021/2022

University of Barcelona
Department of Earth and Ocean Dynamics

under the Double Degree Agreement with the
University of Milano-Bicocca

Geochemical and mineralogical studies to assess the significance of temperate coralline algae as paleoclimate archives

Giulia Piazza
NIUB 17749583

PhD programme in
Earth Sciences - HDK09

Tutors: **Prof. Daniela Basso**, **Prof. Isabel Cacho**
Coordinator: **Prof. Alberto Sáez**

Academic year 2022-2023

Abstract

Calcareous red algae are globally distributed foundation species and ecosystem engineers. The morphology of cells, reproductive structures, and thallus organisation are commonly used for their classification using Scanning Electron Microscopy (SEM). Nonetheless, due to their general plasticity, species identification based on morphology frequently leads to uncertainty and the advances in molecular phylogeny produced numerous cases of systematic revisions. These algae have been featured in evolutionary and environmental studies for their ecological significance in both recent and past oceans. Paleoecological and paleoenvironmental reconstructions relying on organisms' associations and geochemical proxies need proper species-specific calibrations and must rely on robust taxonomy. Investigating the cell wall ultrastructure has been the first goal of this research to develop new potential diagnostic tools for species identification while unveiling new insights into the principles governing the calcification mechanisms. A new deep learning approach and highly resolved analyses on SEM images indicate a high diagnostic value of calcification patterns, which contribute significantly to species segregation. The second goal of this research was to test geochemical proxies in diverse species, with particular attention to the boron (B) element. The B/Ca ratio in calcareous marine species provides information about past seawater CO_2 concentrations. Spectrometric analyses of Mg, Sr, Li, and B were performed at seasonal resolution on samples collected from various geographic settings and depths across the Mediterranean Sea and the Atlantic Ocean. Unlike Mg, Li and Sr, fluctuations in B/Ca did not mirror yearly seasonal temperature oscillations, excluding a significant temperature influence. Nevertheless, the direct proportion between growth rates and B/Ca values suggested a growth rate influence over B incorporation. The boron isotope-pH proxy was tested on calcareous red algae grown in naturally acidified ecosystems near CO_2 seeps. A multi-specific calibration of boron isotopes was also proposed using previously published data on cultured coralline algae and new data from wild-grown specimens, significantly increasing the range over which boron isotopes have previously been calibrated in the literature. A crystallographic control over B incorporation was confirmed by the different isotopic compositions of aragonitic and calcitic algae, and an up-regulation of the calcifying fluid pH was observed. Analyses on B speciation also revealed a significant percentage of trigonal boron in calcareous red algae, higher in calcites ($\sim$40%), questioning direct and exclusive incorporation of aqueous borate, which is the main hypothesis of current proxy reconstructions.

Acknowledgements

I would like to express my gratitude to:

- Prof. Daniela Basso for her wise guidance and support during my research, and to all the colleagues of the University of Milano-Bicocca for their honest feedback and friendship;

- Prof. Isabel Cacho for giving me the exciting opportunity to work at the University of Barcelona, and to all the colleagues that offered me their support during my stay;

- The colleagues from the Department of Material Sciences at the University of Milano-Bicocca and from the CEMHTI laboratory of the CNRS in Orléans who shared their knowledge and offered me their precious collaboration;

- My dear family and friends on whom I can always count on.

Dedication

To my Family, always tight to my soul.

C'est par la mer que le globe a pour ainsi dire commencé, et qui sait s'il ne finira pas par elle! Là est la suprême tranquillité.

—Jules Verne, *Vingt mille lieues sous les mers: Tour du monde sous-marin,* 1870

Contents

Abstract **i**

Acknowledgements **iii**

1 Introduction: Background Theory and Objectives **1**

1.1 Calcareous red algae (Rhodophyta) 1

1.1.1 Supervised classification 4

1.1.1.1 I Objective: Deep learning for automatic classification 7

1.1.2 Biomineralization 8

1.1.2.1 II Objective: Calcification traits in cryptic species 10

1.2 Calcareous red algae as paleoclimate archives 10

1.2.1 Trace and major element/Ca 13

1.2.1.1 III Objective: Multiple influences on Mg, Li, Sr and B/Ca . . . 14

1.2.2 The boron isotope-pH proxy 15

1.2.2.1 IV Objective: The boron isotope calibration 18

1.2.2.2 V Objective: Boron speciation 19

2 Materials and methods 20

2.1 Sample collection . . . 20

2.2 Environmental data . . . 25

2.3 Scanning Electron Microscopy . . . 26

2.4 Deep learning . . . 29

2.4.1 Data augmentation . . . 29

2.4.2 Convolutional Neural Networks . . . 30

2.4.3 CNN interpretability . . . 32

2.4.4 CNN evaluation strategy . . . 33

2.5 X-Ray Diffraction . . . 35

2.6 Mass Spectrometry . . . 35

2.6.1 Laser Ablation ICP-MS and growth rates . . . 35

2.6.2 Sample pre-purification and cleaning . . . 36

2.6.3 Micro-sublimation and Multi-Collector ICP-MS . . . 37

2.7 Boron isotope calibrations . . . 39

2.8 Magic Angle Spinning NMR . . . 39

2.9 Statistical analysis . . . 40

3 Results 42

3.1 Environmental data . . . 42

3.2 Scanning Electron Microscopy: calcification traits as a new diagnostic tool? . . . 45

3.2.1 *L. racemus* micro-anatomy . . . 45

3.2.2 *L. racemus* calcification . . . 47

3.2.3 *L. pseudoracemus* micro-anatomy . . . 50
3.2.4 *L. pseudoracemus* calcification . . . 52
3.2.5 *L.* cf. *racemus* micro-anatomy . . . 53
3.2.6 *L.* cf. *racemus* calcification . . . 54
3.3 Deep learning can support conventional taxonomic classification? . . . 61
3.3.1 Internal Validation . . . 61
3.3.1.1 Categories . . . 62
3.3.2 External Test . . . 67
3.3.2.1 Categories . . . 68
3.3.3 Explanation . . . 71
3.4 Laser Ablation ICP-MS: do temperature and growth rate affect B/Ca? . . . 75
3.4.1 Temperature proxies . . . 75
3.4.2 The B/Ca ratio . . . 78
3.4.3 Growth rates . . . 82
3.5 X-Ray Diffraction . . . 83
3.6 Multi-Collector ICP-MS . . . 86
3.7 Boron isotope calibrations . . . 89
3.8 Magic Angle Spinning NMR: is trigonal boron being incorporated? . . . 94

4 Discussion **104**
4.1 The taxonomic value of the cell wall calcification . . . 104
4.2 Biomineralization in calcareous red algae . . . 109
4.3 Temperature and growth rate influences on B/Ca . . . 111

4.4 The multi-specific calibration of the boron isotope-pH proxy 114

4.5 Boron incorporation in calcareous red algae 115

5 Conclusions 117

A Supplementary materials 120

B Peer-reviewed papers 135

References 249

List of Tables

2.1 Calcareous red algal samples used to run CNN models (I Objective, Section 1.1.1.1) (s1-11), to investigate calcification traits under SEM (II Objective, Section 1.1.2.1) (s1-6), for trace element analysis (III Objective, Section 1.2.1.1) (s8, s12-14), for boron isotopes (s2-4, s8, s12-32), among which s15-23 were used to calibrate boron isotopes near CO_2 seeps (IV Objective, Section 1.2.2.1), and to investigate boron speciation (V Objective, Section 1.2.2.2) (s2-4, s8, s10-14, s24-32). For CNN models, the number of SEM images per sample is also shown. 21

3.1 Environmental data for the sampling sites where *Lithothamnion corallioides* for LA-ICP-MS was collected (Table 2.1, Section 2.6.1). Monthly temperature means were extracted by 11 years of ORAS5 reanalysis; the pH and DIC for each sampling site were measured over an 18 years time period from monthly mean biogeochemical data provided by CMEMS (Section 2.2). 42

3.2 Environmental data for the sampling sites near CO_2 seeps (Table 2.1, Section 2.7). In Methana, data were derived from *in situ* data [37] (Section 2.2). In Ischia, pH was reviewed from literature data [235], while temperature and salinity were extracted by 7 years of monthly physical reanalysis [220] (Section 2.2). 44

3.3 Biometrical data (mean±SD) measured from SEM images (μm). 49

3.4 Calcification data (mean±SD) measured from SEM images (μm^2 for the cell wall area, μm for other measurements). 50

3.5 Resulting performances in each classification task: *Lithophyllum pseudoracemus* versus the other species (i.e., Others) (2 classes); diverse genera (3 classes) and diverse species (4 classes). The *Global accuracy* and the *Class Recall* are shown for the proposed model (CNN), the human classifier (HC) and the dummy classifier (DC). 63

3.6 *Class Recall* results per morphological category for each class (*Lithophyllum pseudoracemus* versus other species, diverse genera, and diverse species). The total number of SEM images in each category is also shown, and images not assigned to a category (n.c.) and showing more than one category (shared) are also included. 64

3.7 *Class Share* for the *Lithophyllum* cf. *racemus* samples s5 and s6 in the three classification tasks: *Lithophyllum pseudoracemus* versus Others (2 class-CNN), diverse genera (3 class-CNN), and diverse species (4 class-CNN). 68

3.8 Sample s5's *Class Share* for each assigned category and class. The total number of SEM images is shown after each category. Images that have not been assigned to a category (n.c.) or that show more than one category (shared) are also included. Note that sample s5 had no images of the hypothallus. 69

3.9 Sample s6's *Class Share* for each assigned category and class. The total number of SEM images is shown after each category. Images that have not been assigned to a category (n.c.) or that show more than one category (shared) are also included. Note that sample s6, as for s5, had no images of the hypothallus. . . . 70

3.10 Trace and major element/Ca measured by LA-ICP-MS in *Lithothamnion corallioides*. 77

3.11 Results of the Rietveld refinements performed on XRD data, indicating phase compositions. An example of the refinement is reported in Figure A.7 for sample s18. 84

3.12 Multi-collector ICP-MS results for δ^{11}B in calcareous red algae ($\delta^{11}B_{algae}$). . . . 86

3.13 Data used to calculate York fit calibrations in calcareous red algae. See Section 2.7 for details on calculations. 90

3.14 ^{11}B MAS NMR parameters from spectra in Figures 3.30, 3.31, 3.32, 3.33, 3.34 and 3.35. Trigonal boron (BO_3) in samples s4, s14 and s32 was simulated by a quadrupolar line shape characterized by a chemical shift (δ_{iso}) and the quadrupolar coupling constant (C_Q). In all other cases, gaussian line shapes were used for simulations, characterized by a chemical shift and width. Relative proportions between BO_3 ad BO_4 are also indicated (mean±SD %). Ambiguous signals are indicated as "n.c." (Table A.8 for the complete record). 96

3.15 Relative proportion of trigonal (BO_3) and tetragonal boron (BO_4) in calcareous red algae determined from peak surface integration of their ^{11}B MAS NMR spectra (1% error bar). Ambiguous signals (6.1-7.7 ppm) are indicated as "n.c." (Table 3.14 for NMR parameters, Table A.8 for the complete dataset). 96

A.1 Statistical tests performed to evaluate the differences of Mg/Ca in *Lithothamnion corallioides* (Kruskal-Wallis) and the differences of Mg/Ca in the short cells of *L. corallioides* collected at different sampling sites (ANOVA). Test significance at $\alpha = 0.05$. 124

A.2 Statistical tests performed to evaluate the differences of Mg/Ca in the long cells of *Lithothamnion corallioides* at different sampling sites (Morlaix Bay = sample s8; Aegadian Isl. = sample s12; Pontian Isl. = sample s14) (Table 2.1). Statistically significant p-values are highlighted in bold. ANOVA test significance at $\alpha = 0.05$. Tukey's test significance at $p \leq \alpha$. 125

A.3 Statistical tests performed to evaluate the differences of B/Ca in *Lithothamnion corallioides* collected at different sampling sites (Morlaix Bay = sample s8; Aegadian Isl. = sample s12; Pontian Isl. = sample s14) (Table 2.1). Statistically significant p-values are highlighted in bold. Kruskal–Wallis test significance at $\alpha = 0.05$; Dunn's test significant at $p < \alpha/2$. 126

A.4 Statistical tests performed to evaluate the differences of B/Ca in the long cells of *Lithothamnion corallioides* at different sampling sites (Morlaix Bay = sample s8; Aegadian Isl. = sample s12; Pontian Isl. = sample s14) (Table 2.1). Statistically significant p-values are highlighted in bold. ANOVA test significance at $\alpha = 0.05$. Tukey's test significance at $p \leq \alpha$. 127

A.5 Statistical tests performed to evaluate the differences of B/Ca in the short cells of *Lithothamnion corallioides* at different sampling sites (Morlaix Bay = sample s8; Aegadian Isl. = sample s12; Pontian Isl. = sample s14) (Table 2.1). Statistically significant p-values are highlighted in bold. ANOVA test significance at $\alpha = 0.05$. Tukey's test significance at $p \leq \alpha$. 128

A.6 Statistical tests performed to evaluate the differences of the perithallial cell area in *Lithophyllum racemus* (s1, s2), *Lithophyllum pseudoracemus* (s3, s4) and *Lithophyllum* cf. *racemus* (s5, s6). Statistically significant p-values are highlighted in bold. ANOVA test significance at $\alpha = 0.05$. Kruskal–Wallis test significance at $\alpha = 0.05$; Dunn's test significant at $p < \alpha/2$. 131

A.7 Statistical tests performed to evaluate the differences of the perithallial SC thickness in *Lithophyllum racemus* (s1, s2), *Lithophyllum pseudoracemus* (s3, s4) and *Lithophyllum* cf. *racemus* (s5, s6). Statistically significant p-values are highlighted in bold. ANOVA test significance at $\alpha = 0.05$. Tukey's test significance at $p \leq \alpha$. 132

A.8 ^{11}B MAS NMR parameters in calcareous red algae. Trigonal boron (BO_3) in samples s8, s24, s25, s27, s28, s30, s31, s32 was simulated by a quadrupolar line shape characterized by a chemical shift (δ_{iso}, [ppm]), width and the quadrupolar coupling constant (C_Q, [MHz]). In all other cases, gaussian line shapes were used for simulations, solely characterized by a chemical shift and width. Relative proportions between BO_3 ad BO_4 are also indicated (mean ± SD %). The error bar is 0.2 ppm for δ_{iso}, 0.02 MHz for C_Q and 1% for the proportion. Ambiguous signals are indicated as "n.c.". 133

List of Figures

1.1 An example of a Mediterranean coralligenous community (a), and a maerl bed (b) from Islas Columbretes, Spain. Modified from Rindi et al. [81]. Copyright: Enric Ballesteros. 2

1.2 Fruticose specimens of *Lithophyllum racemus* (a) and *Litophyllum pseudoracemus* (b). Modified from Caragnano et al. [6]. 3

1.3 Conceptual map summarizing the approach used in this research project for the study of the significance of calcareous red algae as paleoclimate archives. Two main aspects were addressed: the problem of taxonomic identification and the application of geochemical proxies. A novel approach to algal classification was tested using Convolutional Neural Networks (CNNs) (Section 1.1.1.1, I objective). A detailed Scanning Electron Microscopy (SEM) investigation of cell wall ultrastructures was then performed to evaluate their use as a new diagnostic tool for taxonomy (Section 1.1.2.1, II objective). Species identification represents a crucial step in the application of proxies given the specificity of the geochemical signature and the consequent need for specific calibrations. Two main geochemical proxies were tested in temperate calcareous red algae: trace and major elements including Mg, Li, Sr and B (Section 1.2.1.1, III objective) and boron isotopes (Sections 1.2.2.1 and 1.2.2.2, IV and V objectives). 5

1.4 SEM images of a longitudinal section through the perithallial long cells of *Lithothamnion corallioides* (a). The thin walls of two adjacent cell filaments are magnified in (b). Modified from Bracchi et al. [267]. 8

1.5 The longest instrumental records of CO_2 and pH variations, occurring from 1958 to 2019. Data: Mauna Loa `https://gml.noaa.gov/webdata/ccgg/trends/co2/co2_mm_mlo.txt`, ALOHA `http://hahana.soest.hawaii.edu/hot/hot-dogs/bextraction.html`. ALOHA pH and pCO_2 are calculated at *in situ* temperature from dissolved inorganic carbon and total alkalinity (measured from samples collected on Hawaii Ocean Time-series (HOT) cruises) using co2sys (Pelletier, v25b06). Modified from `https://www.pmel.noaa.gov/co2/file/Hawaii+Carbon+Dioxide+Time-Series`. 11

1.6 (a) The relative abundance of dissolved boron species in seawater, where [BT] = 432.6 $\mu mol\ kg^{-1}$, pK_B^* = 8.60 for the surface ocean (with S = 35, T = 25 °C and p = 1 bar, solid lines) and pK_B^* = 8.67 for the deep ocean (with S = 34.8, T = 2 °C and p = 401 bar, dashed lines) [89, 119]. (b) Boron isotope partitioning between dissolved $B(OH)_3$ and $B(OH)_4^-$ at T = 25 °C, S = 35, p = 1 bar, $\delta^{11}B_{sw}$ = 39.61‰ [95] and [BT] = 432.6 $\mu mol\ kg^{-1}$ [152]. α_{B3-B4} was either 1.0194 [99], 1.0272 [150] or 1.026 [209]. The grey box in (b) indicates the boron isotopic composition of modern marine carbonates. Modified from Hönisch et al. [31] 15

1.7 CO_2 seeps in Ischia (Italy) at the highest intensity venting zone (3-6 m depth). Modified from Gambi et al. [179]. 19

2.1 Map of the sampling sites in (a) Ischia, where *Corallina officinalis* and *Peyssonnelia* sp. were collected and (b) Methana, where *Amphiroa* sp. was collected. In Ischia, the venting area, including sites S3 and S2, is circled in grey. In Methana, the main venting site is close to N. Site F is located 200 m westward from the vents. Service Layer Credits: Esri, HERE, Garmin, (c) OpenStreetMap contributors and the GIS user community. 24

2.2 An example for each morphological category assigned to SEM images. (a) *Mesophyllum philippii* coaxial hypothallus (hypothallus category), (b) *Lithophyllum racemus* epithallial cells (curly bracket) with the underlying perithallus (epithallial cell and perithallus categories), (c) a magnification of *L. racemus* perithallial cells showing secondary crystallites (crystallites category), (d) a surface view of a *Lithophyllum pseudoracemus* sample (surface category). 27

2.3 *Corallina officinalis* (a) and *Peyssonnelia* sp. (b) collected in Ischia, stations S3 (samples s17 and s20, on the left) and S2 (samples s16 and s19, on the right) (Table 2.1). SEM observations were aimed at identifying any morphological modification in the calcified thalli grown in an acidified environment. An example of random points located to guide the analysis is shown in the left image (plus signs). 28

2.4 Examples of augmented images of a SEM image showing a *Lithophyllum racemus* conceptacle given the original image in (a). 29

2.5 Modified Visual Geometry Group 16 (VGG16) architecture adopted for SEM image classification. 31

3.1 Longitudinal sections of *Lithophyllum racemus* (samples s1 and s2) under SEM. (a) Fountain pattern in the arrangement of perithallial cells and growth bands (arrowheads). (b) Four epithallial cells (numbered); note the evidence of meristematic division (arrows). (c) Magnification of the inset in (b) to show a primary (PC), secondary (SC) and inner calcification (IC). (d) Perithallial cells with primary and secondary pit-connections; the cell wall area corresponds to the surface included between the two dashed lines. (e) Magnification of (d) to show perithallial thin PC and rod-shaped crystallites of the SC. (f) Conceptacles weakly protruding from the surface (white arrows). (g) A conceptacle chamber showing a well-developed calcified columella (arrow). (h) Magnification of the inset in (g) showing the secondary hypothallus (arrow). 46

3.2 Calcification of *Lithophyllum racemus* under SEM. (a) Calcified perithallial cells; (b) magnification of the inset in (a) showing rhomboidal crystallites of the primary calcification (PC) embedded in organic microfibrils. (c) Transverse section of the perithallus; (d) magnification of the inset in (c) showing the innermost calcified layer (IC). (e) Secondary hypothallus over the conceptacle pore canal in Fig. 3.1; (f) magnification of the inset in (e) showing regular rhomboidal crystallites of the hypothallial PC. 48

3.3 Longitudinal sections of *Lithophyllum pseudoracemus* (samples s3 and s4) under SEM. (a) The fountain-like arrangement of perithallial cell filaments that diverge toward the thallus surface. (b) Epithallial cells' primary calcification (PC), secondary calcification (SC), and the innermost calcified layer (IC). (c) Perithallus. (d) Depressed conceptacle in surface view (arrow). (e) Conceptacle chamber with no calcified columella and a trichocyte (arrow); (f) magnification of the inset in (e) showing the secondary hypothallus (arrow) over the pore canal. (g) PC and SC in the perithallus; (h) magnification of the PC and SC crystallites. 51

3.4 Calcification of *Lithophyllum pseudoracemus* under SEM. (a) Multiple layers of secondary calcification (SC) forming the thick cell wall; (b) magnification of the inset in (a) showing the contact of two SC layers (arrow). (c) Secondary hypothallus of the pore canal in Fig. 3.3; (d) magnification showing the rhomboidal crystallites in the hypothallial primary calcification (PC), the SC rods and the innermost calcified layer (IC). 52

3.5 Longitudinal sections of *Lithophyllum* cf. *racemus* sample s5 under SEM. (a) Epithallial calcified cells are covered by a thick cuticle and bordered by a primary calcification (PC), a secondary calcification (SC), and an innermost calcified layer (IC). (b) Conceptacle with a well-defined calcified columella (white arrow). (c) Secondary hypothallial cells in the proximity of a pore canal and IC; (d) magnification of the inset in (c) showing the SC rhomboidal crystallites and the PC rhomboids. 54

3.6 Longitudinal sections of *Lithophyllum* cf. *racemus* sample s6 under SEM. (a) The epithallial cell is bordered by the rods of the secondary calcification (SC), and the innermost calcified layer (IC). (b) The calcified perithallus. (c) Conceptacle with a short calcified columella (arrow). (d) The transverse section shows the SC and the primary calcification (PC). (e) The primary hypothallus growing over the substrate; (f) magnification of the inset in (e) showing multiple layers of hypothallial PC rhomboids and SC rods. 56

3.7 Results of the perithallial cell area measurement. The numbers inside the plots indicate the mean values. 57

3.8 Principal component analysis (PCA); (a) score plot and (b) loading plot of PCA on calcification data in both perithallial (P.) and epithallial (E.) cells. The plots model 83% of the total data variance. Variance proportions are shown along each component axis. Calcification types are evidenced with circles and classified in *Lithophyllum racemus* type and *Lithophyllum pseudoracemus* type. 58

3.9 Results of the perithallial SC thickness measurement. The numbers inside the plots indicate the mean values. 59

3.10 Mean values of the measurements in short and long cells of *Lithophyllum racemus* sample s2. The numbers inside the plots indicate the mean values for the cell wall area, cell lumen area, SC thickness and PC thickness. 60

3.11 Examples of SEM images belonging to the n.c. category: (a) *Lithophyllum racemus* pore canal; (b) a magnification showing perithallial cells near the pore canal. These features proved to be significant contributors to the correct classification of *Lithophyllum* spp. in the 2 and 3 class-CNNs (Table 3.6). 65

3.12 Number of SEM images classified in the 2, 3, and 4 class-CNNs that have been assigned to different categories. Percentages within each category represent the proportion of images correctly and incorrectly classified. 66

3.13 An example of the output from the three approaches (LIME, Saliency, and Grad-CAM) that shows the pixels that contribute the most to the CNN classification in the various models used (2, 3 and 4 class-CNNs). Positive and negative contributions to classification are coloured green and red in LIME, respectively. Brighter colour highlights the pixels that contribute the most to the class attribution in Saliency, whereas the most significant areas for the final classification have a warmer colour tone in the Grad-CAM visualisation. Every model correctly identified the SEM image as *Lithothamnion corallioides*, and it shows a magnification of the cell wall ultrastructure (crystallites category). 73

3.14 LIME, Saliency, and Grad-CAM techniques reveal the pixels that make the most significant contributions to CNN classification. (a) Magnification of the epithallial cell wall in *Lithophyllum racemus* demonstrates the significant contribution of calcification, formed by rod-shaped crystallites. (b) *Mesophyllum philippii* conceptacle shape focused by Saliency. (c) Starch grains within the perithallial cells of *L. racemus* did not impede correct identification. (d) The background beyond the epithallial cell of *Lithothamnion corallioides* was most likely responsible for this image's incorrect classification. 74

3.15 Correlation of Mg/Ca with Li/Ca and Sr/Ca. Spearman's coefficient r, the *p*-value, and the line equation are also given. 75

3.16 Mg/Ca in *Lithothamnion corallioides* collected at different sampling sites. The horizontal black lines indicate the median values; the black dots and the numbers inside the plot indicate the mean values. 76

3.17 Mg/Ca in the long and short cells of *Lithothamnion corallioides* collected at different sites. 77

3.18 Correlation between Mg/Li and seawater temperature. Data are shown for cultured *Clathromorphum compactum* from Anagnostou et al. [66] and *Lithothamnion corallioides* from this study, which shows results separately in long and short cells per sampling site. 78

3.19 Mg/Li in *Lithothamnion corallioides* collected in Morlaix Bay (sample s8). Note the lack of cyclic variations. In the timeline, the coldest and the warmest months per year have been reported. Mg/Li ratios in the missing bands (asterisks) have been calculated as the means of the values measured in warm and cold periods. . 79

3.20 Elemental ratios in *Lithothamnion corallioides* sample s8, collected in Morlaix Bay (scale bar: 200 μm). Mg, Li, and Sr/Ca exhibit cyclic variations that correspond to the local seawater temperature. The coldest and warmest months have been reported in the timeline, which correspond to dark and light bands of growth respectively. The element/Ca ratios in the missing bands (asterisks) were calculated as the average of the values measured in warm and cold periods. ORAS5 reanalysis was used to extract monthly temperature means. 80

3.21 Correlation B/Ca with temperature proxies in *Lithothamnion corallioides* collected in Morlaix Bay (sample s8). Spearman's coefficient r, the *p*-value, and the line equations are given. 81

3.22 B/Ca in *Lithothamnion corallioides* collected at different sampling sites. The horizontal black lines indicate the median values; the black dots and the numbers inside the plot indicate the mean values. 81

3.23 B/Ca in the long and short cells of *Lithothamnion corallioides* collected at different sites. 82

3.24 Correlation of growth rates and seawater temperature with B/Ca. Spearman's coefficient r, the *p*-value, and the line equations are given. Temperature variations (ΔT) are the differences in maximum and minimum temperatures recorded over 11 years of monthly reanalysis (ORAS5) (Section 2.2). The B/Ca means in long and short cells correspond to the maximum and minimum temperature, respectively. 82

3.25 (a) Samples s17 (*Corallina officinalis*) and (b) s20 (*Peyssonnelia* sp.) collected near CO_2 seeps in Ischia (Italy). Surficial damaged areas are indicated by arrows. Here, the first layers of epithallial cells were removed, exposing the underlying cells. 83

3.26 Spearman's correlation between $\delta^{11}B_{algae}$ (Table 3.12) and the proportion of aragonite over calcite in the algal samples (Table 3.11). Correlation significance at p<0.05. Colours indicate which order the sample belongs to. 88

3.27 Calibration data showing MC-ICP-MS measurements of $\delta^{11}B_{algae}$ versus solution $\delta^{11}B_{borate}$ for published calcareous red algal cultures [42, 43, 102] and wild-grown algae (this study). Shaded polygons show 0.90 confidence intervals, considering standard errors of replicate measurements in the $\delta^{11}B_{algae}$ and one standard deviation of 10000 Monte Carlo simulations in the $\delta^{11}B_{borate}$. Uncertainties for points other than *A. anceps* are shown in Figure 3.28. Note that all the calibrations plot above the 1:1 line (dotted line). Data are shown in Table 3.13. 92

3.28 Multi-specific calibration proposed in this study grouping all published MC-ICP-MS measurements of calcareous red algae. The shaded polygon shows 0.90 confidence intervals, considering standard errors of replicate measurements in the $\delta^{11}B_{algae}$ and one standard deviation of 10000 Monte Carlo simulations in the $\delta^{11}B_{borate}$. Note that all the points plot above the 1:1 line (dotted line). Data are shown in Table 3.13. 93

3.29 Principal component analysis (PCA); (a) score plot and (b) loading plot of PCA on XRD (Table 3.11), MC-ICP-MS (Table 3.12) and ^{11}B MAS NMR (Table 3.15) data of calcareous red algae. The plots model 92% of the total data variance. Variance proportions are shown along each component axis. *Peyssonnelia* sp. and *Polystrata* sp. belong to the order Peyssonneliales; *Mesophyllum philippii* belongs to the order Hapalidiales; all the other species are Corallinales. 95

3.30 ^{11}B MAS NMR spectra and deconvolution of Mg-calcite samples s2-4. The blue line indicates the experimental spectra, the red line the simulated spectra and the overlapping bottom lines indicate the deconvolution. Note the presence of two components in the BO_4 peaks. The determined NMR parameters are reported in Table 3.14 and A.8. 98

3.31 ^{11}B MAS NMR spectra and deconvolution of Mg-calcite samples s8, s12-23. The blue line indicates the experimental spectra, the red line the simulated spectra and the overlapping bottom lines the deconvolution. Note the presence of two components in both BO_3 and BO_4 peaks. The determined NMR parameters are reported in Table 3.14 and A.8. 99

3.32 ^{11}B MAS NMR spectra and deconvolution of Mg-calcite samples s14, s24-25. The blue line indicates the experimental spectra, the red line the simulated spectra and the overlapping bottom lines indicate the deconvolution. Note the presence of two components in both BO_3 and BO_4 peaks. Sample s24 has two BO_3 peaks in one of the two BO_3 components. The 6.1 ppm signal in sample s25 was ambiguous and not classified (n.c.). The determined NMR parameters are reported in Table 3.14 and A.8. 100

3.33 ^{11}B MAS NMR spectra and deconvolution of Mg-calcite samples s26-28. The blue line indicates the experimental spectra, the red line the simulated spectra and the overlapping bottom lines the deconvolution. Note the presence of two components in both BO_3 and BO_4 peaks. The determined NMR parameters are reported in Table 3.14 and A.8. 101

3.34 ^{11}B MAS NMR spectra and deconvolution of Mg-calcite sample s29 and aragonite samples s30-31. The blue line indicates the experimental spectra, the red line the simulated spectra and the overlapping bottom lines indicate the deconvolution. Note the 7.7 ppm signal in samples s30-31, ambiguous and not classified (n.c.). The determined NMR parameters are reported in Table 3.14 and A.8. 102

3.35 ^{11}B MAS NMR spectra and deconvolution of aragonite sample s32. The blue line indicates the experimental spectra, the red line the simulated spectra and the overlapping bottom lines indicate the deconvolution. Note the 7.2 ppm signal, ambiguous and not classified (n.c.). The determined NMR parameters are reported in Table 3.14 and A.8. 103

A.1 Temperature and carbon data in Aegadian Isl. at sampling depth (40 m). The temperature was extracted by 11 years of ORAS5 monthly mean reanalysis preceding the date of sample collection (August 1993). Dissolved inorganic carbon (DIC) and pH data were extracted by CMEMS biogeochemical models spanning 1999-2017. 120

A.2 Temperature and carbon data in Elba at sampling depth (45 m). The temperature was extracted by 11 years of ORAS5 monthly mean reanalysis preceding the date of sample collection (December 1990). Dissolved inorganic carbon (DIC) and pH data were extracted by CMEMS biogeochemical models spanning 1999-2017. 121

A.3 Temperature and carbon data in Pontian Isl. at sampling depth (66 m). The temperature was extracted by 11 years of ORAS5 monthly mean reanalysis preceding the date of sample collection (July 2016). Dissolved inorganic carbon (DIC) and pH data were extracted by CMEMS biogeochemical models spanning 1999-2017. 122

A.4 Temperature and carbon data in Morlaix at sampling depth (12 m). The temperature was extracted by 11 years of ORAS5 monthly mean reanalysis preceding the date of sample collection (May 1991). Dissolved inorganic carbon (DIC) and pH data were extracted by CMEMS biogeochemical models spanning 1999-2017. 123

A.5 Li/Ca, Sr/Ca and Mg/Li in *Lithothamnion corallioides* collected in different sampling sites. The horizontal black lines indicate the median values; the black-filled circles and the numbers inside the plot indicate the mean values. 123

A.6 X-ray powder diffraction patterns for samples s15-23. 129

A.7 Rietveld refinement results for *Peyssonnelia* sp. sample s18 based on the presence of aragonite and calcite phases. 130

Chapter 1

Introduction: Background Theory and Objectives

1.1 Calcareous red algae (Rhodophyta)

Calcareous red algae are a diverse group of marine species that are widely recognised for their global ecological importance and provide a variety of ecosystem services, including habitat formation [5, 9, 70, 75, 86, 91, 96, 266] and carbonate production [50, 71, 98, 161, 166, 264]. This is due to the fact that they are marine calcifiers, which precipitate calcium carbonate in their cell walls as high-Mg calcite or aragonite along polysaccharide microfibrils [50, 144, 178, 183, 186]. The most abundant groups are the calcitic Corallinophycidae Le Gall & G.W. Saunders, also known as "coralline algae" and the aragonitic Peyssonneliales Krayesky, Fredericq, & J.N. Norris. Calcareous red algae are found on hard substrata throughout the marine photic zone [83], and are especially common in Mediterranean benthic communities, where they range from the intertidal zone to circalittoral depths [49, 85]. In the Mediterranean, non-geniculate "crustose" forms, constituting maerl beds and coralligenous reefs [58, 71, 269] (Fig. 1.1), enhance seafloor structural complexity and provide substrate for the settlement, protection, and reproduction of a variety of marine species, increasing habitat biodiversity [12, 70].

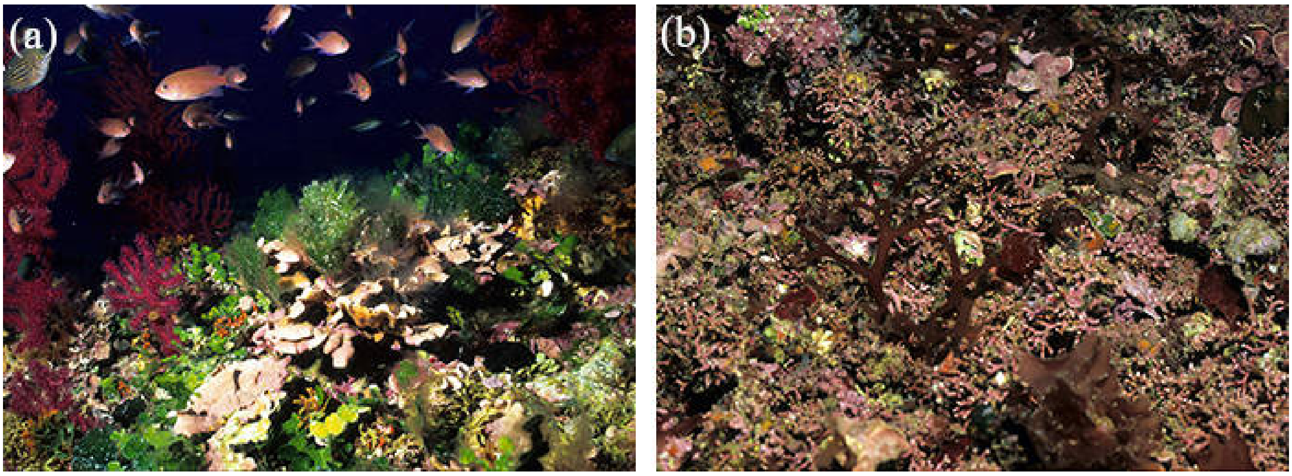

Figure 1.1: An example of a Mediterranean coralligenous community (a), and a maerl bed (b) from Islas Columbretes, Spain. Modified from Rindi et al. [81]. Copyright: Enric Ballesteros.

The morphological characteristics of cells and reproductive structures, as well as the organisation of the thallus (i.e., the undifferentiated algal body [78]), are generally used to differentiate between species [47, 48, 111, 272], either by light microscopy of thin sections or by high-resolution Scanning Electron Microscopy (SEM) [135]. The basic structure of an algal thallus is given by a basal hypothallus (not always evident), with cell filaments growing tangentially to the substrate and then bending toward the thallus surface, becoming more or less perpendicular to the hypothallus, forming the perithallus. Finally, there are one or more epithallial cells that terminate each perithallial filament and are in contact with the external environment. The reproductive structures are called conceptacles and can be found in both sexuate and asexuate phases of the algal life cycle. Tetrasporangial conceptacles produce spores for asexual reproduction, while spermatangial and carpogonial conceptacles are respectively the male and female reproductive structures [103]. A brief description of some of the most common Mediterranean species is given hereafter. *Lithothamnion corallioides* (P. Crouan & H. Crouan) P. Crouan & H. Crouan is widely distributed in the Mediterranean Sea and the north-eastern Atlantic Ocean, from Scotland to the Canary Islands [27, 164, 249], where is typically found in maerl beds [16, 55, 189, 216, 242]. It produces rhodoliths [56], in the form of free-living branchlets or nodules that are frequently sterile [164]. In terms of micro-anatomy, *L. corallioides* has rectangular perithallial cells connected by multiple fusions, and the epithallus is characterised by multiple layers of flattened cells, typically flared in the first layer below the surface [47].

Lithothamnion minervae Basso, commonly encountered in Mediterranean rhodolith beds, has a significant fossil record [268] and is particularly promising in registering temperature and pH records [77]. *L. minervae* has oval to subrectangular cells in the perithallus, where multiple cell fusions are common [47]. The hypothallus is composed of up to five cell filaments, and conceptacles have a typical cavity on top, which is left by perithallial filaments that grow above [47, 54]. The non-geniculate *Lithophyllum racemus* (Lamarck) Foslie is frequently found together with *L. corallioides* and *L. minervae* [16, 27, 55, 189, 216, 242]. It is a Mediterranean endemic coralline alga that forms unattached globular rhodoliths [49, 56] and has a typical "praline" morphotype [49, 56, 57, 65, 72, 80, 87, 258] with many densely spaced and apically broadened branches [57] (Fig. 1.2). A phylogenetic study [6] revealed the previously unknown species *Lithophyllum pseudoracemus* Caragnano, Rodondi & Rindi, which had been mistaken for the morphologically similar *L. racemus* (Fig. 1.2). Secondary pit connections join the perithallial cells of adjacent cell filaments in both *L. racemus* and *L. pseudoracemus*, and there can be up to five layers of flattened epithallial cells [6, 57].

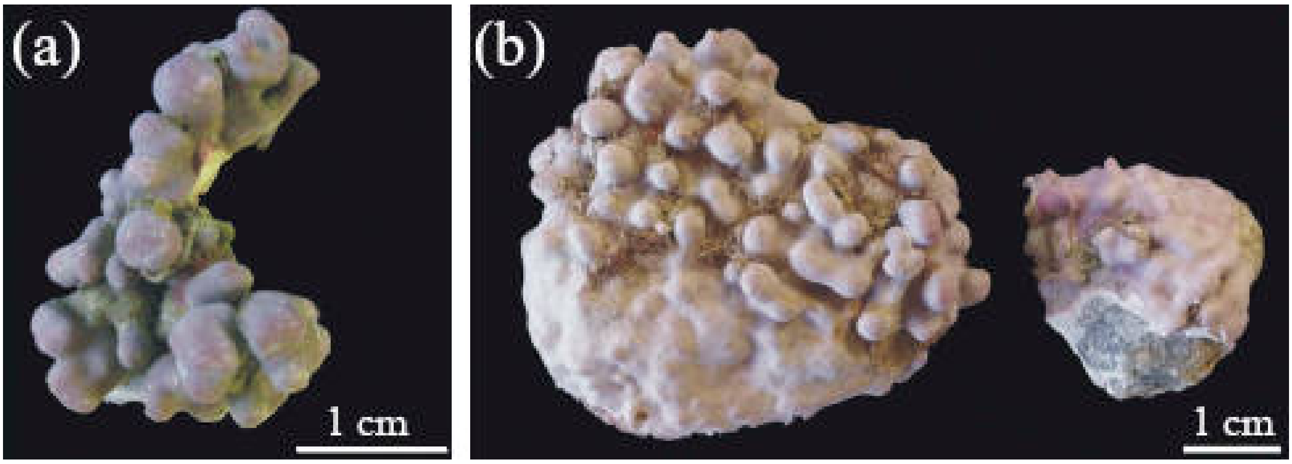

Figure 1.2: Fruticose specimens of *Lithophyllum racemus* (a) and *Litophyllum pseudoracemus* (b). Modified from Caragnano et al. [6].

Mesophyllum philippii (Foslie) Adey, another common species of coralline alga in Mediterranean waters, is one of the main bioconstructors of the Mediterranean coralligenous concretions, occurring in the form of layered crusts [263], sometimes with protuberances. *M. philippii* is characterised by a thick coaxial hypothallus and a single layer of rounded to flattened epithallial cells. Cell fusions are common in perithallial cells, and buried multiporate sporangial

conceptacles, which are hemispherical in shape, are typically infilled with large, irregular cells [48, 263]. Peyssonneliales have a crustose prostrate thallus that is attached to the substrate by uni- or multicellular rhizoids and exhibits partial or total calcification in the form of aragonite crystals [211]. The genus *Peyssonnelia* is found from the intertidal zone to the deep coastal detritic bottoms [238] and is distinguished by the presence of a basal hypothallial layer, from which departs a dorsal perithallus devoid of secondary pit-connections [168]. Reproductive characters are frequently absent or exhibit little variation among species [219, 244].
Morphological-based species identification in calcareous red algae can be challenging, given their general plasticity. The increasing use of molecular systematic tools has revealed numerous cases of cryptic diversity [6, 7, 11, 14, 160] and several systematic revisions based on molecular genetics have been produced [2, 7, 11, 39, 134, 139, 160, 163]. Paleontologists need a reliable taxonomy to reconstruct the paleoecology and the paleoclimate [52, 88, 196, 268]. In particular, the application of geochemical proxies in paleoclimate research needs specific calibrations, since differences in geochemical signatures among species can be very relevant [42, 77]. As a consequence, there is a growing interest in developing new diagnostic tools for the taxonomic identification of coralline algae [84, 267], which rely on morphological parameters that could be used even in fossils where genetics is not possible. Recent observations at the micro- and nanoscale revealed a diagnostic potential of the calcified ultrastructures for taxonomy [84, 267] and new insights into coralline algal biomineralization that will be further discussed in Section 1.1.2. This research broadly focused on two areas: the taxonomy and biomineralization of calcareous red algae, and their use as palaeoenvironmental proxies. These aspects are deeply interconnected and a graphical representation of this research approach is given in Figure 1.3.

1.1.1 Supervised classification

Machine learning techniques are a powerful tool for automating classification, assisting human operators in processing massive amounts of data and potentially revealing new diagnostic features through post-doc analyses. Artificial neural networks are popular machine learning algorithms whose goal is to find the set of weights that minimise a defined loss function over

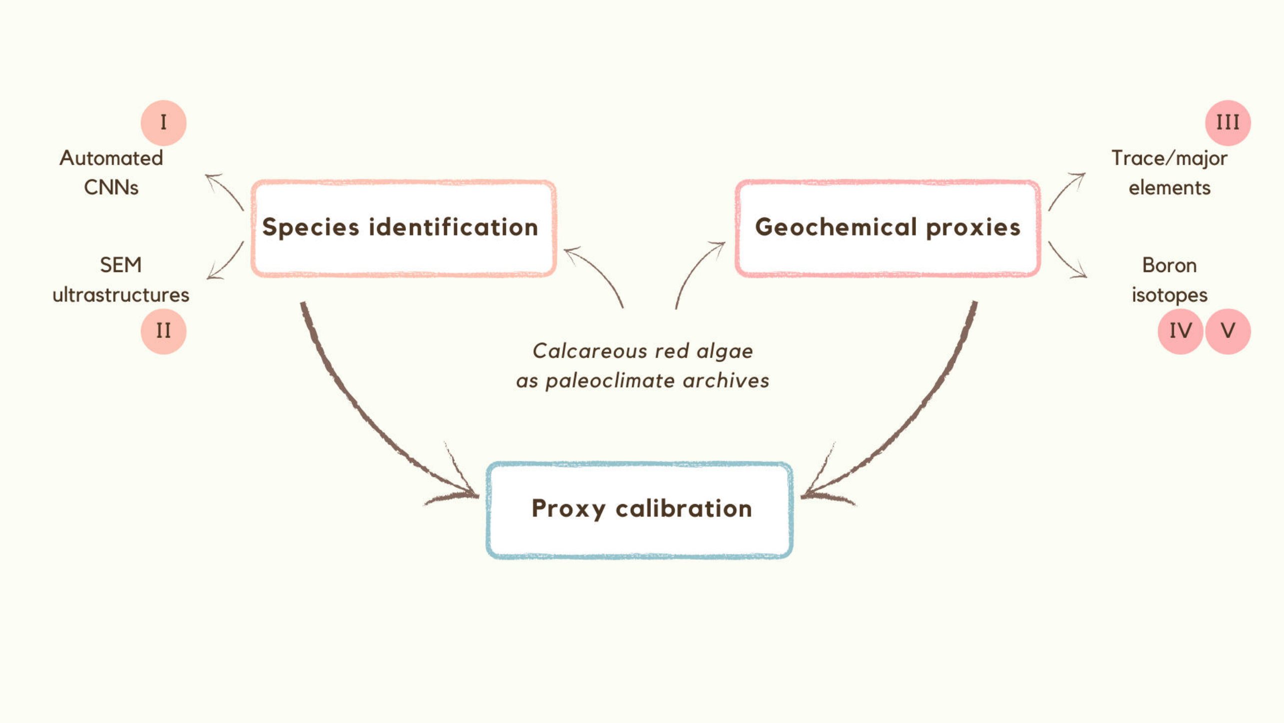

Figure 1.3: Conceptual map summarizing the approach used in this research project for the study of the significance of calcareous red algae as paleoclimate archives. Two main aspects were addressed: the problem of taxonomic identification and the application of geochemical proxies. A novel approach to algal classification was tested using Convolutional Neural Networks (CNNs) (Section 1.1.1.1, I objective). A detailed Scanning Electron Microscopy (SEM) investigation of cell wall ultrastructures was then performed to evaluate their use as a new diagnostic tool for taxonomy (Section 1.1.2.1, II objective). Species identification represents a crucial step in the application of proxies given the specificity of the geochemical signature and the consequent need for specific calibrations. Two main geochemical proxies were tested in temperate calcareous red algae: trace and major elements including Mg, Li, Sr and B (Section 1.2.1.1, III objective) and boron isotopes (Sections 1.2.2.1 and 1.2.2.2, IV and V objectives).

the predicted and real classes [221]. This is accomplished through an iterative process that alternates between a feed-forward step in which weights connecting different layers are used to compute the output and a backpropagation step in which the weights are adjusted by computing the gradient of the loss function. Deep learning is commonly used to describe artificial neural networks with more than two hidden layers. It avoids the time-consuming and difficult feature extraction process required by other classification methods in the context of image classification [35, 275]. Indeed, deep learning provides end-to-end learning by automatically extracting information from raw data and eliminating all extra overheads associated with selecting feature descriptors and feature selection. In particular, Convolutional Neural Networks (CNNs) have emerged as the cutting-edge image recognition method [105]. CNN architectures have been used in a variety of ways, but in general, they consist of stacked convolutional and pooling layers, followed by one or more fully connected layer(s). CNNs are built around convolutional layers, which are essentially pattern extractors using a set of trainable filters or kernels. The inputs are convolved with the weights, which are optimized during the training phase, to produce a new representation of the original images, that is, a new feature map. The pooling layer compresses the information in these feature maps, usually keeping the maximum value (i.e. max-pooling layer). Convolutional and pooling layers are followed by fully connected or dense layers, which are made up of neurons that are connected to all of the neurons in the previous and subsequent dense layers. The number of neurons in the output layer is equal to the number of classes to be predicted for classification purposes, and each of these neurons outputs the probability that the image belongs to the corresponding class. CNNs are data-hungry, which means they require a large number of training images to be trained on [105]. Thus, for small datasets (less than a thousand images), it is preferable to begin with a pre-trained network, which is a CNN whose weights have already been trained on thousands of images [1, 112]. Unlike random weights, pre-trained CNN weights have already been trained to distinguish some simple and common geometrical patterns. To obtain the desired output, the last fully connected layer of the pre-trained CNN is typically substituted, which may imply a different number of classes. The CNN can then be trained on the images of interest, as in the case of transfer learning and/or fine-tuning depending on the training procedure. In the former case, all or some of the CNN layers will be trained on the images of interest for a few epochs, whereas the latter involves tuning some hyperparameters (such as the learning rate) to adapt the network to the new classification purpose. CNNs have already been used successfully to classify fish species [61, 126], bivalves [239], and foraminifera [231]. The classified images in such cases were photographs of the entire organism. Liu and Song [275] achieved model accuracy comparable to human classifiers by finetuning on pre-trained CNNs for the recognition of different taxonomic groups of microfossils observed in thin sections. Modarres et al. [185] used CNN for SEM image recognition of generic nanostructures, the majority of which were not of biological origin. Prior to this research, CNNs have never been used on SEM images for taxonomic identification, and there have been no previous attempts to classify calcareous red algae using CNNs.

1.1.1.1 I Objective: Deep learning for automatic classification

SEM images of the calcareous red algae *L. corallioides*, *M. philippii*, *L. racemus* and *L. pseudoracemus* were classified using CNNs. Each image was processed along with the vectorized representation of the observed morphological features (i.e., categories) to enrich the models. Six relevant morphological categories were considered, including the calcified cell wall ultrastructure, and each image was manually paired with one or more of them.

Three models were trained on the same images that were classified at various taxonomic levels:

1. to discriminate *L. pseudoracemus* from all the other species (2 class-CNN model);
2. to classify the three genera (3 class-CNN model);
3. to classify the four species (4 class-CNN model).

Finally, the model's utility was tested as a diagnostic tool for the classification of two samples morpho-anatomically similar to *L. racemus* and *L. pseudoracemus*, lacking genetic characterisation and generically referred to as *L.* cf. *racemus*.

1.1.2 Biomineralization

Knowing the geochemical incorporation of elements and molecules within the algal thallus requires understanding the biomineralization mechanism. The mineralized thallus of calcareous red algae (Fig. 1.4) provides them with strength and protection from grazing and other disturbances [24], and it can be preserved in the fossil record over geological time [106, 161, 247, 265, 268, 269]. The cell walls of calcareous red algae are either composed of aragonite or, more commonly, high-magnesium calcite with more than 8-12 mol% $MgCO_3$ by the endothermic substitution of Ca^{2+} ions with Mg^{2+} [144]. Each carbonate polymorph has its own elemental and isotopic composition and forms a unique equilibrium with seawater [100]. Previous research on coralline algae has found aragonite, brucite, and dolomite crystals, in addition to calcite, which are thought to be secondary precipitation events within the empty conceptacles and other micro-cavities [50, 143, 182, 252].

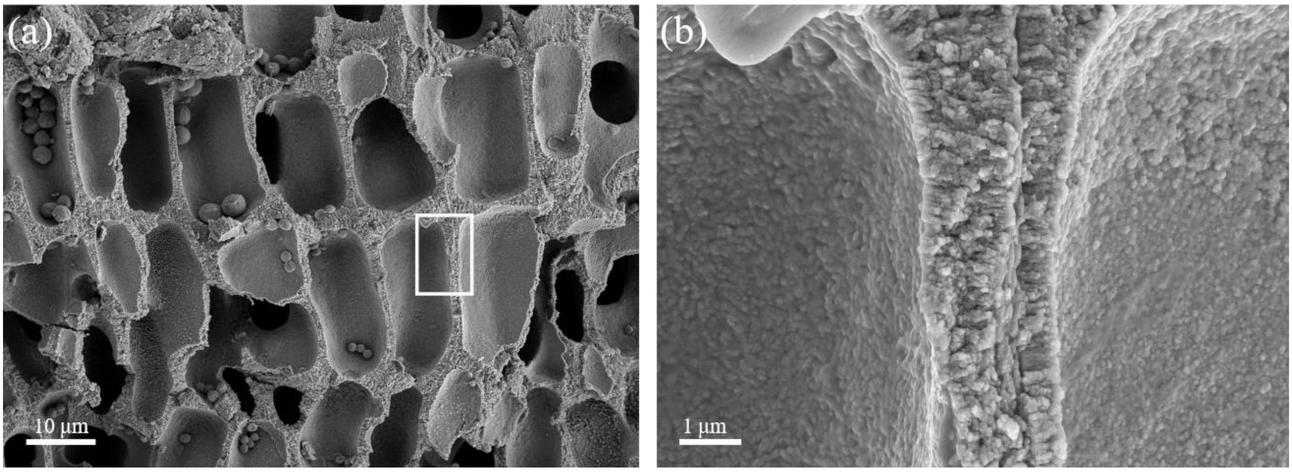

Figure 1.4: SEM images of a longitudinal section through the perithallial long cells of *Lithothamnion corallioides* (a). The thin walls of two adjacent cell filaments are magnified in (b). Modified from Bracchi et al. [267].

Longitudinal sections of coralline algae show light and dark bands alternating, which indicate a seasonal growth pattern [9, 47, 48, 109, 189, 189]. Dark bands are formed by short, thick-walled cells, whereas light bands are formed by long, thin-walled cells [201, 267] (Fig. 1.4). Light bands with higher Mg content correspond to warm periods of growth, while dark bands with low Mg content correspond to cold periods [117, 222]. Hereafter, short cells are referred to as slow-growing cells within dark bands produced during the cold season, while long cells are referred to as fast-growing cells within light bands produced during the warm season [9, 48, 79, 201, 267] (Fig. 1.4). Annual growth bands can be used to determine the age of an alga as well as for high-resolution geochemical analyses [4, 117, 201]. The cell wall calcification is made up of nanometric crystallites that differ in shape among families and even genera [84, 267]. Secondary calcification (SC) is made up of radial high-Mg calcite crystallites, whereas primary calcification (PC) is constituted by tangentially arranged crystallites, which are usually visible at the boundary between two adjacent cell filaments [79, 84, 90, 183, 267, 274]. The pattern of mineralization has been widely used for taxonomic identification in other calcifying marine organisms such as foraminifera [36, 121, 137], coccolithophores [23] and corals [22, 59, 123, 127], demonstrating consistency with molecular phylogeny. Recent research into coralline algal cell walls and their calcified nanostructures supports the hypothesis that the crystallite shape is actively determined by the alga [84, 267]. SEM analysis of a diverse collection of coralline algae revealed family-specific patterns in the shape of the nanostructures that comprise PC and SC [84]. Auer and Piller [84] correlated cell wall micro- and nanomorphology with molecular phylogeny, classifying different genera based on crystallite shape in epithallial and meristematic cell walls. Recent studies on the cell wall ultrastructure of *L. corallioides* agreed on this classification, revealing a consistent pattern in the crystallite shape and arrangement that appears to be unaffected by the environment [267]. Aside from the taxonomic implications, these findings support the previously controversial hypothesis of a biologically controlled biomineralization. Controlled biomineralization in calcareous red algae was initially supported [176], but recently questioned by de Carvalho et al. [64] and Nash et al. [180]. New insights into the biomineralization process of high-Mg calcites revealed that crystallite unities are multiple mineral phases rather than single crystals, as observed in the calcareous red algae *Jania* sp. and *Corallina* sp. [194, 195]. They show a low-Mg calcite matrix containing incoherent high-Mg calcite nanoparticles formed by the spinodal decomposition of an amorphous calcium carbonate (ACC) phase. Corals had previously demonstrated the presence of an ACC precursor phase [255]. These new findings spark an interesting debate about the incorporation mechanism of geochemical proxies, which may not be as simple as previously thought.

1.1.2.1 II Objective: Calcification traits in cryptic species

The two morphologically similar but genetically distinct species *L. racemus* and *L. pseudoracemus* were analysed by highly resolved SEM imagery to test the suitability of putative descriptors based on calcification traits as new taxonomic characters for calcareous red algae identification at the species level. The ultrastructural calcification traits in both PC and SC and various classical morphological descriptors were measured in molecularly identified *L. racemus* and *L. pseudoracemus* samples, and in *L.* cf. *racemus* samples lacking molecular phylogeny to highlight possible species-specific patterns.

1.2 Calcareous red algae as paleoclimate archives

Climate Change is one of the most pressing issues of our time, and the most effective tool for forecasting future climate evolution is knowledge of former variability, particularly from the recent past [28, 146]. Accurate instrumental environmental data on the Globe only go back to the 1850s and are available in a few locations [203] (Fig. 1.5); thus, reconstructions of the past must rely on paleo-proxies. The global average climate has warmed since industrialization in the 1850s [104], with temperatures rising by nearly 1°C [118]. Between 1959 and 2014, approximately one-third (27%) of the carbon dioxide released by burning hydrocarbons was dissolved in the sea, lowering the pH by 0.1 part of a pH unit compared to pre-industrial levels [45, 256] (Fig. 1.5). Despite this evidence, natural climate variability may obscure anthropogenic Climate Change. As a result, comparing previous climate fluctuations to recent changes allows us to assess the magnitude of anthropogenic impacts in the current climate scenario. Along with global warming, ocean acidification is the major anthropogenic perturbation of today's Oceans [25, 28, 97, 128, 147, 218, 259], posing a serious threat to marine calcifiers such as calcareous red algae [50, 132, 144, 241]. Acidification reduces the saturation state of calcium carbonate, which is the component of habitat-forming species of critical ecological importance including calcareous red algae and corals [50, 78, 107, 108, 132, 144, 208]. Calcite is less soluble than aragonite, but its solubility increases with increasing magnesium relative molar abundance ($MgCO_3$) [108]. Corallinophycidae, which are high-Mg calcite (containing more than 8-12 mol% $MgCO_3$) [144], are thus particularly sensitive to pH changes [50, 78, 241, 261]. A further increase in CO_2 concentration in the atmosphere is expected in the future, causing the carbonate compensation depth and the lysocline to rise, thereby further increasing the dissolution threshold of carbonates that compose calcareous organisms and sediments.

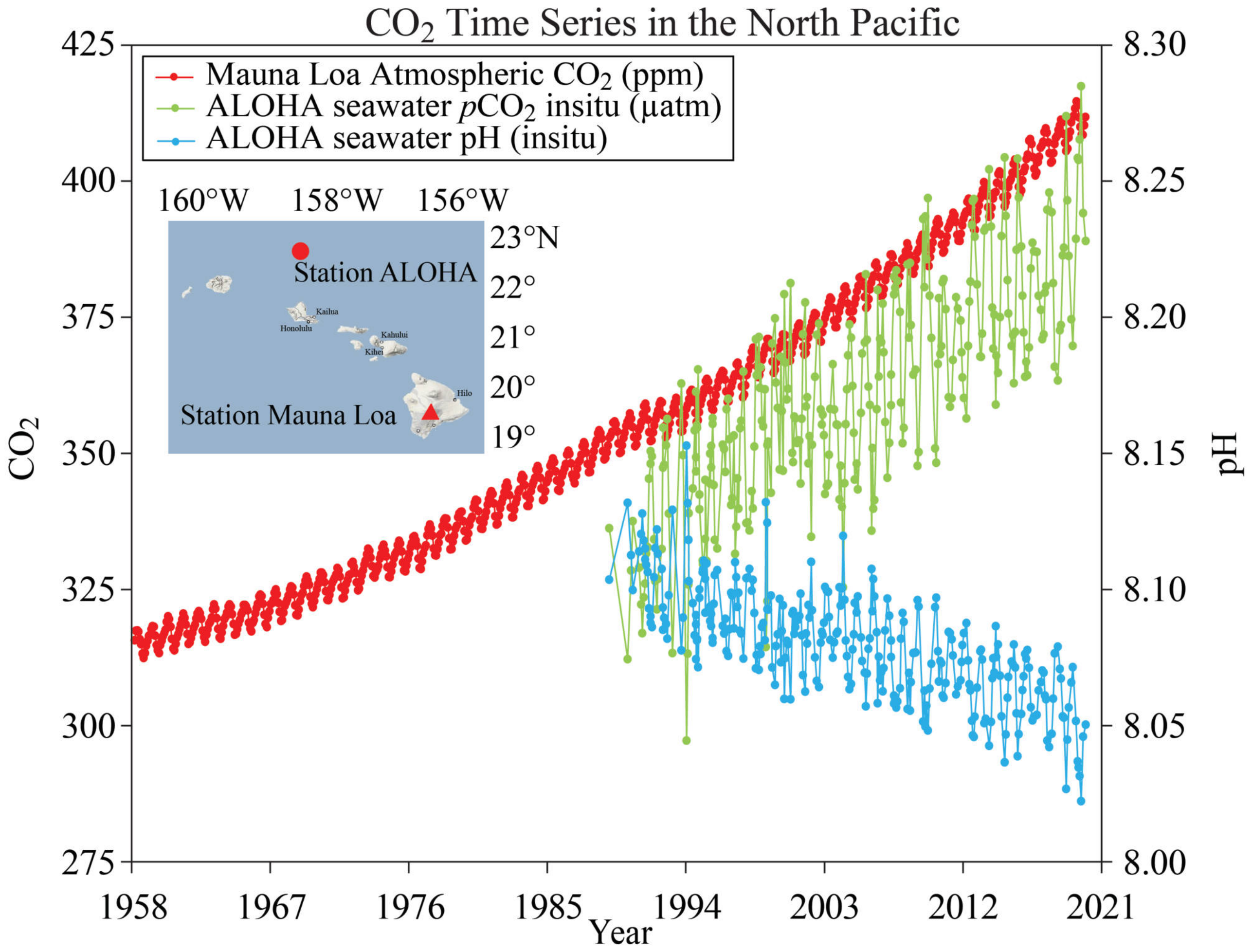

Figure 1.5: The longest instrumental records of CO_2 and pH variations, occurring from 1958 to 2019. Data: Mauna Loa `https://gml.noaa.gov/webdata/ccgg/trends/co2/co2_mm_mlo.txt`, ALOHA `http://hahana.soest.hawaii.edu/hot/hot-dogs/bextraction.html`. ALOHA pH and pCO_2 are calculated at *in situ* temperature from dissolved inorganic carbon and total alkalinity (measured from samples collected on Hawaii Ocean Time-series (HOT) cruises) using co2sys (Pelletier, v25b06). Modified from `https://www.pmel.noaa.gov/co2/file/Hawaii+Carbon+Dioxide+Time-Series`.

Several studies on the effects of acidification in coralline algae have been conducted [76, 78, 181, 182, 198, 199, 241]. Significant negative effects were reported, including thallus weakening and altered skeletal mineralogy with high-Mg calcite replaced by gypsum [199]. With decreasing seawater pH near CO_2 seeps in Ischia (Italy), the abundance of calcifying organisms, including coralline algae, declines, favouring the settlement of fleshy algae [140]. The same phenomenon is observed in Methana, where decreasing seawater pH results in a generalized loss of coralline algae, with an increase in the settlement of canopy-forming macroalgae [37], thus confirming the susceptibility of coralline algae to changes in seawater carbonate chemistry. Nonetheless, coralline algae have demonstrated some resistance to the pH drop. Laboratory experiments have revealed evidence of species-specific biological up-regulation of calcifying fluid pH in response to ambient pH manipulations [42, 43], as previously observed in corals [43, 172, 234], implying that algae could promote calcification even when growing in an acidic environment. The impact of Climate Change on the Mediterranean Sea is particularly devastating [73, 159, 230, 254]; climate models predict that it will be one of the regions most affected by the ongoing warming trend and an increase in extreme events [38, 214]. It has also been proposed that the Mediterranean basin could serve as a model for the World's Oceans to investigate the consequences of Climate Change [38], so understanding its future climatic pattern is of particular interest. Records in temperate regions are primarily based on terrestrial proxies, which do not always reflect marine environmental conditions [116]. Coralline algae are the marine algae with the richest fossil record [106, 262], and they play an important role in palaeontology. Their calcified thallus can be preserved over geological time, allowing researchers to investigate their geochemical interactions with the paleoenvironment [33, 116]. During biomineralization, calcareous red algae incorporate major and trace elements that mirror the chemical properties of their growth environment, becoming important proxy records for paleoecology and palaeoceanography [77, 114, 117, 237]. Coralline algae are well-suited for paleoclimate reconstructions on weekly to multi-centennial time scales because they are globally distributed and particularly long-lived, and they lack an ontogenetic growth trend (i.e. they do not slow down growth with age, unlike bivalves) [33, 116, 200]. Optical microscopy of algal thin sections reveals bands that reflect the growth pattern [47, 48, 109, 189] (Section 1.1.2), similar to tree rings [79], which can be targeted for high-resolution geochemical analyses. Geochemical studies of marine coralline algae have been conducted since the mid-1990s. There are still knowledge gaps in their calcification and geochemistry, both of which are critical topics for their use in paleoenvironmental reconstructions. This is exacerbated in Mediterranean calcareous red algae, which are understudied since the majority of the literature is based on high-latitude or tropical species.

1.2.1 Trace and major element/Ca

Trace element variations in marine calcareous species help reconstruct changes in environmental parameters that characterised seawater during their growth [215, 237]. The high Mg-calcite of calcareous red algae records ambient seawater temperature [117, 181, 200, 236], primary productivity [10, 210] and salinity [202], making it an ideal paleoclimate archive. Most of the data come from high-latitude [66, 200] and tropical species [4, 196], with mid-latitude coralline algae receiving less attention. Laser Ablation Inductively Coupled Plasma Mass Spectrometry (LA-ICP-MS) on growth bands enables the high-resolution analysis of a wide range of trace elements in solid-state samples. In biogenic carbonates, this technique has been widely used to extract records of seawater temperature, salinity, and water chemistry [34, 77, 114, 236, 237, 253]. Chave [156] and Chave and Wheeler [157] discovered cyclic variations in Mg content within the algal thallus and demonstrated a link between Mg cycles and seasonal temperature fluctuations. Later, Moberly [225] suggested that Mg variations are affected by growth rates, which are in turn function of seawater temperature, light, and physiological cycles. In corallines, the Mg/Ca ratio is a well-established SST (Sea Surface Temperature) proxy [77, 114, 116, 200, 233]. In *Lithothamnion glaciale* Kjellman 1883 [200], *Clathromorphum* spp. [237], *Lithophyllum* sp. [4] and *Sporolithon* sp. [196], Sr/Ca and Li/Ca ratios also showed significant positive correlations with temperature. In cultured *C. compactum* (Kjellman) Foslie 1898 [66] and in empirical studies on *Lithophyllum* sp., *Hydrolithon* sp. and *Neogoniolithon* sp. [130], Mg/Li revealed an exponential relationship with temperature. On the other hand, the Mg/Li calibration did not show any improvement in the Mg/Ca or Li/Ca proxies in *Lithophyllum* spp. from Caragnano et al. [3, 4]. In various empirical studies on benthic foraminifera [133, 141, 142] and synthetic aragonite [171], the boron-to-calcium ratio (B/Ca) proved to be informative about past seawater CO_3^{2-} concentrations. The majority of boron research has focused on its isotopic composition [42, 77, 114, 151, 188, 204], with less attention paid to B/Ca records, particularly in coralline algae. According to recent research, B/Ca is a function of seawater pH as well as other environmental variables such as temperature, the effect of which should be considered when attempting to reconstruct surface ocean pH and atmospheric pCO_2 [149, 155, 191]. It is critical to recognise the influence of multiple factors on a proxy in order to achieve the highest reliability of climate reconstructions [102, 149]. The effects of temperature and growth rate on B incorporation have recently been studied using experiments on both synthetic and biogenic carbonates [102, 124, 142, 149, 191, 229, 260]. A culture experiment on the coralline alga *Neogoniolithon* sp., in particular, revealed a positive correlation of B/Ca with growth rate and a negative correlation with Sr/Ca, the latter being proposed as a proxy for dissolved inorganic carbon (DIC) [102]. Furthermore, a culture experiment on the high latitude species *C. compactum* revealed that temperature had no effect on B/Ca and had a significant inverse relationship with growth rate [66]. The factors influencing B incorporation in calcareous red algae are still being debated, and no studies on the correlation between temperature proxies (Mg, Sr, Li/Ca) and B/Ca have been conducted thus far.

1.2.1.1 III Objective: Multiple influences on Mg, Li, Sr and B/Ca

LA-ICP-MS analysis was performed on wild-grown coralline algae belonging to *L. corallioides* species and spread across a large geographical area, providing the first data of putative temperature proxies (Mg/Ca, Sr/Ca, Li/Ca, Mg/Li) and B/Ca from various geographic settings and depths across the Mediterranean Sea and the Atlantic Ocean. The effect of temperature and growth rate on B incorporation was investigated, which could be important in determining the accuracy of B/Ca as a proxy for the seawater carbonate system.

1.2.2 The boron isotope-pH proxy

Boron in the ocean exists in two molecular species: trigonally coordinated boric acid $B(OH)_3$ and tetragonally coordinated borate ion $B(OH)_4^-$, which are linked by the acid-base equilibrium reaction:

$$B(OH)_3 + H_2O \leftrightarrow B(OH)_4^- + H^+ \tag{1.1}$$

that clearly shows the dependence of the two species' concentrations on pH variations (-log$[H^+]$), with the relative abundances of B species being pH-controlled (Fig. 1.6).

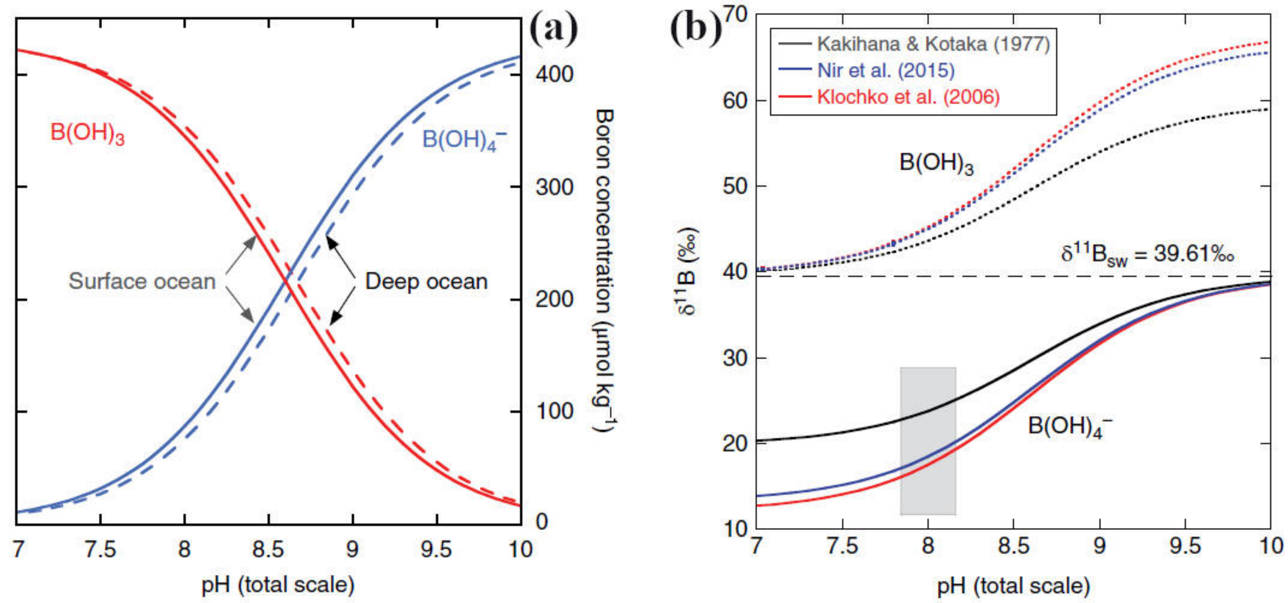

Figure 1.6: (a) The relative abundance of dissolved boron species in seawater, where [BT] = 432.6 $\mu mol\ kg^{-1}$, $pK_B^* = 8.60$ for the surface ocean (with S = 35, T = 25 °C and p = 1 bar, solid lines) and $pK_B^* = 8.67$ for the deep ocean (with S = 34.8, T = 2 °C and p = 401 bar, dashed lines) [89, 119]. (b) Boron isotope partitioning between dissolved $B(OH)_3$ and $B(OH)_4^-$ at T = 25 °C, S = 35, p = 1 bar, $\delta^{11}B_{sw} = 39.61$‰ [95] and [BT] = 432.6 $\mu mol\ kg^{-1}$ [152]. α_{B3-B4} was either 1.0194 [99], 1.0272 [150] or 1.026 [209]. The grey box in (b) indicates the boron isotopic composition of modern marine carbonates. Modified from Hönisch et al. [31]

The equilibrium constant of the reaction shown in Eq. 1.1, K_B^*, is $10^{-8.6}$ which corresponds to a pK_B^* of 8.6, very close to seawater pH. As the pH of the surrounding environment decreases (increases), the equilibrium between the two species shifts in favour of boric acid (borate ion) (Fig. 1.6). Boron has two stable isotopes: the heavier ^{11}B (80.1% in abundance) and the lighter ^{10}B (19.9% in abundance), with an enrichment factor ϵ_{B3-B4} of 27.2 ± 0.6% [150]. The isotopic composition of seawater ($\delta^{11}B_{sw}$) varies with the isotopic composition of $B(OH)_3$ and $B(OH)_4^-$, which in turn vary their concentrations with pH. Given the differences in coordination between the two species and the corresponding changes in the B-O vibrational frequencies of chemical bonds, this equilibrium undergoes isotopic fractionation, resulting in boric acid being isotopically heavier than borate (Fig. 1.6). During calcite precipitation, boron is incorporated into marine carbonates, particularly the cell walls of calcareous red algae. Carbonates' B isotopic composition ($\delta^{11}B_{CaCO_3}$) is similar to that of borate in seawater ($\delta^{11}B_{borate}$) [18, 205] (Fig. 1.6); thus, it has been proposed that carbonates preferentially incorporate borate over boric acid in seawater. As a result, the $\delta^{11}B_{CaCO_3}$ should increase with pH in accordance with the $\delta^{11}B_{borate}$. This principle underpins the $\delta^{11}B$ proxy, which is used to reconstruct past seawater pH [29, 31, 94, 133], using the equation

$$pH = pK_B^* - log(-\frac{\delta^{11}B_{sw} - \delta^{11}B_{CaCO_3}}{\delta^{11}B_{sw} - \alpha_{B3-B4} \times \delta^{11}B_{CaCO_3} - \epsilon_{B3-B4}}) \tag{1.2}$$

where: pK_B^* is the dissociation constant for the boric acid/borate equilibrium in seawater; $\delta^{11}B_{sw}$ is the seawater isotopic composition, which is 39.61 ± 0.04‰ in the modern ocean [95]; α_{B3-B4} is the aqueous boron isotope fractionation factor, which is 1.0272 ± 0.0006 [150]; and ϵ_{B3-B4} is the enrichment factor as

$$\epsilon_{B3-B4} = (\alpha_{B3-B4} - 1) \times 1000 \tag{1.3}$$

Several calibrations for foraminifera [94, 125, 133, 187] and corals [67, 240] indicate that marine organisms exert species-specific control over B incorporation. York fits [63] of the following equation can be used to calculate species-specific calibrations, with analytical uncertainties in $\delta^{11}B_{CaCO_3}$ and reported uncertainties in $\delta^{11}B_{borate}$ of solution pH [188]:

$$\delta^{11}B_{borate} = (\delta^{11}B_{CaCO_3} - c)/m \tag{1.4}$$

where c is the intercept and m is the slope of the fit. By replacing Eq. 1.2 with Eq. 1.4, the calculated $\delta^{11}B_{borate}$ can be used to reconstruct pH:

$$pH = pK_B^* - log(-\frac{\delta^{11}B_{sw} - \delta^{11}B_{borate}}{\delta^{11}B_{sw} - \alpha_{B3-B4} \times \delta^{11}B_{borate} - \epsilon_{B3-B4}}) \tag{1.5}$$

Despite the fact that the $\delta^{11}B$-pH theory described above has been widely applied in the literature for ocean pH reconstructions, the reliability of these calculations has recently been called into question, highlighting the importance of problems related to isotope fractionation, mechanisms of boron incorporation into marine carbonates, so-called "vital effects" (i.e. metabolic activities that can bias the isotopic signal), analytic methods, and the seawater isotopic composition [173]. Several experiments on calcites and aragonites, mostly synthetics, had revealed differences in the isotopic composition of carbonates and seawater borate [93, 167, 209, 260]. Under low pH conditions, laboratory experiments on synthetic and biogenic calcium carbonate revealed enrichment of ^{11}B in carbonates compared to borate in solution. This enrichment is difficult to interpret. As the pH decreases, the concentration of boric acid increases; because boric acid is more enriched in ^{11}B than borate, boric acid incorporation could explain the shift in the isotopic composition of seawater borate and carbonate. Spectroscopic studies have revealed the presence of both BO_3 and BO_4 in carbonates [207, 246], with calcite incorporating a higher fraction of BO_3 than aragonite [206, 260]. Magic Angle Spinning Nuclear Magnetic Resonance (MAS NMR) is well suited to provide information on boron speciation in carbonates [167, 260]. Recent MAS NMR techniques on a limited set of biogenic samples revealed that corals, foraminifera [40, 129, 151, 207, 250], and calcareous red algae [167] contain 30-48% of BO_3. The amount of BO_3 in carbonates is unrelated to the concentrations of boron species in seawater [167] or pH [260]. It has frequently been interpreted as a coordination change of borate from BO_4 to BO_3 during crystal formation without isotopic fractionation [93, 151, 206, 207, 260]. Indeed, the coordination change would be a quick process in comparison to the carbonate growth rate, limiting potential kinetic fractionation [228]. Nonetheless, isotopic compositions that are heavier than expected from the exclusive incorporation of borate molecules could indicate direct boric acid incorporation, as many authors have suggested [40, 120, 277]. Recent theoretical models did not rule this out [68, 69], particularly in disordered mineral phases where boric acid molecules could be scavenged directly from the solution. As a result, boron incorporation in biogenic calcites and aragonites remains a source of contention, with the majority of current knowledge derived from laboratory experiments, synthetic materials, and theoretical models. Boron speciation data are currently only available for the coralline algae *Goniolithon* sp. [246] and *L. glaciale* from Scotland [167], which showed 80% and 30% of BO_3 incorporation, respectively. Boron concentration in calcite and aragonite artificially precipitated at 25°C by Mavromatis et al. [260] increases with solution pH (concordant with previous studies [15, 192, 193, 278]) and is significantly higher in the aragonite (in accordance with other observations of Kakihana et al. [99] and Hemming et al. [206]). This evidence suggests that boron is incorporated in carbonate as borate (which increases in solution with pH) rather than boric acid. Boron incorporation in calcareous red algae can be influenced by a variety of factors [102], and calibration studies on $\delta^{11}B$ have only been conducted on a few cultured species [42, 43, 102]. Recent research also suggests that coralline algae, like corals [234], can control the pH of the calcifying fluid (pH_{cf}) [42]. Both organisms can raise pH at calcification sites in response to changes in ambient pH, which influences precipitation rates [42]. Differences in carbonate polymorphs were also highlighted [43, 172], with aragonitic corals having higher pH_{cf} than calcites, indicating the importance of mineralogical control on biological up-regulation. Naturally acidified environments allow for *in situ* observations of marine organisms' responses to a decrease in seawater pH without resorting to complex manipulative laboratory experiments that do not account for all of the variables that characterize a real-world scenario [257]. So far, no studies on pH_{cf} changes in natural systems have been conducted on calcareous red algae.

1.2.2.1 IV Objective: The boron isotope calibration

The boron isotope-pH proxy was tested in calcareous red algae grown close to CO_2 seeps, obtaining the first measurements of $\delta^{11}B$ in *Corallina officinalis* Linnaeus 1758 (Corallinophycidae) and *Peyssonnelia* sp. (Peyssonneliales) from Ischia (Italy), and *Amphiroa* sp. (Corallinophycidae) from Methana (Greece). The $\delta^{11}B$ results were compared to previously collected data from cultured calcareous red algae, and they were used to calculate a new multi-specific calibration of the proxy in calcareous red algae, broadening the pH range considered for $\delta^{11}B$ calibrations in the literature thus far. The presence of morphological anomalies on the algal thallus was also investigated where the highest pH variations were registered.

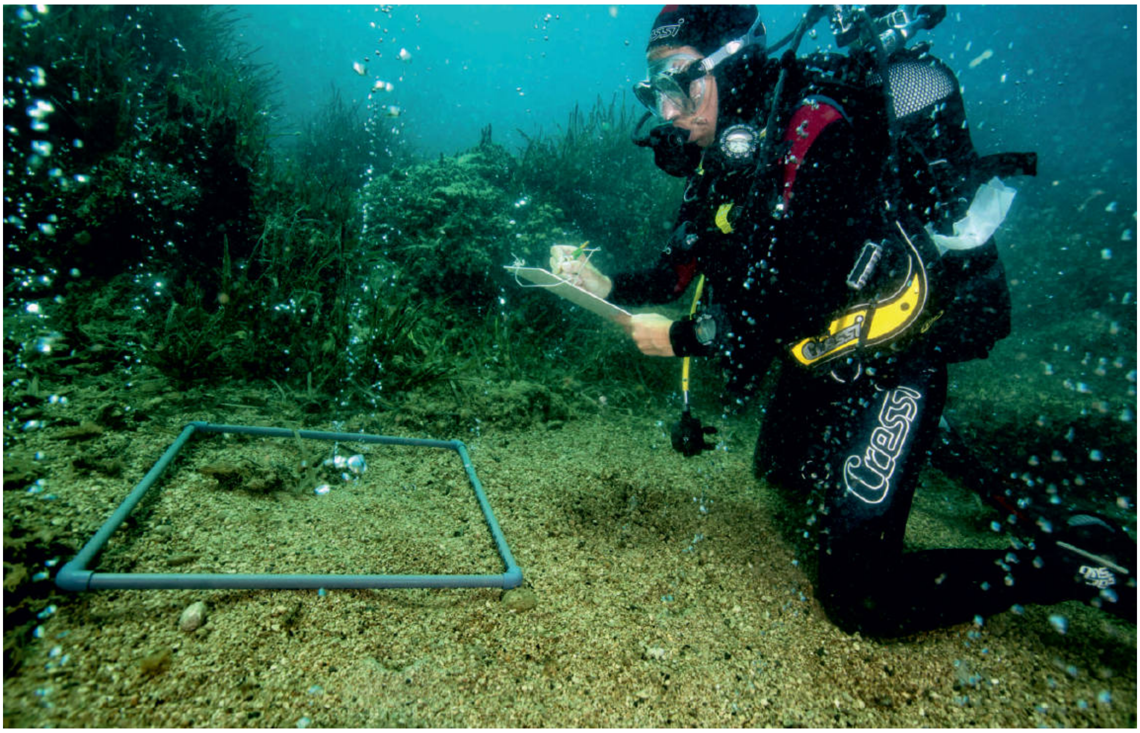

Figure 1.7: CO_2 seeps in Ischia (Italy) at the highest intensity venting zone (3-6 m depth). Modified from Gambi et al. [179].

1.2.2.2 V Objective: Boron speciation

For the first time in the literature, a large dataset of MAS NMR and isotope results in various aragonitic and calcitic red algal species was provided. Except for one species that has an Atlantic counterpart, all the algae analysed were grown across the Mediterranean Sea and belong to different algal families. This valuable collection offered the opportunity to study the variations in the amount of BO_3 and BO_4 among species grown in different locations. Eventual differences were discussed in light of a possible species-specific algal control over B speciation and statistical tools were used to highlight specificities between carbonate polymorphs. Given the scarcity of data currently available, the findings significantly improve our understanding of boron incorporation in calcareous red algae.

Chapter 2

Materials and methods

2.1 Sample collection

Calcareous red algal samples were collected from various locations in the Western and Eastern Mediterranean Sea (Table 2.1). They were recovered by grab during R/V Minerva Uno cruises, as part of the Marine Strategy Campaigns, or by SCUBA diving during local surveys. Sample s10 and s24 were respectively collected in the framework of the "Taphonomy and Sedimentology on the Mediterranean shelf" and BIOcostruzioni MArine in Puglia (BIOMAP)" projects. Morphological analyses of SEM images, which included careful examination of the thallus organization, reproductive structures, and epithallial and perithallial cells, were used for species identification following literature classification and dichotomous keys [85, 168] (e.g. *L. corallioides* [164, 271], *M. philippii* [111, 263]). At the Università Politecnica delle Marche (Italy), four samples were targeted for a multi-gene molecular phylogeny [6] and identified as *L. racemus* and *L. pseudoracemus* (Table 2.1). The neotype of *L. racemus* is represented by sample s1 [57]. Samples s5 and s6, lacking molecular identification, were morphologically classified as *L.* cf. *racemus* [57] (Table 2.1). The samples used for phylogeny are now housed in the Herbarium Universitatis Florentinae, Natural History Museum (Florence, Italy). One sample of *L. corallioides* was collected in Morlaix Bay (North Eastern Atlantic Ocean) (Table 2.1), where this species is the only component of the maerl, together with *Phymatolithon* spp. [27, 162].

Table 2.1: Calcareous red algal samples used to run CNN models (I Objective, Section 1.1.1.1) (s1-11), to investigate calcification traits under SEM (II Objective, Section 1.1.2.1) (s1-6), for trace element analysis (III Objective, Section 1.2.1.1) (s8, s12-14), for boron isotopes (s2-4, s8, s12-32), among which s15-23 were used to calibrate boron isotopes near CO_2 seeps (IV Objective, Section 1.2.2.1), and to investigate boron speciation (V Objective, Section 1.2.2.2) (s2-4, s8, s10-14, s24-32). For CNN models, the number of SEM images per sample is also shown.

Sample	**Site (latitude, longitude)**	**Date**	**Depth (m)**	**Species**	**Images**
s1	Capri, Italy (40°34’08”N, 14°13’32”E)	Aug 1990	50.0	*L. racemus*	43
s2	Pontian Islands, Italy (40°54’47”N, 12°52’58”E)	Jul 2016	64.9	*L. racemus*	24
s3	Villasimius, Italy (39°08’32”N, 9°31’14”E)	Jul 2017	40.0	*L. pseudoracemus*	48
s4	Pontian Islands, Italy (40°54’55”N, 12°53’07”E)	Jul 2016	66.4	*L. pseudoracemus*	9
s5	Sveta Katarina, Croatia (45°04’32”N, 13°37’38”E)	Jul 2004	10.0	*L.* cf. *racemus*	28
s6	Torre dell’Orso, Italy (40°14’00”N, 18°28’00”E)	Nov 2015	44.0	*L.* cf. *racemus*	13
s7	Villasimius, Italy (39°08’32”N, 9°31’14”E)	Jul 2017	40.0	*L. corallioides*	24
s8	Morlaix, France (48°34’42”N, 3°49’36”W)	May 1991	12.0	*L. corallioides*	25
s9	Portofino, Italy (44°17’56”N, 9°13’08”E)	Jul 2009	40.0	*M. philippii*	11
s10	Capraia, Italy (43°01’04”N, 9°46’26”E)	Jan 1988	24.0	*M. philippii*	14
s11	Cavoli Island, Italy (39°05’20”N, 9°32’33”E)	May 2017	31.0	*M. philippii*	16
s12	Aegadian Islands, Italy (37°58’10”N, 12°03’26”E)	Aug 1991	40.0	*L. corallioides*	

Table 2.1 (continue)

Sample	**Site (latitude, longitude)**	**Date**	**Depth (m)**	**Species**
s13	Elba, Italy [53] (42°44’56”N, 10°07’08”E)	Dec 1990	45.0	*L. corallioides*
s14	Pontian Islands, Italy (40°54’55”N, 12°53’07”E)	Jul 2016	66.4	*L. corallioides*
s15	Ischia, Italy (S1) (40°43’48”N, 13°57’49”E)	May 2012	1.0	*C. officinalis*
s16	Ischia, Italy (S2) (40°43’50”N, 13°57’47”E)	May 2012	1.0	*C. officinalis*
s17	Ischia, Italy (S3) (40°43’52”N, 13°57’47”E)	May 2012	1.0	*C. officinalis*
s18	Ischia, Italy (S2) (40°43’50”N, 13°57’47”E)	May 2012	1.0	*Peyssonnelia* sp.
s19	Ischia, Italy (S2) (40°43’50”N, 13°57’47”E)	May 2012	1.0	*Peyssonnelia* sp.
s20	Ischia, Italy (S3) (40°43’52”N, 13°57’47”E)	May 2012	1.0	*Peyssonnelia* sp.
s21	Methana, Greece (F1) (37°38’18”N, 23°21’34”E)	Feb 2012	1.0	*Amphiroa* sp.
s22	Methana, Greece (F2) (37°38’18”N, 23°21’34”E)	Feb 2012	1.0	*Amphiroa* sp.
s23	Methana, Greece (N) (37°38’18”N, 23°21’41”E)	Feb 2012	1.0	*Amphiroa* sp.
s24	Polignano, Italy (40°59’41”N, 17°14’13”E)	May 2013	30.0	*M. philippii*
s25	Aegadian Islands, Italy (37°58’10”N, 12°03’26”E)	Aug 1993	40.0	*L. crispatum*
s26	Villasimius, Italy (39°08’32” N, 9°31’14” E)	Jul 2017	40.0	*L. minervae*

Table 2.1 (continue)

Sample	Site (latitude, longitude)	Date	Depth (m)	Species
s27	Elba, Italy (42°44’56”N, 10°07’08”E)	Dec 1990	45.0	*L. minervae*
s28	Pontian Islands, Italy (40°54’36”N, 12°52’09”E)	Jul 2016	66.9	*L. minervae*
s29	Polignano, Italy (40°59’41”N, 17°14’11”E)	May 2013	30.0	*L. stictiforme*
s30	Pontian Islands, Italy (40°54’00”N, 12°52’00”E)	Jul 2017	65.0	*Peyssonnelia* sp.
s31	Pontian Islands, Italy (40°54’00”N, 12°52’00”E)	Jul 2017	65.0	*Peyssonnelia* sp.
s32	Villasimius, Italy (39°08’32” N, 9°31’14” E)	Jul 2017	40.0	*Polystrata* sp.

Calcareous red algal samples in Ischia and Methana were collected by SCUBA diving at approximately 1 m depth (Fig. 2.1). Ischia is located West of the Bay of Naples (Italy) and has hydrothermal vents ranging in depth from 1 to 48 meters (Fig. 1.7). The area was formed during the Plio-Quaternary period [13] and is volcanically and tectonically active [179]. The research was conducted at the South vent of Castello Aragonese, Ischia’s Eastern coast. Here, gas is emitted at 1.4 × 106 L per day in an area of 3000 m^2, with more than five vents per m^2 [92, 140]. Samples of *C. officinalis* and *Peyssonnelia* sp. were collected in stations S2 and S3, respectively, along the transect of Hall-Spencer et al. [140], within the venting area (Fig. 2.1). *C. officinalis* was also collected at station S1, which was the furthest away from the vents (Fig. 2.1). Methana is located in the hydrothermally active Saronic Gulf area, on the North-Eastern coast of the Peloponnese (Greece). Volcanic activity first appeared at the Pliocene-Pleistocene boundary, and geothermal phenomena are common throughout the peninsula [270]. Methane concentrations (17-26 ppm) are lower in Methana than in Ischia (200-800 ppm) [37, 140]. *Am-*

phiroa sp. was collected near the main seeps (N) and in two replicates 200 m west of the seep area (F1, F2) (Fig. 2.1). Sites N and F correspond to the SEEP and 200 W sites, as defined by Baggini et al. [37] .

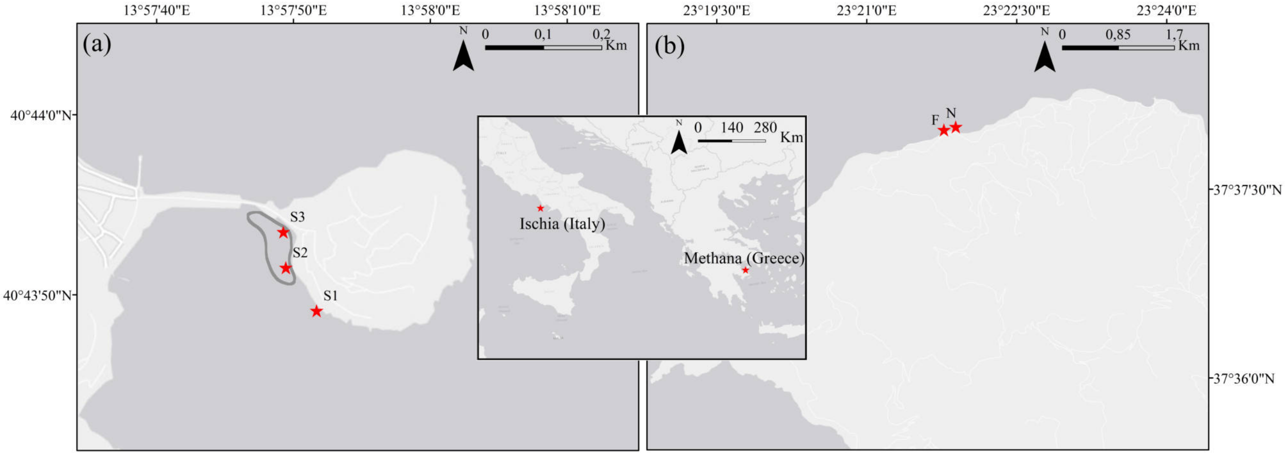

Figure 2.1: Map of the sampling sites in (a) Ischia, where *Corallina officinalis* and *Peyssonnelia* sp. were collected and (b) Methana, where *Amphiroa* sp. was collected. In Ischia, the venting area, including sites S3 and S2, is circled in grey. In Methana, the main venting site is close to N. Site F is located 200 m westward from the vents. Service Layer Credits: Esri, HERE, Garmin, (c) OpenStreetMap contributors and the GIS user community.

2.2 Environmental data

In the absence of *in situ* environmental data, the seawater temperature in the collection sites of *L. corallioides* samples s8, s12-14 (Table 2.1) was calculated using 11 years of monthly reanalysis spanning 1979-2016 from Ocean ReAnalysis System 5 (ORAS5), at 0.25-degree horizontal resolution [101]. Each extraction time interval corresponded to 11 years before sample collection [267]. When discussing temperature proxies in different geographical locations (III Objective, Section 1.2.1.1), temperature data were used in terms of the amplitude of temperature variation (ΔT), and temperature peaks (minimum and maximum). Minimum, maximum, and mean temperature values refer to the temperature at sampling depth and were measured over the entire extraction time interval. ΔT was used to compare the sampling sites and represents temperature fluctuations during algal growth. It was calculated as the difference between the temperature peaks over an 11-year period. When comparing the mean elemental ratios of long and short cells per sampling site, which are related to warm and cold growth periods, respectively (Section 1.1.2), we used the maximum and minimum temperatures over the entire time interval. The good visibility of the growth bands in *L. corallioides* sample s8 allowed us to correlate the temperature record with the geochemical signal in the alga at annual resolution. Here, the temperature peaks for each year were used to reconstruct the algal age model. All of the element ratios were plotted against the seawater temperature values of the coldest and warmest months of the year, which is a methodology widely applied in the literature [4, 32, 77, 225, 253]. Carbon system parameters were also estimated for the collection sites of *L. corallioides* samples s8 and s12-14 (Table 2.1). The EU's Copernicus Marine Service Information (CMEMS) global biogeochemical hindcast spanning 1999-2017 was used to calculate monthly mean seawater pH at 0.25-degree horizontal resolution. CMEMS biogeochemical reanalysis for the Mediterranean Sea, with a horizontal resolution of 0.042 degrees [17], was used to extract monthly means of DIC in the same time interval. Similarly, monthly means of DIC in the Atlantic site were calculated using the CMEMS IBI biogeochemical model at 0.083-degree horizontal resolution. Environmental parameters in Methana (pH, temperature, salinity), where *Amphiroa* sp. was collected (Table 2.1), were derived from *in situ* data collected by Baggini et al. [37] using a multiprobe (YSI 63) calibrated before use with pH 4.01, 7.01 and 10.01 NBS standards. The pH data from the various sampling sites in Ischia, where *C. officinalis* and *Peyssonnelia* sp. were collected (Table 2.1), were cited from Foo et al. [235], who reviewed several studies that recorded total pH and provided the standard deviation, representative of the pH variability in each site. Annual mean temperature and salinity records in Ischia were extracted at sampling depth from the Mediterranean Sea monthly physical reanalysis, spanning seven years before sample collection [220]. Previous research in the area found that hydrothermal vents have no effect on seawater temperature or salinity, which are both stable across sites and similar to surrounding waters [140, 158, 213]. As a result, Ischia sites have been assigned the same temperature and salinity values. Environmental data extraction was performed in R 4.1.2 software.

2.3 Scanning Electron Microscopy

Specimens were washed and air-dried before microscopical analysis [267]. The samples were fragmented along the growth direction, mounted on stubs with graphite paste, and finally chrome-coated for being analyzed on a Gemini 500 Zeiss Field Emission Gun SEM (SEM-FEG) at the University of Milano-Bicocca. To test the automatic classification of SEM images by deep learning, a total of 11 specimens were chosen, at least two from each species under consideration (Table 2.1). The final dataset considered for CNN automatic classification consisted of 255 SEM images from samples s1-11 (Table 2.1). The greyscale images had a resolution of 2046 x 1369 pixels (single channel). According to the morphological features observed (Fig. 2.2), each image in the dataset was assigned to one or more categories (conceptacles, perithallus, crystallites, epithallial cell, hypothallus, and surface), and each category information was added as metadata. Twenty-one images were assigned to more than one category because they show multiple structures at the same time. The presence of thallus growth over some old conceptacles revealed the secondary hypothallus [273], where the PC was particularly visible. Ten images, including those depicting the secondary hypothallus, were not assigned to a specific category. For a detailed analysis of samples s1-6 (*L. racemus*, *L. pseudoracemus* and *L.* cf. *racemus*) (Table 2.1), biometry and calcification data were extracted from 370 SEM images of longitudinal or transverse sections. Among biometrical data, the size of epithallial and perithallial cells [51] and cell lumen [267], conceptacle size [54], pore canal length, the number of cells in the pore canal filament, and the number of epithallial cells were all measured. Other traditional descriptors included cell, conceptacle, and pore canal shapes, pit connections, conceptacle elevation, and the presence and development of a calcified columella. For the description of the columella development, H refers to conceptacle height [273] and h1 refers to the distance between the top of the columella and the conceptacle roof [57]. Within the calcified cell wall, PC refers to the outer layer of Mg-calcite crystallites arranged parallel to the cell membrane (PW in Bracchi et al. [267]), whereas SC refers to the calcified layer made up of crystallites that are radial to the cell membrane and normal to the PC crystallites (SW in Bracchi et al. [267]) (Section 1.1.2).

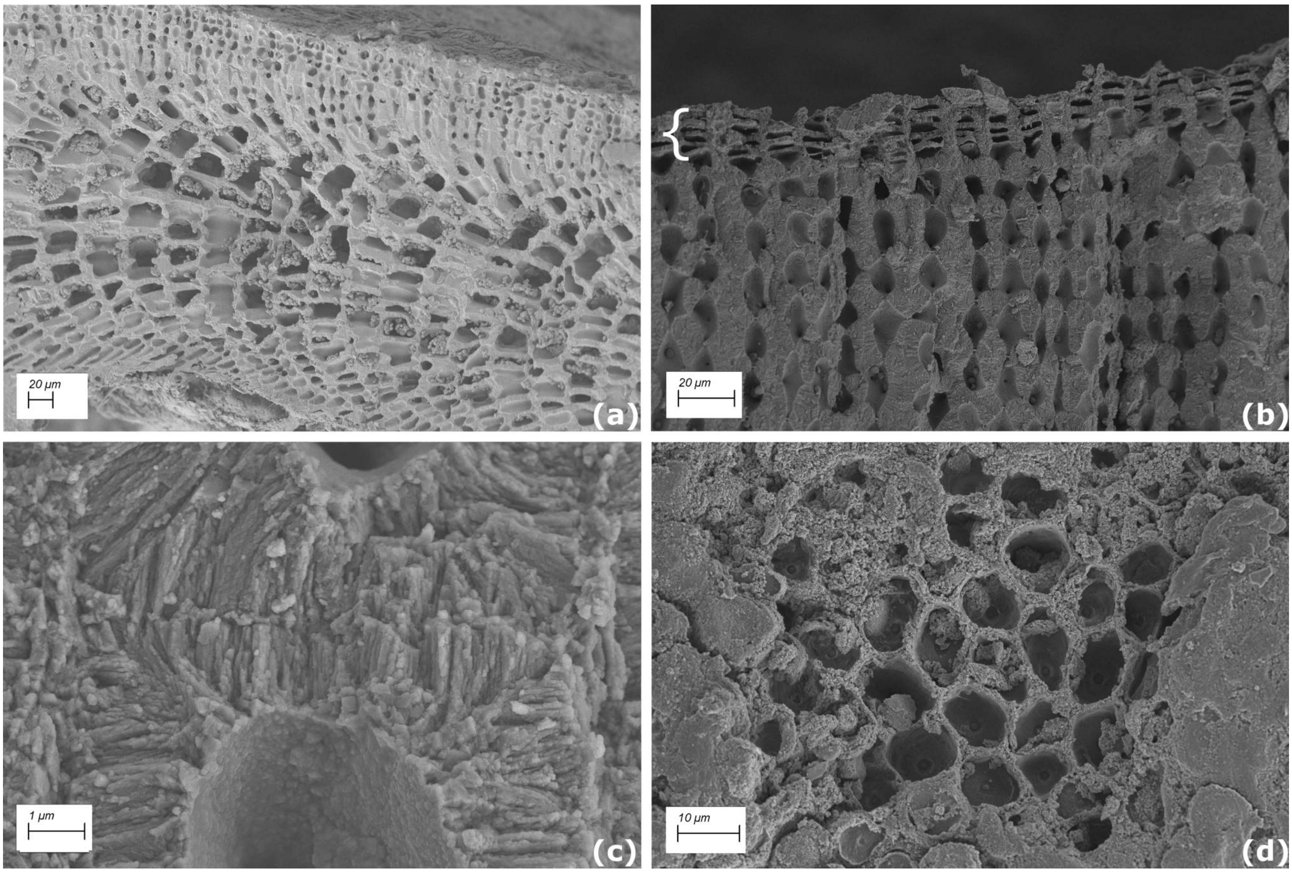

Figure 2.2: An example for each morphological category assigned to SEM images. (a) *Mesophyllum philippii* coaxial hypothallus (hypothallus category), (b) *Lithophyllum racemus* epithallial cells (curly bracket) with the underlying perithallus (epithallial cell and perithallus categories), (c) a magnification of *L. racemus* perithallial cells showing secondary crystallites (crystallites category), (d) a surface view of a *Lithophyllum pseudoracemus* sample (surface category).

The cell wall area was measured in longitudinal sections as the calcified surface area surrounding the cell lumen and delimited by the cell's outer borders. Each cell's boundaries run at half of the PC, which may be very thin. The calcification process was studied primarily in epithallial and perithallial cells. The SC maximum thickness, PC maximum thickness, and cell wall area of epithallial and perithallial cells were all measured as calcification traits. Furthermore, the shape and size of the primary crystallites that form the PC, and the secondary crystallites that form the SC were described. In *L. racemus* specimen s2, the same information was extracted separately for short and long cells. Also, specific observations were conducted by SEM in the samples collected near CO_2 seeps in Ischia, where the highest pH variation among sites was expected [235], to evaluate morphological anomalies due to the low pH. Observations were assessed on several random points both in *Peyssonnelia* sp. (20 points) and *C. officinalis* (30 points) (Fig. 2.3).

Figure 2.3: *Corallina officinalis* (a) and *Peyssonnelia* sp. (b) collected in Ischia, stations S3 (samples s17 and s20, on the left) and S2 (samples s16 and s19, on the right) (Table 2.1). SEM observations were aimed at identifying any morphological modification in the calcified thalli grown in an acidified environment. An example of random points located to guide the analysis is shown in the left image (plus signs).

2.4 Deep learning

2.4.1 Data augmentation

A realistic data augmentation [41] was performed to increase the number of SEM images used for CNN classification and, thus, improve the variance of the available training set (Fig. 2.4).

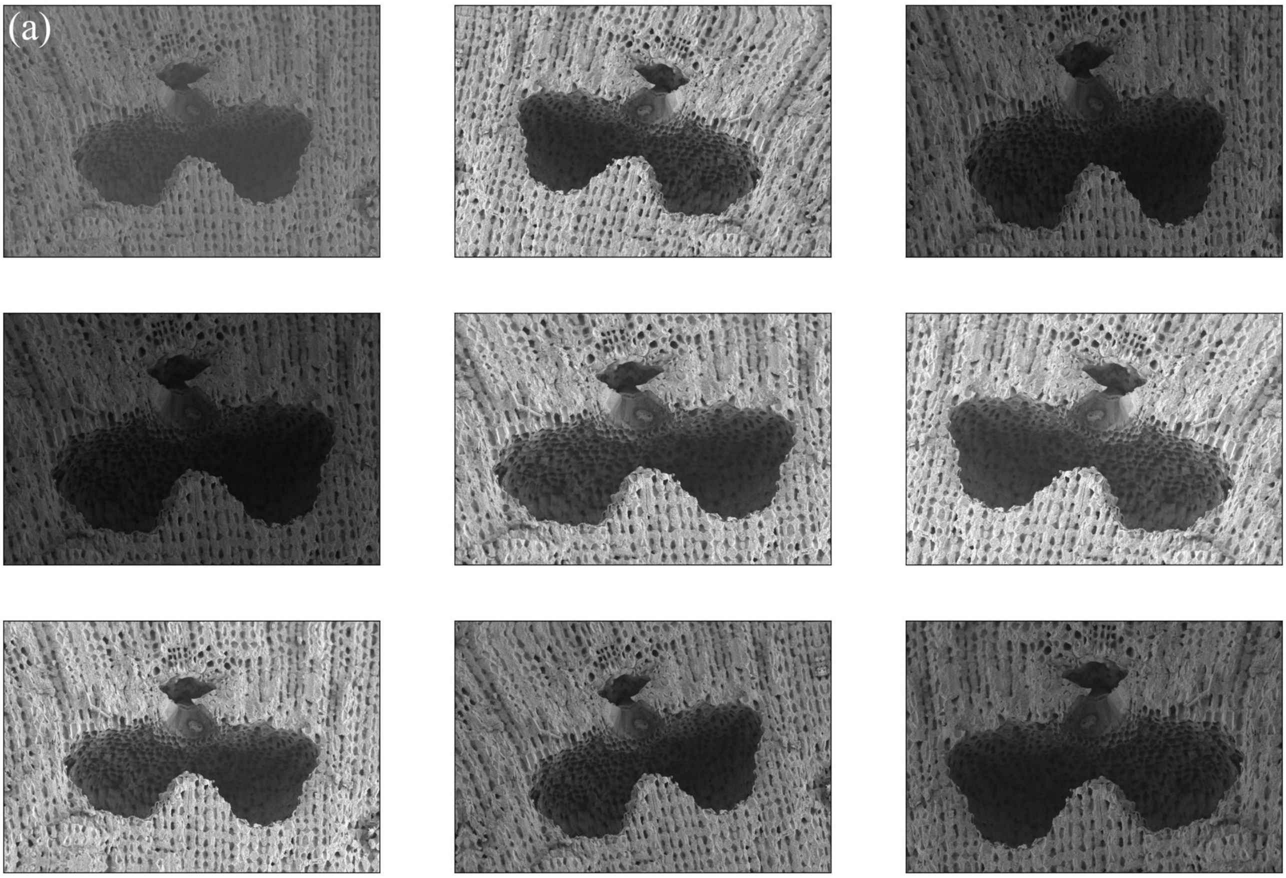

Figure 2.4: Examples of augmented images of a SEM image showing a *Lithophyllum racemus* conceptacle given the original image in (a).

Specifically, during model training, each image in the training set was duplicated five times, each time with a random change in brightness in the range [0.5-1.8], a random rotation up to 10 degrees, a random zoom to a maximum of 0.7, and a random horizontal flip (Fig. 2.4). The criteria were chosen in order to obtain realistic augmented images, that is, images that are compatible with normal variability in SEM images.

2.4.2 Convolutional Neural Networks

Classification (or, more formally, supervised classification) is a subset of machine learning that aims to classify objects into one of several predefined classes. In this research, the objects, i.e. the classification input, are represented by images with categorical metadata (morphological features), whereas the classes are considered species or genera (Section 1.1.1). A fine-tuned deep neural network called Visual Geometry Group 16 (VGG16) [154] was adapted, and pretrained on the "imagenet" dataset [112]. This dataset contains 14 million images assigned to 1000 classes. The modified VGG16 architecture (Fig. 2.5) was made up of:

- an input layer of fixed size 224 x 224 Red-Green-Blue image;
- a stack of convolutional layers, with filters of 3 x 3 receptive field;
- 5 max-pooling layers (not all the convolutional layers are followed by max-pooling);
- a dense layer, whose input is the output of the previous max-pooling layer and concatenated with the one-hot-encoded categories;
- a softmax output layer.

VGG16 architecture is well-suited for geometrical recognition, which makes it useful for this application because the shape of cells and reproductive structures is one of the most important parameters for species identification in coralline algae (Section 1.1). The VGG16 approach was also the most promising in terms of diagnostic accuracy compared to other architectures (ResNet50, InceptionV3, MobileNet). The ReLU activation function [21, 154] was present in all hidden layers, i.e. the layers between the input and output layers. SEM images were resized and the same greyscale image was replicated for each of the three RGB channels, before being injected into the input layer. All of the original VGG16's convolutional layer parameters were kept frozen (that is, they were not changed during the learning procedure), while pretraining the last dense layer and the output layer of the specific classification tasks. In addition, a new input layer made up of six neurons that map the one-hot encoded representation of the morphological features seen in each image was added and directly connected to the dense layer.

Given an image x and a vector of morphological categories c, each output neuron o_g associated with algae class g was computed as

$$o_g = softmax(\sum_i W^o_{i,g} d_i); d_i = ReLU(\sum_j W^d_{j,i} h_j + \sum_l W^d_{l,i} c_l) \tag{2.1}$$

where d_i is the i-th component of the dense layer, h_j is the j-th component of the last max-pooling layer of VGG16's image x representation, and c_l is the l-th component of the one-hot encoded category input layer. W^d and W^o are the weights learned by the model for the dense and output layers respectively. When the softmax function is applied to the output layer, the output is projected in the interval [0, 1], such that $o_g = P(g|x, c)$ for each class g. As a result, the predicted class $\hat{g}$ is assigned to the class g with the highest probability.

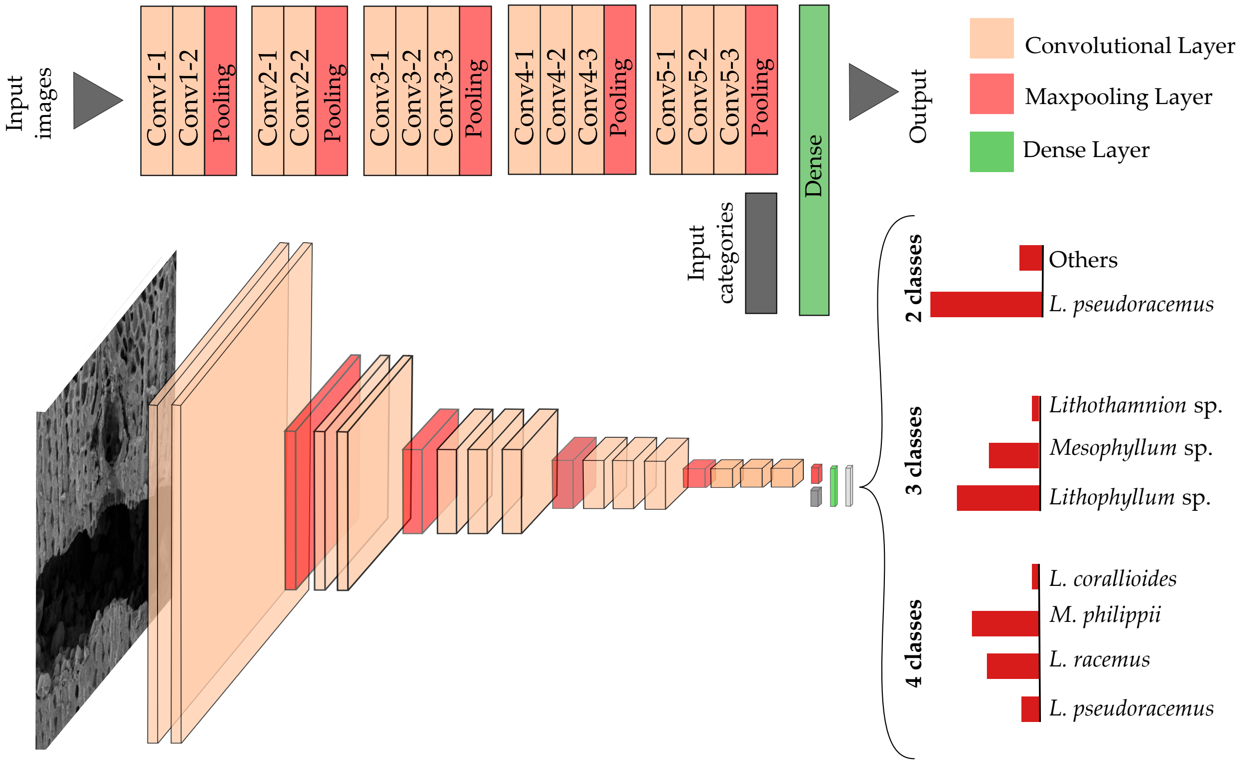

Figure 2.5: Modified Visual Geometry Group 16 (VGG16) architecture adopted for SEM image classification.

Because *L. pseudoracemus* and *L. racemus* are nearly indistinguishable from a traditional morphological approach [6] (Section 1.1), the classification task became more difficult depending on the taxonomic level considered. As a result, three architectures were built, to address different classification tasks, each grouping the SEM images at different levels:

1. the 2 class-CNN model (*L. pseudoracemus* versus Others, i.e., all the other species), with a last dense layer of 128 neurons and an output layer of 2 neurons;
2. the 3 class-CNN model, at the genus level (*Lithothamnion* sp., *Mesophyllum* sp. and *Lithophyllum* sp.), with a last dense layer of 256 neurons and an output layer of 3 neurons;
3. the 4 class-CNN model, at the species level (*L. corallioides*, *M. philippii*, *L. racemus* and *L. pseudoracemus*), with a last dense layer of 64 neurons and an output layer of 4 neurons.

The number of epochs was set to 20 for all three architectures, and the learning rate was set to 10^{-5}. We optimized the VGG16 hyperparameters, such as the number of neurons in the last hidden dense layer, training epochs, and learning rate, to obtain the best weights for the problem at hand. The best hyperparameters were chosen based on the best cross-validation performance, as it is common practice [217]. Furthermore, we used a weighted class assignment, in which the class contributions are inversely proportional to the classes' different representativeness.

2.4.3 CNN interpretability

Despite widespread adoption, CNNs are frequently regarded as black boxes due to the difficulty in interpreting model predictions. Understanding the reasons behind predictions, on the other hand, is a matter of intuition. To make CNNs replicable, various approaches from the field of explainable artificial intelligence were developed, in terms of local approximations of the model's behaviour. Three approaches were considered in this project: Saliency [153], Local Interpretable Model-Agnostic Explanation (LIME) [190] and Gradient-weighted Class Activation Mapping (Grad-CAM) [232]. The computation of the gradient of an output class with respect to an input image, as explained in Simonyan et al. [153], provides information on how the output class value changes in response to a small change in input image pixels. All of the positive gradient values indicate that a small change to that pixel will increase the output value. As a result, a

Saliency map is a visual representation of these gradients, which have the same shape as the image and provide an intuitive representation of the information learned by the model. LIME [190] is a model-independent explanation technique that attempts to explain the model by perturbing the input objects and understanding how these perturbations affect the predictions. LIME masks random regions of an image to define their importance for CNN prediction given an input image. Grad-CAM, like Saliency, employs the class-specific gradient, but in this case, takes into account the final convolutional layer of a CNN to produce a coarse location map of important regions in the image [232]. These explanation techniques were applied to the sampled SEM images to generate variously explained overlays. As a result, the techniques were assessed based on their relevance and utility for the classification task. The CNNs and explanation models were created in Python 3.6 using Keras [74], Keras Vis [223] and Lime [190] packages with a TensorFlow [165] backend.

2.4.4 CNN evaluation strategy

Two different setups to thoroughly evaluate the effectiveness of the classification tasks were considered. In the first, *Internal Validation*, the model's ability to identify the correct class for each image in the study was assessed. For this purpose, only the images from samples for which a certain diagnosis is given as ground truth (based on morphology and molecular phylogeny) were chosen. As a result, the images referring to *L.* cf. *racemus* samples (s5 and s6 in Table 2.1) were excluded. The dataset eventually included 214 tagged SEM images. A 4-fold cross-validation was considered to include the entire set of images while avoiding overfitting [217], in which the original dataset was divided into four disjoint sets (i.e. folders). A folder was used as a validation set (on which classification metrics were computed) in each round, while the other folders were used to train the model. The procedure was repeated until all of the folders (and thus all of the images) were validated. Furthermore, the CNN models' performances were compared to average baselines produced by dummy classifiers, whose random predictions (repeated 1000 times) follow the a priori class distribution, and to a human classifier, which was interviewed to diagnose each SEM image considered in *Internal Validation*.

A post-doc researcher in Paleoecology at Milano-Bicocca University was specifically asked to identify the species shown in each SEM image (previously anonymized and shuffled) by filling out a multiple-choice questionnaire and relying on scientific experience and the literature [6, 57, 111, 164, 263, 271]. The comparison of the model's and expert's performances allowed us to assess the method's practical usefulness in supporting the classification task [26, 224]. To assess the performance of the model, two well-defined classification metrics were used: *Global Accuracy* and *Class Recall* [217]. The *Global Accuracy* for each model is the fraction of correctly predicted images in cross-validation, whereas *Class Recall* for the g-th class is the fraction of correctly predicted images in cross-validation of the sample belonging to class g. The *Class Recall* fractions for each morphological category (Fig. 2.2) were also given. In the second setup, *External Test*, the model was tested in a simulated scenario in which an expert must identify the correct classes (genus or species) of new unknown samples of coralline algae. This case study was simulated by training the CNN classification model on all 214 tagged SEM images and then applying it to each image of the *L.* cf. *racemus* samples s5 and s6. As a result, the *Class Share* (*CS*) of each class g, for a specific sample s, is:

$$CS_s(g) = \frac{1}{N_s}\sum_{n=1}^{N_s}\delta_n \qquad where \quad \delta_n = \begin{cases} 1, \text{if } \hat{g_n} = g, \\ 0, \text{otherwise} \end{cases} \tag{2.2}$$

where N_s is the number of SEM images in sample s, δ_N is 1 if the n-th image in sample s is assigned to class g by the classification model (therefore the predicted class $\hat{g_n}$ is equal to g), and 0 otherwise. In addition, the *Class Share* per category was calculated using the various subsets of SEM images assigned to each morphological category (Fig. 2.2).

2.5 X-Ray Diffraction

Under the optical microscope, samples for mineralogical analyses (s2-4, s8, s12-32 in Table 2.1) were carefully cleaned from epiphytes and encrustations. Then, they were rinsed ultrasonically in distilled water for 10 minutes and dried in the oven for 24 hours at 30°C. Clean samples were powdered using an agate mortar and pestle and stored at room temperature. At the University of Milano Bicocca, the mineral composition of the prepared powders was investigated using powder X-Ray Diffraction (XRD) on a Rigaku Miniflex 600. XRD data were acquired in the 5°-90° angular range with a size step of 0.02° and an averaging time of 0.1 deg/min using Cu Kα radiation. To quantify the aragonite/calcite ratio, Rietveld refinements were performed using the FullProf suite [122] and multi-phase fitting was considered. The multi-phase refinements were based on the presence of calcite (reference ICSD 98-018-0349) and aragonite (reference ICSD 98-016-9893). SiO_2 (reference 98-001-6335) was introduced to account for all of the observed peaks in *Peyssonnelia* sp. and was quantified at $< 5\%$ in all samples. For all samples, the background was fitted by points, and the refined parameters were: cell parameters, scale, background point, and isotropic thermal factors.

2.6 Mass Spectrometry

2.6.1 Laser Ablation ICP-MS and growth rates

The algal branches of samples s8 and s12-14 were embedded in Epo-Fix resin, which was stirred for 2 minutes with a hardener (13%), and then dried at room temperature for 24 hours. Following that, the treated branches were cut along the growth direction with an IsoMet diamond wafering blade 15HC. The sections were polished with a MetaServ Grinder-Polisher (400 RPM) in the laboratory of the Institute of Geosciences and Earth Resources (IGG) of the National Research Council (CNR) in Pavia (Italy), then cleaned ultrasonically in distilled water for 10 minutes and dried at 30°C for 24 hours. Laser Ablation Inductively-Coupled Plasma Mass Spectrometry (LA-ICP-MS) analyses were performed on one algal branch per sampling site at the IGG-CNR. The contents of ^{43}Ca, ^{7}Li, ^{25}Mg, ^{88}Sr and ^{11}B were determined using an Agilent ICP-QQQ 8900 quadrupole ICP-MS coupled to an Excimer laser ablation system (193 nm wavelength, MicroLas with GeoLas optics). For these isotopes, element/Ca ratios and Mg/Li ratios were calculated. The measurements were carried out using laser energy densities of 4 J/cm^2 and helium as carrier gas. With a spot size of 50 μm, the laser transects crossed the algal growth direction, attempting to target each growth band change that marked the transition between cells produced in the warm season and those produced in the cold season, referred to as long and short cells (Section 1.1.2). As an external standard, NIST 612 was used [113, 212], while Ca was used as an internal standard. Precision and accuracy were better than 4% for NIST 612 and 8% for the Ca standard. Ca = 16.91 ppm, Li = 0.07 ppm, Mg = 0.11 ppm, Sr = 0.004 ppm, and B = 2.64 ppm were the minimum detection limits (99% confidence). Each analysis was performed in MS/MS mode for 3 minutes, with the laser on the polished surface acquiring 60 seconds of background before and after the sampling period. To avoid surface contamination, the first part of the signal was not used for integration. Glitter 4.4.4 software was used for data reduction. Under a light microscope, growth rates were calculated by measuring the length of the LA-ICP-MS transect and dividing it by the number of annual growth bands crossed by the transect [267]. The results were expressed in linear extension per year (mm/yr). The Mg/Ca results were also used to check for the correspondence of Mg peaks with growth bands in the samples.

2.6.2 Sample pre-purification and cleaning

The same powders prepared for XRD (Section 2.5, samples s2-4, s8, s12-32 in Table 2.1) were later used for geochemical analyses at the Department of Earth and Ocean Dynamics, University of Barcelona (Barcelona, Spain). Boron purification was completed at the Laboratori d'Isotops Radiogenics I Ambientals (LIRA), an ultraclean laboratory facility in the same Department. Prior to the mass spectrometry purification procedures, all samples were oxidatively cleaned to remove organic matter. The oxidative protocol was carried out on a clean bench in the presence of a laminar flow hood. First, 500 μl of a solution 10% H_2O_2 buffered with NaOH was added to

2 mg of each powdered sample. The solution was then heated for 5 minutes on a hot plate with boiling water before being sonicated for 15 seconds. Heating and ultrasonic bathing were both done three times. Oxidation was stopped by adding MilliQ water to the solution, and samples were centrifuged for two minutes at 1000 ppm. The supernatant was removed, and the pellet was rinsed with MilliQ three times. The samples were then dried on a clean bench.

2.6.3 Micro-sublimation and Multi-Collector ICP-MS

To dissolve organic matter-free carbonate, 40 μl of 0.8 M HNO_3 was added per mg of cleaned sample (Section 2.6.2), resulting in a final HNO_3 concentration of ~0.3 M. After that, the solution was sonicated for 15 minutes and centrifuged for 5-10 minutes. Boron purification was accomplished through micro-sublimation, following a protocol adapted from previously published contributions [35, 174, 243]. In brief, 40 μl of the sample was loaded into the centre of the lid of a conical 5 ml PFA beaker (Savillex) and placed upside down on a hotplate at 95°C for 15 hours. During this step, boron was collected in the condensed solution at the conical tip of the vial, while matrix elements remained on the lid. After cooling, the beakers were quickly flipped over and the lids were replaced. The samples were then diluted in 960 μl of 0.3 M HNO_3. At the CCiT-UB (Scientific and Technological Centres of the University of Barcelona, Spain), the samples were analyzed using Multi Collector Inductively-Coupled Plasma Mass Spectrometry (MC-ICP-MS) with a Plasma 3 spectrometer (Nu Instruments-AMETEK). The instrument has 16 Faraday cup detectors, 2 ion counters, and a switchable preamplifier bin with one 10^{11} Ω resistor for each Faraday cup preamplifier and six 10^{12} Ω resistors in fixed positions. In this research, ^{11}B was found on a Faraday cup with a 10^{11} Ω resistor, while ^{10}B was found on a Faraday cup with a 10^{12} Ω resistor. A PFA-100 nebulizer (ESI) fitted to a Peltier-cooled cyclonic spray chamber was used for sample introduction. Background and procedural blank signals (3-5 per session) were subtracted systematically. After 3 minutes of rinsing with 0.3 M HNO_3, the background signal dropped to about 1% of the signal for the previous sample/standard and remained stable throughout the analytical session. By analyzing the isotopically certified standard SRM 951a (NIST) before and after each sample, mass bias was corrected using the standard-sample-standard bracketing method. The matrices and concentrations of the samples and standards were matched. The analytical procedure's accuracy was demonstrated by analyzing the reference material RM 8301, which consisted of simulated coral and foraminifera solutions. JCp-1 and JCt-1, two other carbonate materials commonly used in the literature, were also investigated. The δ^{11}B values determined for the RM 8301 (foram) and RM 8301 (coral) were 14.65 ± 0.23 ‰ (2SD, N = 4) and 24.43 ± 0.25 ‰ (2SD, N = 5), respectively. These findings are consistent with those reported by other laboratories in the characterization of this reference material [131]. The δ^{11}B values for JCp-1 and JCt-1 in the unoxidized form were 24.47 ± 0.20 ‰ (2SD, N = 5) and 16.29 ± 0.63 ‰ (2SD, N = 3), respectively, which agree with values reported in a recent inter-laboratory comparison study [169]. The method's external reproducibility (2SD$_{meas}$) was determined using the approach previously published by Rae et al. [133]. A standard solution was made by combining the boric acid standard SRM 951a with a ^{11}B spike solution, with the resulting solution having a δ^{11}B of about 15 ‰. This solution was tested at five different levels of signal intensity (N = 15). The 2SD$_{meas}$ of the 15 replicates at each intensity level were then plotted against the total boron signal (SB = signal for ^{11}B + signal for ^{10}B) and fitted to a 2-term exponential model ($R^2 >$ 0.999). The resulting equation was:

$$2SD_{meas} = 0.4606^{-0.9929 \times S_B} + 1.637^{-19.79 \times S_B} \tag{2.3}$$

The 2SD$_{meas}$ obtained for the samples examined in this research ranged from 0.2 to 0.35 %. Multiple analyses on a dissolved coral sample confirmed that the micro-sublimation did not introduce any significant uncertainty to the results. The analysis of this solution resulted in a 2SD of 0.31 % (N = 14) for a signal with a 2SD of 0.30 %, whereas the coral solution resulted in a 2SD of 0.22 % (N = 23) for a higher signal with a 2SD of 0.20 %. However, for some samples, the procedural blanks significantly contributed to the uncertainty of the results. Because of it, the reproducibility associated with the procedural blank correction (2SD$_{blank}$) was estimated by calculating n δ^{11}B values for each sample by subtracting the signal of n procedural blanks from the same analytical session (typically 5) individually. The reproducibility of these n δ^{11}B values was then determined (2SD$_{blank}$). Finally, 2SD$_{meas}$ and 2SD$_{blank}$ were propagated, resulting in final expanded uncertainties (k = 2) less than 0.6% (i.e., < 0.1 pH units).

2.7 Boron isotope calibrations

To the best of our knowledge, the only data on δ^{11}B at different ambient pH for calcareous red algae currently available are from culture experiments on *Neogoniolithon* sp. [42, 102], *Amphiroa anceps* (Lamarck) Decaisne [42], *Sporolithon durum* (Foslie) R.A.Townsend & Woelkerling [42], and *Hydrolithon reinboldii* (Weber Bosse & Foslie) Foslie [43]. Calibrations of these data were calculated in this work by York fits [63] in R 4.1.2 software for each species and experiment, deriving the intercept and slope of regression lines as in Eq. 1.4. Published uncertainties in $\delta^{11}B_{CaCO_3}$, referred to as $\delta^{11}B_{algae}$, were used in terms of standard errors of replicate measurements (SE), while mean values and uncertainties (as standard deviation, SD) in $\delta^{11}B_{borate}$ were determined from Eq. 1.5 using 10000 Monte-Carlo simulations in MATLAB R2021b software, by randomly sampling temperature, salinity, and pH within their given uncertainty bounds [145]. A multi-specific calibration was also calculated, grouping $\delta^{11}B_{algae}$ measurements from samples collected near CO_2 seeps (s15-23 in Table 2.1) and previously published data for cultured calcareous red algae.

2.8 Magic Angle Spinning NMR

Solid-state Magic Angle Spinning Nuclear Magnetic Resonance (MAS NMR) was used to investigate boron speciation in samples s2-4, s8, s12-14 and s24-32 (Table 2.1) as it is a particularly well-suited technique for the task [167, 260]. The ^{11}B analyses were performed at CEMHTI facilities (Orléans, France) using a high field Bruker AVANCE III spectrometer (850 MHz-19.9 T), which allowed for complete resolution of the BO_3 and BO_4 contributions even at low boron concentrations [260]. The spectrometer was outfitted with a Doty probe designed specifically to acquire the ^{11}B signal and a "boron-free" stator. Around 150-200 mg of powdered sample (the same powder used for XRD and MC-ICP-MS: Sections 2.5, 2.6.3) were loaded into a 3 mm rotor, which allowed for magic angle rotation conditions of approximately 18 kHz. After a short excitation pulse to ensure homogeneous irradiation of boron species, the spectra were acquired at an observation frequency of 272.8 MHz for ^{11}B. The recycling delay was set to 3 seconds, and the number of accumulated scans was adjusted based on the sample's boron content. The chemical shifts were calculated relative to a $BF_3 \times OEt_2$ solution [260]. Using a boron-free probe and multiple scans, reliable spectra for solids with B concentrations as low as 10 ppm can be obtained. Peak surface integration with the DMfit software was used to determine the relative amounts of BO_3 and BO_4 [60].

2.9 Statistical analysis

Principal Component Analysis (PCA) was performed on variously combined datasets of the measurements taken from SEM images of cryptic species (samples s1-s6, Section 2.3). The first dataset contained only biometrical data, the second only calcification data, and the third contained both biometrical and calcification data. The biometrical data included epithallial and perithallial cell sizes. Instead, calcification data included the SC thickness, cell wall area, and PC thickness in both epithallial and perithallial cells. Furthermore, for both biometrical and calcification datasets, parametric and non-parametric univariate analysis of variance was used to assess the statistical significance of differences in group medians and means. Univariate analysis was also used to compare the outcomes in biometrical and calcification data of short and long cells. The PCA was also performed on a dataset including boron isotopes, boron speciation and XRD data from samples s2-4, s8, s12-14 and s24-32 (Table 2.1) to evaluate possible species-specific, family-specific or site-specific groupings. Univariate statistics were also run on both the LA-ICP-MS dataset containing all of the spot analyses and the same dataset containing records from long and short cells separately (Section 2.6.1). Image analysis on sections used for LA-ICP-MS was used to distinguish between the cell type in each spot. To provide statistical comparisons between Mg/Ca, Li/Ca, Sr/Ca, and B/Ca records from LA-ICP-MS analyses in *L. corallioides*, Spearman's correlation was tested. Spearman's correlations were also calculated to evaluate the relationships between B speciation and mineralogical content. The Kruskal-Wallis test, followed by Dunn's test, and the One-way ANOVA, followed by Tukey's test, were used to compare geochemical signals across sampling sites and to test differences in group medians and means. The PCA analysis was performed in MATLAB R2020a software using the Ballabio [46] PCA toolbox. All of the other statistical analyses were carried out using the R 3.6.3 software.

Chapter 3

Results

3.1 Environmental data

The standard deviation and ΔT values in Table 3.1 show that the amplitude of the seasonal temperature change in the Mediterranean samples used for LA-ICP-MS (Section 2.6.1) was lower than in the Atlantic site.

Table 3.1: Environmental data for the sampling sites where *Lithothamnion corallioides* for LA-ICP-MS was collected (Table 2.1, Section 2.6.1). Monthly temperature means were extracted by 11 years of ORAS5 reanalysis; the pH and DIC for each sampling site were measured over an 18 years time period from monthly mean biogeochemical data provided by CMEMS (Section 2.2).

Sample	**Site, depth (m)**	**Temperature (°C)**				**pH**	**DIC (μmol/kg)**
		min	**max**	**ΔT**	**mean±SD**	**mean±SD**	**mean±SD**
s8	Morlaix, 12	8.3	17.2	8.9	12.4±2.5	8.05±0.04	2155.60±15.27
s12	Aegadian Isl., 40	13.7	18.8	5.1	15.9±1.3	8.11±0.02	2303.72±11.58
s13	Elba, 45	12.9	17.5	4.6	15.0±1.2	8.13±0.02	2322.24±7.08
s14	Pontian Isl., 66	13.9	16.7	2.8	15.0±0.6	8.13±0.01	2321.29±6.71

This difference is explained by the different sampling depths, with seasonal variations decreasing as depth increases (Figs. A.1, A.2, A.3 and A.4 for the complete time-series of temperature and carbon data). Temperature variations were greater in Morlaix Bay (sample s8), with an overall mean seawater temperature of 12.4°C (Table 3.1). Aegadian Isl. (sample s12) had the highest mean seawater temperatures among Mediterranean sites, followed by Elba (s13) and Pontian Isl. (s14) (Table 3.1). Aegadian Isl. also had the greatest temperature variations among Mediterranean sites. Elba had moderate temperature variations and the lowest monthly mean temperature among Mediterranean sites (Table 3.1). Pontian Isl. had the lowest seawater temperature variations, which is consistent with the fact that it is the deepest sampling site at 66 m depth (Table 3.1). The Mediterranean pH estimates were all similarly high (∼8.13) and less variable than the Atlantic site (Morlaix Bay: 8.05) (Table 3.1). Pontian Isl. and Elba had slightly higher mean pH values than Aegadian Isl. (Table 3.1). Similarly, DIC was higher in the Mediterranean sites and lower in Morlaix, as this is a major determinant of pH (Table 3.1). The temperature of the seawater in the sites near CO_2 seeps varies significantly seasonally (>4°C), as expected in shallow coastal waters (Table 3.2). Salinity fluctuates moderately, being higher in Methana (∼0.60 ppt) than in Ischia (∼0.20 ppt). As a result of gas venting and lateral transport currents, the pH varies between 6.8 and 8.08 by mean in Ischia and between 7.57 and 7.77 in Methana (Table 3.2). The highest pH variability is found in the vicinity of Ischia's hydrothermal vents (site S3; pH 6.80 ± 0.43), with significant variations also occurring in site S2 (pH 7.77 ± 0.32) (Table 3.2). Site S1, which is the furthest away from the vents in Ischia, has normal pH and a significantly lower amplitude of variation (8.08 ± 0.07) (Table 3.2). In Methana, site F and N, which are the furthest and closest to the seeps, have similar pH variability (∼0.30), with mean values of 7.77 and 7.57 units, respectively (Table 3.2).

Table 3.2: Environmental data for the sampling sites near CO_2 seeps (Table 2.1, Section 2.7). In Methana, data were derived from *in situ* data [37] (Section 2.2). In Ischia, pH was reviewed from literature data [235], while temperature and salinity were extracted by 7 years of monthly physical reanalysis [220] (Section 2.2).

Sample	**Site**	**Species**	**Temperature (°C)**	**Salinity (ppt)**	**pH**
			mean±SD	**mean±SD**	**mean±SD**
s15	Ischia S1	*C. officinalis*	19.93±4.48	37.91±0.19	8.08±0.07
s16	Ischia S2	*C. officinalis*	19.93±4.48	37.91±0.19	7.77±0.32
s17	Ischia S3	*C. officinalis*	19.93±4.48	37.91±0.19	6.80±0.43
s18	Ischia S2	*Peyssonnelia* sp.	19.93±4.48	37.91±0.19	7.77±0.32
s19	Ischia S2	*Peyssonnelia* sp.	19.93±4.48	37.91±0.19	7.77±0.32
s20	Ischia S3	*Peyssonnelia* sp.	19.93±4.48	37.91±0.19	6.80±0.43
s21	Methana F1	*Amphiroa* sp.	21.38±5.42	39.05±0.59	7.77±0.30
s22	Methana F2	*Amphiroa* sp.	21.38±5.42	39.05±0.59	7.77±0.30
s23	Methana N	*Amphiroa* sp.	21.51±5.42	39.00±0.65	7.57±0.31

3.2 Scanning Electron Microscopy: calcification traits as a new diagnostic tool?

3.2.1 *L. racemus* micro-anatomy

Specimens s1 and s2 (Table 2.1) were pink, non-geniculate and fruticose, with protuberances up to 1 cm long (up to 5 mm in s2). A longitudinal section of protuberances revealed perithallial filaments with a "fountain" pattern, with rows of cells that ran parallel and then diverged in opposite directions towards the thallus surface (Fig. 3.1). Dark and light growth bands were also observed (Fig. 3.1) [6]. Three superposed flattened epithallial cells (up to 5 in s1; Fig 3.1), were 2.92-3.72 μm long (L) and 11.48-12.59 μm in diameter (D) (Table 3.3). Primary and secondary pit connections linked perithallial cells, but there were no cell fusions (Fig. 3.1). In the longitudinal section, perithallial cells were rectangular, with L 17.87-27.20 μm and D 11.16-13.23 μm (Fig. 3.1; Table 3.3). Trichocytes were not found. Asexual uniporate conceptacles protruded weakly from the surface, each with a sunken pore aperture (Fig. 3.1). In the longitudinal medial section, the conceptacle chamber was kidney-shaped, with D 275.34-321.93 μm and H 112.48-120.82 μm (Fig. 3.1; Table 3.3), yielding a mean D/H ratio of 2.55. From the conceptacle floor rose a well-defined calcified columella (Fig. 3.1). Because the columella was taller than half the height of the conceptacle chamber (H), the distance between the columella top and the chamber roof (h1 in Caragnano et al. [6]) was H/2. Only in the neotype s1, the pore canal was cut medially. It was conical, triangular in section, $\sim$41 μm long, bordered by filaments made up of 3-4 cells, and had a rhomboidal enlarged cavity on top (Fig. 3.1; Table 3.3).

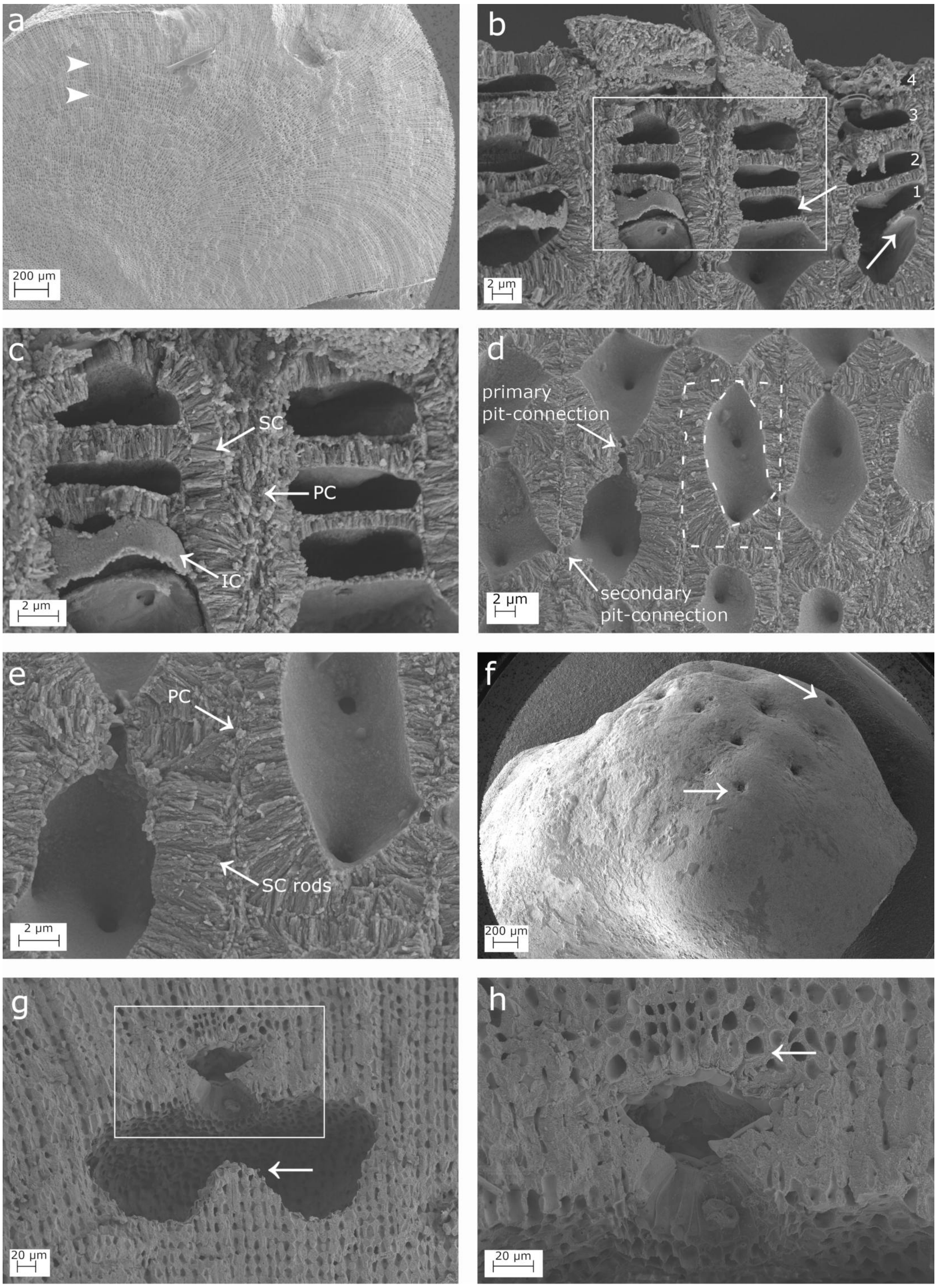

Figure 3.1: Longitudinal sections of *Lithophyllum racemus* (samples s1 and s2) under SEM. (a) Fountain pattern in the arrangement of perithallial cells and growth bands (arrowheads). (b) Four epithallial cells (numbered); note the evidence of meristematic division (arrows). (c) Magnification of the inset in (b) to show a primary (PC), secondary (SC) and inner calcification (IC). (d) Perithallial cells with primary and secondary pit-connections; the cell wall area corresponds to the surface included between the two dashed lines. (e) Magnification of (d) to show perithallial thin PC and rod-shaped crystallites of the SC. (f) Conceptacles weakly protruding from the surface (white arrows). (g) A conceptacle chamber showing a well-developed calcified columella (arrow). (h) Magnification of the inset in (g) showing the secondary hypothallus (arrow).

3.2.2 *L. racemus* calcification

The epithallial cells (Fig. 3.1) were highly calcified, with a cell wall area ranging from 30.17 to 174.39 μm^2 (Table 3.4). The PC between different cell filaments was made up of rod-shaped crystallites that ran parallel to the cell membrane (Fig. 3.1), whereas the PC between epithallial cells on the same filament was very thin and barely visible. The SC consisted of one layer of rods perpendicular to the cell membrane, which appeared locally as flattened, loosely packed elements (Fig. 3.1). It calculated a maximum SC thickness of 1.54 ± 0.3 μm (Table 3.4). An additional, distinct innermost thin calcified layer (IC) in contact with the plasma membrane was observed, made up of irregular granules with crenate margins and resembling a granular surface bordering the cell lumen (Fig. 3.1). A meristematic cell with primary and secondary pit connections lay below several epithallial cells with only primary pit connections (Fig. 3.1). As seen at the boundary of adjacent cell filaments, the meristem cell and its several generations of superposed epithallial cells shared the same PC and thick SC. Transversal division of the distal part of the meristematic cell results in the formation of a new epithallial cell. The IC formed the weak calcification of the newly formed horizontal portion of the cell membrane (Fig. 3.1), with the SC forming later and then gradually thickening in older epithallial cells. In the longitudinal section, the perithallial cells had an oblong lumen and strongly calcified cell walls with an area of 116.57-174.39 μm^2 (Fig. 3.1, Table 3.4). Perithallial PC was in the form of packed irregular rhomboids with smooth indented margins that were oriented parallel to the cell membrane (Fig. 3.2). The PC thickness measured between two adjacent cell filaments was 0.54-0.87 μm^2 (Table 3.4). The perithallial SC was formed in a single layer with a maximum thickness of 2.94 μm^2. The SC was composed of rod-shaped crystallites perpendicular to the cell membrane (Fig 3.1, Table 3.4). The internal surface of the cell lumen had granular calcification. An IC composed of irregular, more or less blocky granules was observed in the transverse section (s2 in Fig. 3.2). The primary hypothallus, or the first algal cells growing directly over the substrate, was not visible, but there were some prostrate cells growing over a conceptacle roof, forming a secondary hypothallus. The hypothallial primary crystallites appeared as 0.4 x 0.4 ± 0.1 μm packed regular and thin rhomboids that clearly progressed between two adjacent cell filaments (Figs. 3.1 and 3.2). The same thin rhomboids appeared as rod-like structures parallel to the cell lumen, perfectly bordering the rounded shape of the outer cell wall, depending on the visual perspective (Fig. 3.2).

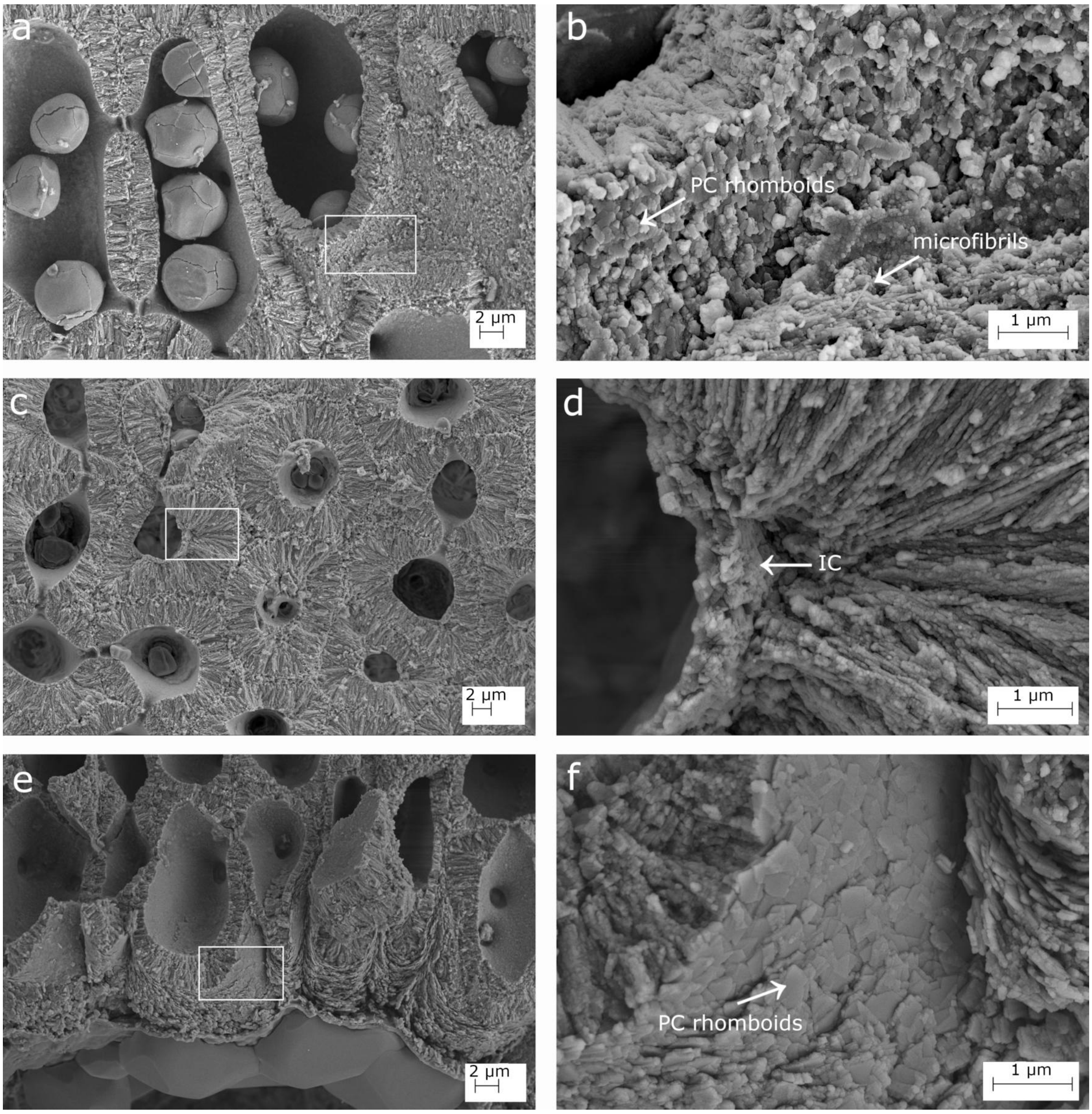

Figure 3.2: Calcification of *Lithophyllum racemus* under SEM. (a) Calcified perithallial cells; (b) magnification of the inset in (a) showing rhomboidal crystallites of the primary calcification (PC) embedded in organic microfibrils. (c) Transverse section of the perithallus; (d) magnification of the inset in (c) showing the innermost calcified layer (IC). (e) Secondary hypothallus over the conceptacle pore canal in Fig. 3.1; (f) magnification of the inset in (e) showing regular rhomboidal crystallites of the hypothallial PC.

Table 3.3: Biometrical data (mean±SD) measured from SEM images (μm).

Species	***L. racemus***		***L. pseudoracemus***		***L.* cf. *racemus***	
Sample	**s1**	**s2**	**s3**	**s4**	**s5**	**s6**
Perithallial cell (LxD)	17.9±4.3 x 11.2±2.4 N=39	27.2±4.6 x 13.2±3.3 N=15	15.4±1.6 x 10.5±1.6 N=42	16.28±2.8 x 10.79±1.2 N=22	20.5±2.5 x 2.5±2.5 N=19	21.1±2.5 x 11.8±1.8 N=34
Perithallial cell lumen (LxD)	13.8±3.2 x 6.3±1.2 N=51	22.1±3.7 x 7.1±1.9 N=32	12.5±2.0 x 4.9±0.9 N=63	14.06±2.6 x 5.43±1.1 N=58	19.4±2.8 x 7.6±1.2 N=23	19.8±2.5 x 7.3±1.1 N=34
Sporangial conceptacle chamber (DxH)	275.3±35.5 x 112.5±19.3 N=23	321.9 x 120.8 N=1	261.1±5.9 x 123.7±22.7 N=3	N=0	325.1 x 136.9 N=1	318.9±20.3 x 142.0±11.4 N=3
Pore canal length	40.9±3.0 N=6	N=0	41.7 N=1	N=0	37.5 N=1	46.8±6.4 N=3
Epithallial cell (LxD)	3.7±0.9 x 11.5±0.7 N=5	2.9±0.6 x 12.6±0.6 N=3	3.8±0.5 x 10.1±1.0 N=3	5.21±0.4 x 9.03±0.7 N=3	4.8±1.0 x 13.1±1.6 N=8	5.2 x 11.3 N=1
Epithallial cell lumen (LxD)	2.1±0.4 x 7.5±1.4 N=18	1.3±0.1 x 8.9±0.1 N=4	2.3±0.4 x 7.2±1.1 N=7	2.75±0.5 x 6.16±0.6 N=5	2.3±0.9 x 8.6±1.4 N=9	3.0±0.6 x 8.6±2.8 N=5
Epithallial cells (number)	3, up to 5	3	1 or 2	1 or 2	1 or 2	1 or 2

Table 3.4: Calcification data (mean±SD) measured from SEM images (μm^2 for the cell wall area, μm for other measurements).

Species	***L. racemus***		***L. pseudoracemus***		***L.* cf. *racemus***	
Sample	**s1**	**s2**	**s3**	**s4**	**s5**	**s6**
Perithallial SC thickness	2.7±0.6 N=50	2.9±0.6 N=31	2.5±0.4 N=62	2.3±0.4 N=57	2.9±0.6 N=23	2.4±0.5 N=34
Perithallial PC thickness	0.5±0.2 N=28	0.9±0.2 N=35	1.0±0.3 N=31	1.6±0.5 N=54	1.3±0.3 N=24	1.2±0.3 N=23
Perithallial cell wall area	116.6±34.7 N=39	174.4±50.2 N=24	99.7±18.9 N=35	100.5±21.3 N=23	137.8±29.2 N=21	117.7±26.0 N=22
Epithallial SC thickness	1.5±0.3 N=18	1.4±0.2 N=3	1.0±0.3 N=3	0.9±0.2 N=5	1.1±0.2 N=4	1.0±0.4 N=9
Epithallial cell wall area	30.2±8.4 N=6	26.0±8.2 N=3	25.0±9.7 N=5	25.0±8.33 N=6	35.8±12.0 N=7	27.2±8.3 N=4

3.2.3 *L. pseudoracemus* micro-anatomy

Specimens were pink, non-geniculate and fruticose, with protuberances up to 5 mm long (up to 2 mm in s4). The same "fountain" pattern in the arrangement of perithallial cells was observed in sample s3, as previously observed in *L. racemus* (Fig. 3.3). There was no evidence of perithallial banding. Each cell filament, 3.84-5.21 μm long (L) and 9.03-10.07 μm in diameter (D), was terminated by one or two epithallial cells (Fig. 3.3, Table 3.3). In longitudinal section, the perithallial cells were rectangular, with numerous secondary pit-connections, L 15.40-16.28 μm and D 10.55-10.79 μm. The asexual conceptacles' external surface appeared depressed, with a sunken pore aperture (Fig. 3.3). The asexual uniporate conceptacles in s3 had a rounded chamber with a D/H ratio of 2.11 (Table 3.3). The triangular pore canal was 42 μm long with three cells in the pore canal. There was no evidence of calcified columella and trichocytes were only found on the outskirts of a conceptacle chamber (Fig. 3.3). Sample s4 was sterile.

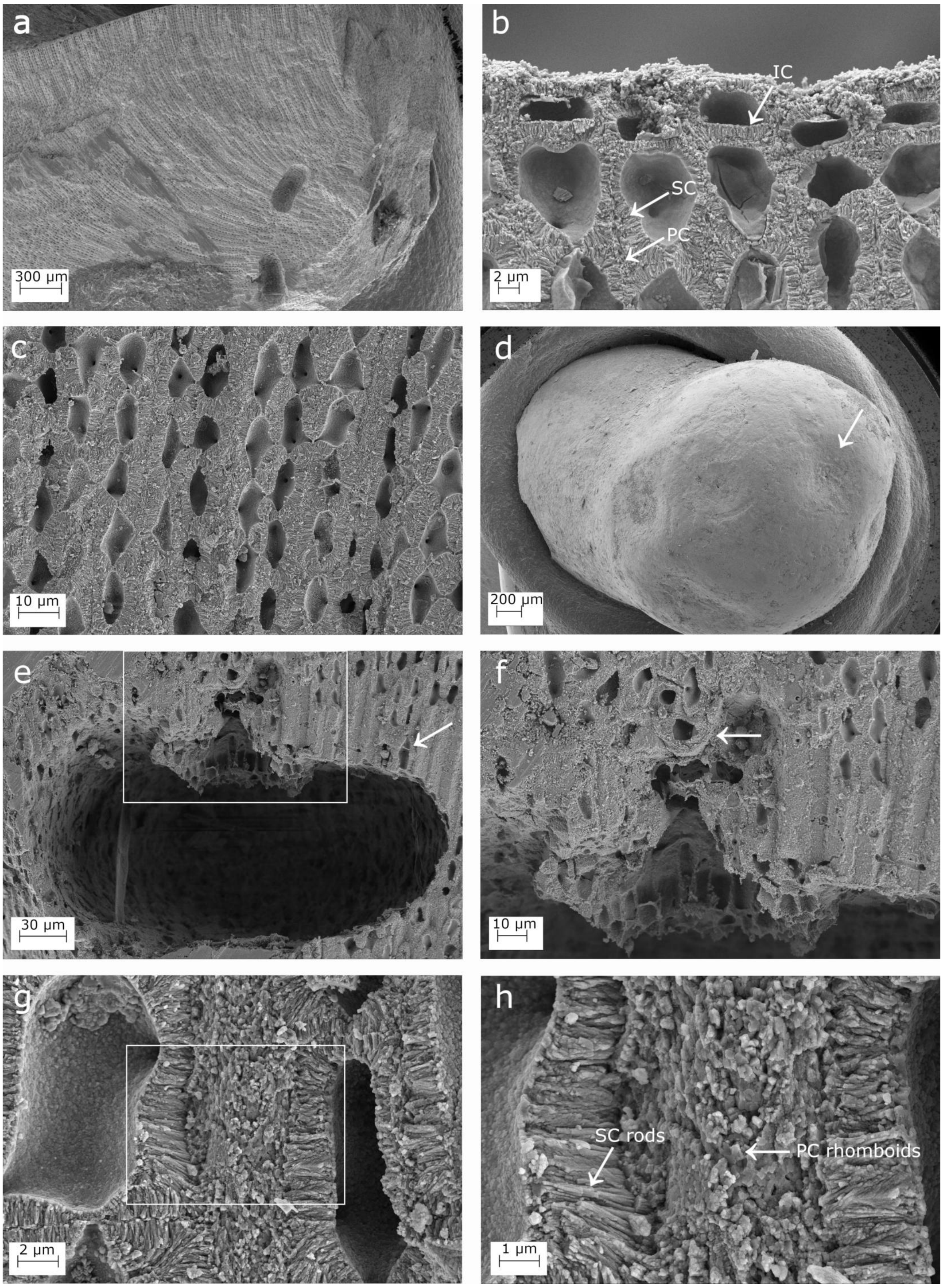

Figure 3.3: Longitudinal sections of *Lithophyllum pseudoracemus* (samples s3 and s4) under SEM. (a) The fountain-like arrangement of perithallial cell filaments that diverge toward the thallus surface. (b) Epithallial cells' primary calcification (PC), secondary calcification (SC), and the innermost calcified layer (IC). (c) Perithallus. (d) Depressed conceptacle in surface view (arrow). (e) Conceptacle chamber with no calcified columella and a trichocyte (arrow); (f) magnification of the inset in (e) showing the secondary hypothallus (arrow) over the pore canal. (g) PC and SC in the perithallus; (h) magnification of the PC and SC crystallites.

3.2.4 *L. pseudoracemus* calcification

The epithallial cells were highly calcified, with a cell wall area ranging from 24.96 to 25.01 μm^2 (Table 3.4).

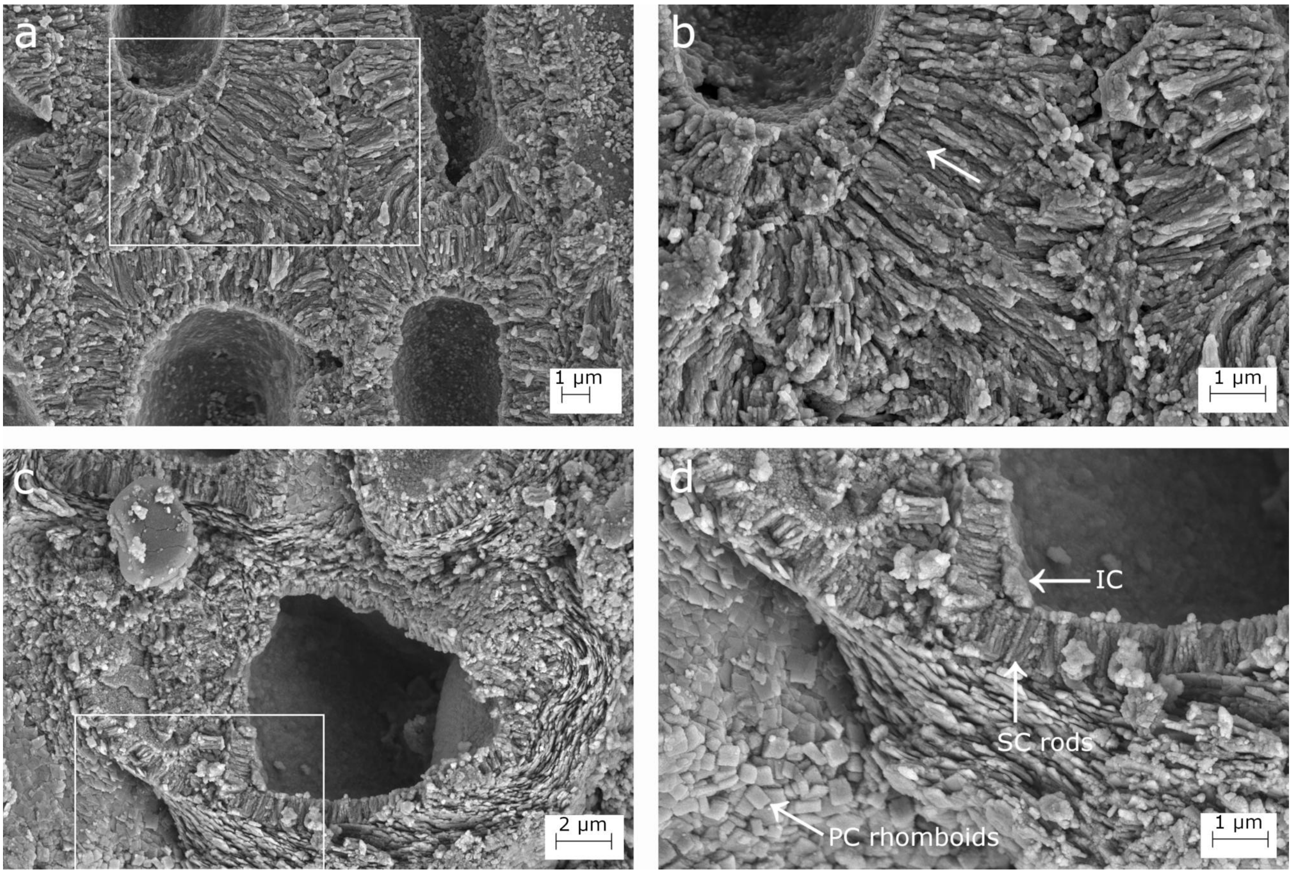

Figure 3.4: Calcification of *Lithophyllum pseudoracemus* under SEM. (a) Multiple layers of secondary calcification (SC) forming the thick cell wall; (b) magnification of the inset in (a) showing the contact of two SC layers (arrow). (c) Secondary hypothallus of the pore canal in Fig. 3.3; (d) magnification showing the rhomboidal crystallites in the hypothallial primary calcification (PC), the SC rods and the innermost calcified layer (IC).

The PC was not detectable between the epithallial cell and the underlying meristem cell in the same filament. Still, it was highly calcified and consisted of irregular granules between two adjacent cell filaments (Fig. 3.3). The epithallial SC had a maximum thickness of 0.98 μm and was composed of 1-2 layers of rods with a granular texture that lay perpendicular to the cell membrane (Fig. 3.3, Table 3.4). The internal surface of the cell lumen was calcified, forming an IC between the plasma membrane and the perpendicular rods of the SC (Fig. 3.3). The perithallus contained oblong cells with calcified cell walls (Fig. 3.3). The perithallial cell walls measured 99.71-100.48 μm^2 in the area (Table 3.4). The perithallial PC had a thickness of 0.95-1.55 μm and was made up of packed irregular rhomboids with smooth indented margins (Fig. 3.3, Table 3.4). The perithallial SC had a maximum thickness of 2.31-2.53 μm and was composed of long perpendicular rods with a granular texture arranged in 1 to 4 layers (Figs. 3.3 and 3.4, Table 3.4).

3.2.5 *L.* cf. *racemus* micro-anatomy

Sample s5 was pink, non-geniculate, and fruticose, with protuberances up to 3 mm long. The "fountain" pattern of perithallial growth was visible at a small scale, as was the banding pattern in some areas. One or two flattened epithallial cells were observed, L 4.78 ± 1.0 μm and D 13.12 ± 1.6 μm (Fig. 3.5, Table 3.3). In longitudinal sections the perithallial cells were rectangular, L 20.52 ± 2.5 μm and D 12.51 ± 2.5 μm (Table 3.3). Trichocytes were not found. The kidney-shaped chamber of the asexual uniporate conceptacle was D 325.13 μm and H 136.94 μm and had a D/H ratio of 2.37 (Fig. 3.5, Table 3.3). The conceptacle chamber had a clearly visible, calcified columella, which reduced the conceptacle chamber height h1 to less than H/2 [57]. The pore canal was 37.5 μm long, triangular in longitudinal section, lined by 3 cells, and had a cavity on top (Fig. 3.5, Table 3.3). Specimen s6 (*Lithophyllum* cf. *pseudoracemus*) was dark pink in colour, non-geniculate, and fruticose, with protuberances up to 4 mm long. Flattened one or two epithallial cells were found, with L 5.18 μm and D 11.31 μm (Fig. 3.6, Table 3.3). L 21.11 ± 2.5 μm and D 11.82 ± 1.8 μm were the measures of the perithallial cells (Fig. 3.6, Table 3.3). The banding pattern of the perithallial zonation was not visible. The kidney-shaped chambers of the asexual uniporate conceptacles were D 318.95 ± 20.3 μm and H 141.96 ± 11.4 μm (Fig. 3.6, Table 3.3), and 2.25 in D/H. A calcified columella was observed rising from the conceptacle floor in some conceptacles (Fig. 3.6). The columella developed differently, but it never grew taller than half the height of the conceptacle chamber, resulting in h1 H/2. The pore canal was triangular in shape, about 47 μm long, and made up of 2-3 cells with a rhomboidal cavity on top (Fig. 3.6, Table 3.3). Some prostrate cells of a secondary hypothallus were clearly visible over a conceptacle roof, close to the pore canal (Fig. 3.3). This was made up of packed rhomboids measuring 0.4 x 0.4 ± 0.1 μm in size (Fig. 3.4). In some places, the rhomboids appeared as thin slips. The IC was detected as a granular layer at the SC's inner boundary (Fig. 3.4).

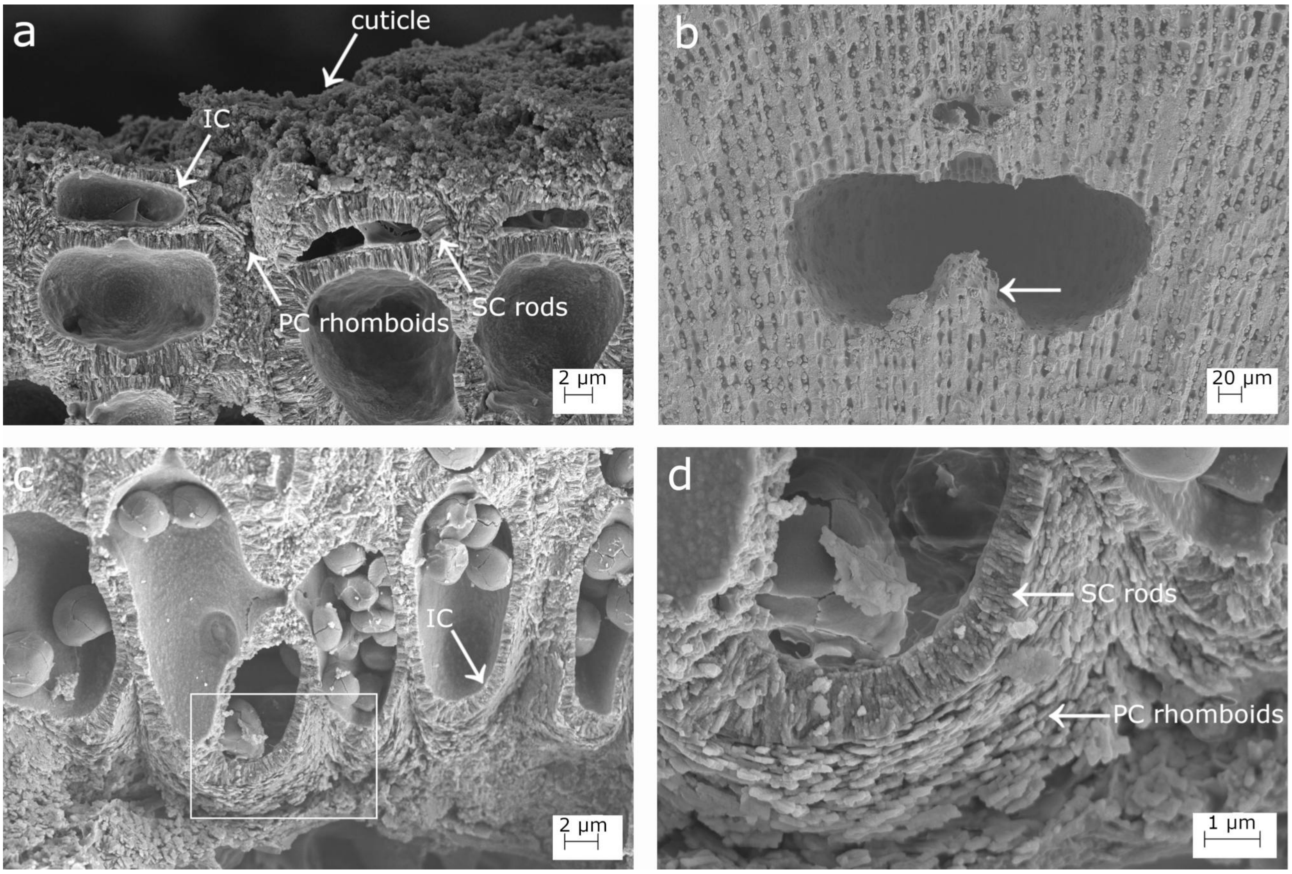

Figure 3.5: Longitudinal sections of *Lithophyllum* cf. *racemus* sample s5 under SEM. (a) Epithallial calcified cells are covered by a thick cuticle and bordered by a primary calcification (PC), a secondary calcification (SC), and an innermost calcified layer (IC). (b) Conceptacle with a well-defined calcified columella (white arrow). (c) Secondary hypothallial cells in the proximity of a pore canal and IC; (d) magnification of the inset in (c) showing the SC rhomboidal crystallites and the PC rhomboids.

3.2.6 *L.* cf. *racemus* calcification

The epithallial cells of specimen s5 (*Lithophyllum* cf. *racemus*) were strongly calcified, with a thick cuticle covering their surface (Fig. 3.5). The area of the epithallial cell wall was 35.80 ± 12.0 μm^2. (Table 3.4). PC was either undetectable or absent between epithallial cells of the same filament. Rhomboidal elements made up the thick epithallial PC between adjacent cell filaments (Fig. 3.5). The epithallial SC had a maximum thickness of 1.05 ± 0.2 μm and was made up of perpendicular rods that were slightly more regular in shape than those in the perithallial SC (Fig. 3.5, Table 3.4). The internal surface of the cell lumen was made of granules that formed a very thin IC (Fig. 3.5). The perithallus contained calcified oblong cells with a cell wall area of 137.79 ± 29.2 μm^2 (Table 3.4). The PC between two adjacent cell filaments was 1.28 ± 0.3 μm thick and made up of small irregular granules (Table 3.4). The PC between cells on the same filament was barely visible. The SC was a single layer of rods oriented perpendicular to the cell membrane with a maximum thickness of 2.87 ± 0.6 μm (Table 3.4). The secondary hypothallus was discovered as prostrate cells growing on a conceptacle roof near the pore canal (Fig. 3.5). These hypothallial cells had a PC made up of packed rhomboids measuring 0.3 x 0.3 ± 0.1 μm and running parallel to the cell membrane (Fig. 3.5). The hypothallial SC was made up of thin granular rods that ran parallel to the cell membrane (Fig. 3.5). From within the cell lumen, the IC in contact with the SC appeared granular (Fig. 3.5). The epithallial cells of sample s6 were heavily calcified (Fig. 3.6). The area of the cell wall was 27.18 ± 8.3 μm^2 (Table 3.4). The PC between the epithallial and subtending meristematic cells was undetectable, whereas the PC between adjacent cell filaments was thick and irregularly formed. The epithallial SC was made up of regular rods perpendicular to the cell membrane, with a maximum thickness of 0.99 ± 0.4 μm (Fig. 3.6, Table 3.4). The cell membrane separated the cell lumina, making it impossible to see the calcification (Fig. 3.6). Nonetheless, an IC of granular elements was found in contact with the SC. The perithallial cells were oblong and organized in rows. The area of the cell walls was 117.68 ± 26.0 μm^2 (Table 3.4). The PC between cells on the same filament was barely visible. The perithallial PC was 1.24 ± 0.3 μm thick and made up of irregular elements that ran parallel to the cell lumen (Table 3.4). The perithallial SC was made up of a single layer of rods oriented perpendicular to the cell membrane, with a maximum thickness of 2.43 ± 0.5 μm (Table 3.4). The internal surface delimiting the cell lumen was granular, forming a visible IC layer in contact with the SC's perpendicular rods. The perithallial cells had a distinct hexagonal perimeter in the transverse section (Fig. 3.6). The primary hypothallus calcified similarly to the secondary hypothallus cells observed in the samples described above (Fig. 3.6). The PC was created by packed rhomboidal slips around the cell (Fig. 3.6). The SC was made up of perpendicular rods arranged in one or two rows and had a very granular texture.

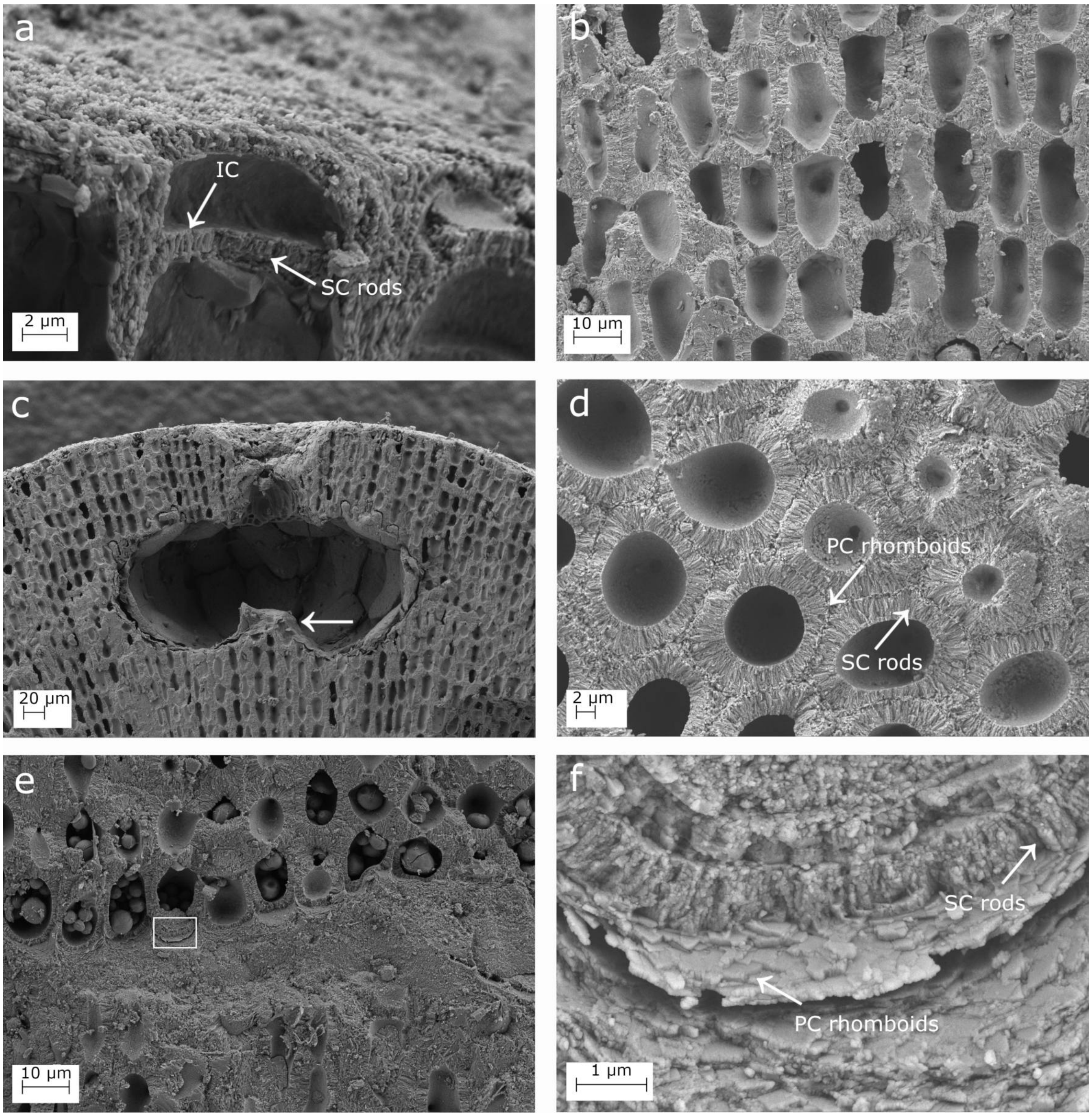

Figure 3.6: Longitudinal sections of *Lithophyllum* cf. *racemus* sample s6 under SEM. (a) The epithallial cell is bordered by the rods of the secondary calcification (SC), and the innermost calcified layer (IC). (b) The calcified perithallus. (c) Conceptacle with a short calcified columella (arrow). (d) The transverse section shows the SC and the primary calcification (PC). (e) The primary hypothallus growing over the substrate; (f) magnification of the inset in (e) showing multiple layers of hypothallial PC rhomboids and SC rods.

The biometrical statistical analyses revealed significant differences in perithallial cell sizes ($p<<0.001$) (Fig. 3.7, Table A.6). Perithallial cells in both *L. pseudoracemus* samples (s4, s3) were significantly smaller than those in *L. racemus* s2 and the two non-molecularly classified s5 and s6 ($p<<0.001$) (Fig. 3.7, Table A.6). Instead, with the exception of *L. pseudoracemus* s4 ($p = 0.23$), the *L. racemus* neotype (s1) showed intermediate perithallial cell size (Fig. 3.7), differing significantly from the other samples ($p<0.01$) (Fig. 3.7, Table A.6).

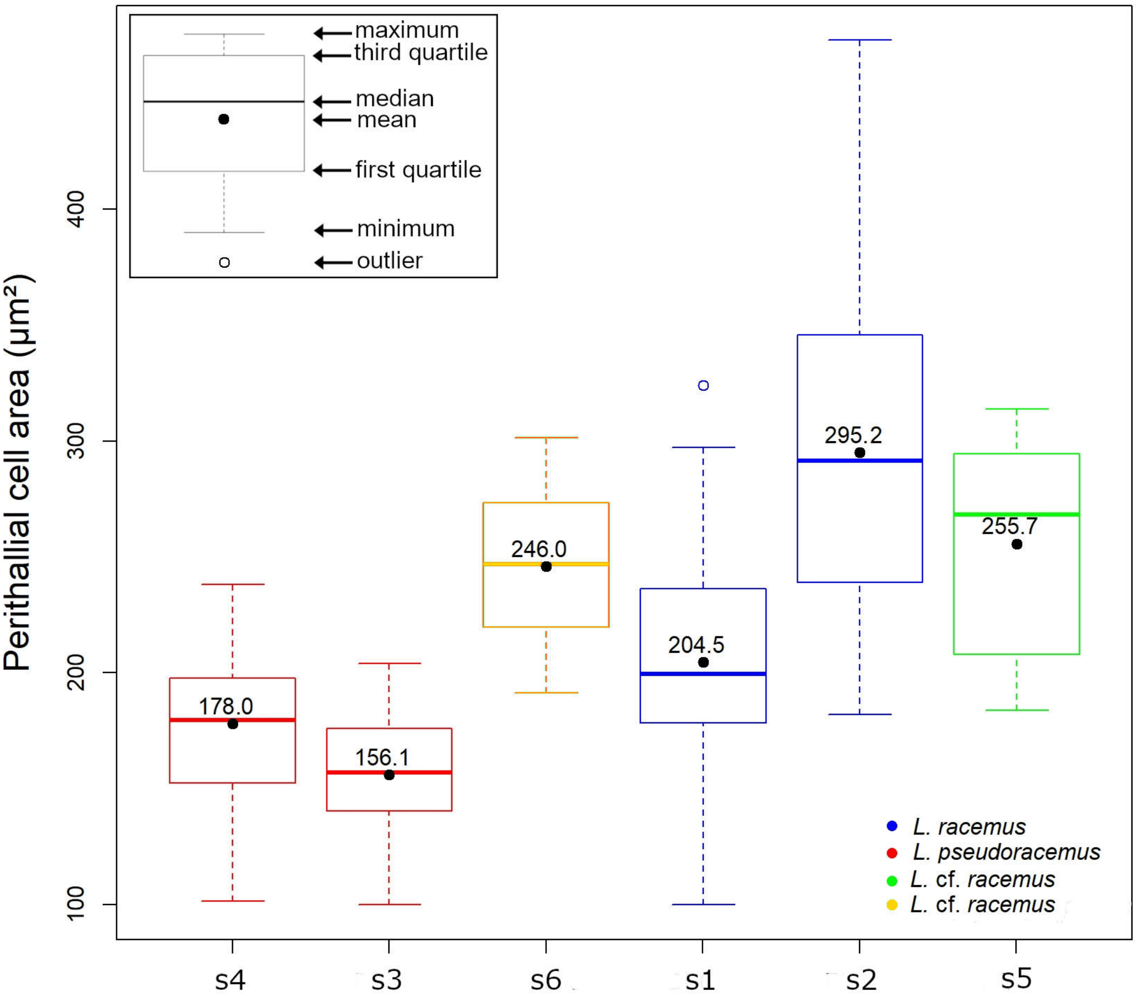

Figure 3.7: Results of the perithallial cell area measurement. The numbers inside the plots indicate the mean values.

Other biometrical variables measured did not reveal any further distinction between *L. pseudoracemus* and *L. racemus*. The only statistical test that supported a significant distinction between *L. racemus* and *L. pseudoracemus* was the multivariate analysis on calcification traits. The first two principal components (PCs) of the PCA model resolved 83% of the total data variance (Fig. 3.8). The main trend on the PC-1 axis was increasing SC thickness with increasing cell wall area, which was expressed as high negative PC-1 loadings for perithallial cell wall area and SC thickness (Fig. 3.8). Simultaneously, as the SC became thinner, the PC thickness increased, as evidenced by the high positive PC-1 loadings. Positive loadings of the cell wall area, perithallial PC thickness, and SC thickness were observed on the PC-2 axis, as were high negative loadings of the epithallial SC thickness (Fig. 3.8).

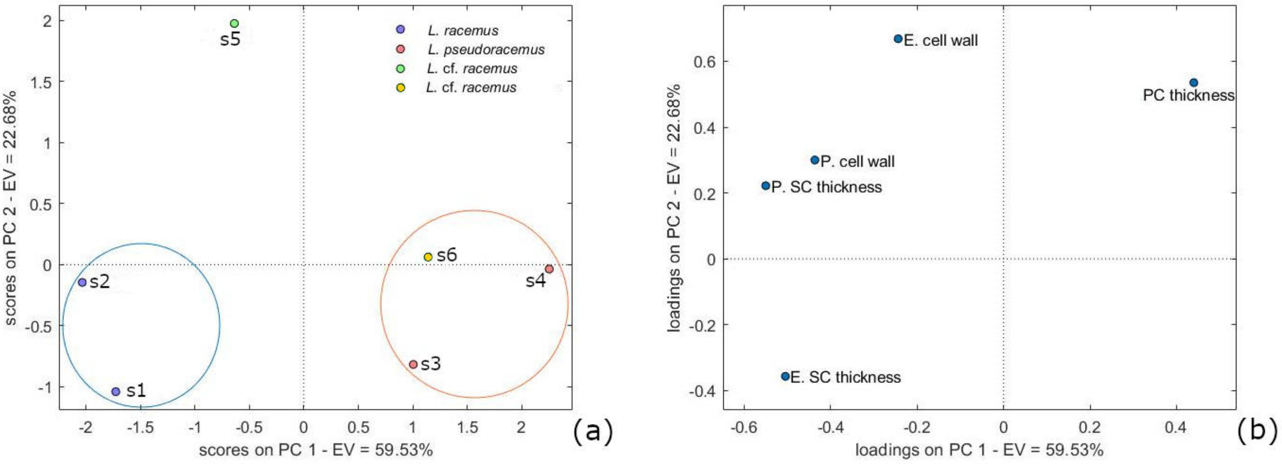

Figure 3.8: Principal component analysis (PCA); (a) score plot and (b) loading plot of PCA on calcification data in both perithallial (P.) and epithallial (E.) cells. The plots model 83% of the total data variance. Variance proportions are shown along each component axis. Calcification types are evidenced with circles and classified in *Lithophyllum racemus* type and *Lithophyllum pseudoracemus* type.

Overall, the PCA revealed two distinct calcification types based on natural groupings in the PC-2 versus PC-1 plot (Fig. 3.8). The *L. racemus* type had negative PC-1 and negative PC-2 scores (Fig. 3.8) and was distinguished by perithallial cells with high cell wall area and SC thickness values (Fig. 3.8, Table 3.4). The *L. pseudoracemus* type was distinguished by positive PC-1 and negative or neutral PC-2 scores, which corresponded to perithallial cells with low cell wall area and thin SC. This category also included *L.* cf *pseudoracemus* s6. The *L.* cf *racemus* s5 sample was distinguished from the others by having highly positive PC-2 and negative PC-1 scores (Fig. 3.8). Because the PC-1 scores explained 60% of the total data variance, they support the inclusion of *L.* cf *racemus* s5 in the type *L. racemus*. The majority of the distinction between sample s5 and the other samples of *L. racemus* type relied on the epithallial cell wall area, which was especially large (Fig. 3.8, Table 3.4). Given the PCA results, the role of the variables under consideration in supporting the separation of *L. racemus* from *L. pseudoracemus* was investigated. The only factor that distinguished the two species with statistical significance was perithallial SC thickness (Fig. 3.9, Table A.7). The PCA assigned *L.* cf *pseudoracemus* s6 to the *L. pseudoracemus* calcification type, while *L.* cf *racemus* s5 to the

L. racemus calcification type (Figs. 3.8 and 3.9, Table 3.3). The mean epithallial SC thickness differed between *L. racemus* and *L. pseudoracemus* (Table 3.4), but the ANOVA results did not support a statistical significance of this feature.

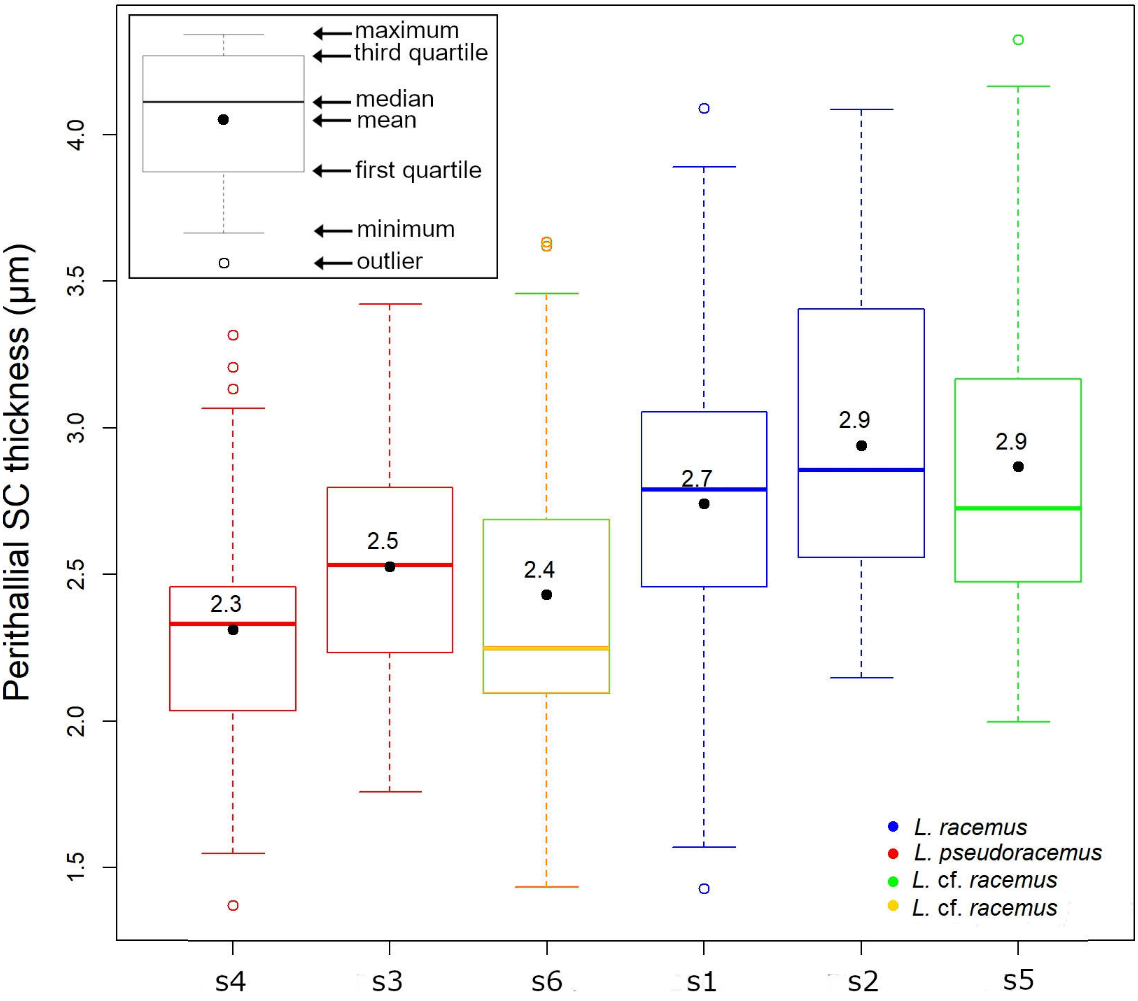

Figure 3.9: Results of the perithallial SC thickness measurement. The numbers inside the plots indicate the mean values.

It was also possible to distinguish between the sizes of short and long cells within the perithallus in *L. racemus* s2 (Fig. 3.10). Long cells were significantly longer than short cells (25.25 μm vs. 19.58 μm, p<0.001). Short and long cells had very similar cell lumen areas, but short cells had more cell wall area and a thicker SC, whereas long cells had a thicker PC (Fig. 3.10). Despite this, none of the differences were statistically significant (p>0.05).

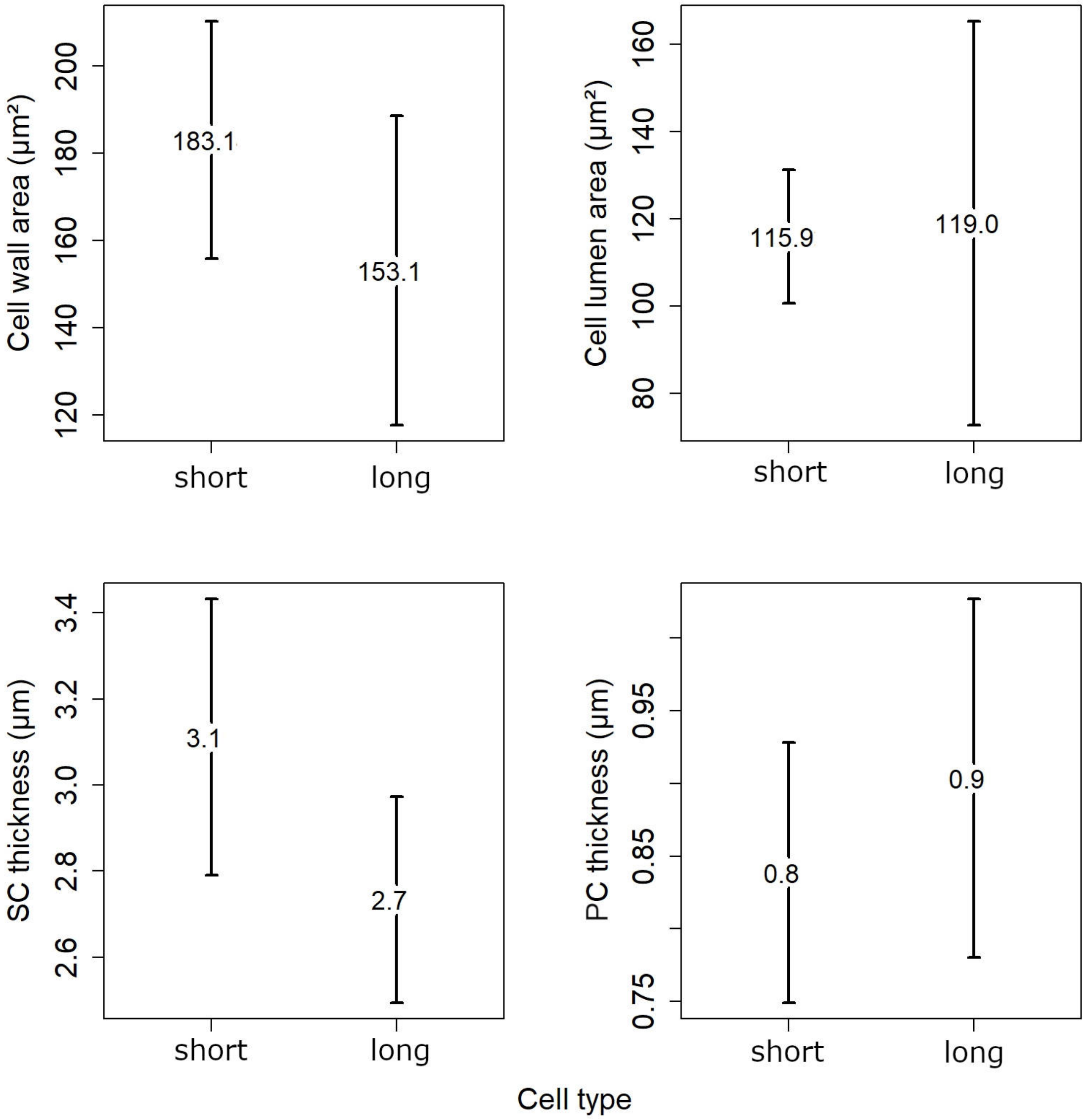

Figure 3.10: Mean values of the measurements in short and long cells of *Lithophyllum racemus* sample s2. The numbers inside the plots indicate the mean values for the cell wall area, cell lumen area, SC thickness and PC thickness.

3.3 Deep learning can support conventional taxonomic classification?

3.3.1 Internal Validation

Table 3.5 compares the results of the *Internal Validation* procedure to the performances of dummy and human classifiers. The 3 class-CNN achieved the highest classification accuracy (64%), while the 4 class-CNN (species level) achieved the lowest (48%) (Table 3.5). The *Global* cross-validation *accuracy* was similar in the 2 class-CNN (*L. pseudoracemus* versus Others, 61%) and the 3 class-CNN (genus level) despite the increased difficulty in the task in the latter, due to the higher number of classes and thus data sparsity. In terms of *Class Recall*, the 2 class-CNN showed a significant improvement in the identification of *L. pseudoracemus* (61% vs. 27% for the dummy baseline and 27% for the human classifier), despite a decrease in *Recall* and *Global accuracy* for Others when compared to expert evaluation (Table 3.5). The *Global accuracy* and the *Class Recall* for both 3 and 4 class-CNNs were higher than the baselines, except for *Lithothamnion* sp. (or *L. corallioides*), where a 55% and 57% *Recall* is achieved, compared to the 73% of the human classifier. Nonetheless, the models significantly outperformed the expert classification in *Recall* (with a maximum of +27% for *Lithophyllum* sp. *Recall*) and *Accuracy* (+15%) (Table 3.5). The model classified the two genera *Lithothamnion* and *Mesophyllum* with a *Recall* that was more than twice as high as the dummy classifier. Similar conclusions can be drawn from the *Recall* at the species level (4 class-CNN). Another intriguing finding is that, despite having a sparser classification task, the *Lithothamnion* genus was predicted slightly better at the species level (*L. corallioides* class), with an increased *Recall* from 55% to 57% (Table 3.5). Because of their morphological similarity, the classification of *L. racemus* and *L. pseudoracemus* in the 4 class-CNN was the most challenging task, and the model's results, as well as the empirical evidence of human evaluation, were consistent with domain-related studies (Table 3.5). Indeed, the increase in *Recall* was consistently between 10% and 15% at the genus and species levels, when compared to the baseline of the dummy classifiers. *L. pseudoracemus* was the most difficult class to identify by the model in the 4 class-CNN, with the lowest *Recall* of 37%.

In comparison to the model, high human performances in *Recall* were limited to the *L. corallioides* class, while all other classes at both the genus and species levels had significantly lower *Recall* (Table 3.5). The computed CNN-based models outperformed in *Global accuracy* human diagnosis at both genus and species levels, as well as in *Recall* of the most difficult distinguishable classes, *L. racemus* and *L. pseudoracemus*.

3.3.1.1 Categories

Table 3.6 summarizes the *Class Recall* results for each class and modelling approach based on the morphological category represented in the image. The 2 class-CNN correctly recognized all images showing the conceptacle and 70% of crystallites and the epithallial cell in *L. pseudoracemus*. However, only 14% of the images of the *L. pseudoracemus* perithallus were correctly classified. With the exception of *L. pseudoracemus* (Others), the percentages of images correctly identified were balanced across classes, with an average accuracy of 64%. Overall, approximately 61% of the SEM images in both *L. pseudoracemus* and Others classes were correctly classified, despite the fact that the class Others had nearly three times more images (Table 3.6). The images with no category (n.c.) were mostly assigned to the correct class, as were the images within the class Others with multiple categories ("shared"), which included five images of the hypothallus, two images of the epithallial cell and perithallus, and one image of the perithallus and crystallites. In the 2 class-CNN model, the n.c. images included the conceptacle pore canal and the perithallus with crystallites near the pore canal in *L. racemus* (Figure 3.11) and *L. pseudoracemus*.

Table 3.5: Resulting performances in each classification task: *Lithophyllum pseudoracemus* versus the other species (i.e., Others) (2 classes); diverse genera (3 classes) and diverse species (4 classes). The *Global accuracy* and the *Class Recall* are shown for the proposed model (CNN), the human classifier (HC) and the dummy classifier (DC).

2 classes				**3 classes**			
	Class Recall				***Class Recall***		
	CNN	HC	DC		CNN	HC	DC
L. pseudoracemus	0.61	0.21	0.27	*Lithothamnion* sp.	0.55	0.73	0.23
Others	0.62	0.92	0.73	*Mesophyllum* sp.	0.56	0.41	0.19
				Lithophyllum sp.	0.69	0.42	0.58
Global accuracy	0.61	0.73	0.62	***Global accuracy***	0.64	0.49	0.43
4 classes							
	Class Recall						
	CNN	HC	DC				
L. corallioides	0.57	0.73	0.23				
M. philippii	0.49	0.41	0.19	See Section 2.4.4, Evaluation strategy			
L. racemus	0.46	0.33	0.31				
L. pseudoracemus	0.37	0.21	0.27				
Global accuracy	0.48	0.40	0.27				

Table 3.6: *Class Recall* results per morphological category for each class (*Lithophyllum pseudoracemus* versus other species, diverse genera, and diverse species). The total number of SEM images in each category is also shown, and images not assigned to a category (n.c.) and showing more than one category (shared) are also included.

2 classes

Class Recall (Images)

	L. pseudoracemus	Others	
conceptacles	1.00 (01)	0.56 (09)	
perithallus	0.14 (07)	0.53 (32)	
crystallites	0.70 (27)	0.61 (67)	See Section 2.4.4, Evaluation strategy
epithallial cell	0.70 (10)	0.71 (24)	
hypothallus	(00)	0.67 (03)	
surface	0.60 (05)	0.57 (07)	
n.c.	1.00 (02)	0.75 (04)	
shared	0.40 (05)	0.73 (11)	

3 classes

Class Recall (Images)

	Lithothamnion sp.	*Mesophyllum* sp.	*Lithophyllum* sp.
conceptacles	(00)	0.75 (04)	0.67 (06)
perithallus	0.65 (20)	0.33 (03)	0.44 (16)
crystallites	0.57 (14)	0.38 (13)	0.85 (67)
epithallial cell	0.42 (12)	0.20 (05)	0.47 (17)
hypothallus	(00)	0.67 (03)	(00)
surface	0.50 (02)	0.50 (04)	0.17 (06)
n.c.	(00)	1.00 (01)	0.80 (05)
shared	0.00 (01)	1.00 (08)	0.57 (07)

4 classes

Class Recall (Images)

	L. corallioides	*M. philippii*	*L. racemus*	*L. pseudoracemus*
conceptacles	(00)	1.00 (04)	0.80 (05)	1.00 (01)

Table 3.6 (continue)

perithallus	0.60 (20)	0.33 (03)	0.22 (09)	0.00 (07)
crystallites	0.71 (14)	0.00 (13)	0.48 (40)	0.37 (27)
epithallial cell	0.50 (12)	0.20 (05)	0.57 (07)	0.70 (10)
hypothallus	(00)	0.67 (03)	(00)	(00)
surface	0.00 (02)	0.75 (04)	0.00 (01)	0.40 (05)
n.c.	(00)	1.00 (01)	0.33 (03)	0.00 (02)
shared	0.00 (01)	1.00 (08)	0.50 (02)	0.20 (05)

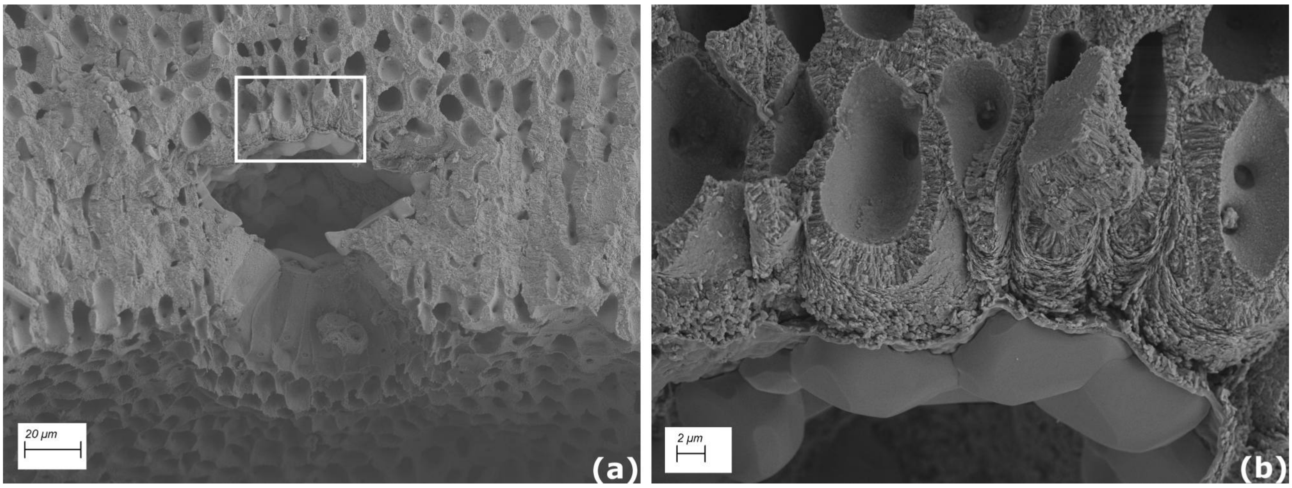

Figure 3.11: Examples of SEM images belonging to the n.c. category: (a) *Lithophyllum racemus* pore canal; (b) a magnification showing perithallial cells near the pore canal. These features proved to be significant contributors to the correct classification of *Lithophyllum* spp. in the 2 and 3 class-CNNs (Table 3.6).

Among the genera, *Lithophyllum* sp. had the highest percentage of correctly classified images (69%). The presence of conceptacles, as well as the perithallus in the *Lithothamnion* sp. and the crystallites in both *Lithothamnion* sp. and *Lithophyllum* sp. (Table 3.6), were still important for correct classification. *Mesophyllum* sp., the only genus with a hypothallus, contributed significantly to identification, accounting for 67% of correct assignations. The “n.c.” images were also of significant assistance to the correct classification in the 3 class-CNN model (Table 3.6). The “shared” images correctly identified as *Mesophyllum* sp. included five hypothallus images, three of which also show the conceptacle and two of which also show the epithallial cell. The “n.c.” images correctly identified in the *Lithophyllum* sp. class included a pore canal of a conceptacle in *L. pseudoracemus*, perithallial cells and crystallites near the same pore canal, and pore canals in two different conceptacles of *L. racemus* (as in Figure 3.11). Conceptacles were also important for identifying algae at the species level (Table 3.6). The perithallus, on the other hand, only aided in the classification of *L. corallioides* (with 60% of correct assignations), to which crystallites also contributed significantly (71%). The epithallial cell images were mostly correctly classified in *L. pseudoracemus* (70%) but misclassified in *M. philippii* (20%). The hypothallus was a significant contributor to the classification of *M. philippii* (67%), as well as images showing the surface (75%). All of the "shared" images of *M. philippii* were correctly classified, matching those described for the 3 class-CNN. The SEM images of conceptacles were the most important contributors to the classification task's success in each model (Fig. 3.12). Except for the 4 class-CNN, crystallites also favoured exact classification, accounting for nearly half of the total number of SEM images in the dataset (Fig. 3.12, Table 3.6).

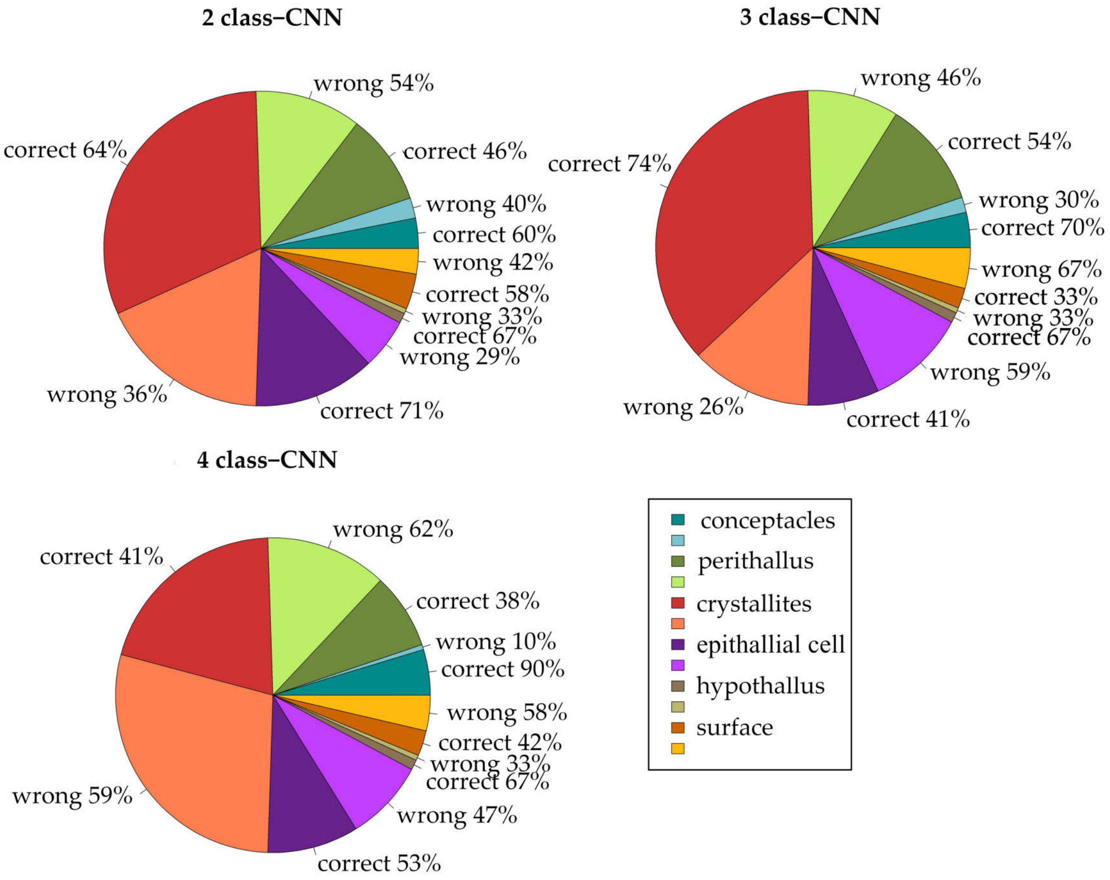
2 class–CNN

3 class–CNN

4 class–CNN

Figure 3.12: Number of SEM images classified in the 2, 3, and 4 class-CNNs that have been assigned to different categories. Percentages within each category represent the proportion of images correctly and incorrectly classified.

Aside from crystallites and conceptacles, the epithallial cell (71%, the highest value) and the hypothallus achieved high percentages of images correctly classified in the 2 class-CNN. In contrast, the epithallial cell, along with the surface, results in the most incorrect classifications in the 3 class-CNN (Fig. 3.12). Here crystallites, like conceptacles, grew in importance. The accuracy of the 4 class-CNN decreased, and fewer images showing the perithallus, surface, and crystallites were correctly classified (Fig. 3.12). Conceptacles were the most robust category for classification success (90% of images correctly classified), followed by the hypothallus, which maintained the same significance across models (67%).

3.3.2 External Test

Table 3.7 displays the *Class Share* for the two test samples, s5 and s6. Using the 2 class-CNN model, we can see how the two samples are classified similarly, with around 70% of the images in both samples belonging to the Others class. This method appears to imply that the two samples do not belong to the *L. pseudoracemus* class. The model in the 3 class-CNN approach is convincing in assigning the images of the two samples to the genus *Lithophyllum*. More specifically, more than 90% of the images in the s6 is classified in that class, while around 80% of the images in the s5 is classified as *Lithophyllum* sp., with the remaining 20% classified as *Lithothamnion* sp. (Table 3.7). Finally, there is a high similarity between the two samples in the 4 class-CNN, species-level classification. In both cases, s5 and s6 images are assigned to *L. racemus* (around 50%) and *L. pseudoracemus* (around 30% each), while 20% of s5 images are assigned to *L. corallioides* and less than 10% of the images are assigned to *L. corallioides* and *M. philippii* (Table 3.7). The *L. racemus* class has the highest *Class Share* with 54%. These findings are consistent with the expert evaluation of samples s5 and s6, which were identified as *L.* cf. *racemus*, despite the fact that it is impossible to distinguish between *L. racemus* and *L. pseudoracemus* without molecular data. Nonetheless, the 4 class-CNN model favoured *L. racemus* over *L. pseudoracemus* (around 50% versus 30%) (Table 3.7).

3.3.2.1 Categories

In terms of predictions, the majority of the SEM images showing the *L.* cf. *racemus* samples s5 and s6 were classified as Others in the 2 class-CNN, with very similar percentages (68% and 69%, respectively, as shown in Table 3.7). All conceptacles, as well as the majority of images showing crystallites and the epithallial cell, were assigned to this class, with a lower percentage for crystallites in sample s6 (67%) (Tables 3.8 and 3.9). The majority of the images showing the perithallus were classified as *L. pseudoracemus*, especially in sample s6. The surface image in this sample was also assigned to the *L. pseudoracemus* class (Table 3.9). The "n.c." images of perithallial cells in the vicinity of a pore canal in sample s5 have been classified as Others. An image of the epithallial cell and crystallites in sample s5 was identified as belonging to *L. pseudoracemus* (Table 3.8). At the genus level, 82% and 92% of the images from samples s5 and s6 were correctly classified as *Lithophyllum* sp., respectively (Table 3.7). In sample s6, the classification was correct for all categories, but the conceptacle in sample s5 was surprisingly assigned to *Lithothamnion* sp. (Tables 3.8 and 3.9).

Table 3.7: *Class Share* for the *Lithophyllum* cf. *racemus* samples s5 and s6 in the three classification tasks: *Lithophyllum pseudoracemus* versus Others (2 class-CNN), diverse genera (3 class-CNN), and diverse species (4 class-CNN).

2 classes			**3 classes**			**4 classes**		
Class Share			***Class Share***			***Class Share***		
	s5	s6		s5	s6		s5	s6
L. pseudoracemus	0.32	0.31	*Lithothamnion* sp.	0.18	0.00	*L. corallioides*	0.18	0.08
Others	0.68	0.69	*Mesophyllum* sp.	0.00	0.08	*M. philippii*	0.00	0.08
			Lithophyllum sp.	0.82	0.92	*L. racemus*	0.50	0.54
						L. pseudoracemus	0.32	0.30

At the species level, the majority of the images from samples s5 and s6 were assigned to *L.*

racemus and *L. pseudoracemus*, with the first class having a higher percentage (Table 3.7). All of the conceptacles, as well as crystallites, were identified as belonging to *L. racemus*, particularly sample s5. The perithallus images were classified as *L. pseudoracemus* with a higher probability in s6 (Tables 3.8 and 3.9). In both samples, the epithallial cell was identified as *L. corallioides*, while the surface was assigned to the *L. pseudoracemus* class in s6. In sample s5, all images with multiple categories were classified as *L. pseudoracemus* (Table 3.8). Every "shared" image showed the epithallial cell, two of which also included crystallites and one of which included the surface.

Table 3.8: Sample s5's *Class Share* for each assigned category and class. The total number of SEM images is shown after each category. Images that have not been assigned to a category (n.c.) or that show more than one category (shared) are also included. Note that sample s5 had no images of the hypothallus.

	2 classes		
	Class Share		
	L. pseudoracemus	Others	
conceptacles (01)	0.00	1.00	
perithallus (03)	0.67	0.33	
crystallites (12)	0.17	0.83)	See Section 2.4.4, Evaluation strategy
epithallial cell (05)	0.20	0.80	
surface (02)	0.50	0.50	
n.c. (02)	0.50	0.50	
shared (03)	0.67	0.33	

	3 classes		
	Class Share		
	Lithothamnion sp.	*Mesophyllum* sp.	*Lithophyllum* sp.
conceptacles (01)	1.00	0.00	0.00
perithallus (03)	0.33	0.00	0.67
crystallites (12)	0.00	0.00	1.00
epithallial cell (05)	0.40	0.00	0.60
surface (02)	0.50	0.00	0.50
n.c. (02)	0.00	0.00	1.00

Table 3.8 (continue)

shared (03)	0.00	0.00	1.00

4 classes

	Class Share			
	L. corallioides	*M. philippii*	*L. racemus*	*L. pseudoracemus*
conceptacles (01)	0.00	0.00	1.00	0.00
perithallus (03)	0.33	0.00	0.00	0.67
crystallites (12)	0.00	0.00	0.83	0.17
epithallial cell (05)	0.80	0.00	0.20	0.00
surface (02)	0.00	0.00	0.50	0.50
n.c. (02)	0.00	0.00	0.50	0.50
shared (03)	0.00	0.00	0.00	1.00

Table 3.9: Sample s6's *Class Share* for each assigned category and class. The total number of SEM images is shown after each category. Images that have not been assigned to a category (n.c.) or that show more than one category (shared) are also included. Note that sample s6, as for s5, had no images of the hypothallus.

2 classes

	Class Share		
	L. pseudoracemus	Others	
conceptacles (02)	0.00	1.00	
perithallus (02)	1.00	0.00	
crystallites (03)	0.33	0.67)	See Section 2.4.4, Evaluation strategy
epithallial cell (01)	0.00	1.00	
surface (01)	1.00	0.00	
n.c. (02)	0.00	1.00	
shared (02)	0.00	1.00	

Table 3.9 (continue)

3 classes

	Lithothamnion sp.	*Mesophyllum* sp.	*Lithophyllum* sp.
conceptacles (02)	0.00	0.00	1.00
perithallus (02)	0.00	0.00	1.00
crystallites (03)	0.00	0.00	1.00
epithallial cell (01)	0.00	0.00	1.00
surface (01)	0.00	0.00	1.00
n.c. (02)	0.00	0.00	1.00
shared (02)	0.00	0.50	0.50

Class Share

4 classes

	L. corallioides	*M. philippii*	*L. racemus*	*L. pseudoracemus*
conceptacles (02)	0.00	0.00	1.00	0.00
perithallus (02)	0.00	0.00	0.00	1.00
crystallites (03)	0.00	0.00	0.67	0.33
epithallial cell (01)	1.00	0.00	0.00	0.00
surface (01)	0.00	0.00	0.00	1.00
n.c. (02)	0.00	0.00	1.00	0.00
shared (02)	0.00	0.50	0.50	0.00

Class Share

3.3.3 Explanation

The areas more relevant to CNN classification were detected by analysing images with explainable artificial intelligence. Each approach used for explanation highlighted different areas of the image by displaying positive and negative contributions (LIME), a heat map of the positive contributions (Grad-CAM), or simply the more relevant pixels (Saliency) (Section 2.4.3)

(Fig. 3.13). Due to differences in the calculation of the outputs, the information provided by the three approaches was sometimes counterintuitively different. As a result, combining the visualisation of the three explanatory techniques could provide more insights into the relevant features displayed in the images. Given the complexity of the structures shown in the SEM dataset, recognising common diagnostic structures was not always possible. Nonetheless, the models correctly identified the shape of cells and conceptacles in the majority of cases (Fig. 3.14). Background areas and starch grains (Fig. 3.14) occasionally "disturbed" the image classification, resulting in incorrect identifications. Notably, crystallites and, more broadly, cell wall calcification can be regarded as critical features for the classification task.

Figure 3.13 depicts an example of *L. corallioides* crystallites in the perithallial cell walls of two adjacent cells that were correctly classified in all three models used by *Internal Validation* (2, 3 and 4 class-CNNs). The LIME, Saliency, and Grad-CAM approaches (Fig. 3.13) consistently revealed a significant contribution of primary calcification [90], i.e., the outermost calcified layer of the cell wall composed of crystallites oriented parallel to the cell lumen, also known as "interfilament," at the cell filament's boundary [267] (Section 1.1.2).

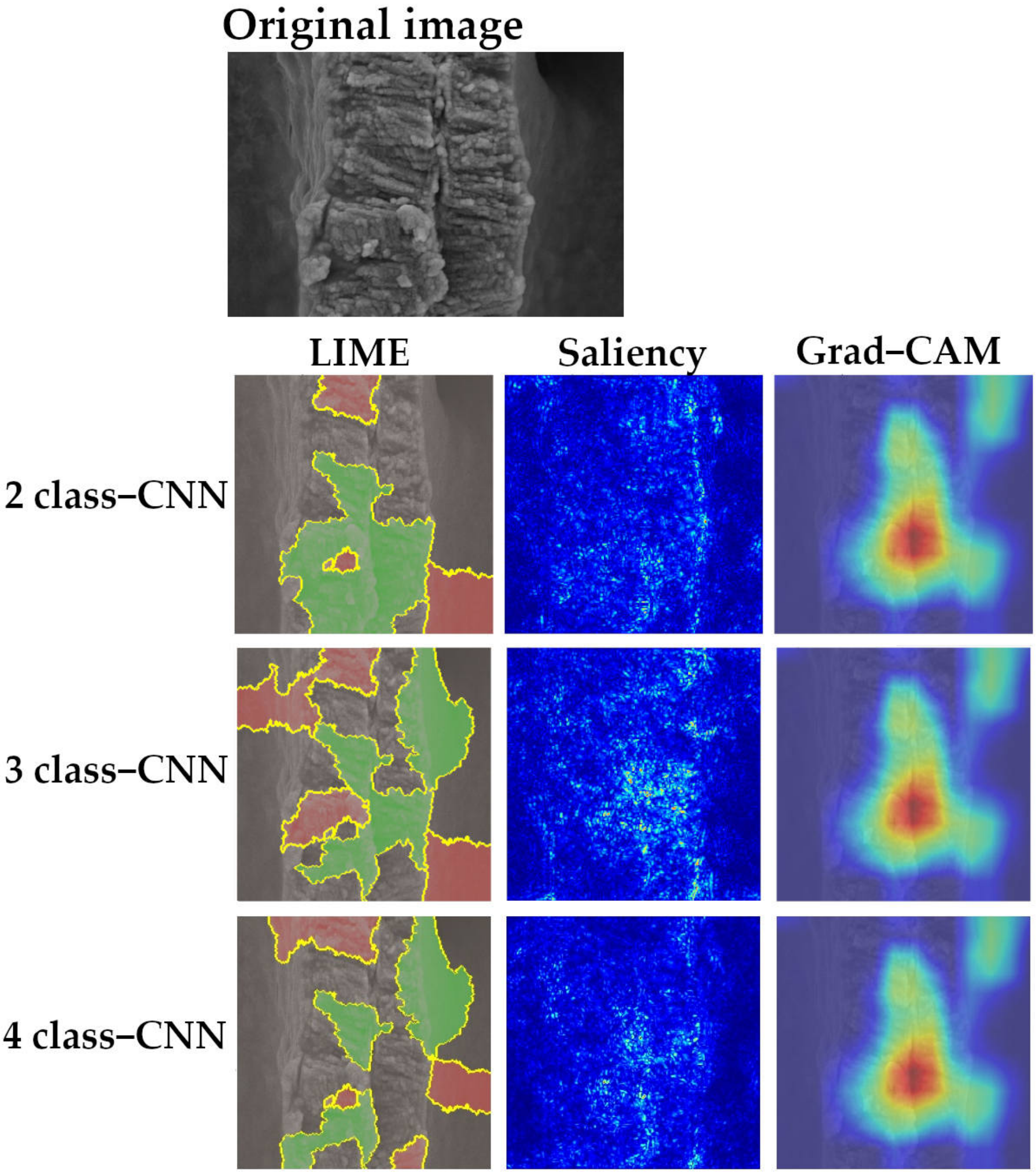

Figure 3.13: An example of the output from the three approaches (LIME, Saliency, and Grad-CAM) that shows the pixels that contribute the most to the CNN classification in the various models used (2, 3 and 4 class-CNNs). Positive and negative contributions to classification are coloured green and red in LIME, respectively. Brighter colour highlights the pixels that contribute the most to the class attribution in Saliency, whereas the most significant areas for the final classification have a warmer colour tone in the Grad-CAM visualisation. Every model correctly identified the SEM image as *Lithothamnion corallioides*, and it shows a magnification of the cell wall ultrastructure (crystallites category).

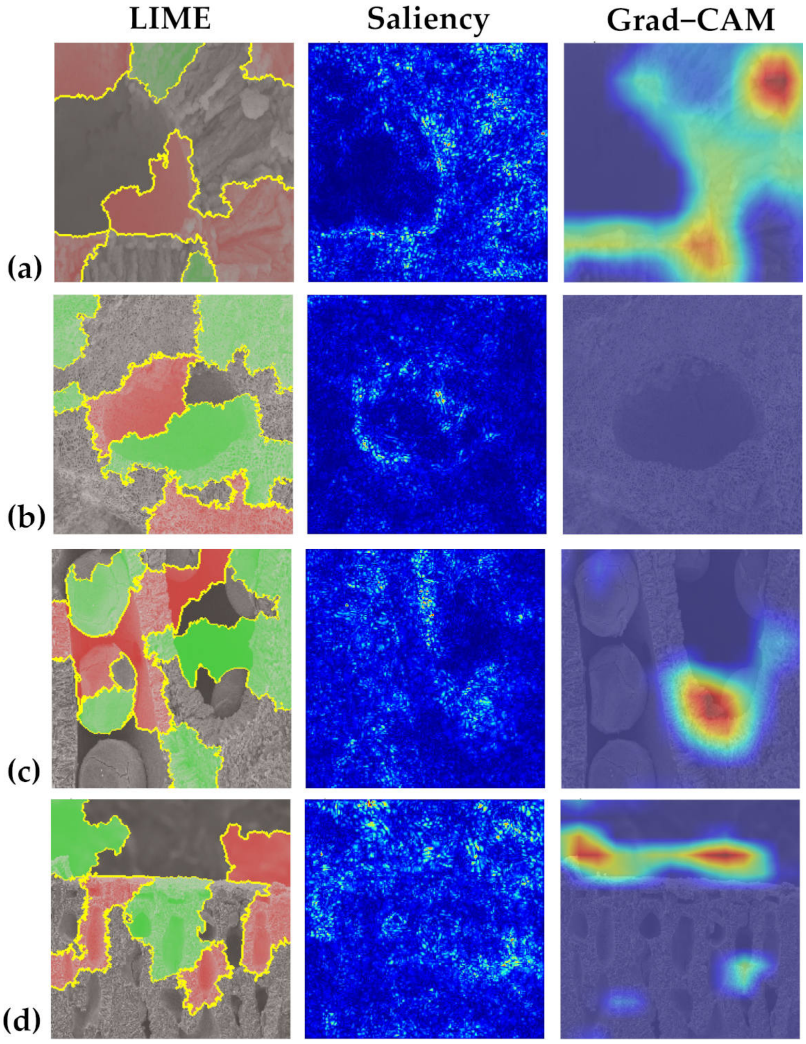

Figure 3.14: LIME, Saliency, and Grad-CAM techniques reveal the pixels that make the most significant contributions to CNN classification. (a) Magnification of the epithallial cell wall in *Lithophyllum racemus* demonstrates the significant contribution of calcification, formed by rod-shaped crystallites. (b) *Mesophyllum philippii* conceptacle shape focused by Saliency. (c) Starch grains within the perithallial cells of *L. racemus* did not impede correct identification. (d) The background beyond the epithallial cell of *Lithothamnion corallioides* was most likely responsible for this image's incorrect classification.

3.4 Laser Ablation ICP-MS: do temperature and growth rate affect B/Ca?

3.4.1 Temperature proxies

In *L. corallioides* samples (s8, s12-14 in Table 2.1), both Li/Ca and Sr/Ca records had positive correlations with Mg/Ca (Figs. 3.15 and A.5). The overall mean Mg/Ca was 225.3 ± 30.4 mmol/mol, with sample s12 (Aegadian Isl.) registering the lowest value (171.7 mmol/mol), while the highest value in sample s8 (Morlaix, 311.2 mmol/mol) (Fig. 3.16, Table 3.10). The Kruskal-Wallis test revealed no significant differences in Mg/Ca between samples (Fig. 3.16, Table A.1).

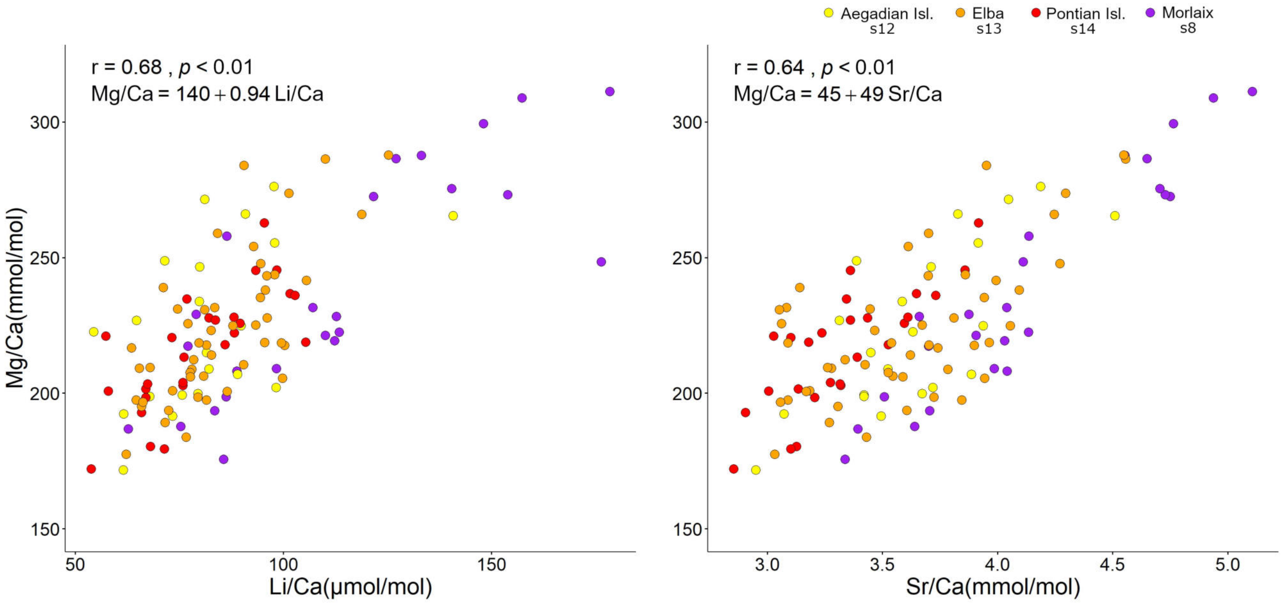

Figure 3.15: Correlation of Mg/Ca with Li/Ca and Sr/Ca. Spearman's coefficient r, the *p*-value, and the line equation are also given.

Sample s12 (Aegadian Isl.) had the highest Mg/Ca mean value among Mediterranean sites, followed by s13 and s14 (Elba and Pontian Isl.), the last having the lowest Mg/Ca mean value of all (Fig. 3.16). Sample s8 (Morlaix) had the highest mean Mg/Ca value, as well as a wide range of data above the median Mg/Ca value (Fig. 3.16). Here, long cells had high Mg/Ca values, whereas short cells were found in areas with a low Mg/Ca ratio. The ANOVA test, followed by Tukey's test for multiple comparisons, revealed a significant variation in Mg/Ca of long cells (Fig. 3.17, Table A.2). The Mg/Ca results in long cells of *L. corallioides* collected from Aegadian and Pontian Isl. (samples s12 and s14) was quite similar (Fig. 3.17, Table A.2). In sample s14, the lowest Mg/Ca ratio was found (Fig. 3.17). Sample s8 (Morlaix) had a higher Mg/Ca mean value, which was significantly different from sample s12 and s14 (Fig. 3.17, Table A.2). The differences in Mg/Ca between samples in short cells were not statistically significant (Table A.1). Magnesium incorporation was slightly higher in sample s8 but very similar in s12 and s14 (Fig. 3.17).

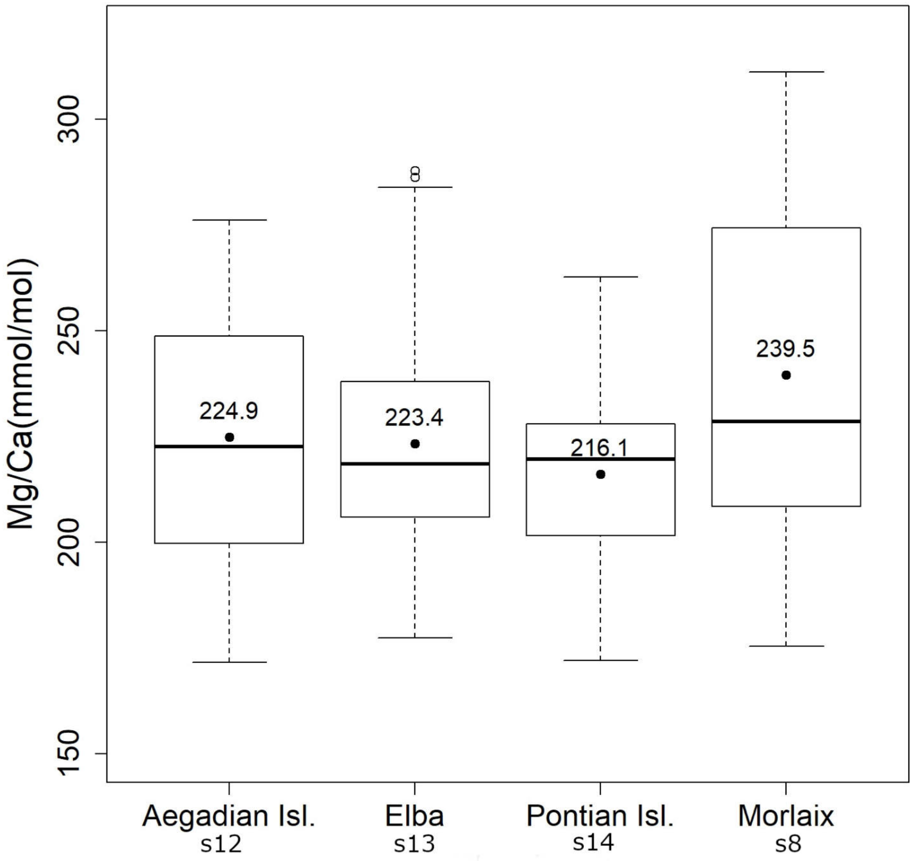

Figure 3.16: Mg/Ca in *Lithothamnion corallioides* collected at different sampling sites. The horizontal black lines indicate the median values; the black dots and the numbers inside the plot indicate the mean values.

Mg/Li values in both long and short cells were within the range discovered by Anagnostou et al. [66] for cultured *C. compactum* (Fig. 3.18). Mg/Li results did not reflect seasonal temperature oscillations when plotted against extracted seawater temperature in Morlaix (s8) (Fig. 3.19). Conversely, Mg, Li and Sr/Ca proxies accurately mirror the seasonal temperature trend (Fig.

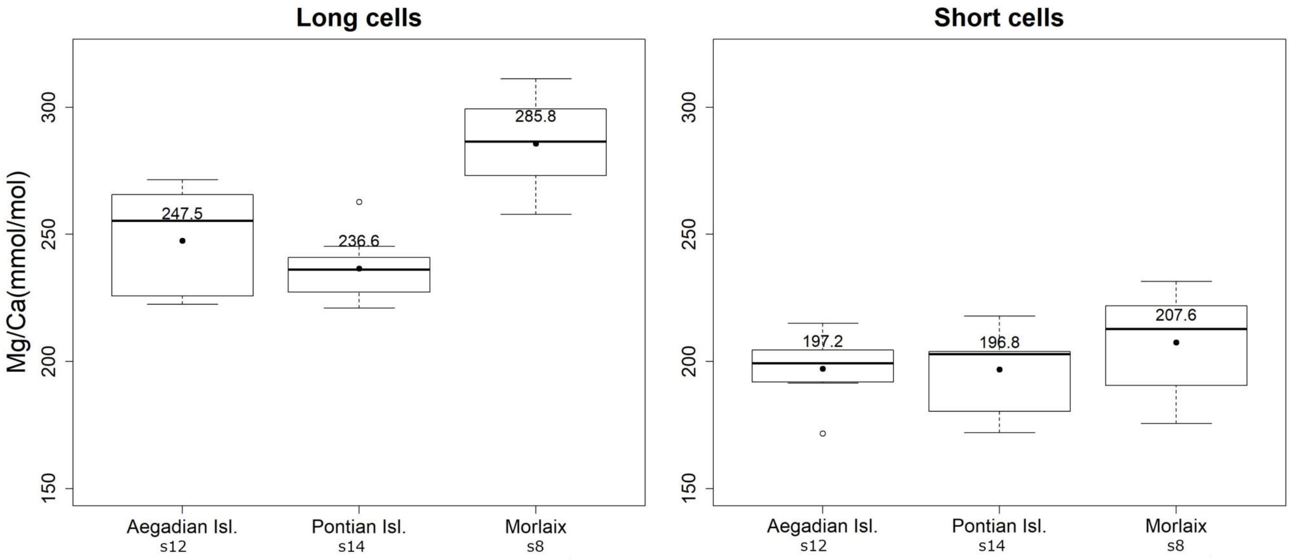

Figure 3.17: Mg/Ca in the long and short cells of *Lithothamnion corallioides* collected at different sites.

Table 3.10: Trace and major element/Ca measured by LA-ICP-MS in *Lithothamnion corallioides*.

Sample, site	**B/Ca (μmol/mol) mean±SD**	**Mg/Ca (mmol/mol) mean±SD**	**Li/Ca (μmol/mol) mean±SD**	**Sr/Ca (mmol/mol) mean±SD**	**Mg/Li (mol/mmol) mean±SD**
s8, Morlaix	726.9±102.8	239.5±41.2	113.1±32.9	4.1±0.5	2.2±0.4
s12, Aegadian Isl.	610.8±63.9	224.9±30.3	81.9±18.4	3.7±0.4	2.8±0.5
s13, Elba	757.7±75.5	223.4±26.4	85.2±14.3	3.6±0.4	2.7±0.3
s14, Pontian Isl.	462.8±49.2	216.1±21.9	79.6±14.6	3.3±0.3	2.8±0.4
Total	661.9±138.9	225.3±30.4	89.0±23.3	3.7±0.5	2.6±0.4

3.20).

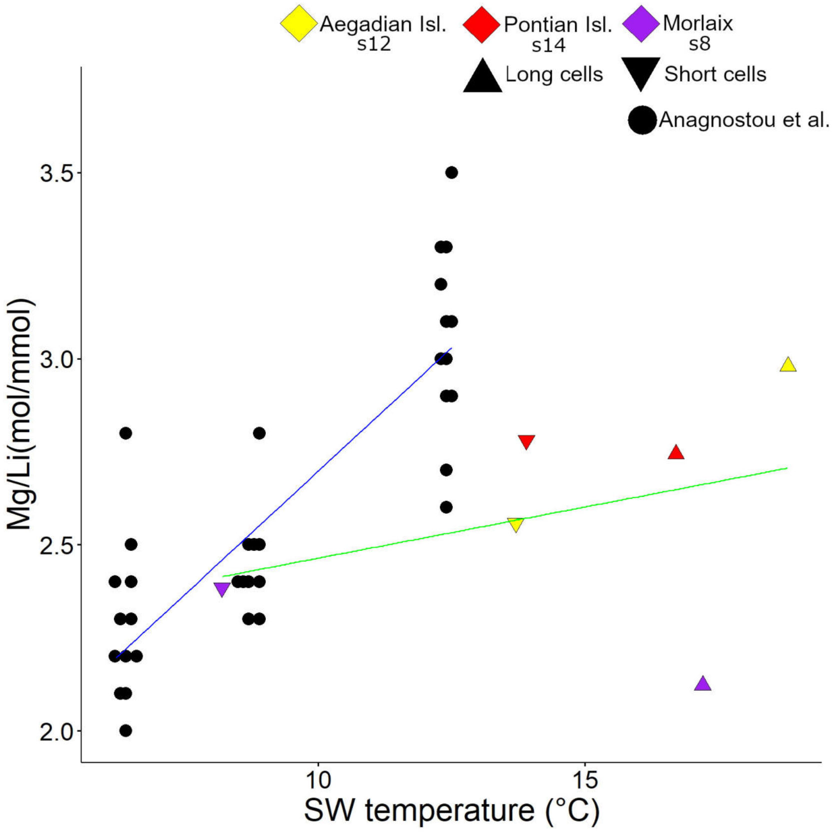

Figure 3.18: Correlation between Mg/Li and seawater temperature. Data are shown for cultured *Clathromorphum compactum* from Anagnostou et al. [66] and *Lithothamnion corallioides* from this study, which shows results separately in long and short cells per sampling site.

3.4.2 The B/Ca ratio

The B/Ca ratio in the Morlaix sample (s8) showed a moderate positive correlation with all of the temperature proxies tested (Mg/Ca, Li/Ca, Sr/Ca), with a more defined trend when plotted against Li/Ca (r = 0.68) and a slightly less defined trend when plotted against Mg/Ca (r = 0.58) and Sr/Ca (r = 0.57) (Fig. 3.21). On the contrary, Spearman's correlation analyses revealed no significant correlations between B/Ca and temperature signals in algae collected elsewhere (p>0.05). In sample s8, the age model reconstruction allowed the evaluation of the temperature influence on B/Ca at the seasonal resolution, highlighting the lack of the cyclic variations typical of temperature proxies (Fig. 3.20).

Overall, the B/Ca ratio in *Lithothamnion corallioides* was 661.9 ± 138.9 μmol/mol, with the

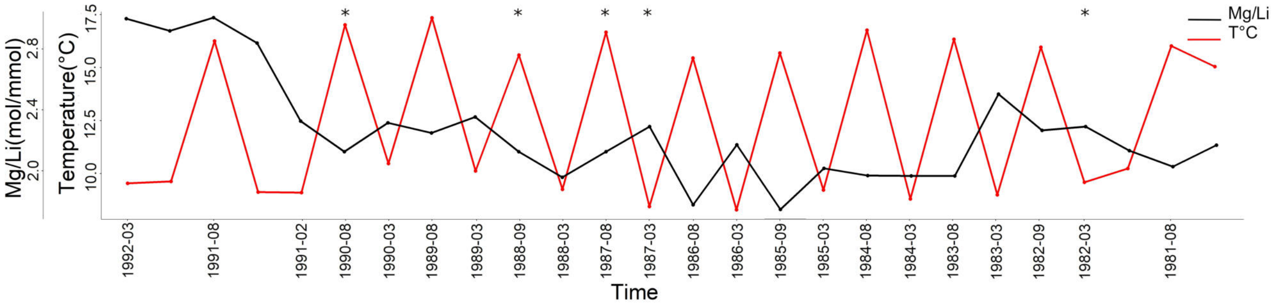

Figure 3.19: Mg/Li in *Lithothamnion corallioides* collected in Morlaix Bay (sample s8). Note the lack of cyclic variations. In the timeline, the coldest and the warmest months per year have been reported. Mg/Li ratios in the missing bands (asterisks) have been calculated as the means of the values measured in warm and cold periods.

lowest value in the long cells of the Pontian Isl. sample (s14, 356.0 μmol/mol) and the highest value in Elba (s13, 954.1 μmol/mol) (Fig. 3.22; Table 3.10). The Kruskal-Wallis coefficient revealed a highly significant difference in the B/Ca value among samples, particularly in s14 (Pontian Isl.), which had the lowest boron incorporation (Fig. 3.22, Table A.3). When compared to s13 and s8, the algae collected in Aegadian Isl. (s12) had significantly lower B/Ca ratios (Fig. 3.22, Table A.3). Sample s13 (Elba) had the highest B/Ca mean value, with medians comparable to s8 (Fig. 3.22, Table A.3). The ANOVA test, followed by Tukey's test for multiple comparisons by sample (i.e., site), for long (Table A.4) and short (Table A.5) cells separately, revealed lower values in Mediterranean sites (s12-14) and higher values in Atlantic sites (s8) (Fig. 3.23). Sample s14 (Pontian Isl.) had the lowest mean B/Ca in both seasons, which was significantly different from samples from Morlaix (s8) and Aegadian Isl. (s12) (Fig. 3.23, Tables A.4 and A.5). In both long and short cells, s8 had the highest mean B/Ca (Fig. 3.23, Tables A.4 and A.5).

L. corallioides from Aegadian Isl. (s12) had an intermediate B/Ca mean value in long cells, which differed significantly from samples s8 and s14 (Fig. 3.23, Table A.4). In short cells, sample s12 differed slightly from sample s8 (Fig. 3.23, Table A.5). Long cells in all samples had higher median B/Ca values than short cells (Fig. 3.23), but only in Morlaix (s8) the differences between B/Ca measured in long and short cells were statistically significant ($\chi^2 = 8.4899$, $p<0.01$).

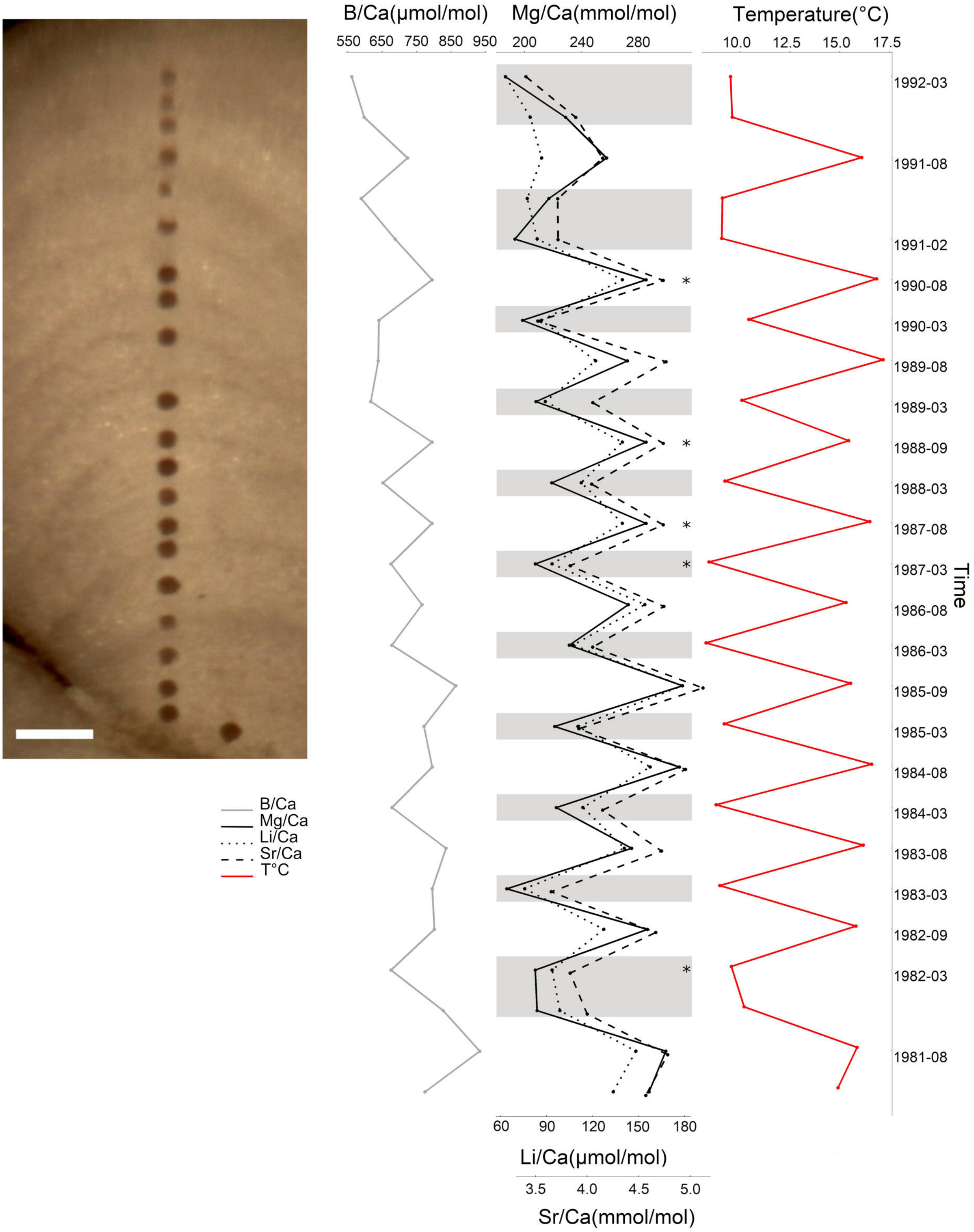

Figure 3.20: Elemental ratios in *Lithothamnion corallioides* sample s8, collected in Morlaix Bay (scale bar: 200 μm). Mg, Li, and Sr/Ca exhibit cyclic variations that correspond to the local seawater temperature. The coldest and warmest months have been reported in the timeline, which correspond to dark and light bands of growth respectively. The element/Ca ratios in the missing bands (asterisks) were calculated as the average of the values measured in warm and cold periods. ORAS5 reanalysis was used to extract monthly temperature means.

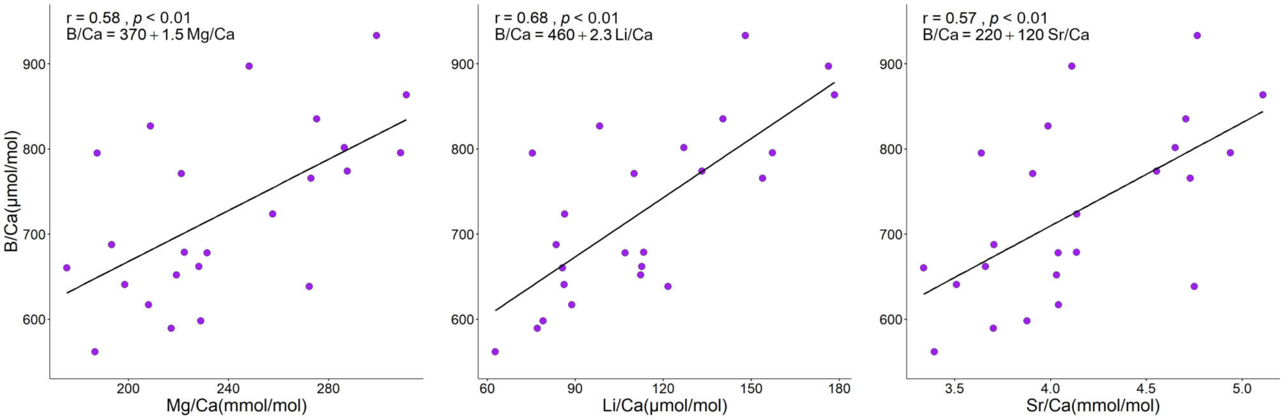

Figure 3.21: Correlation B/Ca with temperature proxies in *Lithothamnion corallioides* collected in Morlaix Bay (sample s8). Spearman's coefficient r, the *p*-value, and the line equations are given.

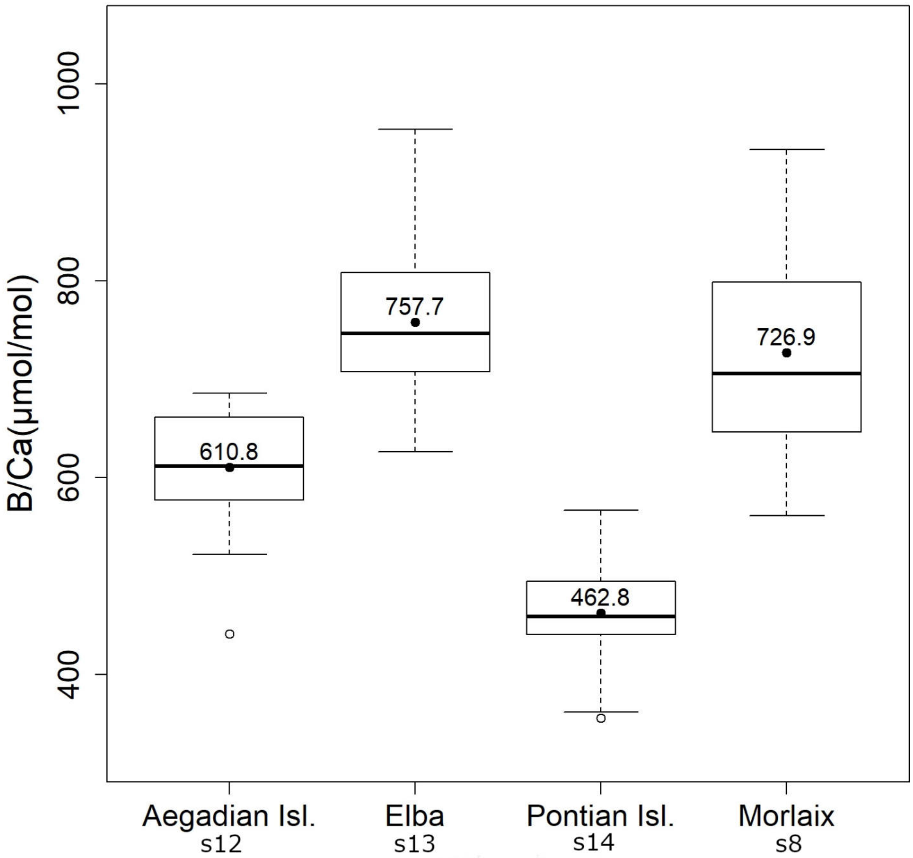

Figure 3.22: B/Ca in *Lithothamnion corallioides* collected at different sampling sites. The horizontal black lines indicate the median values; the black dots and the numbers inside the plot indicate the mean values.

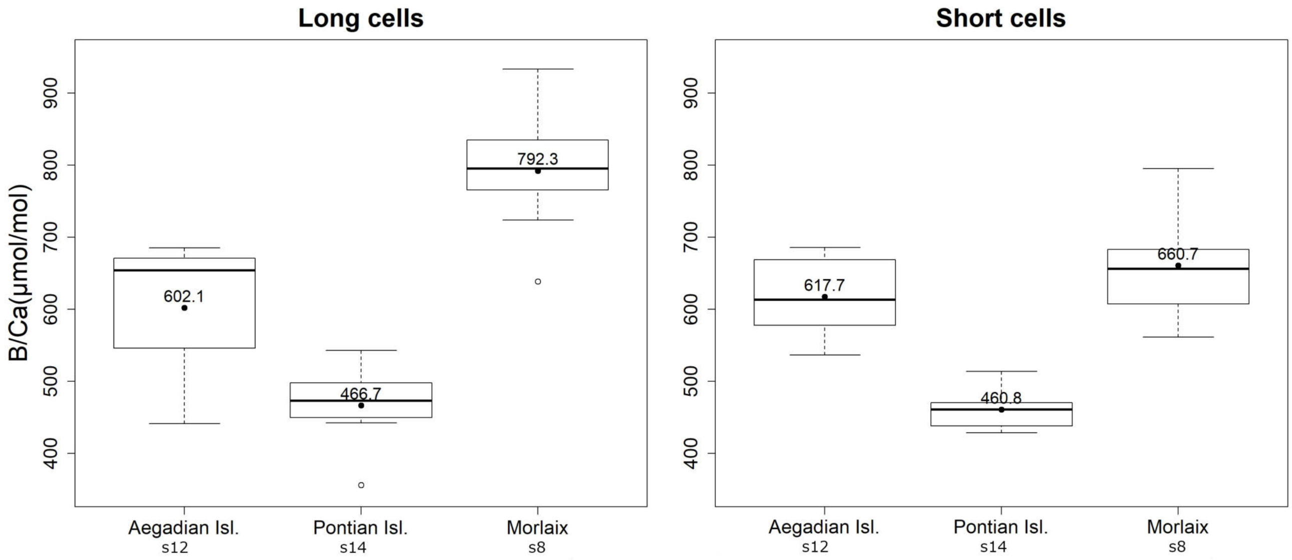

Figure 3.23: B/Ca in the long and short cells of *Lithothamnion corallioides* collected at different sites.

3.4.3 Growth rates

Growth rates had no linear relationship with Mg, Li, or Sr/Ca, but they were positively correlated with the mean B/Ca values of the samples (Fig. 3.24).

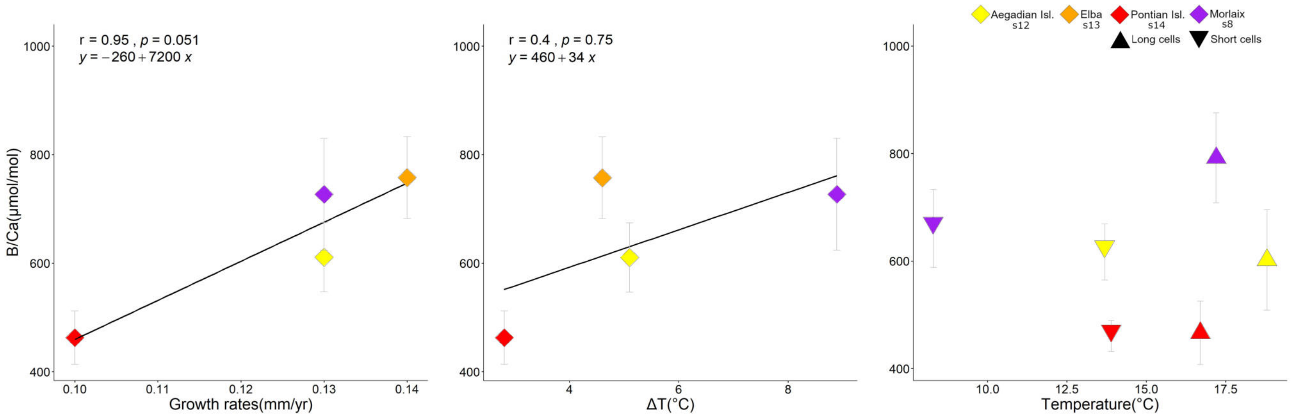

Figure 3.24: Correlation of growth rates and seawater temperature with B/Ca. Spearman's coefficient r, the *p*-value, and the line equations are given. Temperature variations (ΔT) are the differences in maximum and minimum temperatures recorded over 11 years of monthly reanalysis (ORAS5) (Section 2.2). The B/Ca means in long and short cells correspond to the maximum and minimum temperature, respectively.

The LA-ICP-MS transect in sample s12 was 1.31 mm long, and 10 years of growth were detected by coupling microscopical imaging and Mg/Ca peaks, resulting in a 0.13 mm/yr growth rate.

The laser transect in sample s13 was 1.15 mm long, crossing 8 years of growth and yielding a growth rate of 0.14 mm/yr. The Pontian Isl. sample (s14) had 1.08 mm of transect with 11 years of growth, resulting in a growth rate of 0.10 mm/yr. Finally, the transect in sample s8 (Morlaix) was 1.38 mm long, with an 11-year growth rate of 0.13 mm/yr.

3.5 X-Ray Diffraction

In the transverse section, morphological anomalies in the samples near CO_2 seeps in Ischia (s15-20 in Table 2.1) were identified as irregularly damaged areas where the most surficial part of the thallus was missing, exposing the underlying layers of perithallial cells (Fig. 3.25).

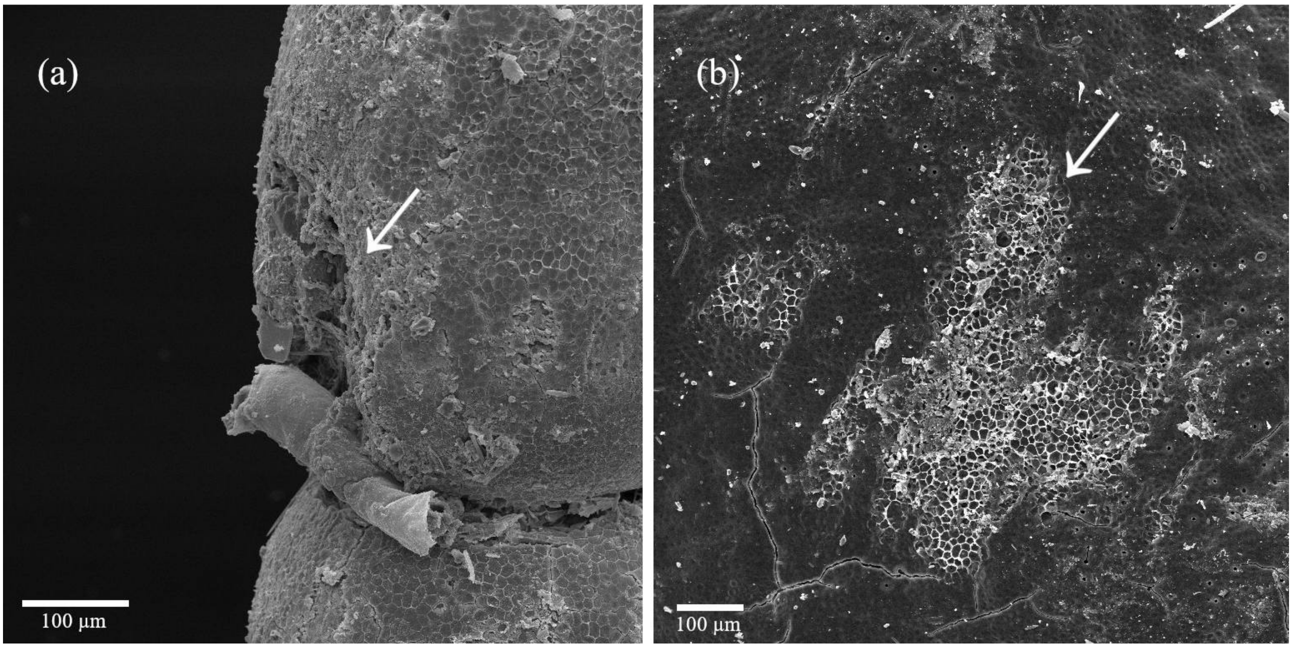

Figure 3.25: (a) Samples s17 (*Corallina officinalis*) and (b) s20 (*Peyssonnelia* sp.) collected near CO_2 seeps in Ischia (Italy). Surficial damaged areas are indicated by arrows. Here, the first layers of epithallial cells were removed, exposing the underlying cells.

This feature was detected in 70% and 87% of the regions observed over *C. officinalis* samples s16 and s17 (sites S2 and S3), respectively. Only 3% of the regions in *C. officinalis* sample s15 (site S1) showed damage. In *Peyssonnelia* sp. sample s20 (site S3), the 20% of the area observed by SEM was concerned, and the 5% in sample s19 (site S2) (Fig. 3.25). *C. officinalis* sample s17 from site S3 had a lower frond density (the number of branches departing from the central axis) (Fig. 2.3) compared to the samples collected in sites S1 and S2 (s15, s16). Table 3.11 summarises the mineral composition of the samples analysed by XRD, showing the percentages of the major mineral phases. Mg-calcites had 13-15 % of Mg content. Examples of XRD spectra are reported in Figure A.6 and an example of refinement is given in Figure A.7. XRD analysis revealed that the Corallinophycidae *L. racemus*, *L. pseudoracemus*, *C. officinalis* and *Amphiroa* sp. were 100% Mg-calcite, whereas *L. corallioides* and *L. minervae* had a non-negligible proportion of aragonite content, up to 35% in *L. minervae* (Table 3.11). On the contrary, *Peyssonnelia* sp. and *Polystrata* sp., belonging to Peyssonneliales, were predominantly made of aragonite, with calcite in percentages ranging from 1% to 9% (Table 3.11).

Table 3.11: Results of the Rietveld refinements performed on XRD data, indicating phase compositions. An example of the refinement is reported in Figure A.7 for sample s18.

Sample	**Site**	**Species**	**aragonite (%)**	**Mg-calcite (%)**
s2	Pontian Isl.	*L. racemus*	0.00	100.00
s3	Villasimius	*L. pseudoracemus*	0.00	100.00
s4	Pontian Isl.	*L. pseudoracemus*	0.00	100.00
s8	Morlaix	*L. corallioides*	0.00	100.00
s12	Aegadian Isl.	*L. corallioides*	2.00	98.00
s13	Elba	*L. corallioides*	0.00	100.00
s14	Pontian Isl.	*L. corallioides*	8.00	92.00
s15	Ischia S1	*C. officinalis*	0.00	100.00
s16	Ischia S2	*C. officinalis*	0.00	100.00
s17	Ischia S3	*C. officinalis*	0.00	100.00
s18	Ischia S2	*Peyssonnelia* sp.	92.00	8.00
s19	Ischia S2	*Peyssonnelia* sp.	98.36	1.64
s20	Ischia S3	*Peyssonnelia* sp.	98.67	1.33
s21	Methana F1	*Amphiroa* sp.	0.00	100.00

Table 3.11 (continue)

Sample	**Site**	**Species**	**aragonite (%)**	**Mg-calcite (%)**
s22	Methana F2	*Amphiroa* sp.	0.00	100.00
s23	Methana N	*Amphiroa* sp.	0.00	100.00
s24	Polignano	*M. philippii*	3.00	97.00
s25	Aegadian Isl.	*L. crispatum*	8.00	92.00
s26	Villasimius	*L. minervae*	3.00	97.00
s27	Elba	*L. minervae*	13.00	87.00
s28	Pontian Isl.	*L. minervae*	35.00	65.00
s29	Polignano	*L. stictiforme*	7.00	93.00
s30	Pontian Isl.	*Peyssonnelia* sp.	91.00	9.00
s31	Pontian Isl.	*Peyssonnelia* sp.	95.00	5.00
s32	Villasimius	*Polystrata* sp.	99.00	1.00

3.6 Multi-Collector ICP-MS

Boron isotopes in algal samples ranged from 20.07 ± 0.26‰ to 27.51 ± 0.28‰ (Table 3.12). Overall, $\delta^{11}B_{algae}$ decreased as the proportion of aragonite over calcite in the alga increased, reaching the minimum value in the aragonitic Peyssonneliales, and the maximum values in calcitic Corallinales (Fig. 3.26). The range of $\delta^{11}B_{algae}$ measured in *C. officinalis* in Ischia varied from 23.10 ± 0.16‰ at pH 6.80 ± 0.43, to 26.59 ± 0.15‰ at pH 7.77 ± 0.32 (Tables 3.2 and 3.12). The $\delta^{11}B_{algae}$ varied from 22.23 ± 0.14‰ at pH 6.80 ± 0.43, to 26.00 ± 0.13‰ at pH 7.77 ± 0.32 in *Peyssonnelia* sp. In Methana, *Amphiroa* sp. $\delta^{11}B_{algae}$ ranged from 25.41 ± 0.14‰ at pH 7.77 ± 0.30, to 26.33 ± 0.15‰ at pH 7.57 ± 0.31 (Tables 3.2 and 3.12). In the same site (S3, S2), *Peyssonnelia* sp. always had lower $\delta^{11}B_{algae}$ values than *C. officinalis*. The two samples of *Peyssonnelia* sp. collected in site S2 (s18, s19) had significantly different $\delta^{11}B_{algae}$ values: 23.93 ± 0.10‰ and 26.00 ± 0.13‰ (Table 3.12). The lowest $\delta^{11}B_{algae}$ was found in the Peyssonneliaceae *Polystrata* sp. (sample s32) and *Peyssonnelia* sp. from Ischia and Pontian Isl. (samples s20 and s31). The highest $\delta^{11}B_{algae}$ values were measured in the Corallinophycidae *L. corallioides* (s8) and *M. philippii* (s24) (Table 3.12).

Table 3.12: Multi-collector ICP-MS results for δ^{11}B in calcareous red algae ($\delta^{11}B_{algae}$).

Sample	**Site**	**Species**	**δ^{11}B$_{algae}$ (‰) mean±SD**
s2	Pontian Isl.	*L. racemus*	26.98±0.26
s3	Villasimius	*L. pseudoracemus*	25.38±0.27
s4	Pontian Isl.	*L. pseudoracemus*	24.96±0.27
s8	Morlaix	*L. corallioides*	27.51±0.28
s12	Aegadian Isl.	*L. corallioides*	24.75±0.24
s13	Elba	*L. corallioides*	26.87±0.26
s14	Pontian Isl.	*L. corallioides*	24.89±0.21

Table 3.12 (continue)

Sample	**Site**	**Species**	δ^{11}**B**$_{algae}$ (‰) **mean±SD**
s15	Ischia S1	*C. officinalis*	25.59±0.28
s16	Ischia S2	*C. officinalis*	26.59±0.27
s17	Ischia S3	*C. officinalis*	23.10±0.28
s18	Ischia S2	*Peyssonnelia* sp.	23.93±0.13
s19	Ischia S2	*Peyssonnelia* sp.	26.00±0.17
s20	Ischia S3	*Peyssonnelia* sp.	22.23±0.15
s21	Methana F1	*Amphiroa* sp.	25.41±0.25
s22	Methana F2	*Amphiroa* sp.	26.30±0.28
s23	Methana N	*Amphiroa* sp.	26.33±0.27
s24	Polignano	*M. philippii*	27.15±0.27
s25	Aegadian Isl.	*L. crispatum*	24.81±0.27
s26	Villasimius	*L. minervae*	26.58±0.27
s27	Elba	*L. minervae*	26.95±0.27
s28	Pontian Isl.	*L. minervae*	26.24±0.28
s29	Polignano	*L. stictiforme*	26.22±0.29
s30	Pontian Isl.	*Peyssonnelia* sp.	25.09±0.16
s31	Pontian Isl.	*Peyssonnelia* sp.	21.96±0.17
s32	Villasimius	*Polystrata* sp.	20.07±0.26

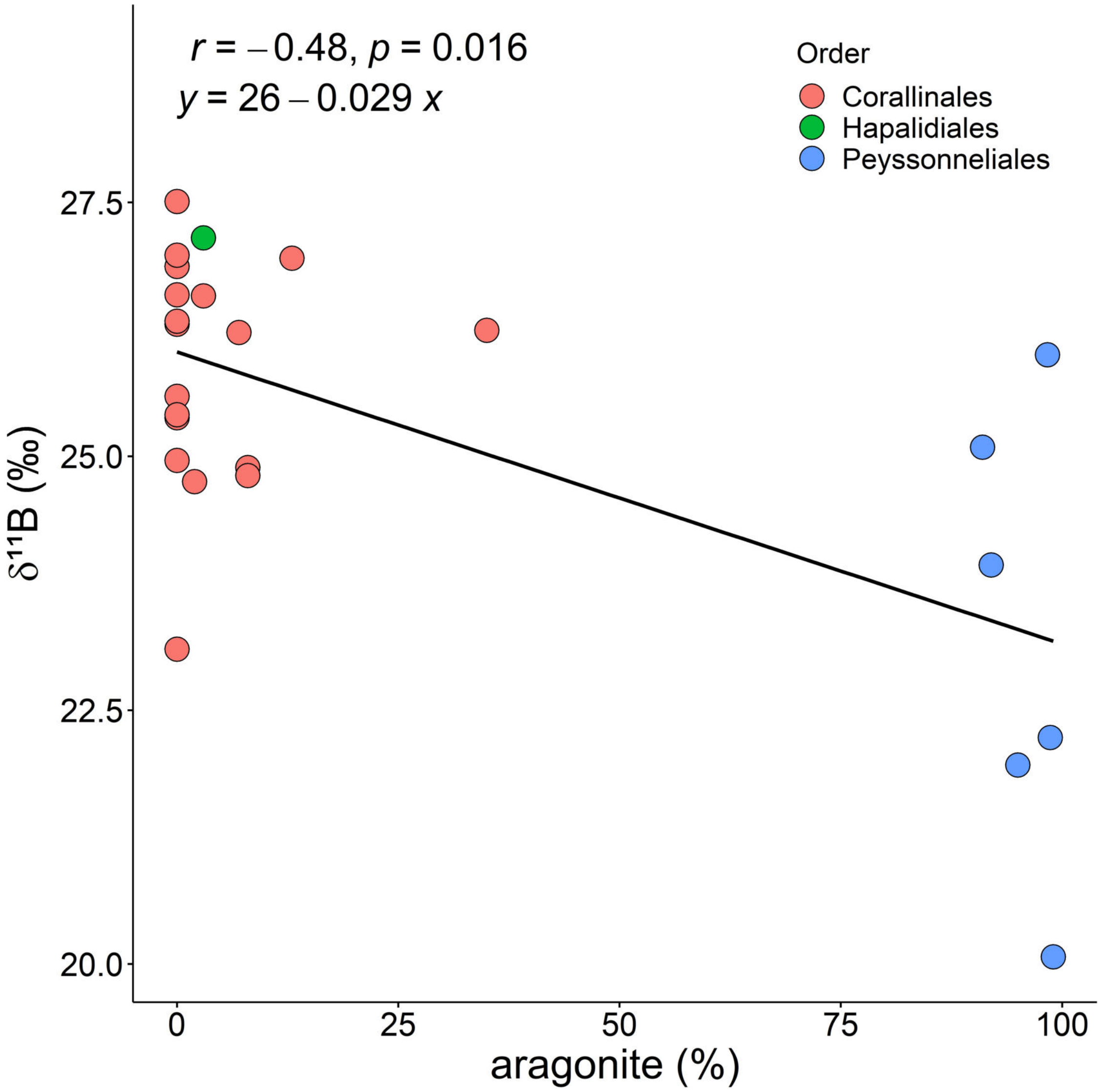

Figure 3.26: Spearman's correlation between $\delta^{11}B_{algae}$ (Table 3.12) and the proportion of aragonite over calcite in the algal samples (Table 3.11). Correlation significance at $p<0.05$. Colours indicate which order the sample belongs to.

3.7 Boron isotope calibrations

MC-ICP-MS results of $\delta^{11}B_{algae}$ from samples near CO_2 seeps (s15-s23), together with data from previous literature [42, 43, 102], were used to calculate York fit calibrations of the form in Eq. 1.4, using $\delta^{11}B_{algae}$ uncertainties as standard errors of replicate measurements and calculating $\delta^{11}B_{borate}$ by 10000 Monte Carlo simulations randomly varying pH, temperature and salinity within their uncertainty bounds (Section 2.7) (Table 3.13). Calibration data for calcareous red algae show that $\delta^{11}B_{algae}$ is always greater than ambient $\delta^{11}B_{borate}$ and always plots above the 1:1 line (Fig. 3.27). In comparison to the other calibrations, the regression slope of the samples examined in this study is closest to one (0.88 ± 0.22). This could imply a pH sensitivity more akin to solution borate. Except for *A. anceps*, uncertainty bounds in this study are comparable to those of cultured algae from the literature (Fig. 3.27). *A. anceps* had the lowest $\delta^{11}B_{algae}$ and the smallest regression slope (0.24 ± 0.11). For these reasons, and due to the lack of comparability between its calibration and the others, data from *A. anceps* were not included in the multi-specific calibration calculation (Fig. 3.28). The multi-specific regression plots above the 1:1 line of $\delta^{11}B_{algae}$ versus $\delta^{11}B_{borate}$, and it is described by the following equation from Eq. 1.4 (p-value < 0.0001):

$$\delta^{11}B_{borate} = \delta^{11}B_{algae} + (3.02 \pm 4.04)/1.89 \pm 0.26 \tag{3.1}$$

The range of $\delta^{11}B_{borate}$ values considered in the calibration ranged from 12.68 ± 0.85% to 19.04 ± 3.52%, significantly expanding the range over which $\delta^{11}B_{algae}$ had previously been calibrated.

Table 3.13: Data used to calculate York fit calibrations in calcareous red algae. See Section 2.7 for details on calculations.

Sample	**Reference**	**Species**	δ^{11}**B**$_{algae}$ (‰) **mean±SE**	δ^{11}**B**$_{borate}$ (‰) **mean±SD**
s15	this study	*C. officinalis*	25.59±0.13	18.05±1.07
s16	this study	*C. officinalis*	26.59±0.12	15.88±2.48
s17	this study	*C. officinalis*	23.10±0.12	12.68±0.85
s18	this study	*Peyssonnelia* sp.	23.93±0.06	15.92±2.52
s19	this study	*Peyssonnelia* sp.	26.00±0.08	15.97±2.52
s20	this study	*Peyssonnelia* sp.	22.23±0.05	12.69±0.86
s21	this study	*Amphiroa* sp.	25.41±0.11	16.01±2.38
s22	this study	*Amphiroa* sp.	26.30±0.13	16.01±2.38
s23	this study	*Amphiroa* sp.	26.33±0.12	14.81±1.90
	Cornwall et al. [42]	*A. anceps*	19.78±0.30	18.09±0.50
	Cornwall et al. [42]	*A. anceps*	19.73±0.31	15.66±0.49
	Cornwall et al. [42]	*A. anceps*	18.99±0.17	14.61±0.50
	Cornwall et al. [43]	*H. reinboldii*	27.80±0.19	18.43±0.82
	Cornwall et al. [43]	*H. reinboldii*	27.97±0.17	19.04±3.52
	Cornwall et al. [43]	*H. reinboldii*	26.01±0.26	15.03±0.61
	Cornwall et al. [43]	*H. reinboldii*	26.49±0.33	15.84±2.97
	Cornwall et al. [42]	*Neogoniolithon* sp.	27.55±0.33	15.66±0.49
	Cornwall et al. [42]	*Neogoniolithon* sp.	29.11±0.59	18.09±0.50
	Cornwall et al. [42]	*Neogoniolithon* sp.	27.00±0.46	14.61±0.50
	Donald et al. [102]	*Neogoniolithon* sp.	34.10±2.01	19.56±0.61

Table 3.13 (continue)

Sample	**Reference**	**Species**	$\delta^{11}\mathbf{B}_{algae}$ (‰) **mean±SE**	$\delta^{11}\mathbf{B}_{borate}$ (‰) **mean±SD**
	Donald et al. [102]	*Neogoniolithon* sp.	33.58±1.08	17.97±0.81
	Donald et al. [102]	*Neogoniolithon* sp.	33.45±1.06	16.58±0.56
	Donald et al. [102]	*Neogoniolithon* sp.	26.75±0.78	13.98±0.49
	Cornwall et al. [42]	*S. durum*	26.66±0.23	18.09±0.50
	Cornwall et al. [42]	*S. durum*	25.87±0.10	15.66±0.49
	Cornwall et al. [42]	*S. durum*	25.05±0.34	14.61±0.50

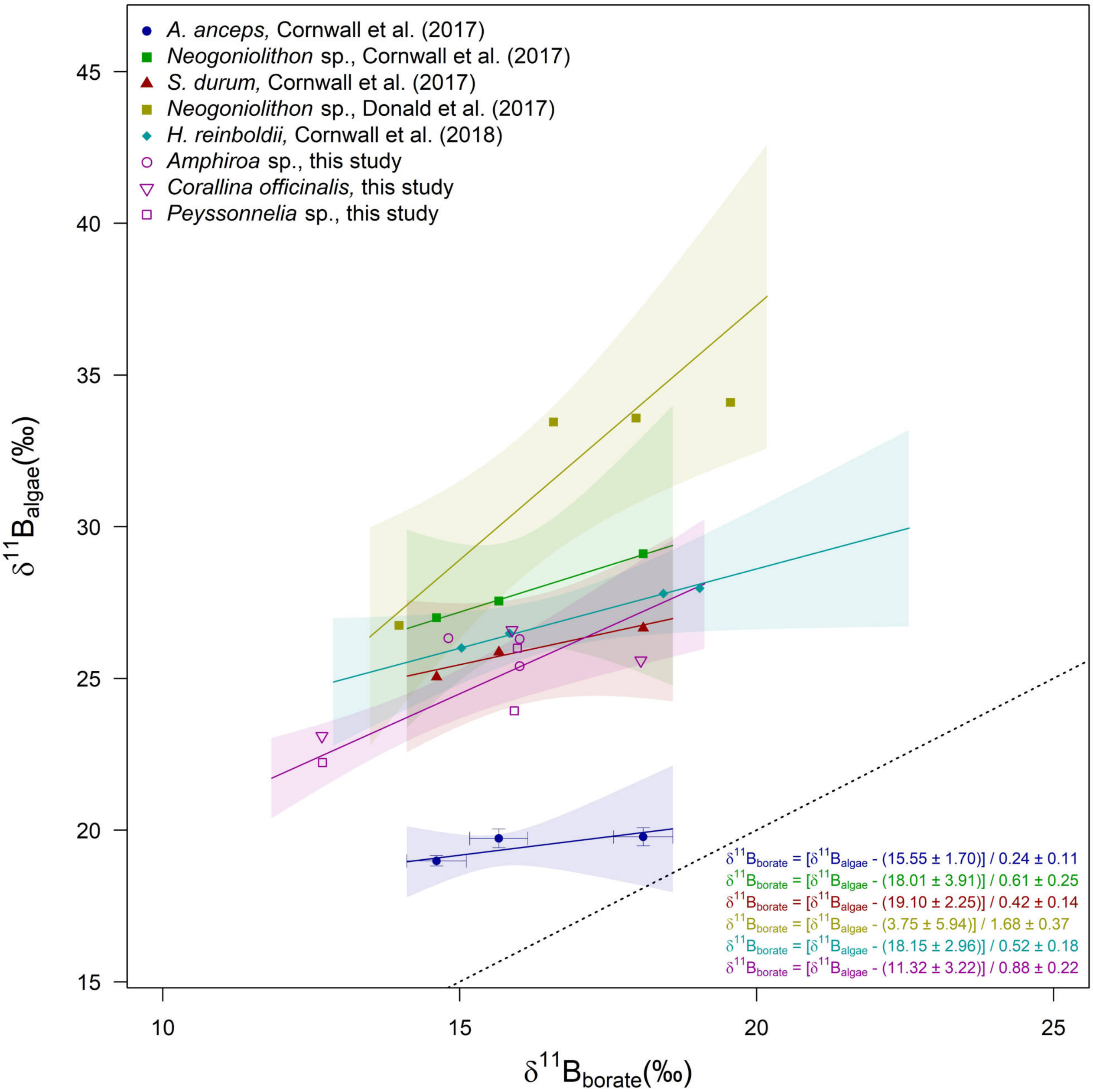

Figure 3.27: Calibration data showing MC-ICP-MS measurements of $\delta^{11}B_{algae}$ versus solution $\delta^{11}B_{borate}$ for published calcareous red algal cultures [42, 43, 102] and wild-grown algae (this study). Shaded polygons show 0.90 confidence intervals, considering standard errors of replicate measurements in the $\delta^{11}B_{algae}$ and one standard deviation of 10000 Monte Carlo simulations in the $\delta^{11}B_{borate}$. Uncertainties for points other than *A. anceps* are shown in Figure 3.28. Note that all the calibrations plot above the 1:1 line (dotted line). Data are shown in Table 3.13.

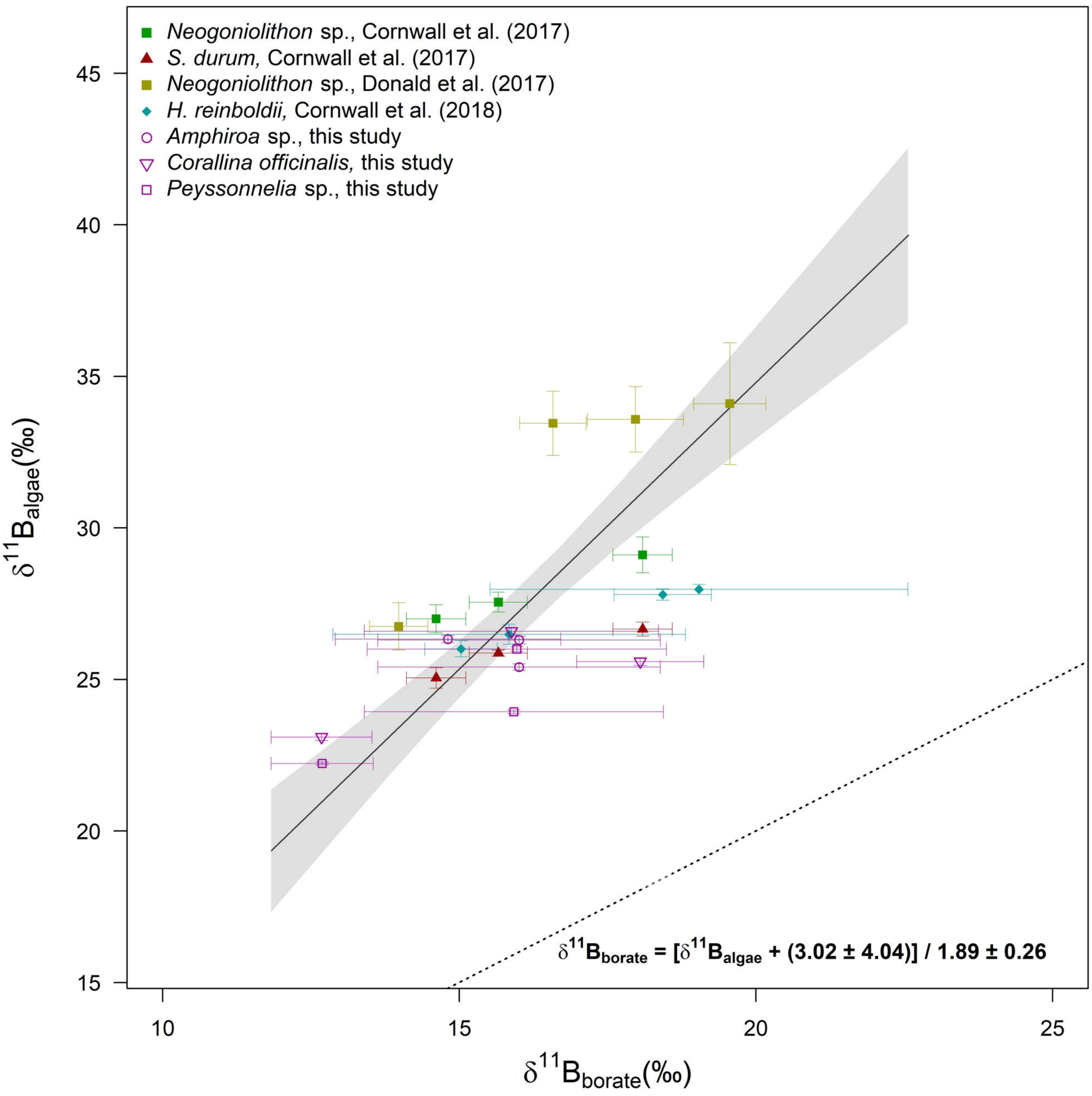

Figure 3.28: Multi-specific calibration proposed in this study grouping all published MC-ICP-MS measurements of calcareous red algae. The shaded polygon shows 0.90 confidence intervals, considering standard errors of replicate measurements in the $\delta^{11}B_{algae}$ and one standard deviation of 10000 Monte Carlo simulations in the $\delta^{11}B_{borate}$. Note that all the points plot above the 1:1 line (dotted line). Data are shown in Table 3.13.

3.8 Magic Angle Spinning NMR: is trigonal boron being incorporated?

The ^{11}B MAS NMR spectra of Mg-calcite and aragonite calcareous red algae analysed in this study are shown in Figures 3.30, 3.31, 3.32, 3.33, 3.34 and 3.35. Estimates of the relative proportions of the different B species obtained by integrating the spectral peaks are given in Tables 3.15 and 3.14. In some cases, the BO_3 signal exhibits the characteristic line shape of a quadrupolar nucleus ($I(^{11}B) = 3/2$), characterized by a quadrupolar coupling constant (C_Q) besides a chemical shift (δ_{iso}). The NMR parameters are given in Table 3.14 as a short summary for Mg-calcites and aragonite. The complete record is given in Table A.8. The results highlight high variability in B speciation, especially in aragonite samples. Almost the 40% of B in Mg-calcite samples occurs as BO_3 (Table 3.14), and the 60% occurs as BO_4. In aragonitic algae, about 30% occurs as BO_3 and 64% as BO_4, with high variability among samples and a non-negligible percentage of hardly interpretable signal (i.e., “n.c.”) (Table 3.14). These statistics consider results on sample s31 after oxidation following the procedure described in Section 2.6.2, which resulted in a much lower proportion of trigonal boron, with 18.1% of BO_3 ($\delta_{iso} = 12.9$ ppm) and 81.9% BO_4 ($\delta_{iso} = 27\%$ at 1.1 ppm and 54.9% at 2.9 ppm), compared to the 41.7% BO_3 and 48.5% BO_4 before the treatment (Tables 3.15 and A.8). Organic compounds could possibly explain the ambiguous “n.c.” signals in aragonite samples (and Mg-calcite sample s25) and eventually bias the relative proportion of B species incorporated. Encrusting forms such as *Peyssonnelia* sp. and *Polystrata* sp. are reasonably more prone to external contamination. The first two principal components (PCs) of the PCA model resolved 92% of the total data variance (Fig. 3.29) and considered NMR results of sample s31 after oxidation. The primary trend on the PC-1 axis was increasing Mg-calcite with increasing $\delta^{11}B$ values (Fig. 3.26), expressed as positive PC-1 loadings (Fig. 3.29). As the proportion of Mg-calcite decreases, the % of aragonite increases, as well as the proportion of ambiguous NMR signals (i.e., “n.c.”) (Fig. 3.29). This is evidenced by negative PC-1 loadings. On the PC-2 axis, positive loadings of the proportion of tetragonal boron (BO_4) were observed, and negative loadings of trigonal boron (BO_3). The PCA revealed two main distinctions based on natural groupings in the PC-2 versus PC-1 plot (Fig.

3.29). Calcareous red algae belonging to the calcitic Corallinales and Hapalidiales had positive PC-1 and were distinguished by higher $\delta^{11}B$ values (Table 3.12). Most of the Corallinales plotted with positive PC-1 and positive PC-2 being more enriched in BO$_4$ than BO$_3$. The only two samples belonging to *L. crispatum* (Corallinales) and *M. philippi* (Hapalidiales) species were distinguished from the other calcitic algae by having negative PC-2 scores (Fig. 3.29) due to the higher percentage of BO$_3$ (Table 3.15). The aragonitic Peyssonneliales were distinguished by negative PC-1, having lower $\delta^{11}B$ values (Figs. 3.26). Two samples out of three also had positive PC-2 loadings, with high percentages of BO$_4$ (Table 3.15). Sample s30, *Peyssonnelia* sp. (non-oxidized), was clearly different from the other Peyssonneliales by having a higher proportion of BO$_3$ and ambiguous ("n.c.") signals (Table 3.15).

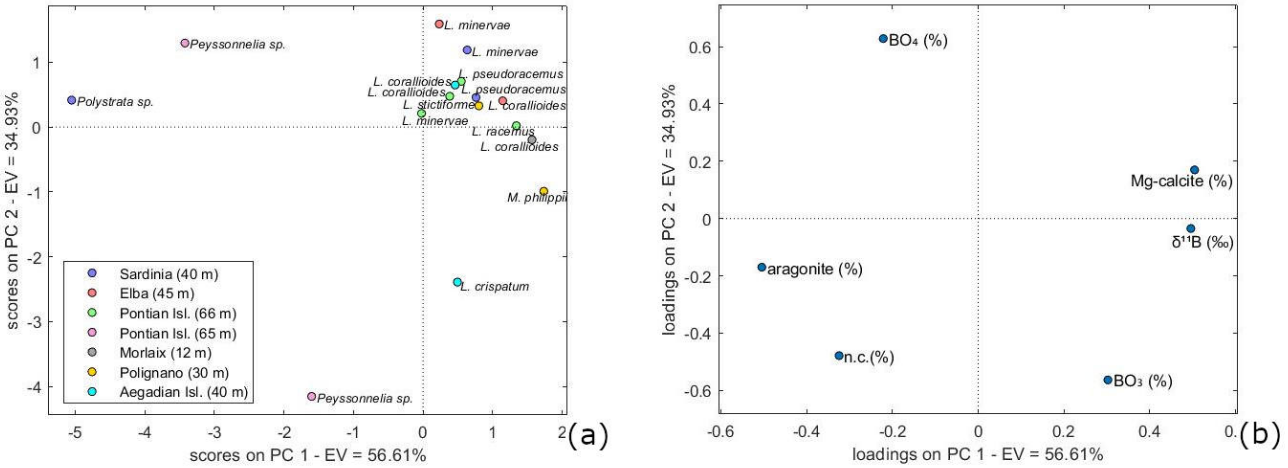

Figure 3.29: Principal component analysis (PCA); (a) score plot and (b) loading plot of PCA on XRD (Table 3.11), MC-ICP-MS (Table 3.12) and ^{11}B MAS NMR (Table 3.15) data of calcareous red algae. The plots model 92% of the total data variance. Variance proportions are shown along each component axis. *Peyssonnelia* sp. and *Polystrata* sp. belong to the order Peyssonneliales; *Mesophyllum philippii* belongs to the order Hapalidiales; all the other species are Corallinales.

Table 3.14: ^{11}B MAS NMR parameters from spectra in Figures 3.30, 3.31, 3.32, 3.33, 3.34 and 3.35. Trigonal boron (BO_3) in samples s4, s14 and s32 was simulated by a quadrupolar line shape characterized by a chemical shift (δ_{iso}) and the quadrupolar coupling constant (C_Q). In all other cases, gaussian line shapes were used for simulations, characterized by a chemical shift and width. Relative proportions between BO_3 ad BO_4 are also indicated (mean±SD %). Ambiguous signals are indicated as "n.c." (Table A.8 for the complete record).

$CaCO_3$ polymorph	**BO_3**			**BO_4**		**n.c.**	
	δ_{iso}	C_Q	%	δ_{iso}	%	δ_{iso}	%
Mg-calcite	10.6-20.3	1.50-1.57	39.2±9.2	0.2-3.1	60.3±10.3	6.1	0.5±1.7
Aragonite	12.9-13.3	1.01	30.5±29.2	2.9	64.3±31.2	7.2-7.7	5.2±4.5

Table 3.15: Relative proportion of trigonal (BO_3) and tetragonal boron (BO_4) in calcareous red algae determined from peak surface integration of their ^{11}B MAS NMR spectra (1% error bar). Ambiguous signals (6.1-7.7 ppm) are indicated as "n.c." (Table 3.14 for NMR parameters, Table A.8 for the complete dataset).

Sample	**Site**	**Species**	**BO_3(%)**	**BO_4(%)**	**n.c. (%)**
s2	Pontian Isl.	*L. racemus*	42.9	57.1	
s3	Villasimius	*L. pseudoracemus*	38.0	62.0	
s4	Pontian Isl.	*L. pseudoracemus*	35.1	64.9	
s8	Morlaix	*L. corallioides*	45.4	54.6	
s12	Aegadian Isl.	*L. corallioides*	35.6	64.4	
s13	Elba	*L. corallioides*	38.3	61.7	
s14	Pontian Isl.	*L. corallioides*	37.0	63.0	
s24	Polignano	*M. philippii*	54.7	45.3	
s25	Polignano	*L. crispatum*	56.4	37.5	6.1
s26	Villasimius	*L. minervae*	28.6	71.4	
s27	Elba	*L. minervae*	22.6	77.4	

Table 3.15 (continue)

Sample	Site	Species	BO_3(%)	BO_4(%)	n.c. (%)
s28	Pontian Isl.	*L. minervae*	36.9	63.1	
s29	Polignano	*L. stictiforme*	38.6	61.4	
s30	Pontian Isl.	*Peyssonnelia* sp.	63.9	28.2	7.9
s31	Pontian Isl.	*Peyssonnelia* sp.	41.7	48.5	9.8
s31*	Pontian Isl.	*Peyssonnelia* sp.	18.1	81.9	
s32	Villasimius	*Polystrata* sp.	9.6	82.7	7.7

*sample s31 after oxidation following the cleaning protocol in Section 2.6.2.

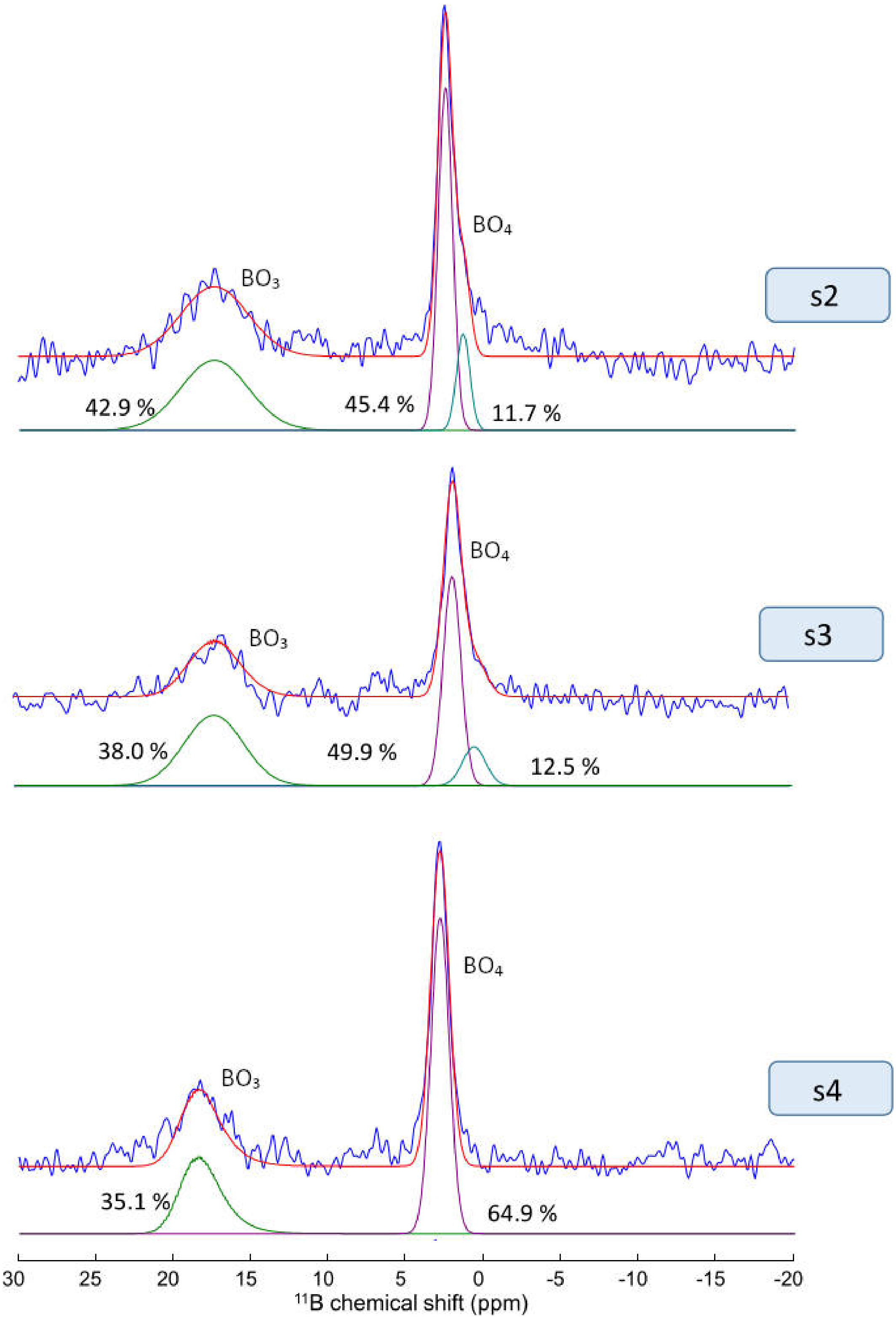

Figure 3.30: ^{11}B MAS NMR spectra and deconvolution of Mg-calcite samples s2-4. The blue line indicates the experimental spectra, the red line the simulated spectra and the overlapping bottom lines indicate the deconvolution. Note the presence of two components in the BO_4 peaks. The determined NMR parameters are reported in Table 3.14 and A.8.

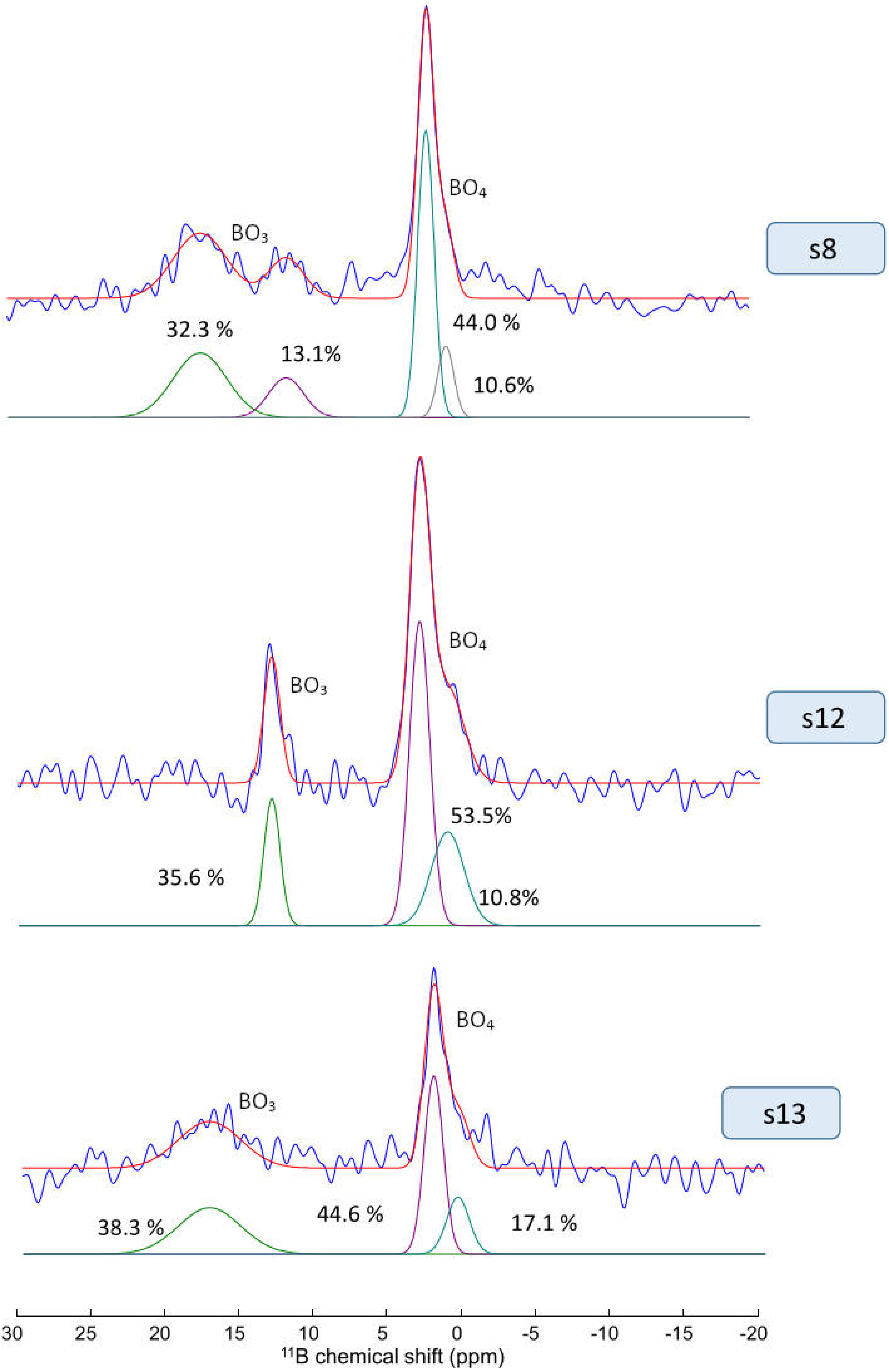

Figure 3.31: ^{11}B MAS NMR spectra and deconvolution of Mg-calcite samples s8, s12-23. The blue line indicates the experimental spectra, the red line the simulated spectra and the overlapping bottom lines the deconvolution. Note the presence of two components in both BO_3 and BO_4 peaks. The determined NMR parameters are reported in Table 3.14 and A.8.

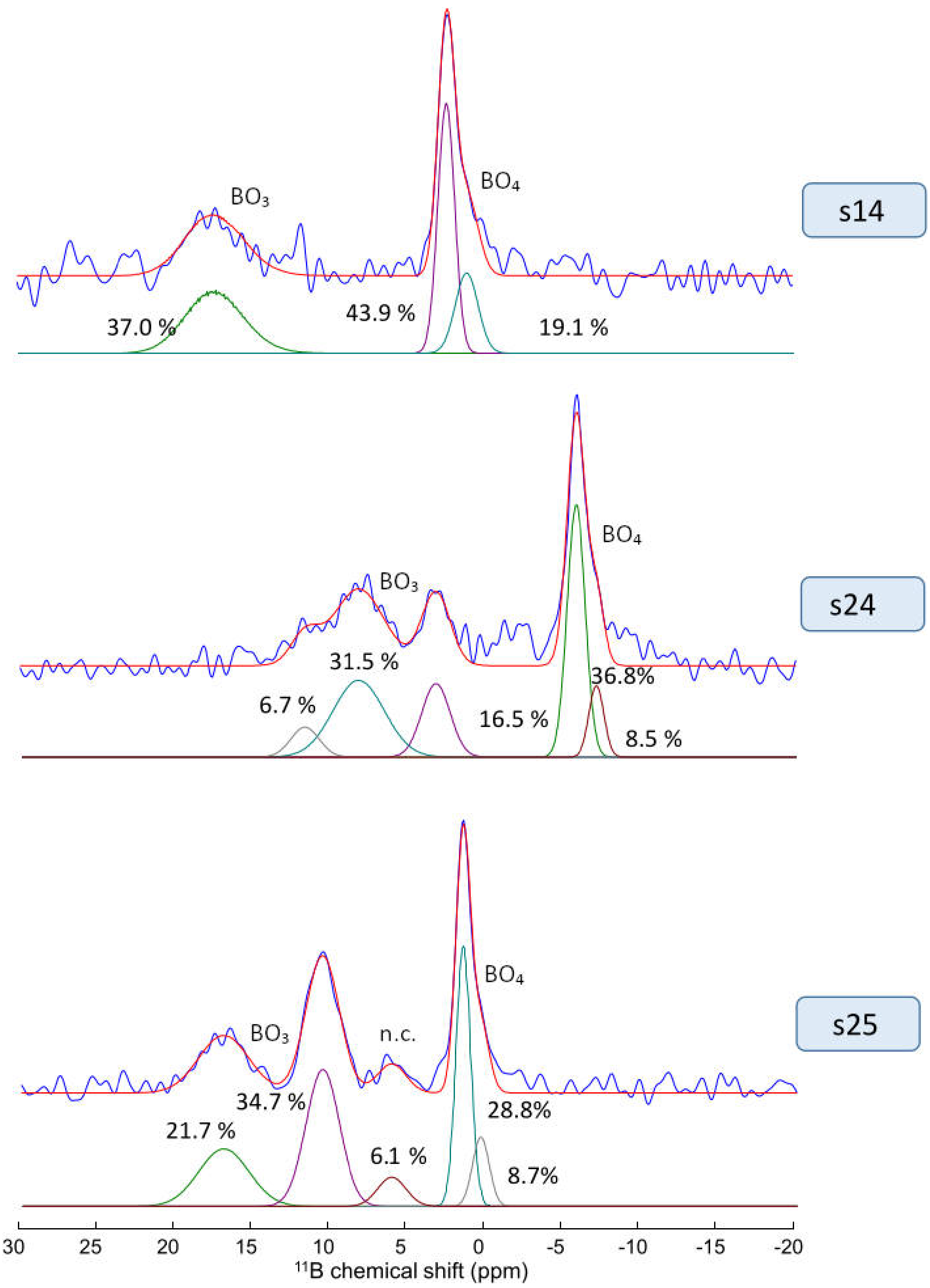

Figure 3.32: ^{11}B MAS NMR spectra and deconvolution of Mg-calcite samples s14, s24-25. The blue line indicates the experimental spectra, the red line the simulated spectra and the overlapping bottom lines indicate the deconvolution. Note the presence of two components in both BO$_3$ and BO$_4$ peaks. Sample s24 has two BO$_3$ peaks in one of the two BO$_3$ components. The 6.1 ppm signal in sample s25 was ambiguous and not classified (n.c.). The determined NMR parameters are reported in Table 3.14 and A.8.

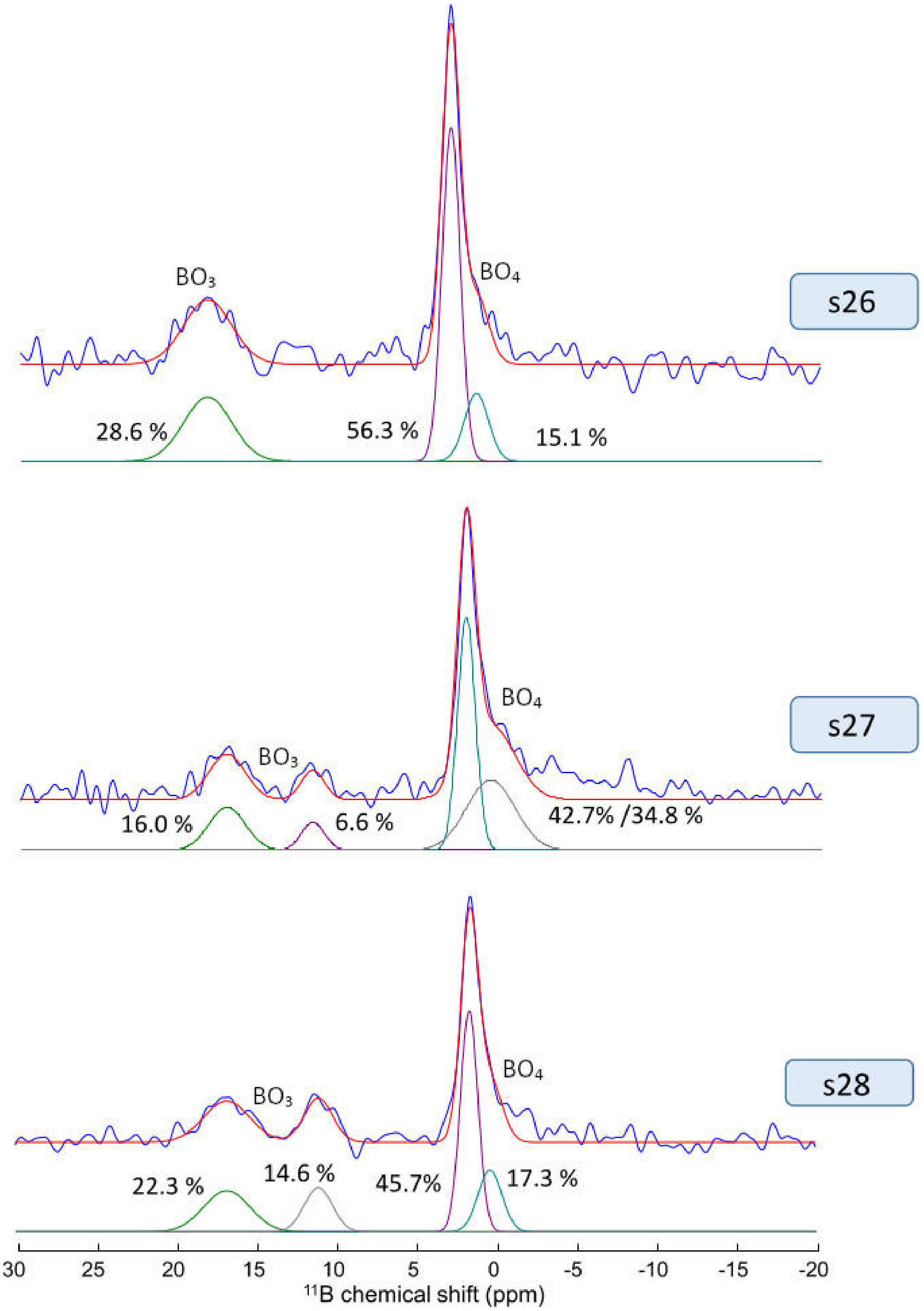

Figure 3.33: ^{11}B MAS NMR spectra and deconvolution of Mg-calcite samples s26-28. The blue line indicates the experimental spectra, the red line the simulated spectra and the overlapping bottom lines the deconvolution. Note the presence of two components in both BO_3 and BO_4 peaks. The determined NMR parameters are reported in Table 3.14 and A.8.

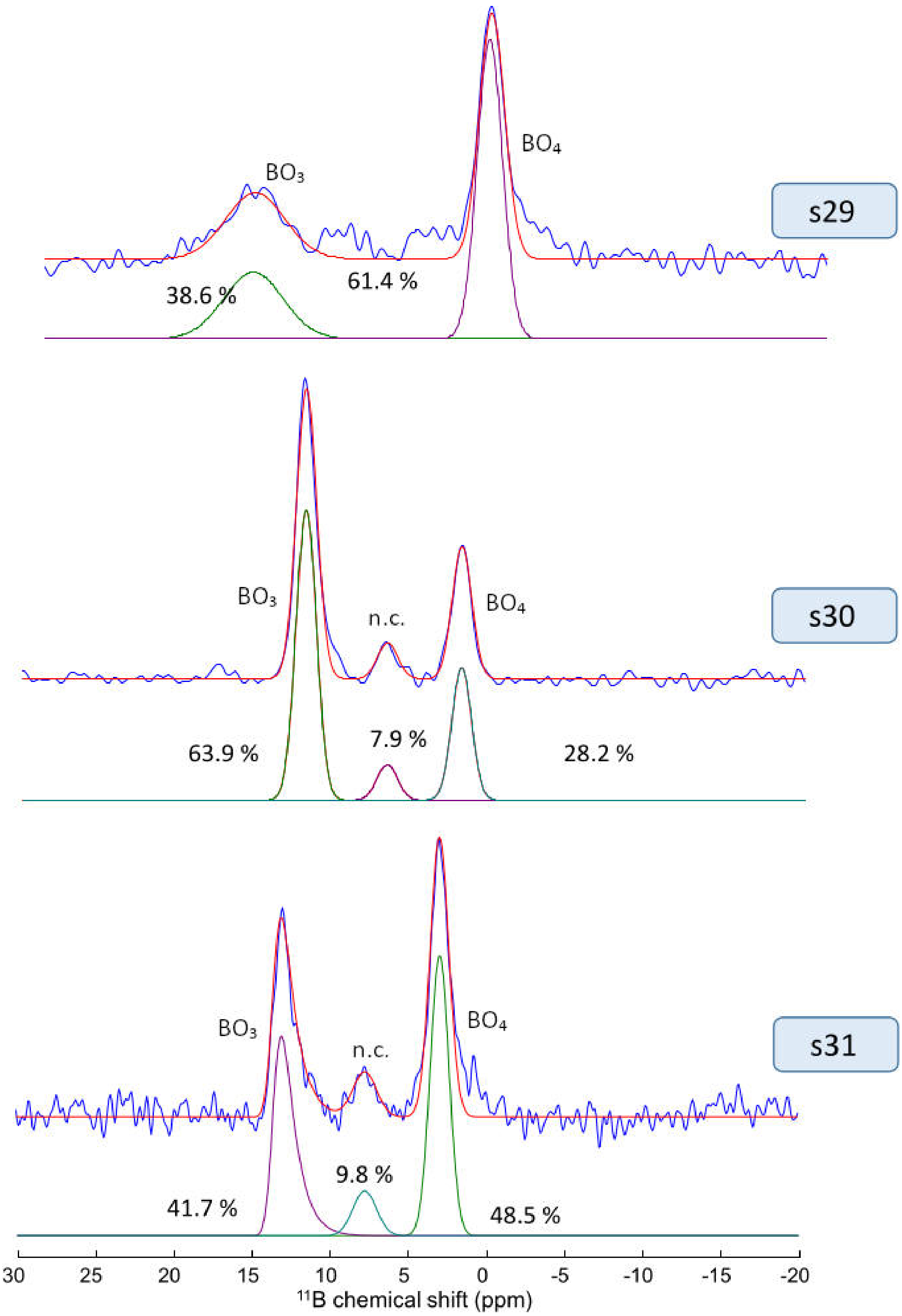

Figure 3.34: ^{11}B MAS NMR spectra and deconvolution of Mg-calcite sample s29 and aragonite samples s30-31. The blue line indicates the experimental spectra, the red line the simulated spectra and the overlapping bottom lines indicate the deconvolution. Note the 7.7 ppm signal in samples s30-31, ambiguous and not classified (n.c.). The determined NMR parameters are reported in Table 3.14 and A.8.

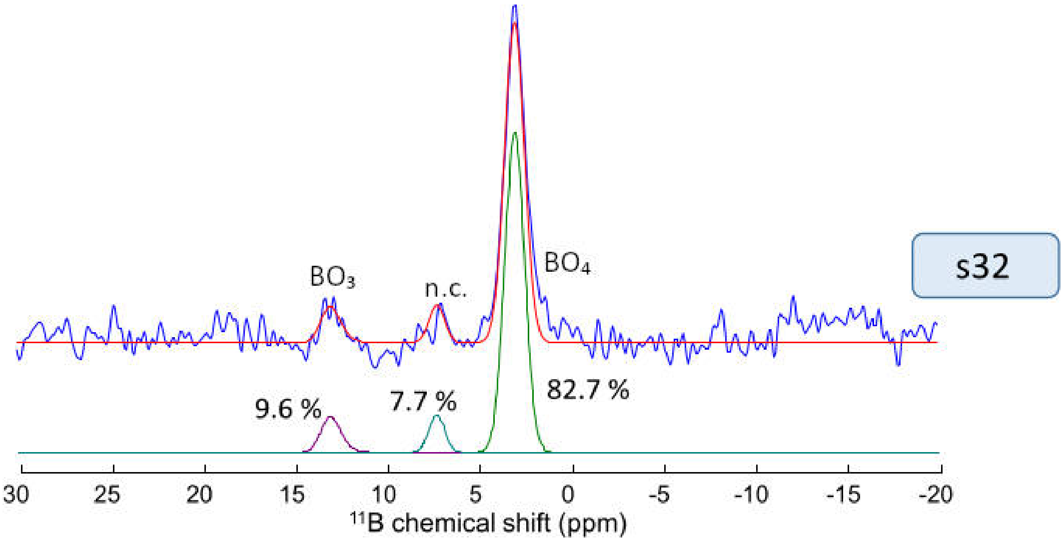

Figure 3.35: ^{11}B MAS NMR spectra and deconvolution of aragonite sample s32. The blue line indicates the experimental spectra, the red line the simulated spectra and the overlapping bottom lines indicate the deconvolution. Note the 7.2 ppm signal, ambiguous and not classified (n.c.). The determined NMR parameters are reported in Table 3.14 and A.8.

Chapter 4

Discussion

4.1 The taxonomic value of the cell wall calcification

Given their morphological plasticity, new diagnostic tools for calcareous red algae species identification could significantly assist experts, particularly for fossil samples with poorly preserved morphological features. This is important for paleontological applications since the reconstruction of the paleoecology and the paleoclimate based on organisms and associations must rely on species-specific calibrations. Indeed each organism, including coralline algae, has a species-specific geochemical signature [42, 77] and ecological niche [88], that can be used as a proxy for environmental reconstructions. The identification of species in calcareous red algae is frequently ambiguous, and advances in molecular phylogeny have revealed numerous cases of cryptic and pseudo-cryptic species. Traditional taxonomic identification relies on thallus organisation and morphometrical measurements of biological structures such as epithallial, perithallial, and hypothallial cells and conceptacles. Statistical analysis revealed a significant difference in the size of perithallial cells between *L. racemus* and *L. pseudoracemus* (Fig. 3.7). However, the molecularly identified samples of *L. racemus* exhibit a very wide range of perithallial cell area values (Fig. 3.7; Table 3.4), putting the applicability of this single character for species separation in jeopardy. The longitudinal medial section of *L. pseudoracemus*'s asexual conceptacle chambers was more rounded than that of *L. racemus*, with a lower D/H ratio (2.11 against 2.55). This pattern was also observed in non-molecularly identified samples (2.25 in s6 vs. 2.37 in s5). According to Caragnano et al. [6], a calcified columella rising from the asexual conceptacle floor was observed in most samples but not in *L. pseudoracemus*. In *L. pseudoracemus* s6, it appeared variably developed and its height was less than half the height of the conceptacle chamber, so h1 [57] was typically >H/2 (Fig. 3.6). However, the small number of observations precludes any statistical analysis of this feature, which merits further investigation to determine its potential value. In agreement with Caragnano et al. [6], these observations revealed high variability in microanatomy among samples and even within the same specimen, preventing a reliable distinction of the two species solely based on the microanatomy and biometrical analysis. Aside from the uncertainty associated with classification based solely on these tools, traditional morphological parameters are frequently poorly preserved due to diagenetic processes, reducing their taxonomic value in fossil samples where molecular techniques cannot be applied. Recently, there has been renewed interest in the calcification patterns of coralline algae, revealing cell wall ultrastructure as the phenotypic expression of genotypic information [84]. At least at the family level, there is taxon-specific regulation of the morphology of crystallites that compose the cell wall. Auer and Piller [84] examined *Lithophyllum incrustans*, *L. kotschyanum*, *L. lichenoides*, *L. pygmaeum* and *L. byssoides* (as *Titanoderma byssoides*) among Lithophylloideae. The defining characteristics of this subfamily are rhombic plates as the dominant morphotype of epithallial cell wall crystallites and perpendicular rod-shaped crystallites in the SC [84]. The cell walls of *Lithothamnion* sp. are rather ultrastructurally composed of fan-like rods in the secondary calcification and blocks and granules in the primary calcification [84]. *Mesophyllum* sp. cell wall ultrastructure has never been thoroughly studied. The detailed SEM observations of *L. racemus* and *L. pseudoracemus* conducted in this research revealed rhomboid-shaped crystallites in the PC and perpendicular rod-shaped crystallites in the SC of both species. Three distinct calcified layers in *L. racemus* and *L. pseudoracemus* were observed: the outer calcification (PC), the median one with perpendicular rods (SC), and the innermost granular layer (IC) (Figs. 3.1 and 3.4). The IC was composed of granular elements (Fig. 3.1); it was located between the plasma membrane and the SC and was frequently covered by organic plasma membrane residue. Regular rhomboids were particularly obvious in both primary and secondary hypothallial cells (Figs 3.2, 3.4, 3.5 and 3.6). The PC rhomboids were apparently absent between epithallial cells of the same filament and were not visible elsewhere, except between adjacent filaments of epithallial cells of *L.* cf. *racemus* sample s5 (Fig. 3.5). Deep learning methods were used to automatically classify *L. racemus*, *L. pseudoracemus*, *L. corallioides* and *M. philippii* found in Mediterranean waters in order to investigate a new potential tool for coralline algae identification. The use of CNNs allowed us to look into the diagnostic value of morphology as a whole, including both traditional parameters and the mineralized ultrastructure. In this way, machine learning has acted as an unbiased operator, able to establish its own classification features and potentially suggest significant diagnostic parameters to the real operator, even more than conventional ones. To maximise species variance, images for each specimen (two/three samples per species) were included in the dataset (Table 2.1). By doing so, we reduced the error associated with the sample's features rather than the species itself. The specific classification task involving the discrimination between *L. racemus* and *L. pseudoracemus* was especially difficult for the machine, given their morphological similarity [6]. The computed CNN-based models outperformed human diagnosis in *Global accuracy* at both the genus and species levels, as well as in *Recall* of the most challenging discernable classes, *L. racemus* and *L. pseudoracemus*, demonstrating the effectiveness of this technique in supporting coralline algae classification. The 3 class-CNN model demonstrated to be the best choice for coralline algae classification, with the highest *Global accuracy* and solid *Class Recall* for each genus (Table 3.5). Nonetheless, when a more fine-grained diagnosis (i.e., at the species level) is required, the 4 class-CNN model would be more convenient. In fact, despite the lower *Global accuracy*, this model could include more classes and still provide reasonable classification support, even in the presence of very similar classes such as *L. pseudoracemus* and *L. racemus*. Background areas and starch grains (Fig. 3.14) may "disturb" the classification in epithallus and perithallus images, leading to incorrect identifications. As a result, the model performances could be implemented by avoiding the use of images with these interferences. The analysis of the various explanatory techniques enabled us to demonstrate the image areas that have had the greatest influence on identification at both the genus and species levels. The explanatory approaches consistently revealed a significant contribution of the calcification features in the classification task (Fig. 3.13). Some traditional morphological parameters were easily recognised, such as conceptacle and cell morphometry, thanks to the explanation comparison, but crystallite morphology undoubtedly contributed to the classification results (Fig. 3.13). Indeed, crystallites were given special consideration, accounting for nearly half of the total images used to run the CNN models (Fig. 3.12). The PCA results (Fig. 3.8) enabled the circumscription and separation of two groups of samples based on calcification traits, which included the genetically classified *L. racemus* (s1, s2) and *L. pseudoracemus* (s3, s4). Overall, perithallial cells in *L. racemus* had a larger cell wall area (145.48 μm^2 by mean) and thicker SC (2.84 μm); perithallial cells in *L. pseudoracemus* had a smaller cell wall area (100.09 μm^2 by mean) and thinner SC (2.42 μm) (Fig. 3.8; Table 3.4). There was a direct relationship between SC thickness and cell wall area in the perithallus of the samples analysed (Fig. 3.8). *L. racemus* sample s2 and *L. pseudoracemus* sample s4 occurred sympatrically and at similar depths (Table 2.1), but showed a highly significant difference in terms of calcification traits (Fig. 3.8). Sample s2 had a thin PC and high SC thickness and cell wall area values, whereas s4 had a thick PC, thin SC, and a small cell wall area (Fig. 3.8; Table 3.4). *L. racemus* s2's distinct zonation (= banding) allowed us to focus on calcification traits in short and long cells separately (Fig 10) [4, 201]. Our findings show that *L. racemus* short perithallial cells have higher SC thickness and thus a larger cell wall area than long perithallial cells while maintaining an almost stable cell lumen area (Fig. 3.10). Long cells produced in the warm months had thicker PC observed between two cells of adjacent filaments, whereas short cells had larger cell wall area due to thicker SC (Fig. 3.10) [267]. As a result, we can speculate that primary crystallites were formed as a result of warmer temperatures and/or longer light periods. The low PC thickness values in short cells could be explained by an SC that grows at the expense of the PC during the cold months. Concerning the identification of the two *L.* cf. *racemus* samples, s5 and s6, the model agreed with the expert in the 3 class-CNN on attributing the *Lithophyllum* class and was leaning towards *L. racemus* in the 4 class-CNN. According to the PCA, sample s6 belonged to the *L. pseudoracemus* calcification type (Fig. 3.8). Surprisingly, samples with thick perithallial SC also had thick SC in epithallial cells (Table 3.4). The epithallial cells in specimen s5 had the largest diameter (Fig. 3.5; Table 3.3), which explains why the cell wall area was so large despite the relatively thin SC. The cell wall area in the perithallus was large, and the SC was thick, which corresponded to the major defining characteristics of *L. racemus* (Fig. 3.8; Table 3.4) The inclusion of *L.* cf. *racemus* s5 in the *L. racemus* calcification type is supported by the PC-1 axis of the PCA, which explained 60% of the data variance (Fig. 3.8). This specimen was collected at the shallowest depth (10 m), whereas all of the other specimens were collected at depths greater than 40 m, raising the possibility of an epithallial cell size response to light availability or other undefined oceanographic controls. To achieve satisfactory classification results, intra-class variability must be lower than inter-class variability. In our case, however, increasing the number of classes reduced inter-class variability (due to the two similar classes *L. racemus* and *L. pseudoracemus*). This was clearly not offset by an increase in intra-class variability, resulting in lower performance. Also, while the number of images among classes was reasonably balanced in the 4 class-CNN, the *Lithophyllum* sp. class accounted for more than half of the total number of images in the 3 class-CNN (Table 2.1), potentially favouring the accuracy of its classification. Despite accounting for roughly one-third of the total images, the *Class Recall* of *L. pseudoracemus* in the 2 class-CNN was comparable to the class Others (60%) (Table 3.5). As a result, the model demonstrated the ability to identify some morphological features of *L. pseudoracemus*, as evidenced by a *Class Recall* value much higher (60%) than both the dummy classifier (27%) and, most notably, the human classifier (21%) (Table 3.5). Future research on CNNs applied to SEM imagery for identifying coralline algae should rely more on standard magnifications for SEM images within each morphological category, with an even distribution of image numbers across classes. Variable sample orientation should be avoided, and SEM images should be collected on longitudinal sections, as in Section 2.1. The following magnifications for SEM images are recommended for the purpose:

- Conceptacles: ~250X, ~500X;
- Perithallus: ~1000X, ~2500X, ~5000X;
- Crystallites: ~10000X, ~20000X, ~30000X;
- Epithallial cell: ~1000X, ~2500X, ~5000X;

- Hypothallus: ~250X; ~1000X;

- Surface: ~1000X.

4.2 Biomineralization in calcareous red algae

Calcification in calcareous red algae has traditionally been thought to be a controlled process involving cell wall mineralization [110, 175, 177]. The report of different Mg/Ca ratios associated with distinct anatomical structures in these algae [184], and in particular, of higher-Mg calcite detected in wound repairs, primary calcification, and hypothallial cells of *Phymatolithon* sp. and *Clathromorphum* sp. [180, 183], called this view into question. Based on the significant Mg/Ca ratio variation observed in Mg-calcite within single specimens, as well as the observed relationship of Mg/Ca with ambient temperature, Nash et al. [180] proposed a biologically induced origin of calcareous red algae calcification. The secondary precipitation of minerals caused by interactions between biological activity and the environment is referred to as biologically induced mineralization [248]. In contrast to the idea of biologically induced calcification in calcareous red algae [184], it has recently been demonstrated that the ultrastructural shape and arrangement of crystallites in cell walls are shared by species from the same phylogenetic clade [84, 267]. Furthermore, Bracchi et al. [267] discovered species-specific distinct styles of PC calcification within the genus *Lithothamnion*. Despite the variable and distinct cell size in *L. racemus* and *L. pseudoracemus*, the ultrastructures observed and analysed in this research confirm the recently described pattern of Lithophylloideae [84], as well as the phylogenetic control over the calcification process and the morphology and orientation of the crystallites produced (Fig. 3.8). The cell walls between adjacent filaments that contain the meristem cell and the epithallial cells issued from it appeared as a pre-existing calcite "envelope" with a well-developed and relatively homogeneous thickness (Fig. 3.1). The pattern of calcification of the new epithallial cells differs in the congeneric species *Lithophyllum kotschyanum* Unger, with an increasing thickness of the SC toward the lower base of the meristem cell observed by Auer and Piller [84]. This finding lends support to the idea that species control calcification traits in calcareous red algae. DNA sequencing combined with calcification trait analysis on a broader range of species could elucidate the diagnostic potential of the meristem calcification pattern cutting off the new epithallial cells. The loss of definition in the primary crystallite shape observed in perithallial cells of *L. racemus* and *L. pseudoracemus* could be attributed to solution/precipitation or recrystallization processes, as previously reported in *L. kotschyanum* along with progressively increasing calcification [84]. Raz et al. [245] demonstrated experimentally that high-Mg calcite forms via an amorphous precursor phase composed of spherical particles. Later, similar findings were made in corals [255], where amorphous calcium carbonate (ACC) precursors precipitated before being transformed into crystalline calcium carbonate (CCC) after about a day. Similar amorphous to crystalline pathways have been reported in crustaceans, annelids and mollusc larval shells [138]. According to this theory, the inner layer of calcified grains seen in the samples analysed in this study (Fig. 3.1) could be an intermediate precursor phase preceding the formation of the rod-shaped crystallites. The IC is the only calcification that occurs immediately after the meristem is cut off, and we frequently observed multiple layers of perpendicular rods within the SC (Fig. 3.4). As a result, the IC is most likely the first step in the formation of SC, with SC multiple-layer thickening resulting from the deposition of a new layer following IC reactivation. According to this theory, the only plausible explanation for Nash et al. [180] is coralline algal calcification progressing from the inner part of the cell wall to its periphery. The Mg/Ca ratio in calcareous red algae varies not only between specimens but also within a single specimen. At a finer level, NanoSIMS analysis of the Mg/Ca ratios in *L. glaciale* revealed higher values in summer cells, with pronounced variation within a single cell wall, both in the natural environment and in controlled conditions with constant temperature, to a lesser extent [79]. This observation would imply that the Mg/Ca ratio is primarily controlled by environmental temperature, as assessed across phyla at a global scale [156], but that living calcareous red algal cells also mediate the calcite Mg/Ca ratio at the ultrastructural scale. The highest ratios were recorded in the PC and at the cell lumen boundary of *L. glaciale*, with NanoSIMS evidence of further high Mg/Ca values, localised concentrically in the SC [79] (Fig. 3.2). This pattern of concentric higher Mg/Ca values lends support to the hypothesis of successive IC activations, which may have resulted in the formation of additional SC crystallite layers. Surprisingly, the best-developed calcite rhomboids were found in the PC between adjacent cell filaments and in the hypothallial cell walls of both the primary and secondary hypothallus. We also found thicker PC in longer cells, which explains why longer perithallial cells produced during the warm season have a higher Mg/Ca ratio [4, 79, 117, 180]. These findings support the hypothesis that primary and secondary calcification are controlled by different processes: calcification of actively (likely fast) developing anatomical parts (hypothallial cells, wound repairs), particularly the PC and IC, could be mediated by a higher Mg/Ca phase regulated by the distinct physiological activity of calcareous red algal cells and their organic templates [183, 186]; on the contrary, calcification of the SC would occur from the IC, partially at the expense of the PC, through the incremental growth of one or more generations of crystallites with a lower Mg/Ca ratio.

4.3 Temperature and growth rate influences on B/Ca

Temperature variations, in general, affect many physiological processes involved in biomineralization, and the rate of calcification, along with the preservation state of mineral structures, influences the content of trace elements in carbonates [120, 136, 149, 197, 226]. The concentrations of trace elements measured in the four *L. corallioides* branches studied in this study were consistent with previously published values for other calcareous red algae [156, 196, 205, 237]. The Mg/Ca ratio ranged from 172 to 311 mmol/mol, which is comparable to previous studies on *Lithothamnion glaciale* Kjellman rhodoliths grown at 6-15 °C (148-326 mmol/mol) [200]. The B/Ca ratio in *L. corallioides* range from 356 to 954 μmol/mol, which is greater than the range measured by solution ICP-MS on bulk samples of *Neogoniolithon* sp. (352-670 μmol/mol) [102] and *C. compactum* (320-430 μmol/mol) [66] cultured at a pH ranging from 7.2 to 8.2. Because of the high resolution provided by laser ablation, the results accounted for the heterogeneity of B/Ca across the thallus, explaining the wider range of our data. As expected, the Mg/Ca results showed a strong relationship with the seawater temperatures extracted from ORAS5 (Fig. 3.20). *L. corallioides* from Aegadian Isl. (s12) had slightly higher Mg/Ca values, followed by Elba (s13) and Pontian Isl. (s14) (Fig. 3.16). This was consistent with local temperature values in the Mediterranean (Table 3.1), as Pontian Isl. had the lowest mean temperature and ΔT, while Aegadian Isl. had the highest mean temperature and ΔT. In contrast, the Morlaix sample (s8), collected at a depth of 12 m, revealed high Mg/Ca values in both long and short cells (Table A.2; Fig. 3.17). Because of the shallower depth (12 m) and geographical location, the monthly mean temperatures varied the most throughout the year (ΔT in Table 3.1). Temperature correlates with seasons, influencing primary production, respiration, and calcification in *L. corallioides* [44, 242], and other calcareous red algae [227]. The high seasonality of the Morlaix sample, as represented by the high ΔT (Table 3.1), was most likely responsible for the greatest variation in Mg/Ca values and undoubtedly accounted for the majority of the differences with Mediterranean samples. For the first time, we validated the temperature proxies Li/Ca and Sr/Ca on a wild-grown coralline alga collected at various depths and locations. Li/Ca and Sr/Ca records in *L. corallioides* were positively correlated with Mg/Ca (Fig. 3.15), which in turn had a strong relationship with seawater temperature. Furthermore, both Li and Sr/Ca showed periodic oscillations in relation to long and short cells, which were related to seasonal temperature variations (Fig. 3.20). As a result, Li/Ca and Sr/Ca, as Mg/Ca, could be used as temperature proxies in *L. corallioides*. The coupling of the Mg/Ca ratio with Li/Ca and Sr/Ca ratios can be regarded as a useful tool for gathering information about past temperature for paleoclimate reconstructions [4, 32, 115, 148, 251]. The B/Ca ratio in coralline algae has rarely been measured, and it is unclear how environmental factors influence its incorporation. Changes in B incorporation are primarily driven by the carbonate system [141, 205]. B/Ca increases with $[CO_3^{2-}]$ [141], whereas there is no agreement on the effect of $[CO_3^{2-}]$ on Mg/Ca and Sr/Ca [8, 276]. Inorganic calcite experiments revealed a positive relationship between B/Ca and [DIC] [124]. Nonetheless, [DIC] had a negative effect on B/Ca in culture experiments with the coralline algae *Neogoniolithon* sp. [102] and corals [20]. DIC and B/Ca values showed a negative relationship in all the samples except for Elba (s13) (Fig. 3.22; Table 3.1). Significant differences in B/Ca values were not expected in the Mediterranean samples because DIC concentrations were comparable (Table 3.1). This evidence suggests that factors other than DIC have an impact on the B signal. The mean estimated growth rate of *L. corallioides* was 0.13 ± 0.02 mm/yr and was expected to decrease with increasing depth as a direct result of lower light availability [115]; in fact, the growth rate of the Pontian Isl. sample (s14) was the lowest (0.10 mm/yr). Previous research on both synthetic and biogenic calcite has suggested that B incorporation is likely affected by growth rate [120, 124, 149, 229, 260]. Indeed, the B/Ca ratio in the cultured calcareous red alga *Neogoniolithon* sp. increases with increasing growth rate [102]. The slowest growth rate found in sample s14 may have contributed to the lowest B/Ca value; similarly, the fastest growth rate (0.14 mm/yr) in the sample s13 (Elba) may have contributed to the highest B/Ca value (Figs. 3.22 and 3.23). The shallowest sample's mean annual growth rate (s8, Morlaix) was intermediate (0.13 mm/yr), and was most likely not constant throughout the year. Here, the alga probably slowed growth during the cold months, when the monthly mean seawater temperature was the lowest of all sampling sites (Table 3.1). Nonetheless, because of the abundant light availability at shallow depths and the warming of seawater (Table 3.1), its growth rate likely accelerated during the warm season, contributing to the significantly higher B/Ca values in long cells (Fig. 3.23). The effect of the growth rate on B/Ca may be significant across depths and geographical regions, according to this interpretation (Fig. 3.24). B/Ca had a weak positive correlation with temperature proxies (Mg/Ca, Li/Ca, and Sr/Ca; Fig. 3.21) in Morlaix. In planktonic foraminifera [142, 191], a positive correlation between B/Ca and Mg/Ca was observed. In order to highlight the influence of temperature, we reconstructed the elemental variations during algal growth in the Morlaix sample at annual resolution (Fig. 3.20). Unlike Mg, Li, and Sr/Ca, B/Ca did not accurately reflect seasonal temperature variations like the other proxies. Seasonal *Delta*T, Mg/Ca, and B/Ca values were the lowest among sites in sample s14. B/Ca in particular was significantly low (Fig. 3.22), differing from the other samples more than Mg/Ca (Fig. 3.16). This implies that in this sample, B incorporation should be influenced by factors other than Mg. In general, the poor correlation with seawater temperature (Fig. 3.20), and especially the lack of distinct seasonal oscillations in B/Ca across the algal thallus, rule out B/Ca as a temperature proxy and point to a more direct relationship with growth rate rather than temperature. Understanding the biogeochemistry and variation of seawater environmental variables is critical for gaining a more complete picture of the reliability of geochemical proxies like the ones investigated here (Mg, Li, Sr/Ca, and B/Ca). More research on *L. corallioides* and other calcareous red algae is needed to understand the environmental factors that influence B/Ca in these organisms and to ensure the reliability of this proxy for paleoclimate reconstructions.

4.4 The multi-specific calibration of the boron isotope-pH proxy

Biological controls, also known as vital effects, are thought to be responsible for significant $\delta^{11}B$ differences between species [18, 205]. As a result, the application of the B isotope-pH proxy (as for most of the other geochemical proxies) is dependent on precise calibrations derived from laboratory culture experiments or field samples. A regression tuned on multiple species (Eq. 3.1) could be useful for calcareous red algae for which calibrations are not available, or for difficult taxonomic identification. The $\delta^{11}B_{algae}$ results from samples collected near CO_2 seeps were compared to previously collected data from cultured calcareous red algae that were combined to broaden the range of $\delta^{11}B_{borate}$ for which $\delta^{11}B_{algae}$ had been calibrated so far. Indeed, the multi-specific calibration proposed here (3.28, 3.1) includes algae collected in naturally acidified sites at very low pH (6.8 ± 0.86) and algae cultured at high pH (8.19 ± 0.06). Figure 3.27 compares the uncertainty bounds of species-specific calibration, with the exception of *A. anceps*, which is excluded from the calibration. When comparing *Peyssonnelia* sp. and *C. officinalis* grown in the same sites, i.e. S3 and S2 in Ischia, species-specific differences among the algal samples analysed in this study are evident (Figs. 3.27 and 3.28; Table 3.12). Samples of *Peyssonnelia* sp. s18 and s19 were both collected in Ischia, site S2, but at a distance of 30 metres one from the other. As a result, we cannot rule out a different set of environmental factors influencing algal growth and geochemical composition in this case, which could explain the different environmental signals between the two (Table 3.12). The carbonate chemistry within a living organism's microenvironment can be altered by metabolic processes such as photosynthesis, respiration, and calcification [30, 62], resulting in a site of calcification restricted from ambient seawater. Recent research found that the calcifying fluid pH (pH_{cf}) of calcareous red algae increases in experiments mimicking the ongoing ocean acidification [42, 43], as previously suggested for corals [19, 82, 170, 172]. Cultured calcareous red algae appeared to have species-specific control over pH_{cf}, with *S. durum* and *Neogoniolithon* sp. elevating it up to 1 unit above seawater pH and *A. anceps* increasing it up to 0.6 unit [42]. The pH_{cf} is thought to be solution pH dependent, with 0.13-0.30 unit declines in pH_{cf} per seawater pH unit [42, 43]. The calculated calibrations in this work consistently plot above the 1:1 line in the $\delta^{11}B_{borate}/\delta^{11}B_{algae}$ space (Fig. 3.27), indicating that algae register higher ^{11}B than solution borate. The proposed multi-specific calibration clearly shows this up-regulation (Fig. 3.28), confirming a species-specific biologically controlled up-regulation of pH in the calcifying fluid.

4.5 Boron incorporation in calcareous red algae

Boron incorporation in marine carbonates remains controversial, raising concerns about its isotopic fractionation, the seawater isotopic composition, and especially the so-called "vital effects" (i.e. the metabolic activities that can bias the proxy record). According to published data, inorganic aragonite has lower $\delta^{11}B$ values than calcite [15, 120, 149, 206]. The aragonitic species analysed in this study measured lower $\delta^{11}B_{algae}$ than Mg-calcites (Fig. 3.29). This evidence supports calcareous red algae actively regulating the deposition of carbonate crystals within their cell walls [84, 267] through controlled biomineralization [120, 176]. It is still unclear whether this enrichment in ^{11}B is due to different B speciation between polymorphs [68, 260]. Boron speciation in calcareous red algae was investigated to provide insights into B incorporation and to test the B isotope proxy, since accounting for a non-zero percentage of $B(OH)_3$ incorporation could possibly change the $\delta^{11}B$ proxy calculations [40]. In our samples, the relative abundance of BO_3 over BO_4 was similar in aragonite and Mg-calcite (Table 3.15). *Peyssonnelia* sp. after oxidation revealed the 82% of BO_4, similarly to *Polystrata* sp., both made of aragonite. These were the highest amounts of BO_4 registered in the analysed algae (Table 3.14). The mean BO_4 value in aragonite (64 ± 31%) dropped because of the NMR analysis on *Peyssonnelia* sp. sample s30, which was particularly low in BO_4 (28.2 %). Given the significantly different results of *Peyssonnelia* sp. sample s31 before and after oxidation (Table 3.14), a similar outcome cannot be excluded in sample s30 as well, which is a crustose form belonging to the same genus. The mean $BO_4\%$ in the aragonitic samples could therefore be underestimated. Theoretical models investigated the most stable B-containing molecular species to be incorporated in biogenic carbonates [68, 69]. These models predict that BO_3 could enter the carbonate lattice as either $BO_2(OH)^{2-}$ or BO_3^{3-} groups. Nonetheless, the ^{11}B MAS NMR parameters discovered in previous studies on aragonitic corals were distinctive of fully protonated $B(OH)_3$ [40, 151]. The presence of disordered mineral phases in corallines [194, 195] could explain the direct incorporation of $B(OH)_3$, which could be scavenged directly from seawater and encapsulated by amorphous phases similar to those observed in the IC (Figs. 3.1 and 3.4). If a preferential bound to carbonate growth sites as $B(OH)_4^-$ is assumed, the NMR results would suggest that a significant proportion of boron undergoes a change in coordination from BO_4 to BO_3 during its incorporation in the mineral lattice, as commonly hypothesized [93, 151, 206, 207, 246, 260], involving an energy barrier to the B uptake (Section 1.2.2).

Chapter 5

Conclusions

Part of this research was dedicated to the problem of taxonomy in calcareous red algae, which was addressed by testing new unconventional diagnostic tools for species identification (I and II Objectives, Sections 1.1.1.1 and 1.1.2.1). Indeed, a reliable identification should be preliminary to paleo-environmental studies, since proxy variability is often species-specific. Then, much effort has been dedicated to investigating the suitability of some common environmental proxies in Mediterranean calcareous red algae (Objectives III, IV and V, Sections 1.2.1.1, 1.2.2.1 and 1.2.2.2). The contribution of this research can be summarized as follows:

- A detailed description of biometrical and calcification traits in the cryptic species *L. racemus* and *L. pseudoracemus* was conducted under SEM to investigate the contribution of both traits in species identification. Morphological identification based solely on detailed biometry of cells and reproductive structures was found to be ineffective for distinguishing the two species. No differences in the ultrastructure of crystallites were found at the species level and the crystallite shape in the cell walls agreed with previous observations on other species in the same genus. A distinction was possible in terms of the degree of cell calcification, highlighting the *L. racemus* and *L. pseudoracemus* calcification types that account for the SC thickness, PC thickness, and cell wall area. The perithallial SC thickness, which was higher in *L. racemus* and lower in *L. pseudoracemus*, explained most of the differences.

- A novel deep learning approach was proposed to support and improve expert capability in the taxonomic identification of a wide range of calcareous red algal species. CNNs were applied to SEM images for the automated identification of four species at different taxonomic levels, and classification models are open-sourced on GitHub at `https://github.com/CValsecchi/VGG16_SEM`. The resulting performances were promising for obtaining a tool that could assist the expert in the classification of coralline algae, even with the limited number of images and samples and the high intra-class variability. Further research should include a larger and more standardised image dataset to ensure method reproducibility and model accuracy.

- There is a taxon-dependent hierarchy of ultrastructural patterns and calcification traits in coralline red algae, which is consistent with the concept of biologically controlled calcification. It was also possible to derive some important information about the biomineralization mechanism in calcareous red algae. SEM images revealed the presence of a granular calcified layer in the innermost part of the cell wall (IC), in addition to the SC and PC previously described. This could be the precursor phase in the formation of secondary crystallites. Cell elongation in both the perithallus and the hypothallus is associated with increased production of PC with a higher Mg/Ca ratio, possibly triggered by warmer temperatures and/or longer light periods. Furthermore, the inverse relationship between perithallial SC and PC thickness, as well as the absence of PC in the newly formed wall that cuts off an epithallial cell from the meristem, supports the existence of two distinct pathways for PC and SC formation.

- Trace elements (Mg, Sr, Li, and B) from the coralline alga *L. corallioides* were measured by LA-ICP-MS, providing the first geochemical data of a wild-grown coralline algal species sampled at different oceanographic settings and depths (12 m, 40 m, 45 m, and 66 m). Mg/Ca, Sr/Ca, and Li/Ca records showed a similar trend, which was primarily controlled by seawater temperatures in the algal habitat. Mg/Li, on the other hand, did not provide a useful temperature proxy in this species. To assess the influence of temperature on B incorporation, we examined the relationship between B/Ca and temperature proxies. Unlike Mg, Li, and Sr/Ca oscillations, B/Ca oscillations across algal growth showed a poor relationship with seasonal variations in seawater temperature. The estimation of growth rate, which was positively correlated with B/Ca values, led to the conclusion that B/Ca is related to growth rate rather than seawater temperature. Boron incorporation is thus subject to specific algal growth patterns and rates, which must be understood in order to assess the accuracy of B/Ca in tracing seawater carbon variations.

- The $\delta^{11}B$ has been used as a proxy for pH in diverse taxa. Calcareous red algae grown in naturally acidified environments showed evidence of up-regulation in the $\delta^{11}B$ signal, revealing a common trend of internal pH elevation. Aragonitic species (Peyssonneliales) revealed a lower $\delta^{11}B$ than calcitic species (Corallinales and Hapalidiales), corroborating previous research that suggests a mineralogical control over the B signal. A multi-specific calibration of the $\delta^{11}B$ proxy in calcareous red algae was proposed in this study. Since laboratory calibrations on extinct or uncertainly classified species are not possible, the proposed calibration can be used in paleoclimate reconstructions using fossil algae and historical archives.

- To obtain more insights into the mechanisms of B incorporation, the B speciation in calcareous red algae belonging to diverse genera and species and collected in different environments was investigated. A significant proportion of boron in the algae was present in the trigonal form: ~40% of BO_3 in calcite and ~30% in aragonite, the last being possibly overestimated. Given the scarcity of data currently available in the literature, the MAS NMR results add significant information for the understanding of B incorporation in calcareous red algae. Adapting theoretical atomic-scale models to biogenic carbonates and particularly calcareous red algae, would yield additional insights on B speciation in these organisms and would allow a more comprehensive discussion on proxy validation in this taxon. As opposed to bulk analyses, in the future, highly resolved analyses of $\delta^{11}B$ and B speciation at the micron-scale (50-100 μm), investigating the variations across the growth bands (long and short cells), would shed light into the growth rate, seasonal and external influences, similarly to what has been done in this research using LA-ICP-MS.

Appendix A

Supplementary materials

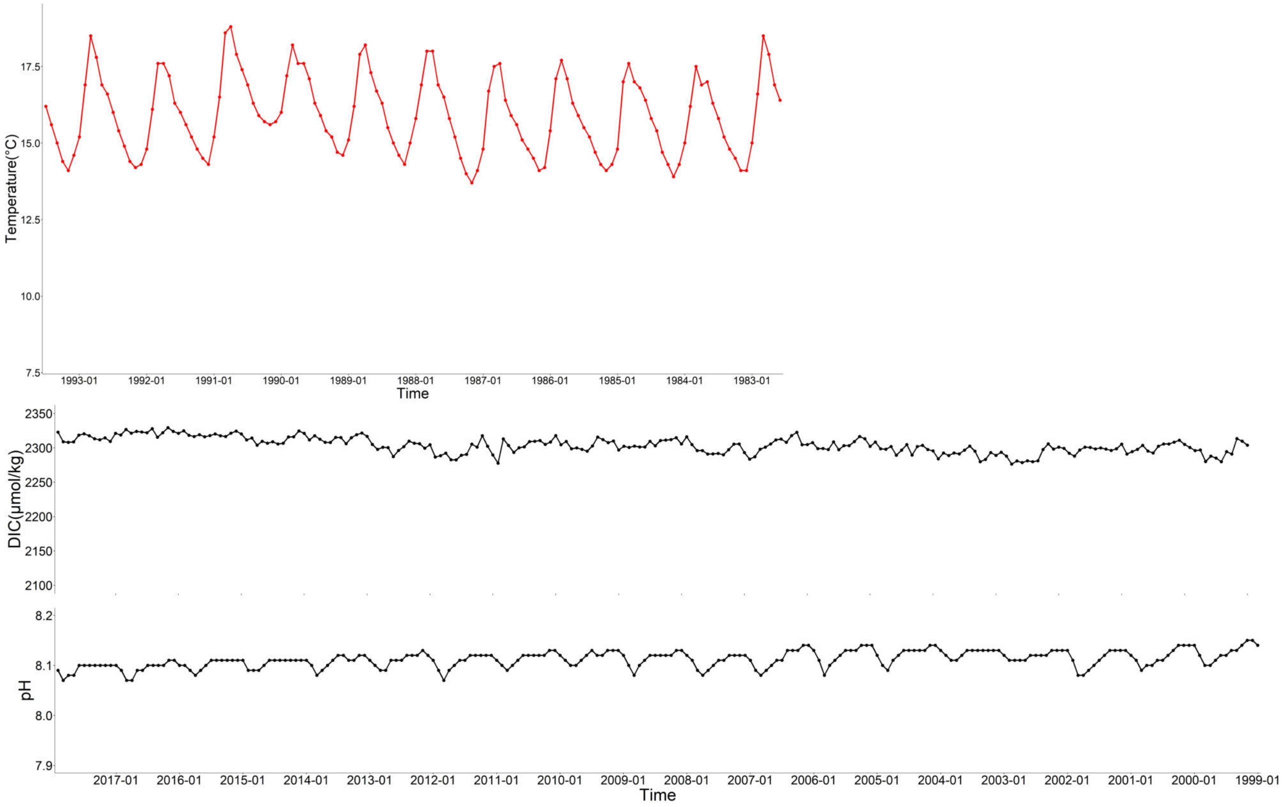

Figure A.1: Temperature and carbon data in Aegadian Isl. at sampling depth (40 m). The temperature was extracted by 11 years of ORAS5 monthly mean reanalysis preceding the date of sample collection (August 1993). Dissolved inorganic carbon (DIC) and pH data were extracted by CMEMS biogeochemical models spanning 1999-2017.

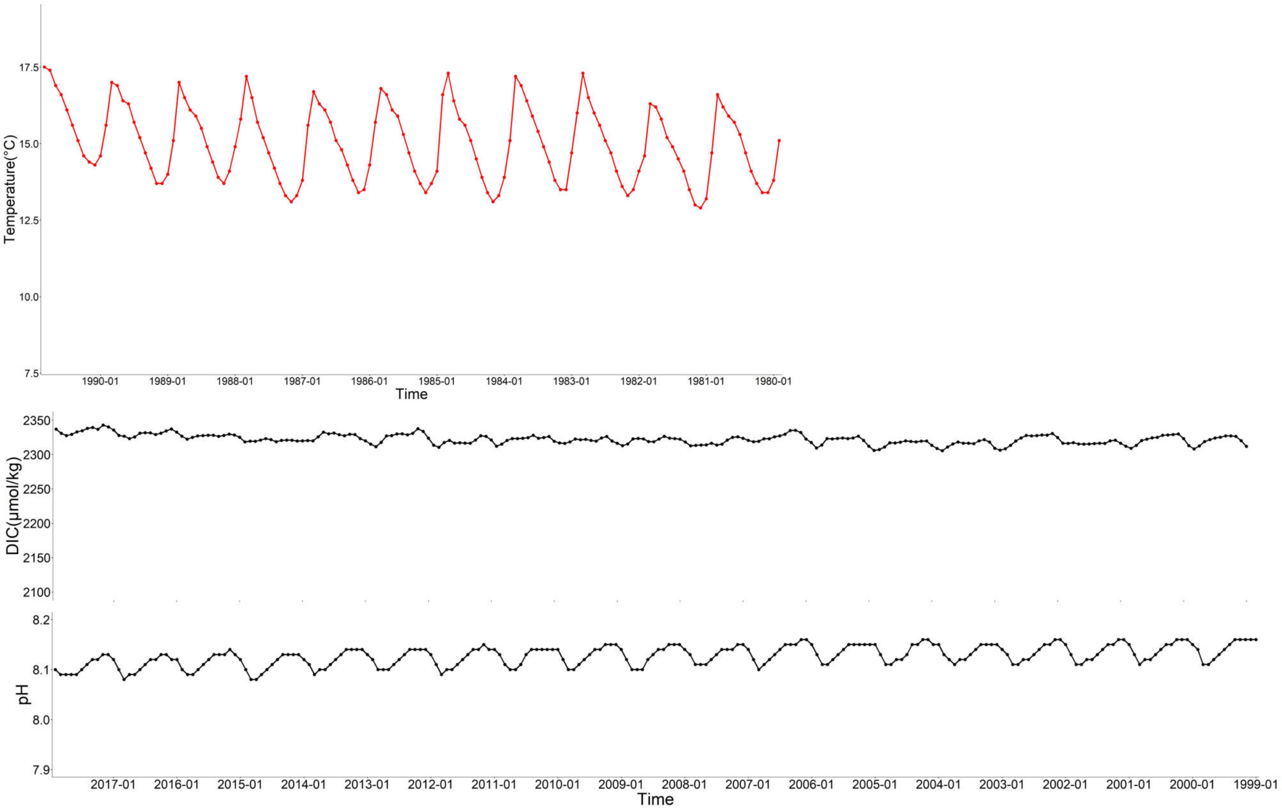

Figure A.2: Temperature and carbon data in Elba at sampling depth (45 m). The temperature was extracted by 11 years of ORAS5 monthly mean reanalysis preceding the date of sample collection (December 1990). Dissolved inorganic carbon (DIC) and pH data were extracted by CMEMS biogeochemical models spanning 1999-2017.

Figure A.3: Temperature and carbon data in Pontian Isl. at sampling depth (66 m). The temperature was extracted by 11 years of ORAS5 monthly mean reanalysis preceding the date of sample collection (July 2016). Dissolved inorganic carbon (DIC) and pH data were extracted by CMEMS biogeochemical models spanning 1999-2017.

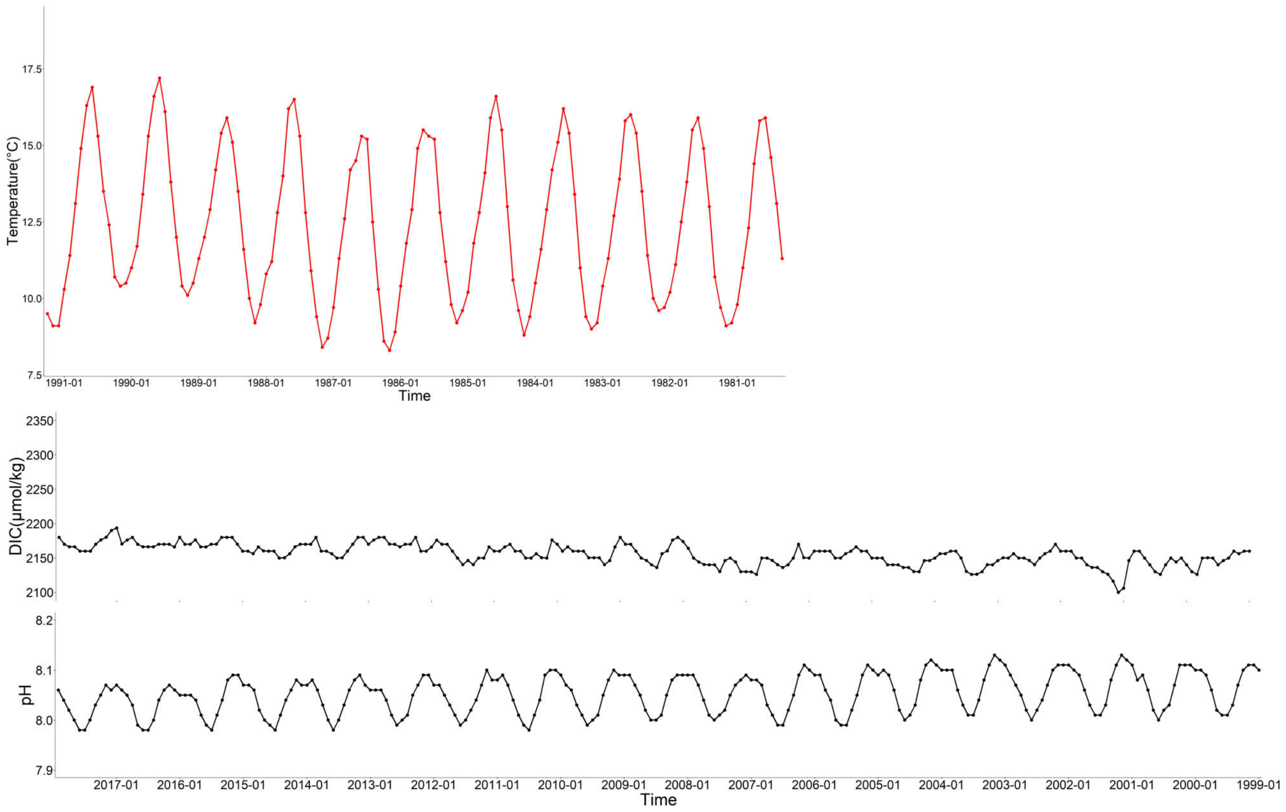

Figure A.4: Temperature and carbon data in Morlaix at sampling depth (12 m). The temperature was extracted by 11 years of ORAS5 monthly mean reanalysis preceding the date of sample collection (May 1991). Dissolved inorganic carbon (DIC) and pH data were extracted by CMEMS biogeochemical models spanning 1999-2017.

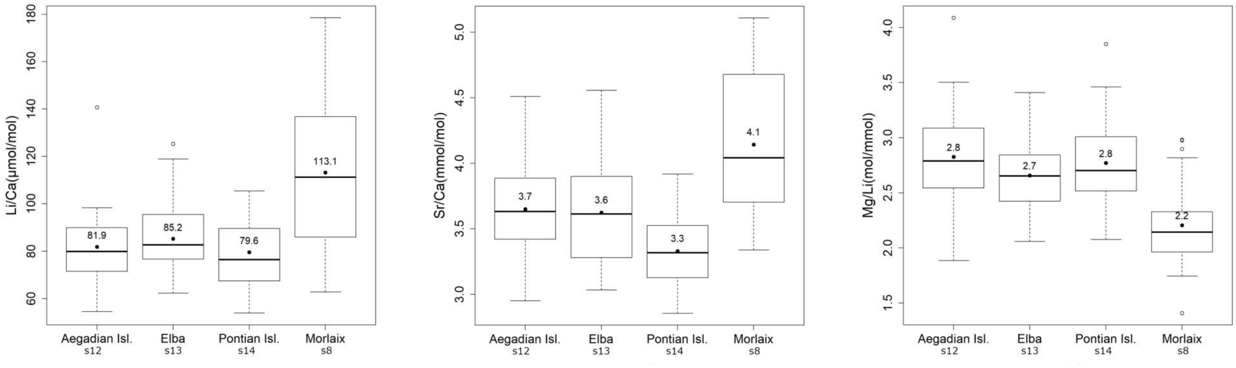

Figure A.5: Li/Ca, Sr/Ca and Mg/Li in *Lithothamnion corallioides* collected in different sampling sites. The horizontal black lines indicate the median values; the black-filled circles and the numbers inside the plot indicate the mean values.

Table A.1: Statistical tests performed to evaluate the differences of Mg/Ca in *Lithothamnion corallioides* (Kruskal-Wallis) and the differences of Mg/Ca in the short cells of *L. corallioides* collected at different sampling sites (ANOVA). Test significance at $\alpha = 0.05$.

Kruskal-Wallis test (Mg/Ca)

	Df	χ^2	P
Site	3	3.799	0.284

One-way ANOVA test (Mg/Ca)

			Short cells		
	Df	Sum sq.	Mean sq.	F value	Pr (F)
Site	2	788.1	394.0	1.4647	0.2496
Residuals	26	6994.5	269.0		

Shapiro-Wilk normality test	$P = 0.6442$
Barlett's K squared	$P = 0.5856$

Table A.2: Statistical tests performed to evaluate the differences of Mg/Ca in the long cells of *Lithothamnion corallioides* at different sampling sites (Morlaix Bay = sample s8; Aegadian Isl. = sample s12; Pontian Isl. = sample s14) (Table 2.1). Statistically significant p-values are highlighted in bold. ANOVA test significance at $\alpha = 0.05$. Tukey's test significance at $p \leq \alpha$.

One-way ANOVA test (Mg/Ca)

Long cells

	Df	Sum sq.	Mean sq.	F value	Pr (F)
Site	2	10897.7	5448.9	16.413	**0.0001**
Residuals	20	6639.8	332.0		

Shapiro-Wilk normality test	$P = 0.1440$
Barlett's K squared	$P = 0.5826$

Tukey's test

Multiple comparisons of means

Site	Mean difference	95% confidence interval		P.adjusted
	Site	lower bound	upper bound	
s8-s12	38.32918	15.09816	61.56019	**0.00130**
s14-s12	-10.84361	-35.48382	13.79661	0.51716
s14-s8	-49.17278	-72.40380	-25.94177	**0.00009**

Table A.3: Statistical tests performed to evaluate the differences of B/Ca in *Lithothamnion corallioides* collected at different sampling sites (Morlaix Bay = sample s8; Aegadian Isl. = sample s12; Pontian Isl. = sample s14) (Table 2.1). Statistically significant p-values are highlighted in bold. Kruskal–Wallis test significance at $\alpha = 0.05$; Dunn's test significant at $p < \alpha/2$.

Kruskal-Wallis test (B/Ca)

	Df	χ^2	*P*
Site	3	79.816	$< \mathbf{2.2 \times 10^{-16}}$

Dunn's test
Comparisons by site (Bonferroni)

Z *P*.adjusted	s12	s13	s8
s13	-4.64580		
	0.00000		
s8	-3.07755	1.17249	
	0.00630	0.72300	
s14	2.80564	8.38673	6.15663
	0.01510	**0.00000**	**0.00000**

Table A.4: Statistical tests performed to evaluate the differences of B/Ca in the long cells of *Lithothamnion corallioides* at different sampling sites (Morlaix Bay = sample s8; Aegadian Isl. = sample s12; Pontian Isl. = sample s14) (Table 2.1). Statistically significant p-values are highlighted in bold. ANOVA test significance at $\alpha = 0.05$. Tukey's test significance at $p \leq \alpha$.

One-way ANOVA test (B/Ca)

Long cells

	Df	Sum sq.	Mean sq.	F value	Pr (F)
Site	2	428364	214182	36.066	**0.0000**
Residuals	20	129546	6477		

Shapiro-Wilk normality test	$P = 0.5527$
Barlett's K squared	$P = 0.5470$

Tukey's test

Multiple comparisons of means

Site	Mean difference	95% confidence interval		P.adjusted
	Site	lower bound	upper bound	
s8-s12	190.11730	87.50374	292.73094	**0.00040**
s14-s12	-135.42490	-244.26303	-26.58672	**0.01342**
s14-s8	-325.54220	-428.15581	-222.92862	**0.00000**

Table A.5: Statistical tests performed to evaluate the differences of B/Ca in the short cells of *Lithothamnion corallioides* at different sampling sites (Morlaix Bay = sample s8; Aegadian Isl. = sample s12; Pontian Isl. = sample s14) (Table 2.1). Statistically significant p-values are highlighted in bold. ANOVA test significance at $\alpha = 0.05$. Tukey's test significance at $p \leq \alpha$.

One-way ANOVA test (B/Ca)

Short cells

	Df	Sum sq.	Mean sq.	F value	Pr (F)
Site	2	216232	108116	35.360	**0.0000**
Residuals	26	79497	3058		

Shapiro-Wilk normality test	$P = 0.1699$
Barlett's K squared	$P = 0.0576$

Tukey's test

Multiple comparisons of means

Site	Mean difference	95% confidence interval		P.adjusted
	Site	lower bound	upper bound	
s8-s12	43.09640	-19.61932	105.81212	0.22146
s14-s12	-156.90170	-223.66771	-90.13574	**0.00001**
s14-s8	-199.99810	-260.58727	-139.40898	**0.00000**

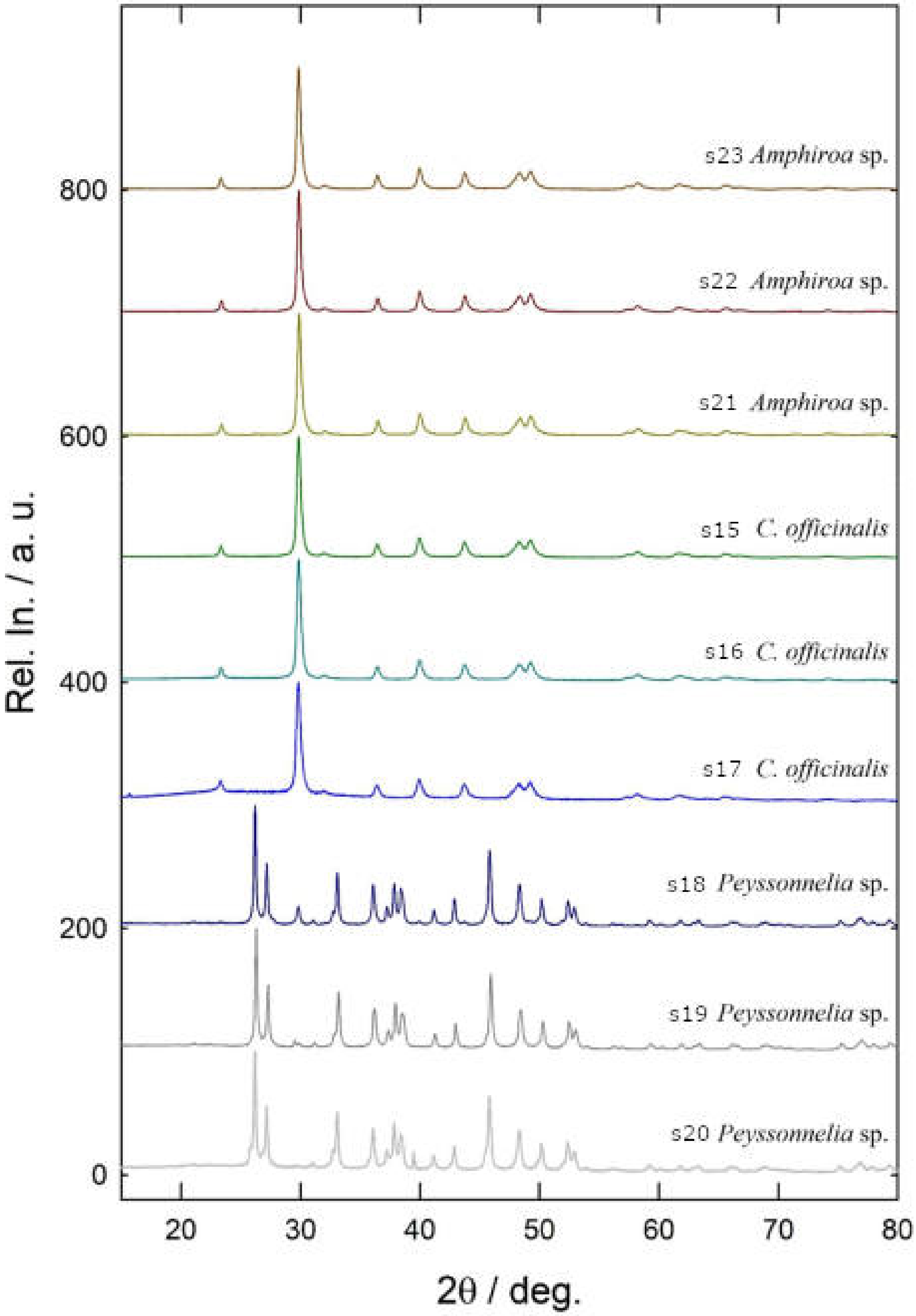

Figure A.6: X-ray powder diffraction patterns for samples s15-23.

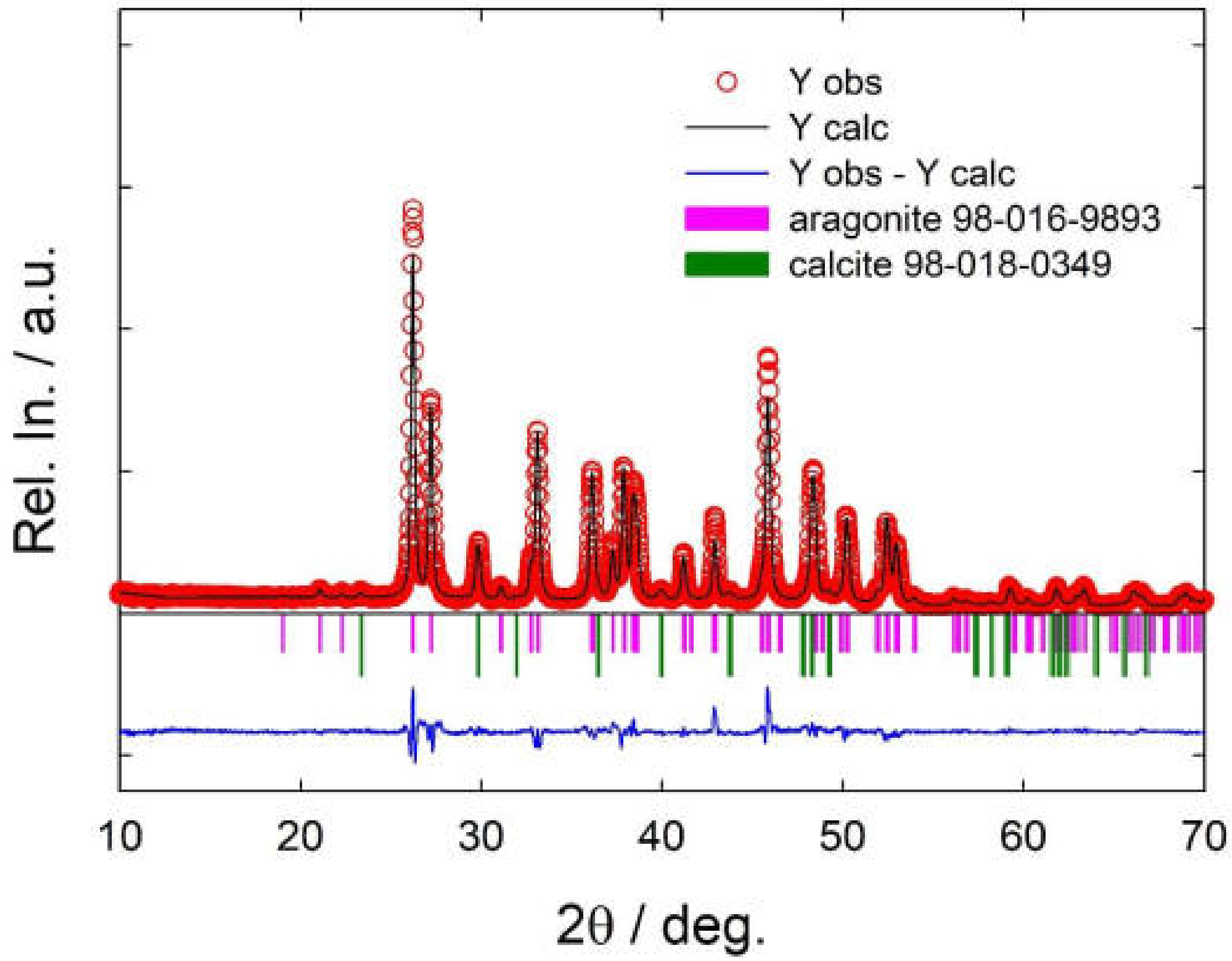

Figure A.7: Rietveld refinement results for *Peyssonnelia* sp. sample s18 based on the presence of aragonite and calcite phases.

Table A.6: Statistical tests performed to evaluate the differences of the perithallial cell area in *Lithophyllum racemus* (s1, s2), *Lithophyllum pseudoracemus* (s3, s4) and *Lithophyllum* cf. *racemus* (s5, s6). Statistically significant *p*-values are highlighted in bold. ANOVA test significance at $\alpha = 0.05$. Kruskal–Wallis test significance at $\alpha = 0.05$; Dunn's test significant at $p < \alpha/2$.

Kruskal-Wallis test (Perithallial cell area)

	Df	χ^2	P
Sample	5	88.104	$< \mathbf{2.2 \times 10^{-16}}$

Dunn's test
Comparisons by sample (Bonferroni)

Z *P*.adjusted	s4	s3	s1	s2	s5
s3	1.609				
	0.807				
s1	2.121	4.250			
	0.254	**0.000**			
s2	-5.464	-7.646	-3.996		
	0.000	**0.000**	**0.000**		
s5	-4.321	-6.290	-2.758	0.971	
	0.000	**0.000**	0.044	1.000	
s6	-4.076	-6.055	-2.467	1.284	0.291
	0.000	**0.000**	0.102	1.000	1.000

Table A.7: Statistical tests performed to evaluate the differences of the perithallial SC thickness in *Lithophyllum racemus* (s1, s2), *Lithophyllum pseudoracemus* (s3, s4) and *Lithophyllum* cf. *racemus* (s5, s6). Statistically significant p-values are highlighted in bold. ANOVA test significance at $\alpha = 0.05$. Tukey's test significance at $p \leq \alpha$.

One-way ANOVA test

(Perithallial SC thickness)

	Df	Sum sq.	Mean sq.	F value	Pr (F)
Sample	5	0.326	0.065	9.432	**0.000**
Residuals	251	1.735	0.007		

Shapiro-Wilk normality test	$P = 0.838$
Barlett's K squared	$P = 0.103$

Tukey's test

Multiple comparisons of means

Sample	Mean difference Sample	95% confidence interval lower bound	 upper bound	P.adjusted
s4-s1	-0.070	-0.116	-0.023	**0.000**
s3-s1	-0.031	-0.076	0.015	0.383
s2-s1	0.033	-0.022	0.088	0.509
s5-s1	0.021	-0.039	0.081	0.916
s6-s1	-0.053	-0.106	0.000	0.054
s3-s4	0.039	-0.005	0.083	0.110
s2-s4	0.103	0.049	0.156	**0.000**
s5-s4	0.091	0.032	0.150	**0.000**
s6-s4	0.017	-0.035	0.069	0.933

Table A.7 (continue)

s2-s3	0.064	0.011	0.116	**0.008**
s5-s3	0.052	-0.007	0.110	0.115
s6-s3	-0.022	-0.073	0.029	0.816
s5-s2	-0.012	-0.078	0.054	0.995
s6-s2	-0.086	-0.145	-0.026	**0.001**
s6-s5	-0.074	-0.138	-0.009	**0.015**

Table A.8: ^{11}B MAS NMR parameters in calcareous red algae. Trigonal boron (BO$_3$) in samples s8, s24, s25, s27, s28, s30, s31, s32 was simulated by a quadrupolar line shape characterized by a chemical shift (δ_{iso}, [ppm]), width and the quadrupolar coupling constant (C$_Q$, [MHz]). In all other cases, gaussian line shapes were used for simulations, solely characterized by a chemical shift and width. Relative proportions between BO$_3$ ad BO$_4$ are also indicated (mean ± SD %). The error bar is 0.2 ppm for δ_{iso}, 0.02 MHz for C$_Q$ and 1% for the proportion. Ambiguous signals are indicated as "n.c.".

Sample, site	**Species**	**BO$_3^{(1)}$**	**BO$_3^{(2)}$**	**BO$_4^{(1)}$**	**BO$_4^{(2)}$**	**n.c.**
s2, Pontian Isl.	*L. racemus*	17.4 ppm 42.9 %		1.5 ppm 11.7	2.6 ppm 45.4 %	
s3, Villasimius	*L. pseudoracemus*	17.9 ppm 38.0 %		0.3 ppm 12.1 %	1.7 ppm 49.9 %	
s4, Pontian Isl.	*L. pseudoracemus*	19.1 ppm 1.50 MHz 35.1 %			2.9 ppm 64.9 %	
s8, Morlaix	*L. corallioides*	17.0 ppm 32.3 %	11.2 ppm 13.1 %	0.4 ppm 10.6 %	1.8 ppm 44.0 %	
s12, Aegadian Isl.	*L. corallioides*	16.9 ppm 35.6 %		0.1 ppm 10.8 %	1.6 ppm 53.5 %	
s13, Elba	*L. corallioides*	17.4 ppm 38.3 %		0.7 ppm 17.1	2.3 ppm 44.6 %	

Table A.8 (continue)

Sample, site	**Species**	**BO$_3^{(1)}$**	**BO$_3^{(2)}$**	**BO$_4^{(1)}$**	**BO$_4^{(2)}$**	**n.c.**
s14, Pontian Isl.	*L. corallioides*	18.3 ppm 1.57 MHz 37.0 %		1.1 ppm 19.1 %	2.4 ppm 43.9 %	
s24, Polignano	*M. philippii*	16.6-20.3 ppm 38.2 %	11.3 ppm 16.5 %	0.2 ppm 8.5 %	1.6 ppm 36.8 %	
s25, Polignano	*L. crispatum*	17.0 ppm 21.7 %	10.6 ppm 34.7 %	0.4 ppm 8.7 %	1.5 ppm 28.8 %	6.1 ppm 6.1 %
s26, Villasimius	*L. minervae*	18.3 ppm 28.6 %		1.5 ppm 15.1 %	3.1 ppm 56.3 %	
s27, Elba	*L. minervae*	17.2 ppm 16.0 %	11.8 ppm 6.6 %	0.7 ppm 34.8 %	2.2 ppm 42.7 %	
s28, Pontian Isl.	*L. minervae*	16.8 ppm 22.3 %	11.1 ppm 14.6 %	0.4 ppm 17.3 %	1.7 ppm 45.7 %	
s29, Polignano	*L. stictiforme*	16.6 ppm 38.6 %			1.5 ppm 61.4 %	
s30, Pontian Isl.	*Peyssonnelia* sp.		12.9 ppm 63.9 %		2.9 ppm 28.2 %	7.7 ppm 7.8 %
s31, Pontian Isl.	*Peyssonnelia* sp.		13.6 ppm 1.56 MHz 41.7 %		2.9 ppm 48.5 %	7.7 ppm 9.8 %
s31*, Pontian Isl.	*Peyssonnelia* sp.	12.9 ppm 18.1 %		1.1 ppm 27.0 %	2.9 ppm 54.9 %	
s32, Villasimius	*Polystrata* sp.		13.3 ppm 1.01 MHz 9.6 %		2.9 ppm 82.7 %	7.2 ppm 7.7 %

*sample s31 after oxidation following the cleaning protocol in Section 2.6.2.

Appendix B

Peer-reviewed papers

diversity

MDPI

Article

Deep Learning Applied to SEM Images for Supporting Marine Coralline Algae Classification

Giulia Piazza [1,*], Cecile Valsecchi [1] and Gabriele Sottocornola [2]

[1] Department of Earth and Environmental Sciences, University of Milano-Bicocca, 20126 Milano, Italy; c.valsecchi18@campus.unimib.it
[2] Department of Information Science and Technology, Free University of Bozen-Bolzano, 39100 Bolzano, Italy; gabriele.sottocornola@stud-inf.unibz.it
* Correspondence: g.piazza15@campus.unimib.it

Abstract: The classification of coralline algae commonly relies on the morphology of cells and reproductive structures, along with thallus organization, observed through Scanning Electron Microscopy (SEM). Nevertheless, species identification based on morphology often leads to uncertainty, due to their general plasticity. Evolutionary and environmental studies featured coralline algae for their ecological significance in both recent and past Oceans and need to rely on robust taxonomy. Research efforts towards new putative diagnostic tools have recently been focused on cell wall ultrastructure. In this work, we explored a new classification tool for coralline algae, using fine-tuning pretrained Convolutional Neural Networks (CNNs) on SEM images paired to morphological categories, including cell wall ultrastructure. We considered four common Mediterranean species, classified at genus and at the species level (*Lithothamnion corallioides*, *Mesophyllum philippii*, *Lithophyllum racemus*, *Lithophyllum pseudoracemus*). Our model produced promising results in terms of image classification accuracy given the constraint of a limited dataset and was tested for the identification of two ambiguous samples referred to as *L.* cf. *racemus*. Overall, explanatory image analyses suggest a high diagnostic value of calcification patterns, which significantly contributed to class predictions. Thus, CNNs proved to be a valid support to the morphological approach to taxonomy in coralline algae.

Keywords: machine learning; CNNs; SEM images; coralline algae; taxonomy; ultrastructure; *Lithophyllum pseudoracemus*

check for updates

Citation: Piazza, G.; Valsecchi, C.; Sottocornola, G. Deep Learning Applied to SEM Images for Supporting Marine Coralline Algae Classification. *Diversity* **2021**, *13*, 640. https://doi.org/10.3390/d13120640

Academic Editor: Márta Ladányi

Received: 21 October 2021
Accepted: 30 November 2021
Published: 3 December 2021

1. Introduction

Calcareous red algae belong to the phylum Rhodophyta and include a multitude of diverse marine species, acknowledged for their ecological importance as ecosystem engineers [1–4]. They are common in Mediterranean benthic communities, constituting biodiversity hotspots known as maerl beds and coralligenous habitats [2,5,6].

Species identification in this taxon can be challenging. A reliable taxonomy is imperative, especially for paleontologists, in the attempt to reconstruct both the paleoecology and the paleoclimate [7–10]. Thallus organization and the morphological characteristics of cells and reproductive structures are generally used to discriminate among species [11–14], either by light microscopy of thin sections or by high-resolution Scanning Electron Microscopy (SEM) [15]. Nevertheless, the increasing application of molecular systematic tools has been revealing many cases of cryptic diversity and has given way to several systematic revisions [16–20]. Recent investigations into coralline algal cell walls and their calcified nanostructures embrace the hypothesis that a biological control exerted by the alga drives the crystallite shape [21]. Particularly, the shape of the nanostructures composing the so-called primary and secondary calcification is diagnostic at the level of family [21].

Recently, a new species of non-geniculate coralline alga, *Lithophyllum pseudoracemus* sp. nov. Caragnano, Rodondi & Rindi, was discovered by molecular phylogeny [16]. Due to their morphological similarity, an expert cannot unequivocally distinguish this species from *Lithophyllum racemus* (Lamarck) Foslie 1901 [16,22]. Common in the Mediterranean Sea, *L. racemus* usually constitutes maerl beds [23,24]. It is a non-geniculate, fruticose alga with many protuberances densely spaced and apically broadened [22]. It is often found in association with *Lithothamnion corallioides* (P. Crouan & H. Crouan) P. Crouan & H. Crouan 1867 [25–30], which grows in the form of free-living branchlets or nodules, often sterile [31]. Another common species of coralline alga in Mediterranean waters is *Mesophyllum philippii* (Foslie) Adey 1970, which is one of the main bioconstructors of the Mediterranean coralligenous concretions, occurring in the form of layered crusts [32], sometimes with protuberances.

Convolutional Neural Networks (CNNs) have been successfully applied for the classification of fish species [33,34], bivalves [35] and foraminifera [36]. In such cases, the classified images were photographs of the entire organism. Liu and Song [37] used fine-tuning on pretrained CNNs for the recognition of different taxonomic groups of microfossils observed in thin sections and obtained a model accuracy comparable to human classifiers. To the best of our knowledge, the application of CNNs to SEM images has never been used for taxonomic identification, and there are no previous attempts to classify calcareous red algae by CNNs. Indeed, Modarres et al. [38] used CNN for SEM image recognition of generic nanostructures, mostly of non-biological origin. Given their morphological plasticity, new diagnostic tools for species identification could provide significant support to the experts, especially for fossil samples with poorly preserved morphological features.

In this work, we used CNNs to classify a set of SEM images belonging to the calcareous red algae *L. corallioides*, *M. philippii*, *L. racemus*, and *L. pseudoracemus*. The models were enriched by processing each image together with the vectorized representation of the observed morphological features (or categories). Six relevant morphological categories were considered, which were manually paired to each image (Figure 1). Three models were trained on the same images, which were grouped at different taxonomic levels to:

1. Discriminate *L. pseudoracemus* from all the other species (2 class-CNN);
2. Classify the three genera (3 class-CNN);
3. Classify the four species (4 class-CNN).

Finally, we tested the model potential as a diagnostic tool for the classification of two uncertain samples, non-molecularly identified and generically referred to as *L.* cf. *racemus*. The experimental results proved that the proposed CNN-based approach could potentially support and improve the expert capability in the taxonomic identification of diverse calcareous red algal species. Thus, we summarize the contribution of this research as follows:

1. We presented a new classification tool for coralline algae diagnosis, by applying a deep learning technique to SEM images for the automated identification of four species at different taxonomic levels;
2. We developed and evaluated CNN-based classification models (open-sourced on GitHub as reported in the Data Availability Statement) against two baselines, namely a dummy classifier and a human-reported classification. Then, our model was tested in a practical scenario, to support the classification of two uncertain samples of coralline algae;
3. We investigated and discussed the contribution of six main morphological categories, shown in the SEM images, to the classification task;
4. We explored a set of explanation methods, which justify the class assignment of the proposed model by visually highlighting the contribution of portions of the processed SEM image.

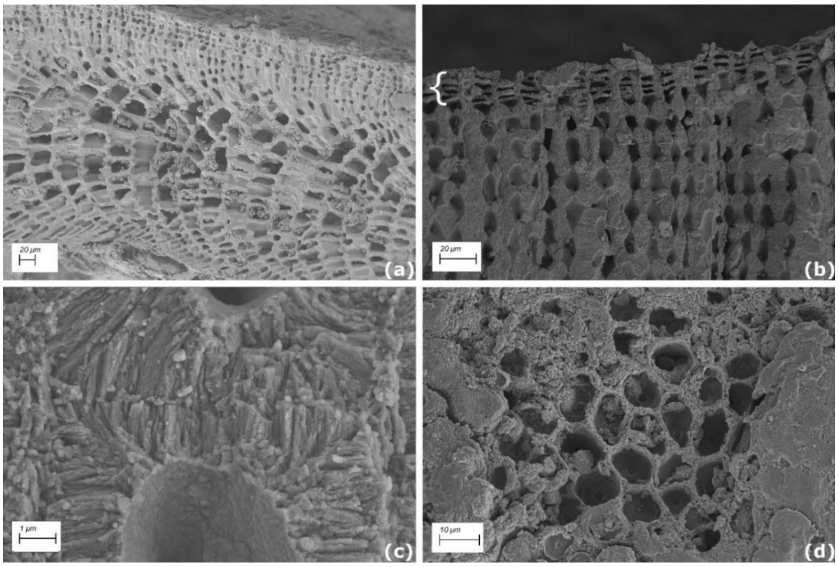

Figure 1. SEM images showing: (**a**) a longitudinal section through *Mesophyllum philippii* coaxial hypothallus assigned to the hypothallus category; (**b**) a longitudinal section through *Lithophyllum racemus* epithallus (curly bracket) with the underlying perithallus assigned to both perithallus and epithallus categories; (**c**) a magnification of *L. racemus* perithallial cells showing crystallites composing the cell walls (crystallites category); (**d**) a *Lithophyllum pseudoracemus* sample in surface view (surface category).

2. Materials and Methods

2.1. Samples and Data Collection

Samples were collected at different locations in the Western and Eastern Mediterranean Sea, and one sample was collected from the NE Atlantic Ocean (Table 1). They were recovered by grab during the cruises of the R/V Minerva Uno, in the framework of the Marine Strategy Campaigns, or by SCUBA diving during local surveys. The sample from Capraia, Tuscany (Italy) was collected in the framework of "Taphonomy and Sedimentology on the Mediterranean shelf " project. A total of eleven specimens were selected, at least two for each species considered (Table 1).

Species identification for *Lithothamnion* sp. and *Mesophyllum* sp. was assessed by morphological analyses of the SEM images. Two samples (iv1, iv2 in Table 1) were identified as *L. corallioides* [31,39]. Three more samples (iv3–5) (Table 1) were identified as *M. philippii* [13,32]. Four samples (iv6–9) (Table 1) were targeted for a multigene molecular phylogeny at Università Politecnica delle Marche (AN) [16], and are currently deposited in the Herbarium Universitatis Florentinae, Natural History Museum (Florence, Italy) with codes FI058894, FI058887, FI058890 and FI058891. They were identified as *L. racemus* (samples iv6, iv7 in Table 1) and *L. pseudoracemus* (samples iv8, iv9 in Table 1). The last two samples considered (DB865 and DB866) (Table 1) were referred to as *L.* cf. *racemus* [22], since they were not molecularly identified, and, thus, they could be used as a real-case test study.

Table 1. Summary of the samples used, site of collection, and the number of SEM images per sample.

Sample	Species	Sampling Site (Latitude, Longitude)	Images (n)
iv1	*Lithothamnion corallioides*	Villasimius, Sardinia (Italy) (39°08′32″ N, 9°31′14″ E)	24
iv2		Morlaix, Brittany (France) (48°34′42″ N, 3°49′36″ W)	25
iv3	*Mesophyllum philippii*	Portofino, Liguria (Italy) (44°17′56″ N, 9°13′08″ E)	11
iv4		Capraia, Tuscany (Italy) (43°01′04″ N, 9°46′26″ E)	14
iv5		Cavoli Island, Sardinia (Italy) (39°05′20″ N, 9°32′33″ E)	16
iv6	*Lithophyllum racemus*	Pontian Islands (Italy) (40°54′47″ N, 12°52′58″ E)	24
iv7		Capri, Gulf of Naples (Italy) (40°34′08″ N, 14°13′32″ E)	43
iv8	*Lithophyllum pseudoracemus*	Pontian Islands (Italy) (40°11′43″ N, 12°53′07″ E)	9
iv9		Villasimius, Sardinia (Italy) (39°08′32″ N, 9°31′14″ E)	48
DB865	*Lithophyllum* cf. *racemus*	Santa Catarina, Rovinj (Croatia) (45°04′32″ N, 13°37′38″ E)	28
DB866		Torre dell'Orso, Puglia (Italy) (40°14′00″ N, 18°28′00″ E)	13

The selected algae were cleaned of sediment and epiphytes, and then prepared for SEM as per Basso [12]. Samples were fragmented along the growth direction to observe morphologies in longitudinal sections, they were mounted on stubs by means of graphite paste, and finally, chrome coated. SEM analysis was performed by a Field Emission Gun Scanning Electron Microscope (SEM-FEG) Gemini 500 Zeiss (Milan, Italy).

The final dataset included 255 SEM images, belonging to the eleven samples listed in Table 1. The images had a resolution of 2046 × 1369 pixels in greyscale (single channel). Furthermore, each image in the dataset was assigned to one or more categories (i.e., conceptacles, perithallus, crystallites, epithallus, hypothallus and surface) according to the morphological features observed (Figure 1), and each category information was added as metadata. Among those, 21 images were assigned to more than one category since they present multiple structures together. Ten images, including those showing details of the conceptacle pore canal (Figure A1), were not attributed to any specific category.

2.2. Data Augmentation

To increase the number of images, and, hence, improve the variance of the available training set, an 'on-the-fly' realistic data augmentation [40] was performed. Namely, during model training, each image in the training set was duplicated five times, each time with some random changes according to the following criteria: a random change in brightness in the range [0.5, 1.8], a random rotation up to 10 degrees, a random zoom to a maximum of 0.7, and a random horizontal flip. Figure 2 shows eight examples of augmented images obtained from the original image located in the upper left corner. The criteria were chosen to obtain realistic augmented images, i.e., images compatible with SEM images.

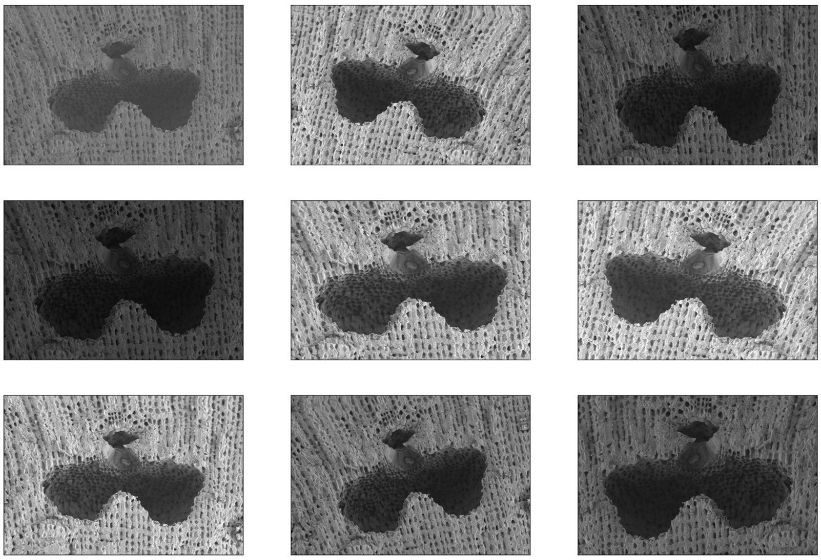

Figure 2. Examples of augmented images of a *Lithophyllum racemus* conceptacle given the original image in the first position (upper left).

2.3. Convolutional Neural Networks

Classification (or, more formally, supervised classification) is the specific area of machine learning that aims at assigning objects to one of several predefined classes. In our case, the objects, i.e., the input of classification, are represented by images associated with categorical metadata (i.e., morphological features), while the classes are the considered species or genera. Artificial neural networks are popular machine learning algorithms whose goal is to determine the set of weights (i.e., the edges connecting neurons of the network) that minimize a defined loss function over the predicted classes and the real classes [41]; this is achieved by an iterative process which alternated a feedforward step, in which weights connecting different layers are used to compute the output (i.e., the predicted classes), to a backpropagation step, whose aim is to adjust the weights by computing the gradient of the loss function. Deep learning usually refers to artificial neural networks with more than two hidden layers.

In the image classification context, deep learning avoids the time-consuming and challenging feature extraction process which is required for other classification methods (such as SVM and kNN) [42,43]. Indeed, deep learning provides end-to-end learning and eliminates all extra overheads of selecting feature descriptors and feature selection by automatically extracting information from the raw data. In particular, Convolutional Neural Networks (CNNs) have become the state-of-the-art image recognition method [44].

Several different variations in CNN architectures have been applied, but in general, they consist of stacked convolutional and pooling layers, followed by one or more fully connected layer(s). The convolutional layers are the core of CNNs and are based on a set of trainable filters or kernels; basically, they can be seen as a pattern extractor. The inputs are convolved over those filters, whose weights are optimized in the training phase to obtain a new representation of the original images, i.e., a new feature map. The pooling layer reduces these feature maps through information compression, usually keeping the maximum value (i.e., maxpooling layer). Convolutional and pooling layers are followed by fully connected or dense layers, which consist of neurons connected to all the neurons of the previous and following dense layers. For classification purposes, the number of neurons in the output layer is equal to the number of classes to be predicted, and each of these neurons provides as output the probability that the image belongs to the corresponding class.

CNNs are data-hungry; that is, they need to be trained on a huge number of training images [44]. Thus, for small datasets (i.e., less than a thousand images) it is convenient to start from a pretrained network, which is a CNN whose weights have been already trained on thousands of images [45,46]. Unlike random weights, the weights of a pretrained CNN have been already trained to distinguish some simple and common geometrical patterns. Typically, the last fully connected layer of the pretrained CNN will be substituted to obtain the desired output, which may imply a different number of classes. Then, the CNN can be trained on the images of interest, and depending on the training procedure, we can speak of transfer learning and/or fine-tuning. In the former case, all or only some layers of the CNN will be trained on the images of interest for a few numbers of epochs, while the latter involves the tuning of some hyperparameters (such as the learning rate) to adapt the network to the new classification purpose.

We adapted and fine-tuned a deep neural network named Visual Geometry Group 16 (VGG16) [47] pretrained on the "imagenet" dataset [48], which includes 14 million images belonging to 1000 classes. Figure 3 depicts the adapted VGG16 architecture, which is constituted by:

1. An input layer of fixed size 224 × 224 Red-Green-Blue image;
2. A stack of convolutional layers, where the filters were used with a very small receptive field: 3 × 3;
3. Five maxpooling layers (not all the convolutional layers are followed by max-pooling);
4. A dense layer, whose input is the output of the previous maxpooling layer and concatenated with the one-hot-encoded categories, and;
5. A softmax output layer.

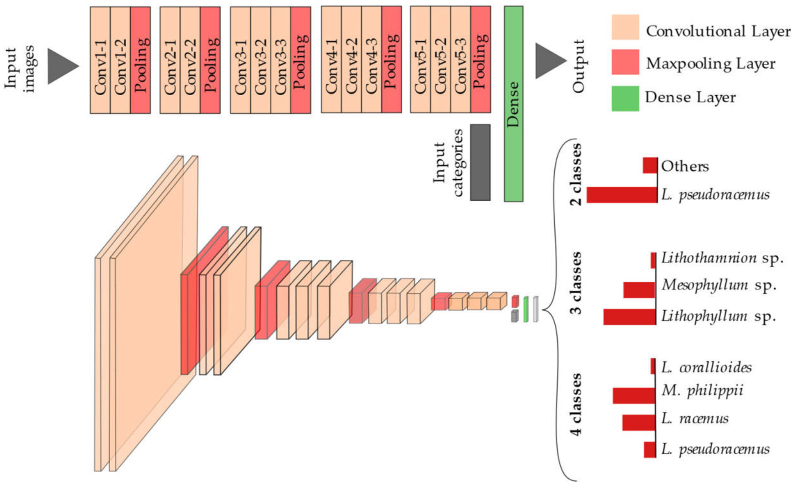

Figure 3. Adapted architecture from Visual Geometry Group 16 (VGG16).

All hidden layers, i.e., the layers between the input and the output layers, are equipped with the ReLU activation function [47,49]. VGG16 architecture is particularly suited for the recognition of geometries, which makes it effective for our application since the shape of cells and reproductive structures is one of the most significant parameters for species identification in coralline algae. In a preliminary analysis, we further considered a set of other CNN-based architectures (namely ResNet50, InceptionV3, MobileNet), where the VGG16 resulted as the most promising approach in terms of diagnostic accuracy.

We resized our sampled SEM images and replicated the same greyscale image for the three RGB channels, to be injected into the input layer. All the convolutional layers' parameters of the original VGG16 are kept frozen (i.e., are not modified during the learning procedure), while we trained the last dense layer and the output layer of our specific classification tasks. Furthermore, we added a new input layer constituted by six neurons, mapping the one-hot encoded representation of the morphological features observed in each image, and directly connected with the dense layer.

Formally, given an image x with a morphological categories vector c, each output neuron o_g, associated to algae class g, is computed as:

$$o_g = softmax\left(\sum_i W^o_{i,g} d_i\right);\ d_i = \mathrm{ReLU}\left(\sum_j W^d_{j,i} h_j + \sum_l W^d_{l,i} c_l\right),$$

where d_i is the i-th component of the dense layer, h_j is the j-th component of the image x representation provided by the last maxpooling layer of VGG16, and c_l is the l-th component of the one-hot encoded category input layer. W^d and W^o are the matrices of weights learned by the model for the dense and output layers respectively.

We stress the fact that the softmax function, applied to the output layer, projects the output in the interval [0, 1], such that $o_g = \mathrm{P}(g \mid x, c)$ for each class g. The predicted class $\hat{g}$ is hence assigned to the class g with the highest probability.

Since *L. pseudoracemus* and *L. racemus* are almost undistinguishable from a traditional morphological approach [16], the difficulty of the classification task changed according to the taxonomic level considered. Therefore, we constructed the following three architectures addressing different classification tasks, each grouping the SEM images at diverse levels (as shown in Figure 3):

1. 2 class-CNN (*L. pseudoracemus* versus Others, i.e., all the other species), last dense layer of 128 neurons, output layer of two neurons;
2. 3 class-CNN, at the genus level (*Lithothamnion* sp., *Mesophyllum* sp. and *Lithophyllum* sp.), last dense layer of 256 neurons, output layer of three neurons;
3. 4 class-CNN, at the species level (*L. corallioides*, *M. philippii*, *L. racemus* and *L. pseudoracemus*), last dense layer of 64 neurons, output layer of four neurons.

For all three architectures, the number of epochs was set to 20 and the learning rate to 10^{-5}.

We optimized the VGG16 hyperparameters, i.e., the number of neurons in the last hidden dense layer, the training epochs and the learning rate in order to obtain suitable weights for the problem under study. As per common practice, the best hyperparameters were chosen according to the highest performance in cross-validation [50]. In addition, we used a weighted class assignment, in which the class contributions are inversely proportional to the different representativeness of the classes.

2.4. Interpretability

Despite widespread adoption, CNNs are often considered as black boxes, because the interpretation of the model predictions is not trivial. However, understanding the reasons behind predictions is a matter of intuition, which is fundamental to act based on the prediction. In order to make CNNs replicable, different approaches belonging to the so-called explainable artificial intelligence were developed, i.e., local approximations of the model's behavior. In this work, we considered three approaches: Saliency [51], LIME [52] and Grad-CAM [53].

As explained in [51], the computing of the gradient of an output class with respect to an input image provides information on how the output class value changes with respect to a small change in input image pixels. All the positive values in the gradients tell us that a small change to that pixel will increase the output value. Hence, a saliency map is the visualization of these gradients, which have the same shape as the image and provide an intuition of the information learned by the model.

Local Interpretable Model-Agnostic Explanation (LIME) [52] is a model-independent explanation technique that attempts to explain the model by perturbing the input samples and understanding how these perturbations affect the predictions. Given an input image, LIME masks random regions of the image to define their importance for the CNN prediction.

Like Saliency, Gradient-weighted Class Activation Mapping (Grad-CAM) also uses the class-specific gradient, but in this case, considers the final convolutional layer of a CNN to produce a coarse location map of important regions in the image [53].

We applied these explanation techniques to the sampled SEM images to obtain different explained overlays. Thus, they were evaluated according to their meaningfulness and helpfulness for the classification task.

The CNNs and the explanation models were built by means of Keras [54], Keras Vis [55] and Lime [52] packages with TensorFlow [56] backend in Python v3.6.

2.5. Evaluation Protocol

To extensively evaluate the effectiveness of our approach for the task of coralline algae classification, we considered two different setups.

In the first one, *Internal Validation*, we measured the capability of the model in identifying the correct class for each image involved in the study. For this purpose, we selected only the images belonging to the samples for which a sure diagnosis is given as ground truth (based on morphology and molecular phylogeny, as described in Section 2.1). Thus, we excluded the images referred to the *L.* cf. *racemus* samples (i.e., DB865 and DB866). We ended up with a dataset of 214 tagged SEM images. In order to consider the whole set of images while avoiding overfitting, we applied a *k*-fold cross validation approach [50]. Specifically, we considered a four-fold cross validation, in which the original dataset was partitioned into four disjoint sets (i.e., folders). In each round, a folder was used as a validation set (on which classification metrics were computed), while the other folders were used to train the model. The procedure iterated until all the folders (and thus all the images) were used for validation. Furthermore, we compared the performances obtained by the CNN models with average baselines produced by dummy classifiers, whose random predictions (repeated 1000 times) follow the *a priori* class distribution, and with a human classifier, required to diagnose each SEM image considered in *Internal Validation*. Specifically, a post-doc researcher in paleoecology at Milano-Bicocca University was invited to identify the species shown in each SEM image (previously anonymized and shuffled), by filling a multiple-choice questionnaire, and relying on scientific experience and provided literature [13,16,22,31,32,39]. The comparison between the model and the expert's performances allowed us to evaluate the practical usefulness of our method in supporting the classification task [57,58].

We applied two well-defined classification metrics to evaluate the performance of our model, namely *Global Accuracy* and *Class Recall* [50]. For each model, the *Global accuracy* is the fraction of correctly predicted images in cross validation, while *Class Recall* for the g-th class is the fraction of correctly predicted images of the sample belonging to class g in cross validation. The *Class Recall* fractions were also given for each morphological category, added as metadata (Figure 1).

In the second setup, *External Test*, we tested our model in a simulated scenario, namely, where an expert is required to identify the correct classes (i.e., genus or species) of new unknown samples of coralline algae. We simulated this case study by training our CNN classification model on the whole set of 214 tagged SEM images, then we applied the model to each image belonging to the *L.* cf. *racemus* samples DB865 and DB866. Therefore, we can measure the *Class Share* (*CS*) of each class g, for a specific sample s, as follows:

$$CS_s(g) = \frac{1}{N_s}\sum_{n=1}^{N_s} \delta_n \; where \; \delta_n = \begin{cases} 1, \; if \; \hat{g}_n = g \\ 0, \; otherwise \end{cases},$$

where N_s is the number of SEM images belonging to sample s, δ_n is equal to 1 if the n-th image of sample s is assigned to class g (i.e., the predicted class $\hat{g}_n$ is equal to g) by our classification model and 0 otherwise. Furthermore, the *Class Share* per category was computed on the different subsets of SEM images assigned to each morphological category (Figure 1).

3. Results

3.1. Internal Validation

In Table 2, we report the results for the *Internal Validation* procedure compared to the results provided by dummy and human classifiers.

Table 2. Model performances in the 3 classification tasks: *L. pseudoracemus* versus the other species (2 classes); diverse genera (3 classes) and diverse species (4 classes). The *Global accuracy* is shown, as well as the *Class Recall* for each class for the proposed approach (CNN), for the human classifier (HC) and dummy classifiers (DC).

2 classes				**3 classes**				**4 classes**			
	Class Recall				*Class Recall*				*Class Recall*		
	CNN	HC	DC		CNN	HC	DC		CNN	HC	DC
L. pseudoracemus	0.61	0.21	0.27	*Lithothamnion* sp.	0.55	0.73	0.23	*L. corallioides*	0.57	0.73	0.23
Others	0.62	0.92	0.73	*Mesophyllum* sp.	0.56	0.41	0.19	*M. philippii*	0.49	0.41	0.19
				Lithophyllum sp.	0.69	0.42	0.58	*L. racemus*	0.46	0.33	0.31
								L. pseudoracemus	0.37	0.21	0.27
Global accuracy	0.61	0.73	0.62		0.64	0.49	0.43		0.48	0.40	0.27

The global cross-validation accuracy was similar in the 2 class-CNN (*L. pseudoracemus* versus Others) and in the 3 class-CNN (genus level), despite the increased difficulty in the task, given the higher number of classes (three rather than two) and thus, data sparsity. The highest classification accuracy was in fact achieved by the 3 class-CNN (accuracy 64%), and the lowest by the 4 class-CNN (species level), with an accuracy of 48% (Table 2).

With respect to the *Class Recall*, in the 2 class-CNN we observe a significant improvement in the identification of *L. pseudoracemus* (61% against the 27% of the dummy baseline and the 27% of the human classifier), despite registering a decrease in the *Recall* for Others, and in the *Global accuracy*, compared to expert evaluation.

For both 3 and 4 class-CNNs the *Global accuracy* and all the *Class Recall* were higher than both the baselines, except for *Lithothamnion* sp. (or *L. corallioides*), where a 55% and 57% *Recall* is achieved, against the 73% of the human classifier. Nevertheless, our models significantly outperform the expert classification on the *Recall* of the two other classes (with a maximum of +27% for *Lithophyllum* sp. *Recall*) and *Accuracy* (+15%). Furthermore, the two genera *Lithothamnion* and *Mesophyllum* were classified by our model with a *Recall* that is more than twice as high as the dummy classifier. Similar observations can be drawn from the *Recall* at the species level (4 class-CNN). Another interesting finding is that the *Lithothamnion* genus is predicted slightly better at the species level (i.e., *L. corallioides*), with an increased *Recall* from 55% to 57%, despite having a sparser classification task. The classification of *L. racemus* and *L. pseudoracemus* in the 4 class-CNN corresponded to the most difficult task due to their morphological similarity, and our analysis, as well as the empirical evidence of human evaluation, was in line with the domain-related studies. In fact, both at genus and species levels the increment in *Recall* was consistently between the 10% and 15%, compared to the dummy classifiers' baseline. *L. pseudoracemus* in the 4 class-CNN was the most difficult class to be identified by our model, with the lowest *Recall* of 37%. Compared to the model, the human performances showed a better in *Recall* limitedly to *L. corallioides* class, while all the other classes at both genus and species levels had a notably lower *Recall*. Concluding, our CNN-based models outperformed the human diagnosis at both genus and species level *Global accuracy*, as well as in the *Recall* of the hardest distinguishable classes, *L. racemus* and *L. pseudoracemus*, proving the effectiveness of our technique in support of coralline algae classification.

Finally, the 3 class-CNN thus appeared to be the best model for coralline algae classification, with the highest *Global accuracy* and solid *Class Recall* for each genus. Nevertheless, it would be convenient to adopt the 4 class-CNN model when a more fine-grained diagnosis (i.e., at species level) is required. This model, indeed, despite the smaller *Global accuracy*, could include more classes and still provide reasonable support for classification even in the occurrence of very similar classes, such as *L. pseudoracemus* and *L. racemus*.

Morphological Categories Analysis

Table 3 is a summary of the results of *Class Recall* for each class and each modeling approach conditioned on the morphological category represented in the image.

Table 3. The total number of SEM images in each class (columns) and categories (rows) according to the three modeling approaches (*L. pseudoracemus* versus other species, diverse genera, and diverse species) is listed, together with the *Class Recall*. Images not assigned to a category (n.c.) and showing more than one category (shared) are also included.

2 class-CNN				
	L. pseudoracemus		Others	
Category	Images (n)	*Class Recall*	Images (n)	*Class Recall*
conceptacles	1	1.00	9	0.56
perithallus	7	0.14	32	0.53
crystallites	27	0.70	67	0.61
epithallus	10	0.70	24	0.71
hypothallus	0	-	3	0.67
surface	5	0.60	7	0.57
n.c.	2	1.00	4	0.75
shared	5	0.40	11	0.73

3 class-CNN						
	Lithothamnion sp.		*Mesophyllum* sp.		*Lithophyllum* sp.	
Category	Images (n)	*Class Recall*	Images (n)	*Class Recall*	Images (n)	*Class Recall*
conceptacles	0	-	4	0.75	6	0.67
perithallus	20	0.65	3	0.33	16	0.44
crystallites	14	0.57	13	0.38	67	0.85
epithallus	12	0.42	5	0.20	17	0.47
hypothallus	0	-	3	0.67	0	-
surface	2	0.50	4	0.50	6	0.17
n.c.	0	-	1	1.00	5	0.80
shared	1	0.00	8	1.00	7	0.57

4 class-CNN								
	L. corallioides		*M. philippii*		*L. racemus*		*L. pseudoracemus*	
Category	Images (n)	*Class Recall*	Images (n)	*Class Recall*	Images (n)	*Class Recall*	Images (n)	*Class Recall*
conceptacles	0	-	4	1.00	5	0.80	1	1.00
perithallus	20	0.60	3	0.33	9	0.22	7	0.00
crystallites	14	0.71	13	0.00	40	0.48	27	0.37
epithallus	12	0.50	5	0.20	7	0.57	10	0.70
hypothallus	0	-	3	0.67	0	-	0	-
surface	2	0.00	4	0.75	1	0.00	5	0.40
n.c.	0	-	1	1.00	3	0.33	2	0.00
shared	1	0.00	8	1.00	2	0.50	5	0.20

As shown in Table 3, considering *L. pseudoracemus*, the 2 class-CNN correctly recognized all the images showing the conceptacle and 70% of crystallites and the epithallus. On the other hand, only 14% of the images of the *L. pseudoracemus* perithallus were assigned to the correct class. Within the class including all the species except for *L. pseudoracemus* (Others), the percentages of images correctly identified were balanced among classes with an average accuracy of 64%. Overall, about 61% of the SEM images in both classes had been correctly classified, despite the class Others had almost three times more images than *L. pseudoracemus* (Table 3). The images with no category (n.c.) were mostly assigned to the correct class, as well as the images within the class, others showed more than one category (shared), which included five images showing the hypothallus, two images showing both epithallus and perithallus and one image showing both perithallus and crystallites. The n.c. images in both classes included the conceptacle pore canal and the perithallus with crystallites in the proximity of the pore canal in *L. racemus* (Figure A1) and *L. pseudoracemus*.

Among genera, *Lithophyllum* sp. had the highest percentage of images correctly classified (69%). The identification of conceptacles, when present, was still significant for the correct classification, as well as the perithallus in *Lithothamnion* sp. and the crystallites in both *Lithothamnion* sp. and *Lithophyllum* sp. (Table 3). In *Mesophyllum* sp., the only genus showing the hypothallus, this contributed significantly to the identification with 67%

of correct assignations. In the 3 class-CNN models as well, the non-categorized images have been of significant support to the correct classification (Table 3). The shared images correctly identified as *Mesophyllum* sp. included five images of the hypothallus, three of which also show the conceptacle, and two showing also the epithallus. The n.c. images correctly identified in the *Lithophyllum* sp. class included the pore canal of a conceptacle in the *L. pseudoracemus*, the perithallial cells and crystallites at the proximity of the same pore canal, and the pore canals in two different conceptacles of *L. racemus* (Figure A1).

Conceptacles were determinants for the identification of the algae also at the species level (Table 3). The perithallus, instead, aided only the classification of *L. corallioides* (with 60% of correct assignations), in which also the crystallites made a significant contribution (71%). The images showing the epithallus were mostly correctly classified in *L. pseudoracemus* (70%) and misclassified in *M. philippii* (20%). As for the 3 class-CNN, also in the 4 class-CNN the hypothallus was a significant contributor for the classification of *M. philippii* (67%), as well as the images showing the surface (75%). All the shared images in *M. philippii* were correctly classified, corresponding to those described for the 3 class-CNN.

The SEM images showing conceptacles were the major contributors to the success of the classification task in each model (Figure 4). Except for the 4 class-CNN, the exact classification was significantly favored by crystallites as well, which represented almost half of the total number of SEM images in the dataset (Table 3, Figure 4). In the 2 class-CNN, besides crystallites and conceptacles, high percentages of images correctly classified were achieved by the epithallus (71%, the highest value), and the hypothallus. Conversely, in the 3 class-CNN, the epithallus, together with the surface, led to the most incorrect classifications (Figure 4). Crystallites further increased in significance, as well as conceptacles. In the 4 class-CNN, the accuracy decreased and a reduced number of images showing the perithallus, the surface and the crystallites had correctly been classified (Figure 4). Conceptacles represented the most robust category for the classification success (90% of images correctly classified), together with the hypothallus which kept the same significance across models (67%).

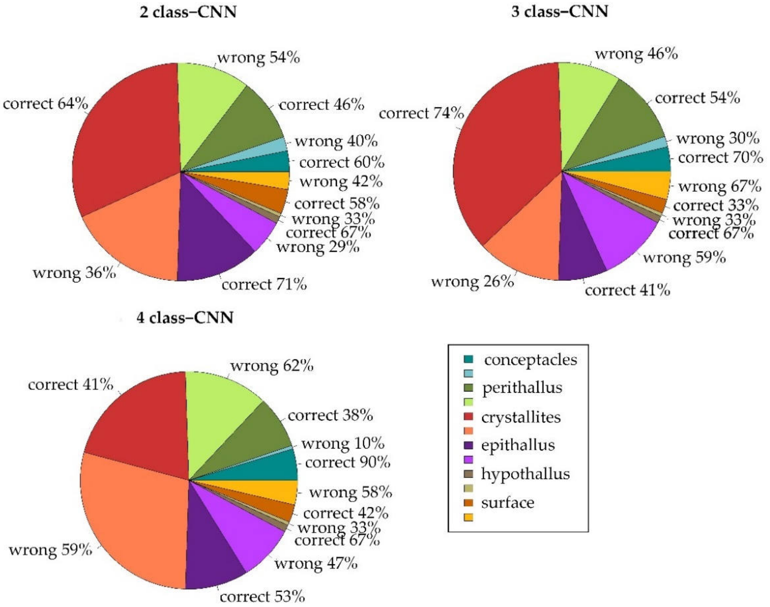

Figure 4. Total number of SEM images assigned to different categories that have been classified in the 2, 3 and 4 class-CNNs. Percentages within each category indicate the proportion between images correctly and wrongly classified.

3.2. External Test

In Table 4, we show the *Class Share* for the two test samples, namely DB865 and DB866. Considering the 2 class-CNN model, we notice how the two samples are classified in a similar way by identifying around 70% of the images in both samples belonging to the Others class. This approach seems to suggest that the two samples do not belong to the *L. pseudoracemus* class.

Table 4. *Class Share* for the *L.* cf. *racemus* samples (DB865, DB866) in the 3 classification tasks: *L. pseudoracemus* versus Others (2 class-CNN), diverse genera (3 class-CNN), and diverse species (4 class-CNN).

	2 class-CNN	
	Sample DB865	Sample DB866
L. pseudoracemus	0.32	0.31
Others	0.68	0.69
	3 class-CNN	
	Sample DB865	Sample DB866
Lithothamnion sp.	0.18	0.00
Mesophyllum sp.	0.00	0.08
Lithophyllum sp.	0.82	0.92
	4 class-CNN	
	Sample DB865	Sample DB866
L. corallioides	0.18	0.08
M. philippii	0.00	0.08
L. racemus	0.50	0.54
L. pseudoracemus	0.32	0.30

In the 3 class-CNN approach, the model is convincing in assigning the images of the two samples to the *Lithophyllum* genus. Specifically, for the DB866, more than 90% of the images are classified in that class, while for DB865 around 80% of the images are classified as *Lithophyllum* sp., and the remaining 20% to *Lithothamnion* sp. class.

Finally, in the 4 class-CNN, species level classification, again there is a high similarity between the two samples. In both cases, DB865 and DB866 images are assigned to *L. racemus* (around 50%) and *L. pseudoracemus* (around 30% each), while 20% of DB865 are identified as belonging to the *L. corallioides* species and less than 10% of the images are assigned to the *L. corallioides* and *M. philippii* for sample DB866. The highest *Class Share* is achieved by the *L. racemus* class with 54% (sample DB866).

These findings are in line with the expert evaluation of samples DB865 and DB866, which were identified as *L.* cf. *racemus*, being impossible to clearly discriminate between *L. racemus* and *L. pseudoracemus* without molecular data. Nevertheless, the 4 class-CNN model favored the *L. racemus* class over *L. pseudoracemus* (around 50% versus 30%).

Morphological Categories Analysis

In the 2 class-CNN most of the SEM images showing the *L.* cf. *racemus* samples DB865 and DB866 were classified in the class Others, with very similar percentages (68% and 69%, respectively as shown in Table 4). All the conceptacles were assigned to this class, as well as most of the images showing crystallites and the epithallus, with a lower percentage for the crystallites in sample DB866 (67%) (Tables 5 and 6). Most of the images showing the perithallus were rather classified as *L. pseudoracemus*, this is particularly true in the sample DB866. In this sample, also the image showing the surface was assigned to *L. pseudoracemus* class (Table 6). The n.c. images showing the perithallial cells in the proximity of a pore canal in sample DB865 have been assigned to the Others class. In sample DB865, an image showing both the epithallus and the crystallites was identified as belonging to *L. pseudoracemus* (Table 5).

Table 5. The *Class Share* of sample DB865 has been reported for each assigned category (rows) and class (columns). The total number of SEM images in every predicted class of the three models (*L. pseudoracemus* versus other species, genus level and species level) are listed. Images not assigned to a category (n.c.) and showing more than one category (shared) are also included.

DB865		**2 class-CNN**	
Category	Images (n)	*L. pseudoracemus*	Others
conceptacles	1	0.00	1.00
perithallus	3	0.67	0.33
crystallites	12	0.17	0.83
epithallus	5	0.20	0.80
hypothallus	0	-	-
[1] surface	2	0.50	0.50
n.c.	2	0.50	0.50
shared	3	0.67	0.33

		3 class-CNN		
Category	Images (n)	*Lithothamnion* sp.	*Mesophyllum* sp.	*Lithophyllum* sp.
conceptacles	1	1.00	0.00	0.00
perithallus	3	0.33	0.00	0.67
crystallites	12	0.00	0.00	1.00
epithallus	5	0.40	0.00	0.60
[1] surface	2	0.50	0.00	0.50
n.c.	2	0.00	0.00	1.00
shared		0.00	0.00	1.00

			4 class-CNN		
Category	Images (n)	*L. corallioides*	*M. philippii*	*L. racemus*	*L. pseudoracemus*
conceptacles	1	0.00	0.00	1.00	0.00
perithallus	3	0.33	0.00	0.00	0.67
crystallites	12	0.00	0.00	0.83	0.17
epithallus	5	0.80	0.00	0.20	0.00
[1] surface	2	0.00	0.00	0.50	0.50
n.c.	2	0.00	0.00	0.50	0.50
shared	3	0.00	0.00	0.00	1.00

[1] no hypothallus in the sample DB865.

Table 6. The *Class Share* of the sample DB866 was reported for each assigned category (rows) and class (columns). The total number of SEM images in every predicted class of the three models is listed. Images not assigned to a category (n.c.) and showing more than one category (shared) are also included.

DB866		**2 class-CNN**	
Category	Images (n)	*L. pseudoracemus*	Others
conceptacles	2	0.00	1.00
perithallus	2	1.00	0.00
crystallites	3	0.33	0.67
epithallus	1	0.00	1.00
hypothallus	0	-	-
[1] surface	1	1.00	0.00
n.c.	2	0.00	1.00
shared	2	0.00	1.00

		3 class-CNN		
Category	Images (n)	*Lithothamnion* sp.	*Mesophyllum* sp.	*Lithophyllum* sp.
conceptacles	2	0.00	0.00	1.00
perithallus	2	0.00	0.00	1.00
crystallites	3	0.00	0.00	1.00
epithallus	1	0.00	0.00	1.00
[1] surface	1	0.00	0.00	1.00
n.c.	2	0.00	0.00	1.00
shared	2	0.00	0.50	0.50

Table 6. *Cont.*

4 class-CNN					
Category	Images (n)	*L. corallioides*	*M. philippii*	*L. racemus*	*L. pseudoracemus*
conceptacles	2	0.00	0.00	1.00	0.00
perithallus	2	0.00	0.00	0.00	1.00
crystallites	3	0.00	0.00	0.67	0.33
epithallus	1	1.00	0.00	0.00	0.00
[1] surface	1	0.00	0.00	0.00	1.00
n.c.	2	0.00	0.00	1.00	0.00
shared	2	0.00	0.50	0.50	0.00

[1] no hypothallus in sample DB866.

At the genus level, most of the images of samples DB865 and DB866 were correctly classified as *Lithophyllum* sp. (82% and 92%, respectively, as shown in Table 4). The classification was correct for all categories in sample DB866, while the conceptacle in sample DB865 was, surprisingly, assigned to *Lithothamnion* sp. (Tables 5 and 6).

At species-level, most of the images of samples DB865 and DB866 were assigned to *L. racemus* and *L. pseudoracemus*, with a higher percentage for the first class (Table 4). All the conceptacles were identified as belonging to *L. racemus*, as well as crystallites, especially for sample DB865. The images of the perithallus were rather classified as *L. pseudoracemus*, with a higher probability in DB866 (Tables 5 and 6). The epithallus in both samples was identified as *L. corallioides*, while the surface was assigned to the *L. pseudoracemus* class in DB866. In sample DB865, all the images showing more than one category were classified as *L. pseudoracemus* (Table 5). Every shared image showed the epithallus, two with also the crystallites and one with the surface.

3.3. Explanation

Image analyses using explainable artificial intelligence allowed us to detect the areas more relevant to CNN classification.

Each explanation approach used highlighted different areas of the image by showing positive and negative contributions (LIME), a heat map of the positive contributions (Grad-CAM), or simply the more relevant pixels (Saliency) (Figure 5). In some cases, the information given by the three approaches was counterintuitively different, due to the differences in the calculation of the outputs. For this reason, the visualization of the three explanatory techniques together could provide more insights into the relevant features displayed in the images.

Given the complexity of the structures shown in the SEM dataset, it was not always possible to recognize common diagnostic structures. Nevertheless, in most cases, the shape of cells and conceptacles were identified by the models (Figure A2). In images showing the epithallus and the perithallus, background areas and starch grains (Figure A2) sometimes “disturbed” the classification, resulting in erroneous identifications. The model performances could, therefore, be implemented by avoiding the use of images containing these interferences.

Notably, crystallites and cell wall calcification, in general, have been considered to be important features for the classification task. Figure 5, which was correctly classified in all three models used by the *Internal validation* (2, 3 and 4 class-CNNs), shows an example of *L. corallioides* crystallites in the perithallial cell walls of two adjacent cells. LIME, Saliency and Grad-CAM approaches (Figure 5) consistently revealed a significant contribution of the primary calcification [59,60], i.e., the outermost calcified layer of the cell wall composed by crystallites oriented parallel to the cell lumen, also called “interfilament”, at the boundary between cell filaments [61]. Thus, this calcification feature appeared to have a particular significance for the classification task, as already observed recently by Auer and Piller [21], and Bracchi et al. [60].

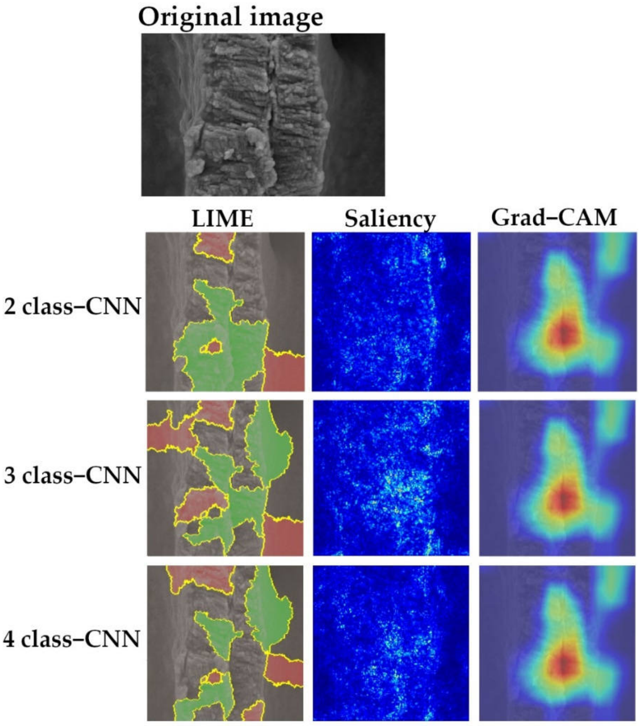

Figure 5. An example of the output obtained from the three approaches (LIME, Saliency, Grad-CAM) that show the pixels giving the major contributions to the CNN classification in the different models used (2, 3 and 4 class-CNNs). In LIME, positive and negative contributions to classification are respectively colored in green and red. In Saliency, brighter color highlights the pixels contributing the most to the class attribution, while in the Grad-CAM visualization the most significant areas for the final classification have a warmer color tone. The SEM image was successfully classified as *Lithothamnion corallioides* by every model and shows a magnification of the cell wall ultrastructure (crystallites category).

4. Discussion

The main goal of this work was to explore a new putative tool for coralline algae identification, by applying deep learning methods to the automatic classification of four algal species common in Mediterranean waters.

Species identification in this taxon is often ambiguous, and advances in molecular phylogeny revealed striking cases of cryptic and pseudocryptic species. The traditional morphological approach to taxonomic identification relies on thallus organization and on the morphometrical measurements of biological structures, including epithallial, perithallial and hypothallial cells and conceptacles. Besides the uncertainty related to the classification based solely on these tools (e.g., *L. racemus* and *L. pseudoracemus*) [16], in fossil samples, where molecular techniques cannot be applied, traditional morphological parameters are often poorly preserved due to diagenetic processes, which reduce their taxonomic value. Recently, new attention has arisen on the calcification patterns of coralline algae, revealing the cell wall ultrastructure as the phenotypic expression of genotypic information [21]. Indeed, there is a taxon-specific regulation of the morphology of crystallites composing the cell wall, also observed at the genus level [60].

The use of CNNs has offered the opportunity to investigate the diagnostic value of morphology as a whole, including both traditional parameters and the mineralized ultrastructure. In doing so, machine learning has played the role of an unbiased operator, which could establish its own classification features and possibly suggest to the real operator significant diagnostic parameters, even more than conventional ones.

The analysis of the different explanatory techniques allowed us to highlight the image areas that have most influenced identification at both genus and species levels. Concerning the morphology of biological structures, an elementary description of the species is given as follows: *L. corallioides* is often sterile lacking conceptacles, it has rectangular perithallial cells connected by multiple fusions and the epithallus is characterized by multiple layers of flattened cells, typically flared in the first layer below the surface [12]. *M. philippii* has a thick coaxial hypothallus and a single layer of rounded to flattened epithallial cells. The perithallial cells commonly present cell fusions and the buried multiporate sporangial conceptacles, hemispherical in shape, are typically infilled with large, irregular cells [11,32]. In *L. racemus* and *L. pseudoracemus*, sporangial conceptacles are rounded and uniporate, secondary pit connections join the perithallial cells of adjacent cell filaments and there can be up to five layers of flattened epithallial cells [16,22]. The two *Lithophyllum* spp. have been unequivocally distinguished from each other only by molecular tools so far since the morphological approach was poorly effective. Therefore, the specific classification task involving their discrimination was particularly challenging. From an ultrastructural point of view, the cell walls in *Lithothamnion corallioides* are constituted by flattened squared bricks with roundish outlines in the secondary calcification and rectangular tiles in the primary calcification [60]. The secondary calcification in *Lithophyllum* sp. is organized in perpendicular rods, while the primary calcification presents rhombohedral crystallites [21]. *Mesophyllum* sp. cell wall ultrastructure has never been specifically characterized. Thanks to the explanation comparison, we recognized some traditional morphological parameters, such as conceptacle and cells morphometry (Figure A2), but also the crystallite morphology undoubtedly contributed to the outcomes of the classification (Figure 5). A particular relevance, indeed, was given to crystallites, which alone constituted almost half of the total images used to run the CNN models. Concerning the identification of the two *L.* cf. *racemus* samples, DB865 and DB866, the model agreed with the expert on attributing the *Lithophyllum* sp. class in the 3 class-CNN and was leaning towards *L. racemus* in the 4 class-CNN.

To maximize the species variance, we included in the dataset the images for each specimen (two/three samples per species) (Table 1). By doing so, we reduced the error related to the features characterizing the sample more than the species itself. To achieve satisfying classification performances, intra-class variability is required to be lower than inter-class variability. However, in our case increasing the number of classes led to a decrease in inter-class variability (due to the two similar classes *L. racemus* and *L. pseudoracemus*). This was clearly not balanced by an increase of intra-class variability and, thus, led to lower performance.

It is essential to remark that the SEM images used were not taken specifically for the purpose of this work. Indeed, while in the 4 class-CNN the number of images among classes was reasonably balanced, in the 3 class-CNN the *Lithophyllum* sp. class accounted for more than half the total number of images, potentially favoring the accuracy of its classification. Nevertheless, even accounting for about one-third of the total images, the *Class Recall* of *L. pseudoracemus* in the 2 class-CNN was similar to the class Others (60%, Table 2). Therefore, the model proved to be able to identify some morphological features of *L. pseudoracemus*, as suggested by a *Class Recall* value much higher (60%) than both the performances of the dummy classifier (27%) and, most notably, the human classifier (21%) (Table 2).

Future experimentation on CNNs applied to SEM imagery for the identification of coralline algae should better rely on standard magnifications for SEM images within each morphological category, with an even distribution of the number of images among classes. We propose the following standards:

- Conceptacles: ~250×, ~500×;

- Perithallus: ~1000×, ~2500×, ~5000×;
- Crystallites: ~10000×, ~20000×, ~30000×;
- Epithallus: ~1000×, ~2500×, ~5000×;
- Hypothallus: ~250×; ~1000×;
- Surface: ~1000×.

Variable sample orientation should be carefully avoided, and the collection of SEM images should be carried out on longitudinal sections, as explained in Section 2.1. Overall, our performances offered promising results for obtaining a useful model that could support the expert for the classification of coralline algae, also considering the reduced number of images and samples, and the high intra-class variability. Further investigations should involve an image dataset wider and standardized, to guarantee the reproducibility of the method and enhance model accuracies.

Author Contributions: Conceptualization, G.P.; software and formal analysis, G.P., C.V. and G.S.; data curation, G.P.; writing—original draft preparation, G.P.; writing—review and editing, C.V., G.S. and G.P.; supervision, G.S. All authors have read and agreed to the published version of the manuscript.

Funding: Some algal samples used in this study were collected in the framework of "Convenzione MATTM-CNR per i Programmi di Monitoraggio per la Direttiva sulla Strategia Marina (MSFD, Art. 11, Dir. 2008/56/CE)". G.P. was funded by a doctoral fellowship in Environmental Sciences of the University of Milano-Bicocca.

Institutional Review Board Statement: Ethical review and approval were waived for this study, because it had no risk for human rights or welfare.

Data Availability Statement: The full SEM dataset is not publicly available. The model scripts are available on GitHub https://github.com/CValsecchi/VGG16_SEM (accessed on 19 November 2021).

Acknowledgments: Our gratitude goes to the anonymous referees whose insightful comments enabled us to make significant improvements to the paper. We are grateful to Daniela Basso, Valentina Alice Bracchi, Guido Bressan, Luigi Piazzi and Francesco Mastrototaro for sample collections. The captain, crew, and scientific staff of the RV Minerva Uno cruise STRATEGIA MARINA LIGURE-TIRRENO are acknowledged for their efficient and skillful cooperation at sea. We also thank Giovanni Coletti for his collaboration as human classifier.

Conflicts of Interest: The authors declare no conflict of interest.

Appendix A

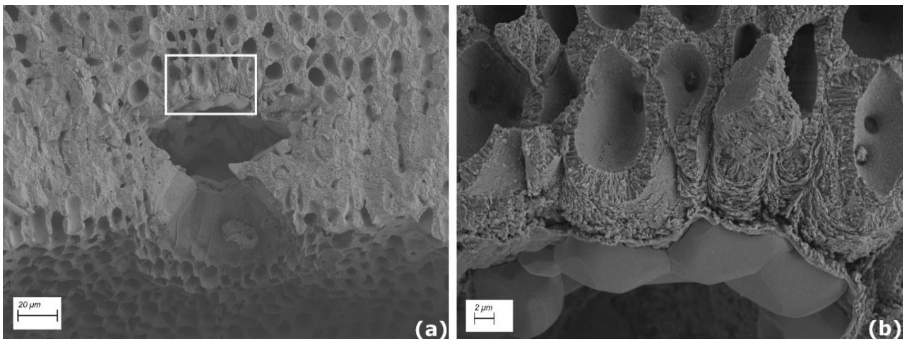

Figure A1. Examples of SEM images that were not assigned to a specific category: (**a**) *Lithophyllum racemus* pore canal; (**b**) a magnification showing perithallial cells near the pore canal. These features proved to be significant contributors to the correct classification of *Lithophyllum* spp. in the 2 and 3 class-CNNs.

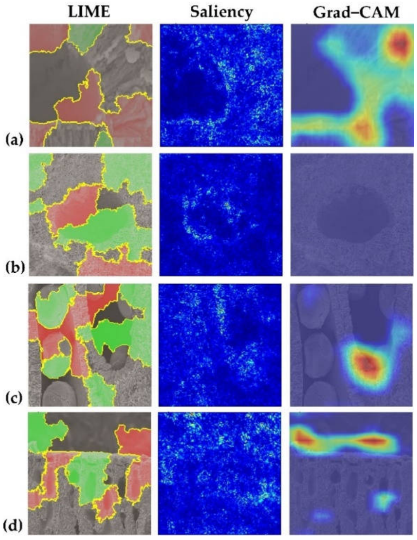

Figure A2. LIME, Saliency and Grad-CAM techniques show the pixels giving the major contributions to CNN classification: (**a**) magnification of the epithallial cell wall in *Lithophyllum racemus* evidence the significant contribution of calcification, formed by rod-shaped crystallites; (**b**) *Mesophyllum philippii* conceptacle shape focused by Saliency; (**c**) starch grains within the perithallial cells of *L. racemus* did not hamper correct identification; (**d**) the background beyond the epithallus of *Lithothamnion corallioides* was likely responsible for the erroneous classification of this image.

References

1. Bracchi, V.A.; Basso, D.; Marchese, F.; Corselli, C.; Savini, A. Coralligenous morphotypes on subhorizontal substrate: A new categorization. *Cont. Shelf Res.* **2017**, *144*, 10–20. [CrossRef]
2. Cebrián, E.; Ballesteros, E.; Canals, M. Shallow rocky bottom benthic assemblages as calcium carbonate producers in the Alboran Sea (Southwestern Mediterranean). *Oceanol. Acta* **2000**, *23*, 311–322. [CrossRef]
3. Basso, D. Production carbonatée par les algues rouges calcaires et changement climatique global. *Geodiversitas* **2012**, *34*, 13–33. [CrossRef]
4. Ballesteros, E. Mediterranean coralligenous assemblages: A synthesis of present knowledge. *Oceanogr. Mar. Biol.* **2006**, *44*, 123–195. [CrossRef]
5. Basso, D.; Nalin, R.; Massari, F. Genesis and composition of the Pleistocene coralligène de plateau of the Cutro Terrace (Calabria, Southern Italy). *Neues Jahrb. Geol. Palaontol. Abh.* **2007**, *244*, 173–182. [CrossRef]
6. Bracchi, V.A.; Nalin, R.; Basso, D. Morpho-structural heterogeneity of shallow-water coralligenous in a Pleistocene marine terrace (Le Castella, Italy). *Palaeogeogr. Palaeoclimatol. Palaeoecol.* **2016**, *454*, 101–112. [CrossRef]
7. Basso, D.; Morbioli, C.; Corselli, C. Rhodolith facies evolution and burial as a response to Holocene transgression at the Pontian islands shelf break. *Geol. Soc. Spec. Publ.* **2006**, *255*, 23–34. [CrossRef]
8. Bracchi, V.A.; Nalin, R.; Basso, D. Paleoecology and dynamics of coralline dominated facies during a Pleistocene transgressive-regressive cycle (Capo Colonna marine terrace, Southern Italy). *Palaeogeogr. Palaeoclimatol. Palaeoecol.* **2014**, *414*, 296–309. [CrossRef]
9. Darrenougue, N.; de Deckker, P.; Eggins, S.; Payri, C. Sea-surface temperature reconstruction from trace elements variations of tropical coralline red algae. *Quat. Sci. Rev.* **2014**, *93*, 34–46. [CrossRef]
10. Coletti, G.; Basso, D.; Corselli, C. Coralline algae as depth indicators in the Sommières Basin (Early Miocene, Southern France). *Geobios* **2018**, *51*, 15–30. [CrossRef]
11. Basso, D. Study of living calcareous algae by a paleontological approach: The non-geniculate Corallinaceae (Rhodophyta) of the soft bottoms of the Tyrrhenian Sea (Western Mediterranean). The genera *Phymatolithon* Foslie and *Mesophyllum* Lemoine. *Riv. Ital. Di Paleontol. Stratigr.* **1995**, *100*, 575–596.
12. Basso, D. Living calcareous algae by a paleontological approach: The genus *Lithothamnion* Heydrich Nom. Cons. from the soft bottoms of the Tyrrhenian Sea (Mediterranean). *Riv. Ital. Di Paleontol. Stratigr.* **1995**, *101*, 349–366. [CrossRef]
13. Cabioch, J.; Mendoza, M.L. *Mesophyllum Alternans* (Foslie) Comb. Nov. (Corallinales, Rhodophyta), a Mediterraneo-Atlantic species, and new considerations on the *Lithothamnion philippii* Foslie complex. *Phycologia* **1998**, *37*, 208–221. [CrossRef]

14. Adey, W.H.; Mcintyre, I.G. Crustose coralline algae: A re-evaluation in the geological sciences. *Geol. Soc. Am. Bull.* **1973**, *84*, 883–904. [CrossRef]
15. Garbary, J.D. An introduction to the Scanning Electron Microscopy of red algae. In *Modern Approaches to the Taxonomy of Red and Brown Algae*; Academic Press: Cambridge, MA, USA, 1978; pp. 205–222.
16. Caragnano, A.; Rodondi, G.; Basso, D.; Peña, V.; Gall, L.; Rindi, F. Circumscription of *Lithophyllum racemus* (Corallinales, Rhodophyta) from the Western Mediterranean Sea reveals the species *Lithophyllum pseudoracemus* sp. nov. *Phycologia* **2020**, *59*, 584–597. [CrossRef]
17. Pezzolesi, L.; Peña, V.; le Gall, L.; Gabrielson, P.W.; Kaleb, S.; Hughey, J.R.; Rodondi, G.; Hernandez-Kantun, J.J.; Falace, A.; Basso, D.; et al. Mediterranean *Lithophyllum stictiforme* (Corallinales, Rhodophyta) is a genetically diverse species complex: Implications for species circumscription, biogeography and conservation of coralligenous habitats. *J. Phycol.* **2019**, *55*, 473–492. [CrossRef]
18. De Jode, A.; David, R.; Haguenauer, A.; Cahill, A.E.; Erga, Z.; Guillemain, D.; Sartoretto, S.; Rocher, C.; Selva, M.; le Gall, L.; et al. From seascape ecology to population genomics and back. Spatial and ecological differentiation among cryptic species of the red algae *Lithophyllum stictiforme/L. cabiochiae*, main bioconstructors of coralligenous habitats. *Mol. Phylogenetics Evol.* **2019**, *137*, 104–113. [CrossRef] [PubMed]
19. Rösler, A.; Perfectti, F.; Peña, V.; Braga, J.C. Phylogenetic relationships of Corallinaceae (Corallinales, Rhodophyta): Taxonomic implications for reef-building corallines. *J. Phycol.* **2016**, *52*, 412–431. [CrossRef] [PubMed]
20. Kato, A.; Baba, M.; Suda, S. Revision of the Mastophoroideae (Corallinales, Rhodophyta) and polyphyly in nongeniculate species widely distributed on Pacific coral reefs. *J. Phycol.* **2011**, *47*, 662–672. [CrossRef] [PubMed]
21. Auer, G.; Piller, W.E. Nanocrystals as phenotypic expression of genotypes-An example in coralline red algae. *Sci. Adv.* **2020**, *6*, eaay2126. [CrossRef]
22. Basso, D.; Fravega, P.; Vannucci, G. Fossil and living corallinaceans related to the Mediterranean endemic species *Lithophyllum racemus* (Lamarck) Foslie. *Facies* **1996**, *35*, 275–292. [CrossRef]
23. Basso, D.; Babbini, L.; Kaleb, S.; Bracchi, V.A.; Falace, A. Monitoring deep Mediterranean rhodolith beds. *Aquat. Conserv. Mar. Freshw. Ecosyst.* **2016**, *26*, 549–561. [CrossRef]
24. Basso, D. Deep rhodolith distribution in the Pontian islands, Italy: A model for the paleoecology of a temperate sea. *Palaeogeogr. Palaeoclimatol. Palaeoecol.* **1998**, *137*, 173–187. [CrossRef]
25. Foster, M.S. Rhodoliths: Between rocks and soft places. *J. Phycol.* **2001**, *37*, 659–667. [CrossRef]
26. Basso, D.; Babbini, L.; Ramos-Esplá, A.A.; Salomidi, M. Mediterranean rhodolith beds. *Coast. Res. Libr.* **2017**, *15*, 281–298. [CrossRef]
27. Carro, B.; Lopez, L.; Peña, V.; Bárbara, I.; Barreiro, R. DNA barcoding allows the accurate assessment of European maerl diversity: A proof-of-concept study. *Phytotaxa* **2014**, *190*, 176–189. [CrossRef]
28. Potin, P.; Floc'h, J.Y.; Augris, C.; Cabioch, J. Annual growth rate of the calcareous red alga *Lithothamnion corallioides* (Corallinales, Rhodophyta) in the Bay of Brest, France. *Hydrobiologia* **1990**, *204*, 263–267. [CrossRef]
29. Savini, A.; Basso, D.; Bracchi, V.A.; Corselli, C.; Pennetta, M. Cartographie du maërl et quantification de la production carbonatée sur les terrasses sous-marines au large de la péninsule du Cilento (Mer Tyrrhénienne, Italie). *Geodiversitas* **2012**, *34*, 77–98. [CrossRef]
30. Martin, S.; Castets, M.D.; Clavier, J. Primary production, respiration and calcification of the temperate free-living coralline alga *Lithothamnion corallioides*. *Aquat. Bot.* **2006**, *85*, 121–128. [CrossRef]
31. Irvine, L.M.; Chamberlain, Y. *Seaweeds of the British isles: Volume 1 Rhodophyta. Part 2B Corallinales, Hildenbrandiales*; Natural History Museum: London, UK, 1994; 284p.
32. Peña, V.; de Clerck, O.; Afonso-Carrillo, J.; Ballesteros, E.; Bárbara, I.; Barreiro, R.; le Gall, L. An integrative systematic approach to species diversity and distribution in the genus *Mesophyllum* (Corallinales, Rhodophyta) in Atlantic and Mediterranean Europe. *Eur. J. Phycol.* **2015**, *50*, 20–36. [CrossRef]
33. Park, J.-H.; Hwang, K.-B.; Park, H.-M.; Choi, Y.-K. Application of CNN for fish species classification. *J. Korea Inst. Inf. Commun. Eng.* **2019**, *23*, 39–46. [CrossRef]
34. Rathi, D.; Jain, S.; Indu, S. Underwater fish species classification using Convolutional Neural Network and Deep Learning. In Proceedings of the 9th International Conference on Advances in Pattern Recognition 2018, Bangalore, India, 23–27 December 2017; pp. 344–349. [CrossRef]
35. Kiel, S. Assessing bivalve phylogeny using Deep Learning and computer vision approaches. *bioRxiv* **2021**. [CrossRef]
36. De Lima, R.P.; Welch, K.F.; Barrick, J.E.; Marfurt, K.J.; Burkhalter, R.; Cassel, M.; Soreghan, G.S. Convolutional Neural Networks as an aid to biostratigraphy and micropaleontology: A test on Late Paleozoic microfossils. *Palaios* **2020**, *35*, 391–402. [CrossRef]
37. Liu, X.; Song, H. Automatic identification of fossils and abiotic grains during carbonate microfacies analysis using Deep Convolutional Neural Networks. *Sediment. Geol.* **2020**, *410*, 105790. [CrossRef]
38. Modarres, M.H.; Aversa, R.; Cozzini, S.; Ciancio, R.; Leto, A.; Brandino, G.P. Neural Network for nanoscience Scanning Electron Microscope image recognition. *Sci. Rep.* **2017**, *7*, 1–12. [CrossRef]
39. Adey, W.H.; McKibbin, D.L. Studies on the maerl species *Phymatolithon calcareum* (Pallas) nov. comb. and *Lithothamnium coralloides* Crouan in the Ria de Vigo. *Bot. Mar.* **1970**, *13*, 100–106. [CrossRef]
40. Shorten, C.; Khoshgoftaar, T.M. A survey on image Data Augmentation for Deep Learning. *J. Big Data* **2019**, *6*, 60. [CrossRef]

41. Hecht-Nielsen, R. Theory of the Backpropagation Neural Network. *Int. Jt. Conf. Neural Netw.* **1989**, *1*, 593–605. [CrossRef]
42. Liu, Q.; Zhang, N.; Yang, W.; Wang, S.; Cui, Z.; Chen, X.; Chen, L. A review of image recognition with Deep Convolutional Neural Network. In *Intelligent Computing Theories and Application*; Lecture Notes in Computer Science (including subseries Lecture Notes in Artificial Intelligence and Lecture Notes in Bioinformatics); Springer: Cham, Switzerland, 2017; Volume 10361 LNCS, pp. 69–80. [CrossRef]
43. Wang, L.; Zhang, K.; Liu, X.; Long, E.; Jiang, J.; An, Y.; Zhang, J.; Liu, Z.; Lin, Z.; Li, X.; et al. Comparative analysis of image classification methods for automatic diagnosis of ophthalmic images. *Sci. Rep.* **2017**, *7*, 41545. [CrossRef] [PubMed]
44. Goodfellow, I.; Bengio, Y.; Courville, A. *Deep Learning*; MIT Press: Cambridge, MA, USA, 2016; 800p.
45. Abdalla, A.; Cen, H.; Wan, L.; Rashid, R.; Weng, H.; Zhou, W.; He, Y. Fine-Tuning Convolutional Neural Network with Transfer Learning for semantic segmentation of ground-level oilseed rape images in a field with high weed pressure. *Comput. Electron. Agric.* **2019**, *167*, 105091. [CrossRef]
46. Deng, Y.; Lu, L.; Aponte, L.; Angelidi, A.M.; Novak, V.; Karniadakis, G.E.; Mantzoros, C.S. Deep Transfer Learning and Data Augmentation improve glucose levels prediction in type 2 diabetes patients. *NPJ Digit. Med.* **2021**, *4*, 1–13. [CrossRef] [PubMed]
47. Simonyan, K.; Zisserman, A. Very Deep Convolutional Networks for large-scale image recognition. *arXiv* **2014**, arXiv:1409.1556.
48. Deng, J.; Dong, W.; Socher, R.; Li, L.-J.; Li, K.; Li, F. ImageNet: A large-scale hierarchical image database. In Proceedings of the IEEE Conference on Computer Vision and Pattern Recognition, Miami, FL, USA, 20–25 June 2009; pp. 248–255. [CrossRef]
49. Agarap, A.F. Deep Learning Using Rectified Linear Units (ReLU). *arXiv* **2018**, arXiv:1803.08375.
50. Tan, P.; Steinbach, M.; Karpatne, A.; Kumar, V. *Introduction to Data Mining*, 2nd ed.; Addison-Wesley: Boston, MA, USA, 2018; 839p.
51. Simonyan, K.; Vedaldi, A.; Zisserman, A. Deep inside Convolutional Networks: Visualising image classification models and Saliency Maps. *arXiv* **2013**, arXiv:1312.6034.
52. Ribeiro, M.T.; Singh, S.; Guestrin, C. "Why should I trust you?" Explaining the predictions of any classifier. In Proceedings of the ACM SIGKDD International Conference on Knowledge Discovery and Data Mining, San Francisco, CA, USA, 13–16 August 2016; Association for Computing Machinery: New York, NY, USA, 2016; Volume 13–17, pp. 1135–1144.
53. Selvaraju, R.R.; Cogswell, M.; Das, A.; Vedantam, R.; Parikh, D.; Batra, D. Grad-CAM: Visual explanations from Deep Networks via gradient-based localization. *arXiv* **2016**, arXiv:1611.07450. [CrossRef]
54. Chollet, F. Keras, GitHub. Available online: https://github.com/fchollet/keras (accessed on 19 November 2021).
55. Kotikalapudi, R.; Contributors. Keras-Vis, GitHub. Available online: https://github.com/raghakot/keras-vis (accessed on 19 November 2021).
56. Abadi, M.; Agarwal, A.; Barham, P.; Brevdo, E.; Chen, Z.; Citro, C.; Corrado, G.S.; Davis, A.; Dean, J.; Devin, M.; et al. TensorFlow: Large-scale Machine Learning on heterogeneous distributed systems. *arXiv* **2015**, arXiv:1603.04467.
57. Hsiang, A.Y.; Brombacher, A.; Rillo, M.C.; Mleneck-Vautravers, M.J.; Conn, S.; Lordsmith, S.; Jentzen, A.; Henehan, M.J.; Metcalfe, B.; Fenton, I.S.; et al. Endless Forams: >34,000 modern planktonic foraminiferal images for taxonomic training and automated species recognition using Convolutional Neural Networks. *Paleoceanogr. Paleoclimatology* **2019**, *34*, 1157–1177. [CrossRef]
58. Mitra, R.; Marchitto, T.M.; Ge, Q.; Zhong, B.; Kanakiya, B.; Cook, M.S.; Fehrenbacher, J.S.; Ortiz, J.D.; Tripati, A.; Lobaton, E. Automated species-level identification of planktic foraminifera using Convolutional Neural Networks, with comparison to human performance. *Mar. Micropaleontol.* **2019**, *147*, 16–24. [CrossRef]
59. Flajs, G. Skeletal structures of some calcifying algae. In *Fossil Algae*; Springer: Berlin/Heidelberg, Germany, 1977; pp. 225–231. [CrossRef]
60. Bracchi, V.A.; Piazza, G.; Basso, D. A stable ultrastructural pattern despite variable cell size in *Lithothamnion corallioides*. *Biogeosciences* **2021**, *18*, 6061–6076. [CrossRef]
61. Nash, M.C.; Adey, W. Multiple phases of Mg-calcite in crustose coralline algae suggest caution for temperature proxy and ocean acidification assessment: Lessons from the ultrastructure and biomineralization in *Phymatolithon* (Rhodophyta, Corallinales). *J. Phycol.* **2017**, *53*, 970–984. [CrossRef] [PubMed]

Biogeosciences, 19, 1047–1065, 2022
https://doi.org/10.5194/bg-19-1047-2022

Biogeosciences
Open Access
Research article

Growth rate rather than temperature affects the B/Ca ratio in the calcareous red alga *Lithothamnion corallioides*

Giulia Piazza[1,2], **Valentina A. Bracchi**[1], **Antonio Langone**[3], **Agostino N. Meroni**[4], **and Daniela Basso**[1]

[1]Department of Earth and Environmental Sciences, University of Milano–Bicocca, CoNISMa Research Unit of Milano–Bicocca, Piazza della Scienza 4, 20126 Milan, Italy
[2]Department of Earth and Ocean Dynamics, University of Barcelona, Martí i Franquès s/n, 08028 Barcelona, Spain
[3]CNR – Institute of Geosciences and Earth Resources, Via Ferrata 1, 27100 Pavia, Italy
[4]Department of Civil and Environmental Engineering, Politecnico of Milan, Piazza Leonardo da Vinci 32, 20133 Milan, Italy

Correspondence: Giulia Piazza (g.piazza15@campus.unimib.it)

Received: 1 February 2021 – Discussion started: 4 February 2021
Revised: 21 December 2021 – Accepted: 28 December 2021 – Published: 17 February 2022

Abstract. The B/Ca ratio in calcareous marine species is informative of past seawater CO_3^{2-} concentrations, but scarce data exist on B/Ca in coralline algae. Recent studies suggest influences of temperature and growth rates on B/Ca, the effect of which could be critical for the reconstructions of surface ocean pH and atmospheric $p\mathrm{CO}_2$. In this paper, we present the first laser ablation inductively coupled plasma mass spectrometry (LA-ICP-MS) analyses of Mg, Sr, Li, and B in the coralline alga *Lithothamnion corallioides* collected from different geographic settings and depths across the Mediterranean Sea and in the Atlantic Ocean. We produced the first data on putative temperature proxies (Mg/Ca, Li/Ca, Sr/Ca, Mg/Li) and B/Ca in a coralline algal species grown in different basins from across the photic zone (12, 40, 45, and 66 m depth). We tested the B/Ca correlation with temperature proxies and growth rates in order to evaluate their possible effect on B incorporation. Our results suggested a growth rate influence on B/Ca, which was evident in the sample with the lowest growth rate of $0.10\,\mathrm{mm\,yr^{-1}}$ (Pontian Isl., Italy; 66 m depth) and in Elba (Italy; 45 m depth), where the algal growth rate was the highest ($0.14\,\mathrm{mm\,yr^{-1}}$). At these two sites, the measured B/Ca was the lowest at $462.8 \pm 49.2\,\mathrm{\mu mol\,mol^{-1}}$ and the highest at $757.7 \pm 75.5\,\mathrm{\mu mol\,mol^{-1}}$, respectively. A positive correlation between B/Ca and temperature proxies was found only in the shallowest sample from Morlaix (Atlantic coast of France; 12 m depth), where the amplitude of temperature variation (ΔT) was the highest (8.9 °C). Still, fluctuations in B/Ca did not mirror yearly seasonal temperature oscillations as for Mg/Ca, Li/Ca, and Sr/Ca. We concluded that growth rates, triggered by the different ΔT and light availability across depth, affect the B incorporation in *L. corallioides*.

1 Introduction

Warming and acidification are major anthropogenic perturbations of present-day oceans (Callendar, 1938; Fairhall, 1973; Brewer, 1997; Gattuso, 1999; Caldeira, 2005; Hönisch et al., 2012; Masson-Delmotte et al., 2021). Ocean acidification reduces the saturation state of calcite and aragonite, lowering the dissolution threshold of biominerals and threatening habitat-forming species of critical ecological importance such as coralline red algae and corals (Morse et al., 2006; Hoegh-Guldberg et al., 2007; Andersson et al., 2008, 2011; Basso, 2012; Ragazzola et al., 2012; Ries et al., 2016). Coralline algae, which precipitate high-Mg calcite (> 8 mol %–12 mol % $MgCO_3$) (Morse et al., 2006), are particularly suitable as proxy archives for paleoclimate reconstruction because of their worldwide distribution and longevity. Importantly, they show indeterminate growth with no ontogenetic trend (Halfar et al., 2008), which means the growth trend of coralline algae does not slow down asymptotically with age, as in bivalves, thus preserving the resolution of the geochemical signals in all stages of growth (Adey, 1965; Frantz et al., 2005; Halfar et al., 2008). Moreover, coralline algae thin sections under optical microscopy reveal

Published by Copernicus Publications on behalf of the European Geosciences Union.

bands that reflect the growth pattern (Cabioch, 1966; Basso, 1995a, b; Foster, 2001), similar to tree rings (Ragazzola et al., 2016) that can be targeted for high-resolution geochemical analyses. Seasonal growth bands, indeed, consist of the perithallial alternation of dark and light bands that together constitute the annual growth patterns (Freiwald and Henrich, 1994; Basso, 1995a, b; Kamenos et al., 2009). Dark bands correspond to slow-growing cells produced in the cold season, which are shorter, thick-walled, and with lower Mg contents, while light bands are fast-growing cells produced in the warm season, which are longer, less calcified, and with higher Mg concentrations (Kamenos et al., 2009; Ragazzola et al., 2016). The high-Mg calcite of calcareous red algae records ambient seawater temperature (Halfar et al., 2000; Kamenos et al., 2008; Nash et al., 2016; Hetzinger er al., 2018), primary productivity (Chan et al., 2017; Hou et al., 2019), and salinity (Kamenos, 2012), proving to be a suitable paleoclimate archive. Most of the data were collected from high-latitude (Kamenos et al., 2008; Anagnostou et al., 2019) and tropical species (Caragnano et al., 2014; Darrenougue et al., 2014), whereas less attention has been given to coralline algae from mid-latitudes.

Trace element variations in marine calcareous species inform the reconstruction of changes in the environmental parameters which characterized the seawater during their growth (Hetzinger et al., 2011; Montagna and Douville, 2017). Boron is incorporated into the mineral lattice of calcareous marine species during calcite precipitation. In the ocean, B occurs in two molecular species: boric acid $B(OH)_3$ and borate ion $B(OH)_4^-$ (Dickson, 1990), which are related by the following acid–base equilibrium reaction:

$$B(OH)_3 + H_2O \leftrightarrow B(OH)_4^- + H^+, \qquad \text{(R1)}$$

which shows the dependence of the two species concentrations on pH. The first analyses of the isotopic signal of marine carbonates evidenced a strong similarity with the isotopic composition of $B(OH)_4^-$ in solution, suggesting that borate would preferentially be incorporated into marine carbonates (Vengosh et al., 1991; Hemming and Hanson, 1992; Zeebe and Wolf-Gladrow, 2001; DeCarlo et al., 2018). The B content and its isotopic signature ($\delta^{11}B$) in calcareous marine species record information about the seawater carbonate system. The $\delta^{11}B$ is used to reconstruct past seawater pH (Hönisch and Hemming, 2005; Foster, 2008; Douville et al., 2010; Paris et al., 2010; Rae et al., 2011). The boron-to-calcium ratio (B/Ca) proved to be informative about past seawater CO_3^{2-} concentrations in different empirical studies on benthic foraminifera (Yu and Elderfield, 2007; Yu et al., 2007; Rae et al., 2011) and in synthetic aragonite (Holcomb et al., 2016). Most of the literature on boron studies is focused on its isotopic composition (Hemming and Hönisch, 2007; Klochko et al., 2009; Henehan et al., 2013; Fietzke et al., 2015; Cornwall et al., 2017; Ragazzola et al., 2020), whereas less attention has been given to B/Ca records, especially in coralline algae. Recent studies suggest that B/Ca is a function of seawater pH, as well as of other environmental variables such as temperature, the effect of which should be considered in the attempt to reconstruct surface ocean pH and atmospheric pCO_2 (Wara et al., 2003; Allen et al., 2012; Kaczmarek et al., 2016).

To achieve the best reliability of geochemical proxies for climate reconstructions, it is important to recognize the influence of multiple factors on a single proxy (Kaczmarek et al., 2016; Donald et al., 2017). For instance, more recently the effects of temperature and growth rate on B incorporation have been investigated through experiments on both synthetic and biogenic carbonates (Wara et al., 2003; Yu et al., 2007; Gabitov et al., 2014; Mavromatis et al., 2015; Uchikawa et al., 2015; Kaczmarek et al., 2016; Donald et al., 2017). In particular, a culture experiment on the coralline alga *Neogoniolithon* sp. showed a positive correlation of B/Ca with growth rate and a negative correlation with Sr/Ca, which was proposed as a proxy for dissolved inorganic carbon (DIC) (Donald et al., 2017). Moreover, a culture experiment on the high-latitude species *Clathromorphum compactum* (Kjellman) Foslie 1898 revealed non-significant temperature influences on B/Ca and a significant inverse relationship with growth rate (Anagnostou et al., 2019). The factors which influence the B incorporation in calcareous red algae are therefore still debated. Recent experiments also suggest that coralline algae can control the calcifying fluid pH (pH_{cf}) (Cornwall et al., 2017), as already observed in corals (Comeau et al., 2017). Both organisms have a species-specific capability to elevate pH at calcification sites in response to variations of ambient pH, also influencing precipitation rates (Cornwall et al., 2017). Differences between carbonate polymorphs were also highlighted (McCulloch et al., 2012; Cornwall et al., 2018), showing more elevated pH_{cf} in aragonitic corals than calcites, pointing to the relevance of the mineralogical control on biological up-regulation. So far, no investigations on pH_{cf} modifications in natural systems have been performed on calcareous red algae.

No studies have been conducted so far on the correlation between temperature proxies (Mg, Sr, Li/Ca) and B/Ca. The Mg/Ca ratio is extensively used as a temperature proxy in coralline algae (Halfar et al., 2008; Kamenos et al., 2008; Fietzke et al., 2015; Ragazzola et al., 2020), since the substitution of Mg^{2+} with Ca^{2+} ions in the calcite lattice is an endothermic reaction. Accordingly, Mg incorporation increases with temperature (Moberly, 1968; Berner, 1975; Ries, 2006; Caragnano et al., 2014, 2017). Sr/Ca and Li/Ca ratios in calcareous red algae have also been investigated as climate proxies, showing significant positive correlations with temperature in different species (Kamenos et al., 2008; Hetzinger et al., 2011; Caragnano et al., 2014; Darrenougue et al., 2014). The Mg/Li ratio showed a strong correlation with seawater temperature in cultured *C. compactum* (Anagnostou et al., 2019) and in empirical studies on high-Mg calcites, including coralline algae (Stewart et al., 2020). Conversely, the Mg/Li calibration did not reveal improvements in the Mg/Ca or Li/Ca proxies in *Lithophyllum* spp. (Caragnano et al., 2014, 2017).

Here, we present laser ablation inductively coupled plasma mass spectrometry (LA-ICP-MS) conducted on a wild-grown coralline alga with a wide geographic scope. This technique, which allows high-resolution analysis of a broad range of trace elements in solid-state samples, has been widely used in biogenic carbonates to extract records of seawater temperature, salinity, and water chemistry (Schöne et al., 2005; Corrège, 2006; Hetzinger et al., 2009, 2011; Fietzke et al., 2015; Ragazzola et al., 2020). Measurements were made on the non-geniculate coralline alga *Lithothamnion corallioides* (P. Crouan and H. Crouan) P. Crouan and H. Crouan 1867, which is widely distributed in the Mediterranean Sea and in the north-eastern Atlantic Ocean from Scotland to the Canary Islands (Irvine and Chamberlain, 1999; Wilson et al., 2004; Carro et al., 2014), usually constituting maerl beds (Potin et al., 1990; Foster, 2001; Martin et al., 2006; Savini et al., 2012; Basso et al., 2017). It forms rhodoliths as unattached branches (Basso et al., 2016) with obvious banding in longitudinal sections (Basso, 1995b). These characteristics combine to make this species a suitable model for the measurement of geochemical proxies by comparing different environmental settings.

In this paper, we provide the first LA-ICP-MS data on putative temperature proxies (Mg/Ca, Sr/Ca, Li/Ca, Mg/Li) and B/Ca measured on *L. corallioides* collected from different geographic settings and depths across the Mediterranean Sea and in the Atlantic Ocean. We test the influence of temperature and growth rate on the B/Ca ratio, which could be crucial in assessing the reliability of B/Ca as a proxy for the seawater carbonate system.

2 Materials and methods

2.1 Sampling sites and collection of *Lithothamnion corallioides*

Samples of the coralline alga *L. corallioides* were collected in the western Mediterranean Sea and in the Atlantic Ocean (Fig. 1). In the Mediterranean Sea, the samples collected in the Pontian Islands (Italy) at 66 m depth were gathered by grab during the cruises of the R/V *Minerva Uno* in the framework of the Marine Strategy Campaigns 2016 (Table 1). The last two Mediterranean samples were collected by one of the authors (DB) by scuba diving during local surveys at 45 m off the coasts of Pomonte (Elba Island, Italy) (Basso and Brusoni, 2004) and at 40 m depth in the Aegadian Islands (Marettimo, Italy). The Atlantic sample was collected by grab at 12 m depth in Morlaix Bay (Brittany, France) (Table 1).

The identification of the algal samples was achieved by morphological analyses of epithallial and perithallial cells using a field emission gun scanning electron microscope (SEM-FEG) Gemini 500 Zeiss. Samples were prepared for SEM according to Basso (1995a). Morphological identification was based on Adey and McKibbin (1970) and Irvine and Chamberlain (1994). Other information about maerl species distribution in Morlaix was provided by Carro et al. (2014) and Melbourne et al. (2017). *L. corallioides* was selected as the target species because of its presence in both Mediterranean and Atlantic waters. The Atlantic sample (Morlaix) was used as voucher specimen for the subsequent identification of the Mediterranean samples, since *Phymatolithon* spp. and *L. corallioides* are the only components of the Morlaix maerl (Carro et al., 2014; Melbourne et al., 2017). Hence, once its inclusion under the genus *Phymatolithon* was excluded, the Morlaix sample identified as *L. corallioides* was used as a reference for the most reliable identification of the other Mediterranean samples.

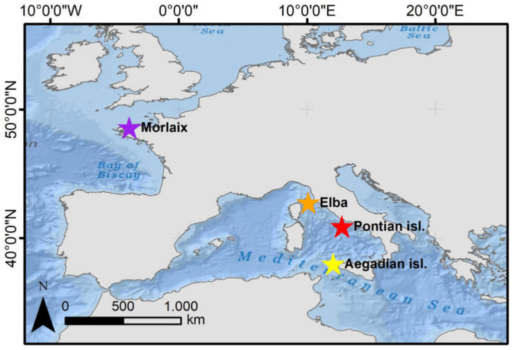

Figure 1. Map showing the distribution of sampling sites where *Lithothamnion corallioides* samples were collected: Morlaix Bay (48°34′42″ N, 3°49′36″ W), Aegadian Islands (37°97′36″ N, 12°14′12″ E), Elba (42°44′56.4″ N, 10°07′08.4″ E), and Pontian Islands (40°54′ N, 12°45′ E). Service layer credits: source Esri, GEBCO, NOAA, National Geographic, Garmin, https://www.geonames.org/ (last access: 21 December 2021), and other contributors.

2.2 Sample preparation

The selected algal branches were embedded in Epo-Fix resin, which was stirred for 2 min with a hardener (13 % w/w); they were then left to dry at room temperature for 24 h. Afterwards, the treated branches were cut by an IsoMet diamond wafering blade 15HC along the direction of growth. In the laboratory of the Institute of Geosciences and Earth Resources of the National Research Council (IGG-CNR) in Pavia (Italy), the sections were polished with a MetaServ grinder–polisher (400 RPM) using a diamond paste solution, finally cleaned ultrasonically in distilled water for 10 min, and dried at 30 °C for 24 h.

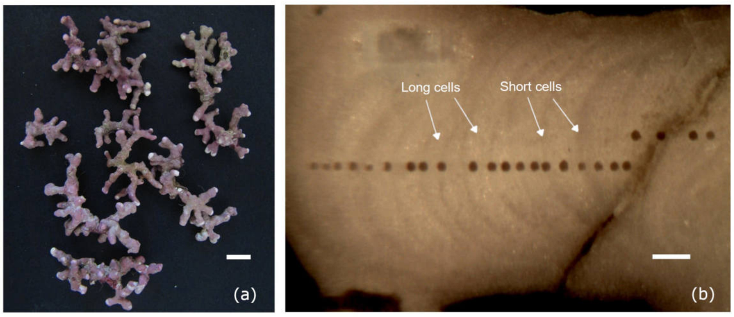

Figure 2. (a) Thalli of *Lithothamnion corallioides* collected in Morlaix (scale bar: 5 mm). **(b)** Longitudinal section through the *L. corallioides* branch sampled in Morlaix showing the LA-ICP-MS transects targeting each growth band (scale bar: 200 µm).

2.3 Trace elements analyses and environmental data

LA-ICP-MS analyses were carried out at the IGG-CNR laboratory on one algal branch per sampling site. ^{43}Ca, ^{7}Li, ^{25}Mg, ^{88}Sr, and ^{11}B contents were measured using an Agilent ICP-QQQ 8900 quadrupole ICP-MS coupled to an Excimer laser ablation system (193 nm wavelength, MicroLas with GeoLas optics). Element / Ca ratios were calculated for these isotopes, as was the Mg/Li ratio. Measurements were performed with laser energy densities of 4 J cm^{-2} and helium as a carrier gas.

The laser transects crossed the algal growth direction with a spot size of 50 µm, attempting to target each growth band change which marked the transition between the cells usually produced in the warm season and those usually produced in the cold season, hereinafter referred to as long and short cells (Figs. 2, S1, S2, S3). NIST 612 was used as an external standard (e.g. Fietzke et al., 2010; Jochum et al., 2012), whereas Ca was adopted as an internal standard. Accuracy and precision were better than 4 % for NIST 612 and 8 % for Ca standard. Minimum detection limits (99 % confidence) of measured elements were Ca = 16.91, Li = 0.07, Mg = 0.11, Sr = 0.004, and B = 2.64 ppm. Each analysis was carried out in MS/MS mode for 3 min by acquiring 60 s of background before and after the sampling period by the laser on the polished surface. The first part of the signal was not used for the integration to avoid surface contamination. The Glitter software (v. 4.4.4) was used for data reduction.

In the absence of in situ environmental data, the seawater temperature has been extracted by 11 years of monthly reanalysis spanning 1979–2016 from from the Ocean ReAnalysis System 5 (ORAS5) at 0.25° horizontal resolution (Zuo et al., 2019). The time interval of extraction for each site corresponded to 11 years before sample collection (Bracchi et al., 2021). Minimum, maximum, and mean values, as reported in Table 1, refer to the temperature at sampling depth and have been measured over the entire time interval of extraction.

For the purpose of this work, we considered temperature data in terms of (a) the amplitude of temperature variation (ΔT) and (b) the temperature maxima and minima. ΔT represents the temperature fluctuations during the algal growth and has been measured as the difference between the maximum and minimum temperature registered at the site over 11 years. We used ΔT when comparing the sampling sites, given their differences in depth and geographical regions. The temperature peaks (maximum and minimum) have rather been used when considering data corresponding to long and short cells, since they are related to warm and cold periods of growth, respectively. We used the temperature peaks over the entire time interval of extraction (11 years) when comparing the mean elemental ratios of long and short cells per sampling site. The maximum and minimum temperature within each year have been used instead for the reconstruction of the algal age model. In the sample from Morlaix Bay, indeed, the good visibility of the growth bands allowed us to relate the temperature record with the algal growth at annual resolution. We therefore plotted all the element ratios against the average seawater temperature values of the coldest and warmest months of the year to reconstruct the temperature variations during the algal growth (Moberly, 1970; Corrège, 2006; Williams et al., 2014; Ragazzola et al., 2020; Caragnano et al., 2014). Missing element ratios, possibly due to non-targeted consecutive bands, were calculated as the means of known values.

Carbon system parameters for each site have also been estimated. Even if they were not available in the same time interval of temperature data, the seasonal variations occurring in the extracted period allowed the characterization of the sampling sites. Monthly mean seawater pH has been derived by the EU Copernicus Marine Service Information (CMEMS) global biogeochemical hindcast spanning 1999–2017 at 0.25° horizontal resolution (Perruche, 2018). Monthly means of DIC in the time interval 1999–2017 have been extracted by CMEMS biogeochemical reanalysis for the Mediterranean Sea at 0.042° horizontal resolution

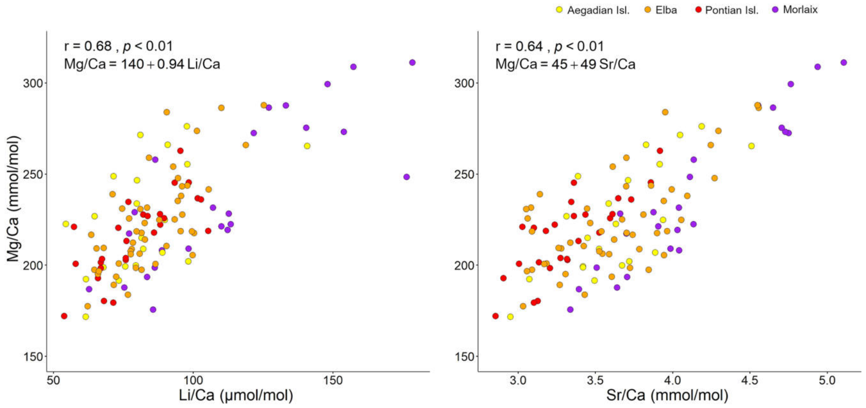

Figure 3. Correlation plots of Mg/Ca with Li/Ca and Sr/Ca. For each analysis the Spearman's coefficient r, the p value, and the line equation are given.

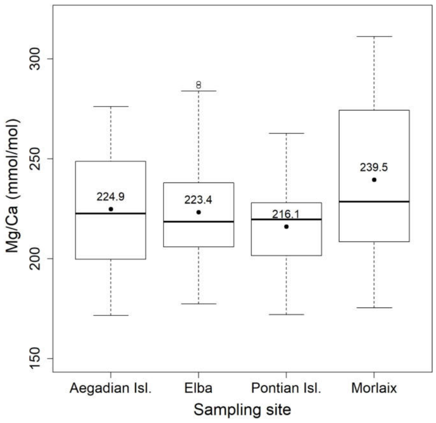

Figure 4. Box plot of the statistical tests performed to evaluate the differences of Mg/Ca in *L. corallioides* collected at different sampling sites. The horizontal black lines indicate the median values. The black dots and the numbers inside the plot indicate the mean values.

(Teruzzi et al., 2021). At the Atlantic site, monthly means of DIC in 1999–2017 were derived from the CMEMS IBI biogeochemical model at 0.083° horizontal resolution (Copernicus Marine Environmental Monitoring Service, 2020). The pH and DIC data showed consistent variations among sites, despite being derived from different biogeochemical models. The mean values of DIC and pH, as reported in Table 1, refer to sampling depth and have been measured over the entire time interval of extraction. The complete timeline of temperature and carbon data used in this paper is shown in Supplement Figs. S5, S6, S7, and S8.

2.4 Growth rate estimation

Growth rates were estimated under light microscope by measuring the length of the LA-ICP-MS transect and dividing it by the number of annual growth bands crossed by the transect (Bracchi et al., 2021). The obtained values are expressed in linear extension per year (mm $\mathrm{yr^{-1}}$). In the samples wherein the growth bands were not easily detectable under microscope, i.e. the Elba sample, we also used the Mg/Ca results in order to check for the correspondence of Mg peaks with growth bands.

2.5 Statistical analysis

Statistics were calculated for both the dataset with all the spot analyses and the dataset with the records from long and short cells separately. Short cells refer to slow-growing cells in dark bands, usually produced in the cold season; long cells correspond to fast-growing cells in light bands, usually produced in the warm season (Kamenos et al., 2009; Ragazzola et al., 2016). For each spot, a distinction between the cells was thus made by image analyses, except for the Elba sample, given the poor resolution of the growth bands. The Spearman's correlation was tested to provide the statistical comparisons between Mg/Ca, Li/Ca, Sr/Ca, and B/Ca records from the LA-ICP-MS analyses in *L. corallioides*. The Kruskal–Wallis test, followed by the Dunn's test for comparisons, and the one-way analysis of variance (ANOVA), followed by the Tukey's test for post hoc analysis, were used to compare the geochemical signals among sampling sites and to evidence the differences between group medians and means. All statistical analyses were run in R 3.6.3 software.

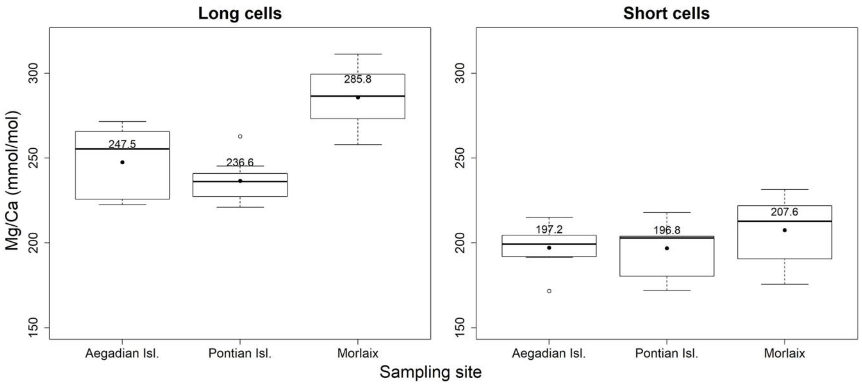

Figure 5. Box plots of the statistical tests performed to evaluate the differences of Mg/Ca in the long and short cells of *L. corallioides* collected at different sampling sites. The horizontal black lines indicate the median values. The black dots and the numbers inside the plot indicate the mean values.

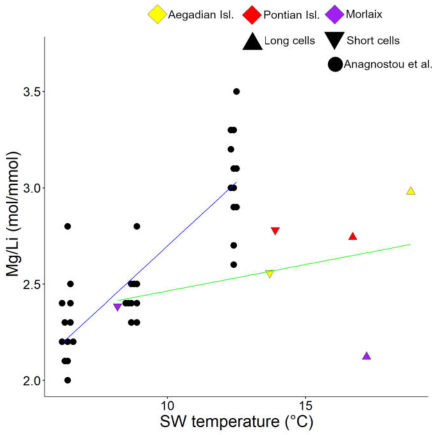

Figure 6. Correlation plot between Mg/Li and seawater temperature. Data are shown for cultured *C. compactum* (Anagnostou et al., 2019) and *L. corallioides* (this paper). *L. corallioides* results are shown separately in long and short cells per sampling site.

3 Results

3.1 Environmental data

The temperature data obtained by ORAS5 reanalysis revealed a lower amplitude of the seasonal temperature change in the Mediterranean samples with respect to the Atlantic site, as shown by the standard deviation and ΔT values in Table 1. This difference is explained in terms of the different sampling depths, with the seasonal variations decreasing with increasing depth.

Temperature variations in Morlaix Bay (Atlantic Ocean) were higher, registering an overall mean seawater temperature of 12.4 °C (Table 1). Among Mediterranean samples, mean seawater temperatures were highest in the Aegadian Isl., followed by Elba and the Pontian Isl. (Table 1). Aegadian Isl. also registered the highest temperature variations among the Mediterranean sites (Table 1). Moderate temperature variations characterized the site in Elba, which registered the lowest monthly mean temperature among Mediterranean sites (Table 1). At the Pontian Isl., consistent with the fact that it is the deepest sampling site at 66 m depth, the lowest seawater temperature variations were found (Table 1).

The pH estimates at the Mediterranean sites were all similarly high at ~ 8.13 and less variable than the Atlantic site (8.05). The mean pH had slightly higher values in Pontian Isl. and Elba than Aegadian Isl. (Table 1). Similarly, DIC was higher in the Mediterranean sites and decreased in Morlaix, as this largely dictates the pH (Table 1).

3.2 Mg/Ca, Li/Ca, Sr/Ca, and Mg/Li

Both Li/Ca and Sr/Ca records had positive correlations with Mg/Ca in our samples of *L. corallioides* (Figs. 3 and S4). The overall mean Mg/Ca was $225.3 \pm 30.4\,\mathrm{mmol\,mol^{-1}}$, registering the minimum value in the sample from Aegadian Isl. ($171.7\,\mathrm{mmol\,mol^{-1}}$) and the maximum value in Morlaix ($311.2\,\mathrm{mmol\,mol^{-1}}$) (Fig. 4; Table 2). The Kruskal–Wallis test did not show significant differences in Mg/Ca among samples (Table A1 in the Appendix; Fig. 4). Among Mediterranean sites, the algal sample from Aegadian Isl. had the highest Mg/Ca mean value, followed by Elba and Pontian Isl., which had the lowest Mg/Ca mean value of all sampling sites (Fig. 4). The highest mean Mg/Ca was registered in the sample from Morlaix Bay, which also showed a large dispersion of data above the median Mg/Ca value (Fig. 4).

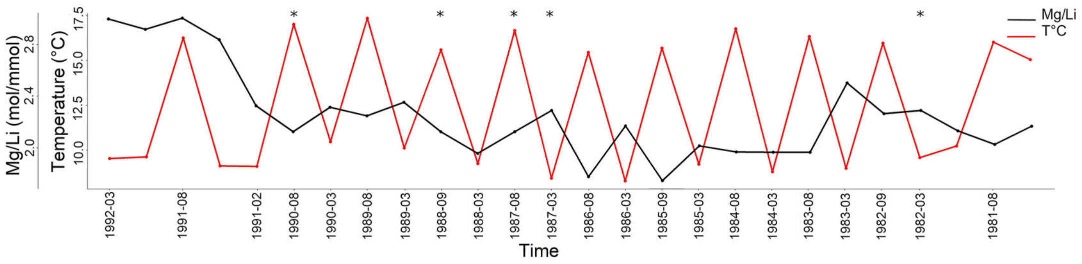

Figure 7. Mg/Li ratio of *L. corallioides* collected in Morlaix Bay. Note the lack of cyclic variations in Mg/Li results. In the timeline, the coldest and the warmest months have been reported. Mg/Li ratios in the missing bands (asterisks) have been calculated as the means of the values measured in warm and cold periods. Monthly means of seawater temperature have been extracted by ORAS5 reanalysis.

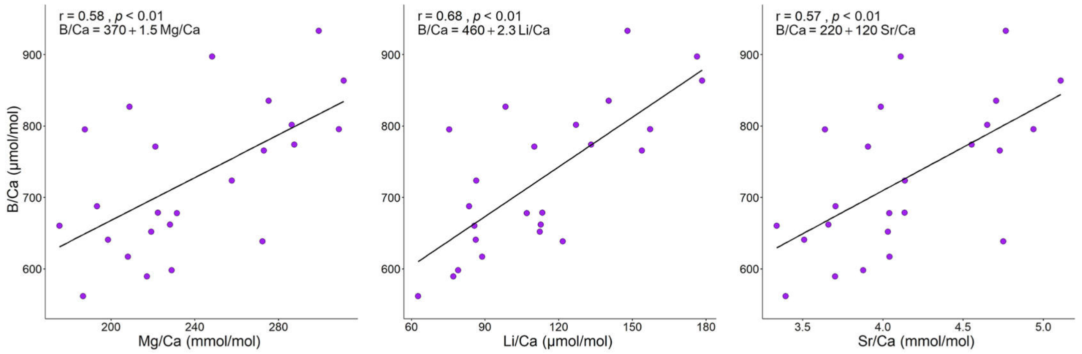

Figure 8. Correlation plots of B/Ca with Mg/Ca, Li/Ca, and Sr/Ca in *L. corallioides* collected in Morlaix Bay. For each analysis the Spearman's coefficient r, the p value, and the line equation are given.

Long cells had high Mg/Ca values; conversely, short cells corresponded to areas with a low Mg/Ca ratio.

The ANOVA test followed by the Tukey's test for multiple comparisons evidenced a significant variability of algal Mg/Ca among three sites in long cells (Table A2; Fig. 5). In the long cells of *L. corallioides* collected from Aegadian Isl. and Pontian Isl., the Mg/Ca data showed a quite similar distribution (Table A2; Fig. 5). The Mg/Ca of the alga from Pontian Isl. was the lowest (Fig. 5). In Morlaix a higher Mg/Ca mean value was registered, which is significantly different compared to Aegadian and Pontian Isl. (Table A2; Fig. 5). In short cells, the differences in Mg/Ca among samples were not statistically significant (Table A1). The magnesium incorporation was slightly higher in Morlaix and very similar between Aegadian and Pontian Isl. samples (Fig. 5).

Mg/Li values in long and short cells fell in the range found by Anagnostou et al. (2019) for cultured *Clathromorphum compactum* (Fig. 6). When plotted against the extracted seawater temperature in Morlaix (Fig. 7), Mg/Li results did not reflect the seasonal oscillations in temperature.

3.3 B/Ca

The B/Ca ratio in the sample collected from Morlaix showed a moderate positive correlation with all the examined temperature proxies (Mg/Ca, Li/Ca, Sr/Ca), with a more defined trend when plotted against Li/Ca ($r = 0.68$) and slightly less defined against Mg/Ca ($r = 0.58$) and Sr/Ca ($r = 0.57$) (Fig. 8). On the contrary, the Spearman's analyses did not evidence significant correlations between B/Ca and the temperature signals in the algae collected elsewhere ($p > 0.05$).

Overall, the B/Ca ratio in *L. corallioides* was $661.9 \pm 138.9\,\mu\text{mol mol}^{-1}$, registering the minimum value in the long cells of the sample from Pontian Isl. ($356.0\,\mu\text{mol mol}^{-1}$) and the maximum value in Elba ($954.1\,\mu\text{mol mol}^{-1}$) (Fig. 9; Table 2).

The Kruskal–Wallis coefficient showed a highly significant difference in the B/Ca value among sites, particularly in the *L. corallioides* from the Pontian Isl., which had the lowest boron incorporation (Table A3; Fig. 9). The algae collected in Aegadian Isl. still had significantly lower B/Ca compared to those collected in Elba and Morlaix (Table A3; Fig. 9).

Table 1. Environmental data from each sampling site. The minimum and maximum monthly means of temperature are indicated, as are the highest temperature variation (ΔT), the mean, and the standard deviation of the time series. Data from monthly means were extracted by 11 years of ORAS5 reanalysis. The pH and DIC for each sampling site are also indicated. The minimum, maximum, mean, and standard deviation values have been measured over the time interval 1999–2017. Carbonate system parameters have been extracted from monthly mean biogeochemical data provided by CMEMS.

Sampling site	Depth (m)	Collection date	Temperature (°C)					pH		DIC (µmol kg^{-1})		Growth rates (mm yr^{-1})
			min	max	ΔT	mean	SD	mean	SD	mean	SD	
Aegadian Isl.	40	25/08/1993	13.7	18.8	5.1	15.9	1.3	8.11	0.02	2303.72	11.58	0.13
Elba	45	01/12/1990	12.9	17.5	4.6	15.0	1.2	8.13	0.02	2322.24	7.08	0.14
Pontian Isl.	66	27/07/2016	13.9	16.7	2.8	15.0	0.6	8.13	0.01	2321.29	6.71	0.10
Morlaix	12	02/05/1991	8.3	17.2	8.9	12.4	2.5	8.05	0.04	2155.60	15.27	0.13

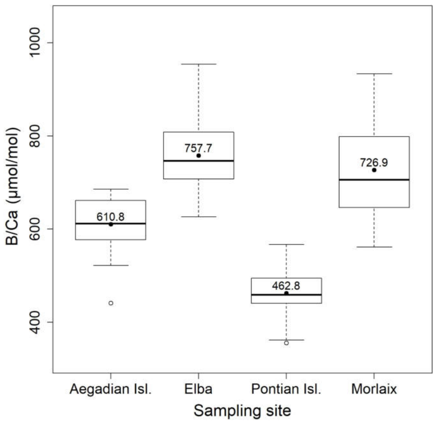

Figure 9. Box plot of the statistical tests performed to evaluate the differences of B/Ca in *L. corallioides* collected at different sampling sites. The horizontal black lines indicate the median values. The black dots and the numbers inside the plot indicate the mean values.

The highest B/Ca mean value was registered in Elba, with medians comparable to Morlaix (Table A3; Fig. 9).

The ANOVA test followed by the Tukey's test for multiple comparisons by site, for long (Table A4) and short cells (Table A5) separately, showed lower values at the Mediterranean sites and higher values at the Atlantic site (Fig. 10).

The sample from Pontian Isl. had the lowest mean B/Ca in both seasons, being significantly different from the samples from both Morlaix and Aegadian Isl. (Tables A4, A5; Fig. 10). Morlaix had the highest mean B/Ca in both long and short cells (Tables A4, A5; Fig. 10). *L. corallioides* from Aegadian Isl. had an intermediate B/Ca mean value in long cells, differing significantly from both the Morlaix and Pontian Isl. samples (Table A4; Fig. 10). In short cells, the sample from Aegadian Isl. slightly differed from the one in Morlaix (Table A5; Fig. 10).

Interestingly, the long cells of all samples had higher median B/Ca values compared to short cells (Fig. 10), although only in Morlaix, the differences between B/Ca measured in long and short cells were statistically significant ($\chi^2 = 8.4899$, $p < 0.01$).

3.4 Growth rates

In the sample from Aegadian Isl., the LA-ICP-MS transect was 1.31 mm long, and 10 years of growth was detected by coupling microscopical imaging and Mg/Ca peaks, resulting in a growth rate of 0.13 mm yr^{-1}. In the Elba sample the laser transect was 1.15 mm long, crossing 8 years of growth, with a resulting growth rate of 0.14 mm yr^{-1}. The Pontian Isl. sample had 1.08 mm of transect including 11 years of growth and hence a growth rate of 0.10 mm yr^{-1}. Finally, the transect from the Morlaix sample was 1.38 mm long, counting 11 years and resulting in a growth rate of 0.13 mm yr^{-1}.

Growth rates did not show any linear relationship with Mg, Li, and Sr/Ca, but they were positively correlated with the sample mean B/Ca values (Fig. 11).

4 Discussion

Temperature variations affect many physiological processes involved in biomineralization, and the rate of calcification, along with the preservation state of mineral structures, influences the content of trace elements in carbonates (Lorens, 1981; Rimstidt et al., 1998; Gussone et al., 2005; Noireaux et al., 2015; Kaczmarek et al., 2016). Trace element concentrations recorded from the four *L. corallioides* branches analysed in this study were consistent with previously published values for other calcareous red algae (Chave, 1954; Hemming and Hanson, 1992; Hetzinger et al., 2011; Darrenougue et al., 2014). Particularly, the Mg/Ca ratios recorded in this study ranged from 172 to 311 mmol mol^{-1}, which is comparable to previous studies on rhodoliths of *Lithothamnion glaciale* Kjellman 1883 grown at 6–15 °C (148–326 mmol mol^{-1}) (Kamenos et al., 2008). The B/Ca

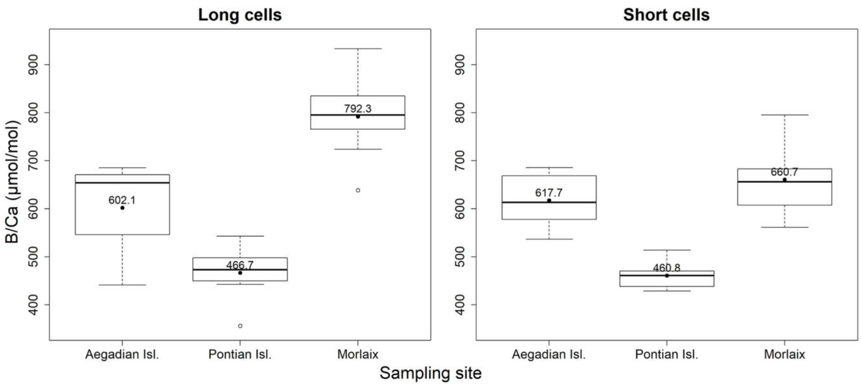

Figure 10. Box plots of the statistical tests performed to evaluate the differences of B/Ca in the long and short cells of *L. corallioides* collected at different sampling sites. The horizontal black lines indicate the median values. The black dots and the numbers inside the plot indicate the mean values.

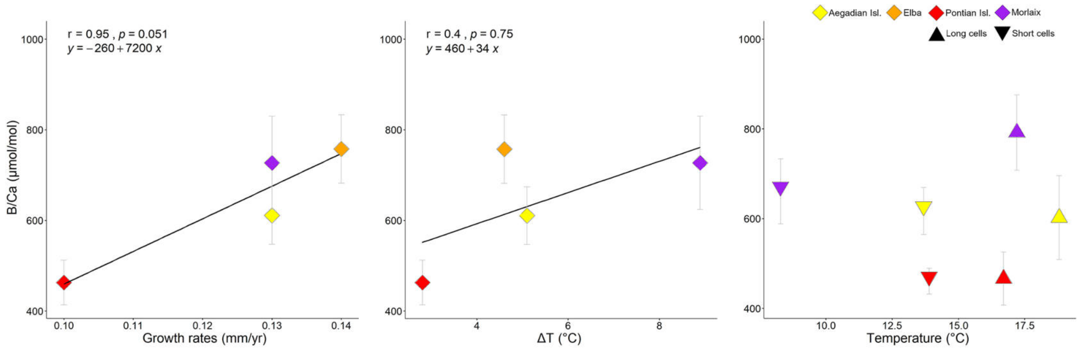

Figure 11. Correlation plots of growth rates and seawater temperature with B/Ca in *L. corallioides* samples analysed in this study. Spearman's coefficient r, the p value, and the line equation are given. Temperature variations (ΔT) correspond to the differences between the maximum and minimum temperature registered over 11 years of monthly reanalysis (ORAS5). The B/Ca means measured in long and short cells respectively correspond to the maximum and minimum temperature.

ratios in *L. corallioides* from our results range from 356 to 954 µmol mol^{-1}, which is wider than the range measured by solution ICP-MS on bulk samples of *Neogoniolithon* sp. (352–670 µmol mol^{-1}) (Donald et al., 2017) and *C. compactum* (320–430 µmol mol^{-1}) (Anagnostou et al., 2019), both cultured with controlled $p\mathrm{CO_2}$ and a pH ranging from 7.2 to 8.2. The high resolution given by laser ablation should be more effective in measuring the heterogeneity of B/Ca across the thallus, thus explaining the wider range of our data.

The Mg/Ca results evidenced a strong relationship with the seawater temperatures extracted from ORAS5 (Table 1; Fig. 12), as expected. *L. corallioides* from Aegadian Isl. had slightly higher Mg/Ca values, followed by Elba and Pontian Isl. (Fig. 4). This was consistent with local temperature values in the Mediterranean (Table 1), since Pontian Isl. registered the lowest mean value and the lowest ΔT, while Aegadian Isl. showed the highest mean temperature and ΔT. On the contrary, the sample from Morlaix, collected at 12 m depth, showed high Mg/Ca values in both long and short cells (Table A2; Fig. 5). The monthly mean temperatures had the highest variations during the year (ΔT in Table 1) due to the shallower depth (12 m) and the geographical location. Temperature correlates with seasons, influencing primary production, respiration, and calcification in *L. corallioides* (Payri, 2000; Martin et al., 2006) as well as other calcareous red algae (Roberts et al., 2002). The high seasonality that characterized the sample from Morlaix, represented by the high ΔT (Table 1), was probably responsible for the highest variation of Mg/Ca values and undoubtedly

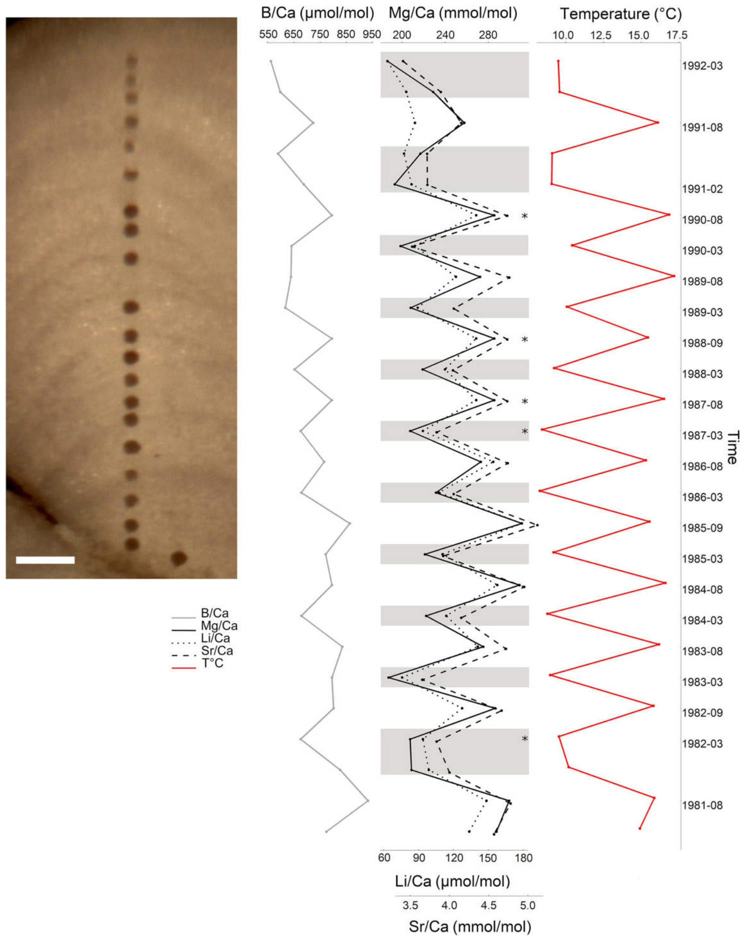

Figure 12. Elemental ratios in *L. corallioides* collected in Morlaix Bay (scale bar: 200 µm). Mg, Li, and Sr/Ca show cyclic variations mirroring the local seawater temperature. In the timeline, the coldest and the warmest months have been reported, which correspond to dark and light bands of growth. Element / Ca ratios in the missing bands (asterisks) have been calculated as the means of the values measured in warm or cold periods. Monthly means of temperature have been extracted by ORAS5 reanalysis.

accounted for most of the differences with Mediterranean samples. For the first time, we confirmed the reliability of the temperature proxies Li/Ca and Sr/Ca on a wild-grown coralline alga collected at different depths and locations. Li/Ca and Sr/Ca records were positively correlated with Mg/Ca in *L. corallioides* (Fig. 3), which, in turn, showed a strong relationship with seawater temperature. Moreover, both Li and Sr/Ca showed periodical oscillations in correspondence to long and short cells, related to seasonal temperature variations (Fig. 12). Therefore, Li/Ca and Sr/Ca could be regarded as temperature proxies in *L. corallioides*, as could Mg/Ca. The coupling of the Mg/Ca ratio with Li/Ca and Sr/Ca can be considered a useful technique to gather information about past temperature for paleoclimate reconstructions (Halfar et al., 2011; Caragnano et al., 2014; Williams et al., 2014; Fowell et al., 2016; Cuny-Guirriec et al., 2019).

The B/Ca ratio in coralline algae has rarely been measured, and it is not clear how the environmental factors control its incorporation. The carbonate system primarily drives the changes in B incorporation (Hemming and Hanson, 1992; Yu and Elderfield, 2007). In benthic foraminifera, B/Ca increases with $[CO_3^{2-}]$ (Yu and Elderfield, 2007), whereas there is no consensus on the effect of $[CO_3^{2-}]$ on Mg/Ca

Table 2. Element / Ca ratio measurements in *L. corallioides*.

Sampling site	B/Ca (μmol mol^{-1})		Mg/Ca (mmol mol^{-1})		Li/Ca (μmol mol^{-1})		Sr/Ca (mmol mol^{-1})		Mg/Li (mol mmol^{-1})	
	mean	SD	mean	SD	mean	SD	mean	SD	mean	SD
Aegadian Isl.	610.8	63.9	224.9	30.3	81.9	18.4	3.7	0.4	2.8	0.5
Elba	757.7	75.5	223.4	26.4	85.2	14.3	3.6	0.4	2.7	0.3
Pontian Isl.	462.8	49.2	216.1	21.9	79.6	14.6	3.3	0.3	2.8	0.4
Morlaix	726.9	102.8	239.5	41.2	113.1	32.9	4.1	0.5	2.2	0.4
Total	661.9	138.9	225.3	30.4	89.0	23.3	3.7	0.5	2.6	0.4

and Sr/Ca (Rosenthal et al., 2006; Dueñas-Bohórquez et al., 2011). Experiments with inorganic calcite showed a positive correlation between B/Ca and [DIC] (Uchikawa et al., 2015). Nevertheless, in culture experiments of the coralline algae *Neogoniolithon* sp. (Donald et al., 2017) and corals (Gagnon et al., 2021), [DIC] had a negative effect on B/Ca. DIC and B/Ca values showed a negative relationship in the samples from Morlaix, Aegadian Isl., and Pontian Isl., which was not observed in Elba (Fig. 9; Table 1). Significant differences among B/Ca values in the Mediterranean samples were not expected, since DIC concentrations were similar (Table 1). This evidence suggests influences other than DIC on the B signal.

The mean estimated growth rate of *L. corallioides* was $0.13 \pm 0.02\,\mathrm{mm\,yr^{-1}}$, and it was supposed to decrease with increasing depth as a direct consequence of lower light availability (Halfar et al., 2011); indeed, the growth rate of the sample from Pontian Isl. was the lowest ($0.10\,\mathrm{mm\,yr^{-1}}$). As already suggested by previous studies on both synthetic and biogenic calcite, B incorporation is likely affected by growth rate (Gabitov et al., 2014; Mavromatis et al., 2015; Noireaux et al., 2015; Uchikawa et al., 2015; Kaczmarek et al., 2016). Indeed, in the cultured calcareous red alga *Neogoniolithon* sp. B/Ca increases with increasing growth rate (Donald et al., 2017). The slowest growth rate found in Pontian Isl. possibly contributed to the lowest B/Ca value; similarly, the highest growth rate ($0.14\,\mathrm{mm\,yr^{-1}}$) in the sample from Elba could be responsible for the highest B/Ca (Figs. 9, 11). The mean annual growth rate of the shallowest sample (Morlaix) was intermediate ($0.13\,\mathrm{mm\,yr^{-1}}$) and likely not constant during the year. In Morlaix, the alga probably significantly slowed down the growth in cold months, when the monthly mean seawater temperature was the lowest of all sampling sites (Table 1). Nevertheless, its growth rate likely sped up in the warm season due to the abundant light availability at shallow depth and the warming of seawater (Table 1), contributing to the significantly higher B/Ca values in long cells (Fig. 10). According to this interpretation, the effect of the growth rate on B/Ca might be significant across depth and geographical regions (Fig. 11).

In Morlaix, B/Ca showed a weak positive correlation with temperature proxies (Mg/Ca, Li/Ca, and Sr/Ca; Fig. 8). A positive correlation between B/Ca and Mg/Ca was already observed in planktonic foraminifera (Wara et al., 2003; Yu et al., 2007). Therefore, we reconstructed the elemental variations during algal growth in the Morlaix sample at annual resolution in order to highlight the influence of temperature (Fig. 12). Contrary to Mg, Li, and Sr/Ca, the B/Ca did not mirror the seasonal temperature variations as accurately as the other proxies.

In the sample from the Pontian Isl., the seasonal ΔT, Mg/Ca, and B/Ca values were the lowest among sites. In particular, B/Ca was significantly low (Fig. 9), differing more from the other samples than the results for Mg/Ca (Fig. 4). This suggests that in this sample the B incorporation should be influenced by factors other than those affecting Mg. In general, the poor correlation with seawater temperature (Fig. 11), and most of all the lack of distinct seasonal oscillations in B/Ca across the algal thallus (Fig. 12), excludes the suitability of B/Ca as a temperature proxy and suggests a closer relationship with growth rate than temperature.

Knowing the biogeochemistry and the variation of the environmental variables of seawater is crucial for a more comprehensive picture of the reliability of geochemical proxies like the ones investigated here (Mg, Li, Sr/Ca, and B/Ca). Boron incorporation in marine carbonates is still debated, raising questions about the boron isotopic fractionation, the seawater isotopic composition, and the so-called "vital effects" (i.e. the metabolic activities that can bias the proxy record). Vital effects include species-specific biologically controlled up-regulations of pH in the calcifying fluid in both corals and coralline algae in response to pH manipulations mimicking the ongoing ocean acidification (Cornwall et al., 2017, 2018). Natural marine pH undergoes pH fluctuations with characteristic ranges of about 0.3 pH units in very shallow coastal water, in areas with restricted circulation, or in shallow nearshore communities supporting high rates of benthic metabolism, such as seagrass beds (Cornwall et al., 2013; Duarte et al., 2013; Hofmann et al., 2011). However, this study analysed the trace element record in a single high-Mg-calcite species grown in a natural wide bathymetric interval (from 10 to 66 m depth) characterized by normal marine pH (range 8.05–8.13, Table 1). Therefore, we considered upregulation, if present, to be constant among our conspecific specimens and thus irrelevant for the measured B/Ca variations. Moreover, no significant yearly pH fluctuations are expected at each site. Thus, within a single specimen, the observed differences in B/Ca between short and long cells (i.e. cold and warm periods of growth) (Fig. 10) are unlikely to be related to changes in $\mathrm{pH_{cf}}$.

The paucity of B/Ca measurements from coralline algae and, most of all, the complete absence of these data on specimens grown in nature make it difficult to compare our B/Ca data with the literature. This observation takes stock of the significance of our results and emphasizes the importance of collecting more representative B/Ca data in coralline algae. Further studies on *L. corallioides* and other calcareous red algae should be carried out to clarify the environmental factors influencing the B/Ca in these organisms and to ensure the reliability of this proxy for paleoclimate reconstructions.

5 Conclusions

This paper presents the first measures of trace elements (Mg, Sr, Li, and B) from the coralline alga *L. corallioides* collected across the Mediterranean Sea and in the Atlantic Ocean at different oceanographic settings and depths (12, 40, 45, and 66 m depth), providing the first geochemical data on a wild-grown coralline algal species sampled at different depths and geographical locations. LA-ICP-MS records of Mg/Ca, Sr/Ca, and Li/Ca have shown a similar trend, primarily controlled by seawater temperatures in the algal habitat. On the contrary, Mg/Li did not provide a valuable temperature proxy in this species. In order to evaluate the control exerted by temperature over B incorporation, we also tested the correlation of B/Ca with Mg/Ca, Li/Ca. and Sr/Ca. This led us to provide the first B/Ca data on wild-grown coralline algae from across the photic zone in different basins. The correlation between B/Ca and Mg/Ca in *L. corallioides* was statistically significant only in the shallow Atlantic waters of Morlaix, where seasonality, and hence the seasonal temperature variations, during the algal growth was the strongest among sites. Accordingly, B incorporation differences between long and short cells of *L. corallioides* strongly depend on seasonality, being statistically significant just in Morlaix. Nevertheless, in contrast to Mg, Li, and Sr/Ca, B/Ca oscillations across the algal growth showed a poor relationship with seasonal variations in seawater temperature. We found high B/Ca values in the Atlantic sample, wherein pH and DIC were the lowest. Carbon data did not explain the low B concentration in the Pontian Isl. sample (66 m depth), though, wherein pH and DIC were similar to the other Mediterranean sites. The estimation of growth rate, which was low in the Pontian Isl. sample ($0.10\,\mathrm{mm\,yr^{-1}}$) and got higher in the other Mediterranean samples and in Morlaix ($\sim 0.13\,\mathrm{mm\,yr^{-1}}$), led us to conclude that B/Ca relates to growth rate rather than seawater temperature. B incorporation is therefore subject to the specific algal growth patterns and rates, knowledge of which is essential in order to assess the reliability of B/Ca in tracing seawater carbon variations.

Appendix A

Table A1. (a) Statistically non-significant results of tests performed to evaluate **(a)** the differences of Mg/Ca in *L. corallioides* and **(b)** the differences of Mg/Ca in the short cells of *L. corallioides* collected at different sampling sites. Test significance at $\alpha = 0.05$.

(a) Kruskal–Wallis test (Mg/Ca)

	Df	χ^2	P
Site	3	3.799	0.284

(b) One-way ANOVA test (Mg/Ca)

	Short cells				
	Df	Sum sq.	Mean sq.	F value	Pr ($> F$)
Site	2	788.1	394.0	1.4647	0.2496
Residuals	26	6994.5	269.0		
Shapiro–Wilk normality test			$P = 0.6442$		
Bartlett's K squared			$P = 0.5856$		

Table A2. Results of statistical tests performed to evaluate the differences of Mg/Ca in the long cells of *L. corallioides* collected at different sampling sites. Statistically significant p values are given in bold. ANOVA test significance at $\alpha = 0.05$; Tukey's test significant at $p \leq \alpha$.

One-way ANOVA test (Mg/Ca)					
	Long cells				
	Df	Sum sq.	Mean sq.	F value	Pr (> F)
Site	2	10 897.7	5448.9	16.413	**0.0001**
Residuals	20	6639.8	332.0		
Shapiro–Wilk normality test			$P = 0.1440$		
Bartlett's K squared			$P = 0.5826$		
Tukey's test					
	Multiple comparisons of means				
Site	Mean difference	95 % confidence interval		P. adjusted	
	Site	lower bound	upper bound		
Morlaix–Aegadian Isl.	38.32918	15.09816	61.56019	**0.00130**	
Pontian Isl.–Aegadian Isl.	−10.84361	−35.48382	13.79661	0.51716	
Pontian Isl.–Morlaix	−49.17278	−72.40380	−25.94177	**0.00009**	

Table A3. Results of statistical tests performed to evaluate the differences of B/Ca in *L. corallioides* collected at different sampling sites. Statistically significant p values are given in bold. Kruskal–Wallis test significance at $\alpha = 0.05$; Dunn's test significant at $p \leq \alpha/2$.

Kruskal–Wallis test (B/Ca)			
	Df	χ^2	P
Site	3	79.816	**$< 2.2 \times 10^{-16}$**
Dunn's test Comparisons by site (Bonferroni)			
Z P. adjusted	Aegadian Isl.	Elba	Morlaix
Elba	−4.64580 **0.00000**		
Morlaix	−3.07755 **0.00630**	1.17249 0.72300	
Pontian Isl.	2.80564 **0.01510**	8.38673 **0.00000**	6.15663 **0.00000**

Table A4. Results of statistical tests performed to evaluate the differences of B/Ca in the long cells of *L. corallioides* collected at different sampling sites. Statistically significant p values are given in bold. ANOVA test significance at $\alpha = 0.05$; Tukey's test significant at $p \leq \alpha$.

One-way ANOVA test (B/Ca)					
	Long cells				
	Df	Sum sq.	Mean sq.	F value	Pr (> F)
Site	2	428 364	214 182	33.066	**0.0000**
Residuals	20	129 546	6477		
Shapiro–Wilk normality test			$P = 0.5527$		
Bartlett's K squared			$P = 0.5470$		

Tukey's test				
	Multiple comparisons of means			
Site	Mean difference	95% confidence interval		P. adjusted
	Site	lower bound	upper bound	
Morlaix–Aegadian Isl.	190.11730	87.50374	292.73094	**0.00040**
Pontian Isl.–Aegadian Isl.	−135.42490	−244.26303	−26.58672	**0.01342**
Pontian Isl.–Morlaix	−325.54220	−428.15581	−222.92862	**0.00000**

Table A5. Results of statistical tests performed to evaluate the differences of B/Ca in the short cells of *L. corallioides* collected at different sampling sites. Statistically significant p values are given in bold. ANOVA test significance at $\alpha = 0.05$; Tukey's test significant at $p \leq \alpha$.

One-way ANOVA test (B/Ca)					
	Short cells				
	Df	Sum sq.	Mean sq.	F value	Pr (> F)
Site	2	216 232	108 116	35.360	**0.0000**
Residuals	26	79497	3058		
Shapiro–Wilk normality test			$P = 0.1699$		
Bartlett's K squared			$P = 0.0576$		

Tukey's test				
	Multiple comparisons of means			
Site	Mean difference	95 % confidence interval		P. adjusted
	Site	lower bound	upper bound	
Morlaix–Aegadian Isl.	43.09640	−19.61932	105.81212	0.22146
Pontian Isl.–Aegadian Isl.	−156.90170	−223.66771	−90.13574	**0.00001**
Pontian Isl.–Morlaix	−199.99810	−260.58727	−139.40898	**0.00000**

Data availability. Data resulting from this study are available at https://doi.org/10.1594/PANGAEA.932201 (last access: 28 January 2022, Piazza et al., 2021). Environmental data were provided by EU Copernicus Marine Service Information. DIC data in the Mediterranean: https://doi.org/10.25423/CMCC/MEDSEA_MULTIYEAR_BGC_006_008_MEDBFM3 (last access: 28 January 2022, Teruzzi et al., 2021). DIC data in the Atlantic Ocean: https://resources.marine.copernicus.eu/?option=com_cswview=detailsproduct_id=IBI_MULTIYEAR_BGC_005_003 (last access: 28 January 2022, Copernicus Marine Environmental Monitoring Service, 2020.) The pH data: https://resources.marine.copernicus.eu/?option=com_cswview=detailsproduct_id=GLOBAL_REANALYSIS_BIO_001_029 (last access: 13 October 2021, Perruche, 2018) Temperature data: https://icdc.cen.uni-hamburg.de/daten/reanalysis-ocean/easy-init-ocean/ecmwf-oras5.html (last access: 28 January 2022, Zuo et al., 2019).

Supplement. The supplement related to this article is available online at: https://doi.org/10.5194/bg-19-1047-2022-supplement.

Author contributions. DB, VAB, and GP conceptualized the research question and study design. AL, DB, and VAB conducted the experimental work. ANM and GP performed the environmental data extraction. GP performed the data analysis and prepared the draft of the paper. All authors contributed to the editing and reviewing of the paper.

Competing interests. The contact author has declared that neither they nor their co-authors have any competing interests.

Acknowledgements. We are grateful to the anonymous referees whose comments enabled us to significantly improve the paper. This paper is a contribution to the project MIUR-Dipartimenti di Eccellenza 2018–2022 DISAT-UNIMIB. The Pontian Isl. sample has been collected in the framework of "Convenzione MATTM-CNR per i Programmi di Monitoraggio per la Direttiva sulla Strategia Marina (MSFD, Art. 11, Dir. 2008/56/CE)". The captain, crew, and scientific staff of the RV *Minerva Uno* cruise Strategia Marina Ligure–Tirreno are acknowledged for their efficient and skilful cooperation at sea. Financial support for GP was provided by the University of Milano–Bicocca as a PhD fellowship.

Financial support. This research has been supported by the national project FISR (grant no. 2019_04543 CRESCIBLUREEF).

Review statement. This paper was edited by Aninda Mazumdar and reviewed by five anonymous referees.

References

Adey, W. H.: The genus *Clathromorphum* (Corallinaceae) in the Gulf of Maine, Hydrobiologia, 26, 539–573, https://doi.org/10.1007/BF00045545, 1965.

Adey, W. H. and McKibbin, D.: Studies on the maerl species *Phymatolithon calcareum* (Pallas) nov. comb. and *Lithothamnion coralloides* Crouan in the Ria de Vigo, Bot. Mar., 13, 100–106, https://doi.org/10.1515/botm.1970.13.2.100, 1970.

Allen, K. A., Hönisch, B., Eggins, S. M., and Rosenthal, Y.: Environmental controls on B/Ca in calcite tests of the tropical planktic foraminifer species *Globigerinoides ruber* and *Globigerinoides sacculifer*, Earth Planet. Sc. Lett., 351, 270–280, https://doi.org/10.1016/j.epsl.2012.07.004, 2012.

Anagnostou, E., Williams, B., Westfield, I., Foster, G. L., and Ries, J. B.: Calibration of the pH-δ^{11}B and temperature-Mg/Li proxies in the long-lived high-latitude crustose coralline red alga *Clathromorphum compactum* via controlled laboratory experiments, Geochim. Cosmochim. Ac., 254, 142–155, https://doi.org/10.1016/j.gca.2019.03.015, 2019.

Andersson, A. J. and Mackenzie, F. T.: Technical comment on Kroeker et al. (2010) Meta-analysis reveals negative yet variable effects of ocean acidification on marine organisms, Ecol. Lett., 13, 1419–1434, https://doi.org/10.1111/j.1461-0248.2011.01646.x, 2011.

Andersson, A. J., Mackenzie, F. T., and Bates, N. R.: Life on the margin: implications on Mgcalcite, high latitude and cool-water marine calcifiers, Mar. Ecol. Prog. Ser., 373, 265–273, https://doi.org/10.3354/meps07639, 2008.

Barker, S., Cacho, I., Benway, H., and Tachikawa, K.: Planktonic foraminiferal Mg/Ca as a proxy for past oceanic temperatures: a methodological overview and data compilation for the Last Glacial Maximum, Quat. Sci. Rev., 24, 821–834, https://doi.org/10.1016/j.quascirev.2004.07.016, 2005.

Basso, D.: Study of living calcareous algae by a paleontological approach: the non-geniculate Corallinaceae (Rhodophyta) of the soft bottoms of the Tyrrhenian Sea (western Mediterranean). The genera *Phymatolithon* Foslie and *Mesophyllum* Lemoine, Riv. Ital. Paleontol. S., 100, 575–596, https://doi.org/10.13130/2039-4942/8602, 1995a.

Basso, D.: Living calcareous algae by a paleontological approach: the genus *Lithothamnion* Heydrich nom. cons. from the soft bottoms of the Tyrrhenian Sea (Mediterranean), Riv. Ital. Paleontol. S., 101, 349–366, https://doi.org/10.13130/2039-4942/8592, 1995b.

Basso, D.: Carbonate production by calcareous red algae and global change, Geodiversitas, 34, 13–33, https://doi.org/10.5252/g2012n1a2, 2012.

Basso, D. and Brusoni, F.: The molluscan assemblage of a transitional environment: the Mediterranean maerl from off the Elba Island (Tuscan Archipelago, Tyrrhenian Sea), Boll. Malacol., 40, 37–45, 2004.

Basso, D., Babbini, L., Kaleb, S., Bracchi, V. A., and Falace, A.: Monitoring deep Mediterranean rhodolith beds, Aquat. Conserv., 26, 549–561, https://doi.org/10.1002/aqc.2586, 2016.

Basso, D., Babbini, L., Ramos-Esplá, A. A., and Salomidi, M.: Mediterranean rhodolith beds, in: Rhodolith/maërl beds: A global perspective, edited by: Riosmena-Rodrìguez, R., Wendy Nelson, W., and Aguirre, J., Springer, Cambridge, 281–298, https://doi.org/10.1007/978-3-319-29315-8_ 11, 2017.

Berner, R. A.: The role of magnesium in the crystal growth of calcite and aragonite from sea water, Geochim. Cosmochim. Ac., 39, 489–504, https://doi.org/10.1016/0016-7037(75)90102-7, 1975.

Bracchi, V. A., Piazza, G., and Basso, D.: A stable ultrastructural pattern despite variable cell size in *Lithothamnion corallioides*, Biogeosciences, 18, 6061–6076, https://doi.org/10.5194/bg-18-6061-2021, 2021.

Brewer, P. G.: Ocean chemistry of the fossil fuel signal: The haline signature of "Business as Usual", Geophys. Res. Lett., 24, 1367–1369, 1997.

Cabioch, J.: Contribution à l'étude morphologique, anatomique et systématique de deux Mélobésiées: *Lithothamnium calcareum* (Pallas) Areschoug et *Lithothamnium corallioides* Crouan, Bot. Mar., 9, 33–53, 1966.

Caldeira, K., Akai, M., Brewer, P., Chen, B., Haugan, P., Iwama, T., Johnston, P., Kheshgi, H., Li, Q., Ohsumi, T., Poertner, H., Sabine, C., Shirayama, Y., and Thomson, J.: Ocean Storage, in: Carbon Dioxide Capture and Storage: A Special Report of IPCC Working Group III, Cambridge University Press, Cambridge UK, ISBN 10-0-521-68551-6, 2005.

Callendar, G. S.: The artificial production of carbon dioxide and its influence on temperature, Q. J. Roy. Meteor. Soc., 64, 223–240, 1938.

Caragnano, A., Basso, D., Jacob, D. E., Storz, D., Rodondi, G., Benzoni, F., and Dutrieux, E.: Coralline red alga *Lithophyllum kotschyanum* f. affine as proxy of climate variability in the Yemen coast, Gulf of Aden (NW Indian Ocean), Geochim. Cosmochim. Ac., 124, 1–17, https://doi.org/10.1016/j.gca.2013.09.021, 2014.

Caragnano, A., Basso, D., Storz, D., Jacob, D. E., Ragazzola, F., Benzoni, F., and Dutrieux, E.: Elemental variability in the coralline alga *Lithophyllum yemenense* as an archive of past climate in the Gulf of Aden (NW Indian Ocean), J. Phycol., 53, 381–395, https://doi.org/10.1111/jpy.12509, 2017.

Carro, B., Lopez, L., Peña, V., Bárbara, I., and Barreiro, R.: DNA barcoding allows the accurate assessment of European maerl diversity: a proof-of-concept study, Phytotaxa, 190, 176–189, https://doi.org/10.11646/phytotaxa.190.1.12, 2014.

Chan, P., Halfar, J., Adey, W., Hetzinger, S., Zack, T., Moore, G. W. K., Wortmann, U. G., Williams, B., and Hou, A.: Multicentennial record of Labrador Sea primary productivity and sea-ice variability archived in coralline algal barium, Nat. Commun., 8, 15543, https://doi.org/10.1038/ncomms15543, 2017.

Chave, K. E.: Aspects of the biogeochemistry of magnesium 1. Calcareous marine organisms, J. Geol., 62, 266–283, 1954.

Copernicus Marine Environmental Monitoring Service: Atlantic-Iberian Biscay Irish-Ocean BioGeoChemistry NON ASSIMILATIVE Hindcast, CMEMS [data set], https://doi.org/10.48670/moi-00028, 2020.

Cornwall, C. E., Hepburn, C. D., McGraw, C. M., Currie, K. I., Pilditch, C. A., Hunter, K. A., Boyd, P. W., and Hurd, C. L.: Diurnal fluctuations in seawater pH influence the response of a calcifying macroalga to ocean acidification, P. Roy. Soc. B-Bio., 280, 20132201, https://doi.org/10.1098/rspb.2013.2201, 2013.

Cornwall, C. E., Comeau, S., and Mcculloch, M. T.: Coralline algae elevate pH at the site of calcification under ocean acidification, Glob. Change Biol., 23, 1–12, https://doi.org/10.1111/gcb.13673, 2017.

Cornwall, C. E., Comeau, S., DeCarlo, T. M., Moore, B., D'Alexis, Q., and McCulloch, M. T.: Resistance of corals and coralline algae to ocean acidification: physiological control of calcification under natural pH variability, P. Roy. Soc. B-Bio., 286, 20181168, https://doi.org/10.1098/rspb.2018.1168, 2018.

Corrège, T.: Sea surface temperature and salinity reconstruction from coral geochemical tracers, Palaeogeogr. Palaeocl., 232, 408–428, https://doi.org/10.1016/j.palaeo.2005.10.014, 2006.

Comeau, S., Cornwall, C. E., and McCulloch, M. T.: Decoupling between the response of coral calcifying fluid pH and calcification under ocean acidification, Sci. Rep., 7, 7573, https://doi.org/10.1038/s41598-017-08003-z, 2017.

Cuny-Guirriec, K., Douville, E., Reynaud, S., Allemand, D., Bordier, L., Canesi, M., Mazzoli, C., Taviani, M., Canese, S., McCulloch, M., Trotter, J., Rico-Esenaro, S. D., Sanchez-Cabeza, J.-A., Ruiz-Fernàndez, A. C., Carricart-Ganivet, J. P., Scott, P. M., Sadekov, A., and Montagna, P.: Coral Li/Mg thermometry: Caveats and constraints, Chem. Geol., 523, 162–178, https://doi.org/10.1016/j.chemgeo.2019.03.038, 2019.

Darrenougue, N., De Deckker, P, Eggins, S., and Payri, C.: Sea-surface temperature reconstruction from trace elements variations of tropical coralline red algae, Quat. Sci. Rev., 93, 34–46, https://doi.org/10.1016/j.quascirev.2014.03.005, 2014.

DeCarlo, T. M., Holcomb, M., and McCulloch, M. T.: Reviews and syntheses: Revisiting the boron systematics of aragonite and their application to coral calcification, Biogeosciences, 15, 2819–2834, https://doi.org/10.5194/bg-15-2819-2018, 2018.

Dickson, A. G.: Thermodynamics of the dissociation of boric acid in synthetic seawater from 273.15 to 318.15 K, Deep-Sea Res., 37, 755–766, https://doi.org/10.1016/0198-0149(90)90004-F, 1990.

D'Olivo, J. P., Sinclair, D. J., Rankenburg, K., and McCulloch, M. T.: A universal multi-trace element calibration for reconstructing sea surface temperatures from long-lived *Porites* corals: removing "vital-effects", Geochim. Cosmochim. Ac., 239, 109–135, https://doi.org/10.1016/j.gca.2018.07.035, 2018.

Donald, H. K., Ries, J. B., Stewart, J. A., Fowell, S. E., and Foster, G. L.: Boron isotope sensitivity to seawater pH change in a species of *Neogoniolithon* coralline red alga, Geochim. Cosmochim. Ac., 217, 240–253, https://doi.org/10.1016/j.gca.2017.08.021, 2017.

Douville, E., Paterne, M., Cabioch, G., Louvat, P., Gaillardet, J., Juillet-Leclerc, A., and Ayliffe, L.: Abrupt sea surface pH change at the end of the Younger Dryas in the central sub-equatorial Pacific inferred from boron isotope abundance in corals (*Porites*), Biogeosciences, 7, 2445–2459, https://doi.org/10.5194/bg-7-2445-2010, 2010.

Duarte, C. M., Hendriks, I. E., Moore, T. S., Olsen, Y. S., Steckbauer, A., Ramajo, L., Jacob Carstensen, J., Trotter, J. A., and McCulloch, M.: Is ocean acidification an open-ocean syndrome?, Understanding anthropogenic impacts on seawater pH, Estuar. Coast., 36, 221–236, 2013.

Dueñas-Bohórquez, A., Raitzsch, M., Nooijer, L. J., and Reichart, G.-J.: Independent impacts of calcium and carbonate ion concentration on Mg and Sr incorporation in cultured benthic foraminifera, Mar. Micropaleontol., 81, 122–130, https://doi.org/10.1016/j.marmicro.2011.08.002, 2011.

Fairhall, A. W.: Accumulation of fossil CO_2 in the atmosphere and the sea, Nature, 245, 20–23, 1973.

Fietzke, J., Heinemann, A., Taubner, I., Böhm, F., Erez, J., and Eisenhauer, A.: Boron isotope ratio determination in carbonates *via* LA-MC-ICP-MS using soda-lime glass standards as reference material, J. Anal. At. Spectrom., 25, 1953–1957, https://doi.org/10.1039/C0JA00036A, 2010.

Fietzke, J., Ragazzola, F., Halfar, J., Dietze, H., Foster, L. C., Hansteen, T. H., Eisenhauer, A., and Steneck, R. S.: Century-scale trends and seasonality in pH and temperature for shallow zones of the Bering Sea, P. Natl. Acad. Sci. USA, 112, 2960–2965, https://doi.org/10.1073/pnas.1419216112, 2015.

Foster, G. L.: Seawater pH, $p\mathrm{CO}_2$ and $[\mathrm{CO}_3^{2-}]$ variations in the Caribbean Sea over the last 130 kyr: a boron isotope and B/Ca study of planktic foraminifera, Earth Planet. Sc. Lett., 271, 254–266, https://doi.org/10.1016/j.epsl.2008.04.015, 2008.

Foster, M. S.: Rhodoliths: between rocks and soft places, J. Phycol., 37, 659–667, https://doi.org/10.1046/j.1529-8817.2001.00195.x, 2001.

Fowell, S. E., Sandford, K., Stewart, J. A., Castillo, K. D., Ries, J. B., and Foster, G. L.: Intrareef variations in Li/Mg and Sr/Ca sea surface temperature proxies in the Caribbean reef-building coral *Siderastrea sidereal*, Paleoceanography, 31, 1315–1329, https://doi.org/10.1002/2016PA002968, 2016.

Frantz, B. R., Foster, M. S., and Riosmena-Rodríguez, R.: *Clathromorphum nereostratum* (Corallinales, Rhodophyta): The oldest alga?, J. Phycology, 41, 770–773, https://doi.org/10.1111/j.1529-8817.2005.00107.x, 2005.

Freiwald, A. and Henrich, R.: Reefal coralline algal build-ups within the Arctic Circle: morphology and sedimentary dynamics under extreme environmental seasonality, Sedimentology, 41, 963–984, https://doi.org/10.1111/j.1365-3091.1994.tb01435.x, 1994.

Gabitov, R. I., Rollion-Bard, C., Tripati, A., and Sadekov, A.: In situ study of boron partitioning between calcite and fluid at different crystal growth rates, Geochim. Cosmochim. Ac., 137, 81–92, https://doi.org/10.1016/j.gca.2014.04.014, 2014.

Gagnon, A. C., Gothmann, A. M., Branson, O., Rae, J. W. B., and Stewart, J. A.: Controls on boron isotopes in a cold-water coral and the cost of resilience to ocean acidification, Earth Planet. Sc. Lett., 554, 116662, https://doi.org/10.1016/j.epsl.2020.116662, 2021.

Gattuso, J.-P., Frankignoulle, M., and Smith, S. V.: Measurement of community metabolism and significance in the coral reef CO_2 source-sink debate, P. Natl. Acad. Sci. USA, 96, 13017–13022, 1999.

Gussone, N., Böhm, F., Eisenhauer, A., Dietzel, M., Heuser, A., Teichert, B. M. A., Reitner, J., Wörheide, G., and Dullo, W.-C.: Calcium isotope fractionation in calcite and aragonite, Geochim. Cosmochim. Ac., 69, 4485–4494, https://doi.org/10.1016/j.gca.2005.06.003, 2005.

Halfar, J., Zack, T., Kronz, A., and Zachos, J. C.: Growth and high-resolution paleoenvironmental signals of rhodoliths (coralline red algae): A new biogenic archive, J. Phys. Res., 105, 22107–22116, https://doi.org/10.1029/1999JC000128, 2000.

Halfar, J., Steneck, R. S., Joachimski, M., Kronz, A., and Wanamaker, A. D. Jr.: Coralline red algae as high-resolution climate recorders, Geology, 36, 463–466, https://doi.org/10.1130/G24635A.1, 2008.

Halfar, J., Williams, B., Hetzinger, S., Steneck, R. S., Lebednik, P., Winsborough, C., Omar, A., Chan, P., and Wanamaker, A. D.: 225 years of Bering Sea climate and ecosystem dynamics revealed by coralline algal growth-increment widths, Geology, 39, 579–582, https://doi.org/10.1130/g31996.1, 2011.

Hall-Spencer, J. M., Kelly, J., and Maggs, C. A.: Background document for maërl beds, in: OSPAR Commission Biodiversity Series, OSPAR Commission, London, ISBN 978-1-907390-32-6, 2010.

Hemming, N. G. and Hanson, G. N.: Boron isotopic composition and concentration in modern marine carbonates, Geochim. Cosmochim. Ac., 56, 537–543, https://doi.org/10.1016/0016-7037(92)90151-8, 1992.

Hemming, N. G. and Hönisch, B.: Boron isotopes in marine carbonate sediments and the pH of the ocean, in: Proxies in Late Cenozoic Paleoceanography, edited by: Hillaire-Marcel, C. and de Vernal, A., Elsevier, 717–734, 2007.

Henehan, M. J., Rae, J. W. B., Foster, G. L., Erez, J., Prentice, K. C., Kucera, M., Bostock, H. C., Martınez-Boti, M. A., Milton, J. A., Wilson, P. A., Marshall, B. J., and Elliott, T.: Calibration of the boron isotope proxy in the planktonic foraminifera *Globigerinoides ruber* for use in palaeo-CO_2 reconstruction, Earth Planet. Sc. Lett., 364, 111–122, https://doi.org/10.1016/j.epsl.2012.12.029, 2013.

Henehan, M. J., Foster, G. L., Rae, J. W. B., Prentice, K. C., Erez, J., Bostock, H. C., Marshall, B. J., and Wilson, P. A.: Evaluating the utility of B/Ca ratios in planktic foraminifera as a proxy for the carbonate system: a case study of *Globigerinoides ruber*: investigating controls on *G. ruber* B/Ca, Geochem. Geophys., 16, 1052–1069, https://doi.org/10.1002/2014GC005514, 2015.

Hetzinger, S., Halfar, J., Kronz, A., Steneck, R., Adey, W. H., Philipp, A. L., and Schöne, B.: High-resolution Mg/Ca ratios in a coralline red alga as a proxy for Bering Sea temperature variations from 1902–1967, Palaois, 24, 406–412, https://doi.org/10.2110/palo.2008.p08-116r, 2009.

Hetzinger, S., Halfar, J., Zack, T., Gamboa, G., Jacob, D. E., Kunz, B. E., Kronz, A., Adey, W., Lebednik, P. A., and Steneck, R. S.: High-resolution analysis of trace elements in crustose coralline algae from the North Atlantic and North Pacific by laser ablation ICP-MS, Palaeogeogr. Palaeocl., 302 , 81–94, https://doi.org/10.1016/j.palaeo.2010.06.004, 2011.

Hoegh-Guldberg, O., Mumby, P. J., Hooten, A. J., Steneck, R. S., Greenfield, P., Gomez, E., Harvell, C. D., Sale, P. F., Edwards, A. J., Caldeira, K., Knowlton, N., Eakin, C. M., Iglesias-Prieto, R., Muthiga, N., Bradbury, R. H., Dubi, A., and Hatziolos, M. E.: Coral reefs under rapid climate change and ocean acidification, Science, 318, 1737–1742, https://doi.org/10.1126/science.1152509, 2007.

Holcomb, M., DeCarlo, T. M., Gaetani, G. A., and McCulloch, M.: Factors affecting B/Ca ratios in synthetic aragonite, Chem. Geol., 437, 67–76, https://doi.org/10.1016/j.chemgeo.2016.05.007, 2016.

Hönisch, B. and Hemming, N. G.: Surface ocean pH response to variations in pCO_2 through two full glacial cycles, Earth Planet. Sc. Lett., 236, 305–314, https://doi.org/10.1016/j.epsl.2005.04.027, 2005.

Hönisch, B., Ridgwell, A., Schmidt, D. N., Thomas, E., Gibbs, S. J., Sluijs, A., Zeebe, R., Kump, L., Martindale, R. C., Greene, S. E., Kiessling, W., Ries, J., Zachos, J. C., Royer, D. L., Barker, S., Marchitto Jr., T. M., Moyer, R., Pelejero, C., Ziveri, P., Foster, G. L., and Williams, B.: The geological record of ocean acidification, Science, 335, 1058–1063, https://doi.org/10.1126/science.1208277, 2012.

Irvine, L. M. and Chamberlain, Y. M. (Eds.): Volume 1 Rhodophyta Part 2B. Corallinales, Hildenbrandiales, Natural History Museum, London, ISBN 0-11-310016-7, 1994.

Hofmann, G. E., Smith, J. E., Johnson, K. S., Send, U., Levin, L. A., Micheli, F., Paytan, A., Price, N. N., Peterson, B., Takeshita, Y., Matson, G. P., Crook, E. D., Kroeker, K. J., Gambi, M. C., Rivest, E. B., A. Frieder, C. A., Yu, P. C., and Martz T. R.: High-frequency dynamics of ocean pH: a multi-ecosystem comparison, PLoS ONE, 6, e28983, https://doi.org/10.1371/journal.pone.0028983, 2011.

Hou, A., Halfar, J., Adey, W., Wortmann, U. G., Zajacz, Z., Tsay, A., Williams, B., and Chan, P.: Long-lived coralline alga records multidecadal variability in Labrador Sea carbon isotopes, Chem. Geol., 526, 93–100, https://doi.org/10.1016/j.chemgeo.2018.02.026, 2018.

Jochum, K. P., Scholz, D., Stoll, B., Weis, U., Wilson, S. A., Yang, Q., Schwalb, A., Börner, N., Jacob, D. E., and Andreae, M. O.: Accurate trace element analysis of speleothems and biogenic calcium carbonates by LA-ICP-MS, Chem. Geol., 318, 31–44, https://doi.org/10.1016/j.chemgeo.2012.05.009, 2012.

Kaczmarek, K., Nehrke, G., Misra, S., Bijma, J., and Elderfield, H.: Investigating the effects of growth rate and temperature on the B/Ca ratio and δ^{11}B during inorganic calcite formation, Chem. Geol., 421, 81–92, https://doi.org/10.1016/j.chemgeo.2015.12.002, 2016.

Kamenos, N. A., Cusack, M., and Moore, P. G.: Coralline algae are global paleothermometers with bi-weekly resolution, Geochim. Cosmochim. Ac., 72, 771–779, https://doi.org/10.1016/j.gca.2007.11.019, 2008.

Kamenos, N. A., Cusack, M., Huthwelker, T., Lagarde, P., and Scheibling, R. E.: Mg-lattice associations in red coralline algae, Geochim. Cosmochim. Ac., 73, 1901–1907, https://doi.org/10.1016/j.gca.2009.01.010, 2009.

Kamenos, N. A., Hoey, T., Nienow, P., Fallick, A. E., and Claverie, T.: Reconstructing Greenland Ice sheet runoff using coralline algae, Geology, 40, 1095–1098, https://doi.org/10.1130/G33405.1, 2012.

Keul, N., Langer, G., Thoms, S., de Nooijer, L. J., Reichart, G. J., and Bijma, J.: Exploring foraminiferal Sr/Ca as a new carbonate system proxy, Geochim. Cosmochim. Ac., 202, 374–386, https://doi.org/10.1016/j.gca.2016.11.022, 2017.

Klochko, K., Cody, G. D., Tossell, J. A., Dera, P., and Kaufman, A. J.: Re-evaluating boron speciation in biogenic calcite and aragonite using ^{11}B MAS NMR, Geochim. Cosmochim. Ac., 73, 1890–1900, https://doi.org/10.1016/j.gca.2009.01.002, 2009.

Lorens, R. B.: Sr, Cd, Mn and Co distribution coefficients in calcite as a function of calcite precipitation rate, Geochim. Cosmochim. Ac., 45, 553–561, https://doi.org/10.1016/0016-7037(81)90188-5, 1981.

Martin, S., Castets, M.-D., and Clavier, J.: Primary production, respiration and calcification of the temperate free-living coralline alga *Lithothamnion corallioides*, Aquat. Bot., 85, 121–128, https://doi.org/10.1016/j.aquabot.2006.02.005, 2006.

Masson-Delmotte, V., Zhai, P., Pirani, A., Connors, S. L., Péan, C., Berger, S., Caud, N., Chen, Y., Goldfarb, Gomis, M. I., Huang, M., Leitzell, K., Lonnoy, E, Matthews, J. B. R., Maycock, T. K., Waterfield, T., Telekçi, O., Yu, R., and Zhou, B.: IPCC: Climate Change 2021: The Physical Science Basis, in: Contribution of-Working Group I to the Sixth Assessment Report 50 of the Intergovernmental Panel on Climate Change, Cambridge University Press, Cambridge UK, ISBN 978-92-9169-158-6, 2021.

Mavromatis, V., Montouillout, V., Noireaux, J., Gaillardet, J., and Schott, J.: Characterization of boron incorporation and speciation in calcite and aragonite from co-precipitation experiments under controlled pH, temperature and precipitation rate, Geochim. Cosmochim. Ac., 150, 299–313, https://doi.org/10.1016/j.gca.2014.10.024, 2015.

McCulloch, M., Trotter, J., Montagna, P., Falter, J., Dunbar, R., Freiwald, A., Försterra, G., Correa, M. L., Maier, C., Rüggeberg, A., and Taviani, M.: Resilience of cold-water scleractinian corals to ocean acidification: boron isotopic systematics of pH and saturation state up-regulation, Geochim. Cosmochim. Ac., 87, 21–34, https://doi.org/10.1016/j.gca.2012.03.027, 2012.

Melbourne, L. A., Hernández-Kantún, J., Russell, S., and Brodie, J.: There is more to maerl than meets the eye: DNA barcoding reveals a new species in Britain, *Lithothamnion erinaceum* sp. nov. (Hapalidiales, Rhodophyta), Eur. J. Phycol., 52, 166–178, https://doi.org/10.1080/09670262.2016.1269953, 2017.

Moberly, R.: Composition of magnesian calcites of algae and pelecypods by electron microprobe analysis, Sedimentology, 11, 61–82, https://doi.org/10.1111/j.1365-3091.1968.tb00841.x, 1968.

Moberly, R: Microprobe study of diagenesis in calcareous algae, Sedimentology, 14, 113–123, https://doi.org/10.1111/j.1365-3091.1970.tb00185.x, 1970.

Montagna, P. and Douville, E.: Geochemical proxies in marine biogenic carbonates: New developments and applications to global change, Chem. Geol., 533, 119411, https://doi.org/10.1016/j.chemgeo.2019.119411, 2020.

Morse, J. W., Andersson, A. J., and Mackenzie, F. T.: Initial responses of carbonate-rich shelf sediments to rising atmospheric $p\mathrm{CO}_2$ and "ocean acidification": role of high Mg-calcites, Geochim. Cosmochim. Ac., 70, 5814–5830, https://doi.org/10.1016/j.gca.2006.08.017, 2006.

Nash, M. C., Martin, S., and Gattuso, J.-P.: Mineralogical response of the Mediterranean crustose coralline alga *Lithophyllum cabiochae* to near-future ocean acidification and warming, Biogeosciences, 13, 5937–5945, https://doi.org/10.5194/bg-13-5937-2016, 2016.

Noireaux, J., Mavromatis, V., Gaillardet, J., Schott, J., Montouillout, V., Louvat, P., Rollion-Bard, C., and Neuville, D. R.: Crystallographic control on the boron isotope paleo-pH proxy, Earth Planet. Sc. Lett., 430, 398–407, https://doi.org/10.1016/j.epsl.2015.07.063, 2015.

Paris, G., Bartolini, A., Donnadieu, Y., Beaumont, V., and Gaillardet, J.: Investigating boron isotopes in a middle Jurassic micritic sequence: primary vs. diagenetic signal, Chem. Geol., 275, 117–126, https://doi.org/10.1016/j.chemgeo.2010.03.013, 2010.

Payri, C. E.: Production primaire et calcification des algues benthiques en milieu corallien, Oceanis, 26, 427–463, 2000.

Perruche, C.: Product user manual for the Global Ocean Biogeochemistry Hindcast GLOBAL_REANALYSIS_BIO_001_029, Version 1, Copernicus Marine Environmental Monitoring Service, [data set], 17 pp., https://doi.org/10.25607/OBP-490, 2018.

Piazza, G., Bracchi, V. A., Basso, D.: Mg, Li, Sr and B/Ca in the calcareous red alga *Lithothamnion corallioides*, PANGAEA [data set], https://doi.org/10.1594/PANGAEA.932201, 2021.

Potin, P., Floc'h, J.-Y., Augris, C., and Cabioch, J.: Annual growth rate of the calcareous red algae *Lithothamnion corallioides* (Corallinales, Rhodophyta) in the Bay of Brest, France, Hydrobiologia, 204–205, 263–267, 1990.

Rae, J. B. R., Foster, G. L., Schmidt, D. N., and Elliott, T.: Boron isotopes and B/Ca in benthic foraminifera: proxies for the deep ocean carbonate system, Earth Planet. Sc. Lett., 302, 403–413, https://doi.org/10.1016/j.epsl.2010.12.034, 2011.

Ragazzola, F., Foster, L. C., Form, A., Anderson, P. S. L., Hansteen, T. H., and Fietzke, J.: Ocean acidification weakens the structural integrity of coralline algae, Glob. Change Biol., 18, 2804–2812, https://doi.org/10.1111/j.1365-2486.2012.02756.x, 2012.

Ragazzola, F., Foster, L. C., Jones, C. J., Scott, T. B., Fietzke, J., Kilburn, M. R., and Schmidt, D. N.: Impact of high CO_2 on the geochemistry of the coralline algae *Lithothamnion glaciale*, Sci. Rep., 6, 20572, https://doi.org/10.1038/srep20572, 2016.

Ragazzola, F., Caragnano, A., Basso, D., Schmidt, D. N., and Fietzke, J.: Establishing temperate crustose Early Holocene coralline algae as archived for paleoenvironmental reconstructions of the shallow water habitats of the Mediterranean Sea, Paleontology, 63, 155–170, https://doi.org/10.1111/pala.12447, 2020.

Ries, J. B.: Mg fractionation in crustose coralline algae: geochemical, biological and sedimentological implications of secular variation in Mg/Ca ratio of seawater, Geochim, Cosmochim. Ac., 70, 891–900, https://doi.org/10.1016/j.gca.2005.10.025, 2006.

Ries, J. B., Ghazaleh, M. N., Connolly, B., Westfield, I., and Castillo, K. D.: Impacts of seawater saturation state ($\Omega A = 0.4$–4.6) and temperature (10, 25 °C) on the dissolution kinetics of whole-shell biogenic carbonates, Geochim. Cosmochim. Ac., 192, 318–337, https://doi.org/10.1016/j.gca.2016.07.001, 2016.

Rimstidt, J. D., Balog, A., and Webb, J.: Distribution of trace elements between carbonate minerals and aqueous solutions, Geochim. Cosmochim. Ac., 62, 1851–1863, https://doi.org/10.1016/S0016-7037(98)00125-2, 1998.

Roberts, R. D., Kühl, M., Glud, R. N., and Rysgaard, S.: Primary production of crustose coralline algae in a high Artic Fjord, J. Phycol., 38, 273–283, https://doi.org/10.1046/j.1529-8817.2002.01104.x, 2002.

Rosenthal, Y., Lear, C. H., Oppo, D. W., and Braddock, K. L.: Temperature and carbonate ion effects on Mg/Ca and Sr/Ca ratios in benthic foraminifera: Aragonitic species *Hoeglundina elegans*, Paleoceanography, 21, PA1007, https://doi.org/10.1029/2005PA001158, 2006.

Savini, A., Basso, D., Bracchi, V. A., Corselli, C., and Pennetta, M.: Maerl-bed mapping and carbonate quantification on submerged terraces offshore the Cilento peninsula (Tyrrhenian Sea, Italy), Geodiversitas, 34, 77–98, https://doi.org/10.5252/g2012n1a5, 2012.

Schöne, B. R., Fiebig, J., Pfeiffer, M., Gleb, R., Hickson, J., Johnson, L. A., Dreyer, A. W., and Oschmann, W.: Climate records from a bivalved Methuselah (*Arctica islandica*, Mollusca; Iceland), Palaeogeogr., Palaeocl., 228, 130–148, https://doi.org/10.1016/j.palaeo.2005.03.049, 2005.

Teruzzi, A., Di Biagio, V., Feudale, L., Bolzon, G., Lazzari, P., Salon, S., Di Biagio, V., Coidessa, G., and Cossarini, G.: Mediterranean Sea Biogeochemical Reanalysis (CMEMS MED-Biogeochemistry, MedBFM3 system) (Version 1) [data set], Copernicus Monitoring Environment Marine Service (CMEMS), https://doi.org/10.25423/CMCC/MEDSEA_MULTIYEAR_BGC_006_008_MEDBFM3 (last access: 28 January 2022), 2021.

Uchikawa, J., Penman, D. E., Zachos, J. C., and Zeebe, R. E.: Experimental evidence for kinetic effects on B/Ca in synthetic calcite: Implications for potential $B(OH)_4^-$ and $B(OH)_3$ incorporation, Geochim. Cosmochim. Ac., 150, 171–191, https://doi.org/10.1016/j.gca.2014.11.022, 2015.

Vengosh, A., Kolodny, Y., Starinsky, A., Chivas, A. R., and McCulloch, M. T.: Coprecipitation and isotopic fractionation of boron in modern biogenic carbonates, Geochim. Cosmochim. Ac., 55, 2901–2910, https://doi.org/10.1016/0016-7037(91)90455-E, 1991.

Wara, M. W., Delaney, M. L., Bullen, T. D., and Ravelo, A. C.: Possible roles of pH, temperature, and partial dissolution in determining boron concentration and isotopic composition in planktonic foraminifera, Paleoceanography, 18, 1100, https://doi.org/10.1029/2002PA000797, 2003.

Williams, B., Halfar, J., Delong, K. L., Hetzinger, S., Steneck, R. S., and Jacob, D. E.: Multi-specimen and multi-site calibration of Aleutian coralline algal Mg/Ca to sea surface temperature, Geochim. Cosmochim. Ac., 139, 190–204, https://doi.org/10.1016/j.gca.2014.04.006, 2014.

Wilson, S., Blake, C., Berges, J. A., and Maggs, C. A.: Environmental tolerances of free-living coralline algae (maerl): implications for European marine conservation, Biol. Conserv., 120, 279–289, https://doi.org/10.1016/j.biocon.2004.03.001, 2004.

Yu, J. M. and Elderfield, H.: Benthic foraminiferal B/Ca ratios reflect deep water carbonate saturation state, Earth Planet. Sc. Lett., 258, 73–86, https://doi.org/10.1016/j.epsl.2007.03.025, 2007.

Yu, J. M., Elderfield, H., and Hönisch, B.: B/Ca in planktonic foraminifera as a proxy for surface water pH, Paleoceanography, 22, 2202, https://doi.org/10.1029/2006PA001347, 2007.

Yu, J., Day, J., Greaves, M., and Elderfield, H.: Determination of multiple element/calcium ratios in foraminiferal calcite by quadrupole ICP-MS, Geochem. Geophys., 6, Q08P01, https://doi.org/10.1029/2005GC000964, 2015.

Zeebe, R. E. and Wolf-Gladrow, D. (Eds.): CO_2 in seawater: equilibrium, kinetics, isotopes, Elsevier Oceanography Book Series, Amsterdam, 65 pp., 2001.

Zuo, H., Balmaseda, M. A., Tietsche, S., Mogensen, K., and Mayer, M.: The ECMWF operational ensemble reanalysis–analysis system for ocean and sea ice: a description of the system and assessment, Ocean Sci., 15, 779–808, https://doi.org/10.5194/os-15-779-2019, 2019.

Biogeosciences, 18, 6061–6076, 2021
https://doi.org/10.5194/bg-18-6061-2021

Biogeosciences Open Access EGU

A stable ultrastructural pattern despite variable cell size in *Lithothamnion corallioides*

Valentina Alice Bracchi, Giulia Piazza, and Daniela Basso

Department of Earth and Environmental Sciences, University of Milano-Bicocca, Milan, 20126, Italy

Correspondence: Valentina Alice Bracchi (valentina.bracchi@unimib.it)

Received: 28 May 2021 – Discussion started: 3 August 2021
Revised: 18 October 2021 – Accepted: 20 October 2021 – Published: 25 November 2021

Abstract. Recent advances on the mechanism and pattern of calcification in coralline algae led to contradictory conclusions. The evidence of a biologically controlled calcification process, resulting in distinctive patterns at the scale of family, was observed. However, the coralline calcification process has been also interpreted as biologically induced because of the dependency of its elemental composition on environmental variables. To clarify the matter, five collections of *Lithothamnion corallioides* from the Atlantic Ocean and the Mediterranean Sea, across a wide depth range (12–66 m), have been analyzed for morphology, anatomy and cell wall crystal patterns in both perithallial and epithallial cells to detect possible ultrastructural changes. *L. corallioides* shows the alternation of tiers of short-squared and long-ovoid/rectangular cells along the perithallus, forming a typical banding. The perithallial cell length decreases according to water depth and growth rate, whereas the diameter remains constant. Our observations confirm that both epithallial and perithallial cells show primary (PW) and secondary (SW) calcite walls. Rectangular tiles, with the long axis parallel to the cell membrane forming a multi-layered structure, characterize the PW. Flattened squared bricks characterize the SW, with roundish outlines enveloping the cell and showing a zigzag and cross orientation. Long and short cells have different thicknesses of PW and SW, increasing in short cells. Epithallial cells are one to three flared cells with the same shape of the PW and SW crystals. Despite the diverse seafloor environments and the variable *L. corallioides* growth rate, the cell walls maintain a consistent ultrastructural pattern with unaffected crystal shape and arrangement. A comparison with two congeneric species, *L. minervae* and *L. valens*, showed similar ultrastructural patterns in the SW but evident differences in the PW crystal shape. Our observations point to a biologically control rather than an induction of the calcification process in coralline algae and suggest a possible new morphological diagnostic tool for species identification, with relevant importance for paleontological applications. Finally, secondary calcite, in the form of dogtooth crystals that fill the cell lumen, has been observed. It represents a form of early alteration in living collections which can have implications in the reliability of climate and paleoclimate studies based on geochemical techniques.

1 Introduction

The subclass Corallinophycidae is spread globally and comprises the crustose coralline algae (CCA), important Mg-calcite calcifiers and habitat builders of rhodolith beds, temperate algal reefs and tropical coralgal reefs (Adey, 1986; Cabioch and Giraud, 1986; Ries, 2006; Caragnano et al., 2009; Bracchi et al., 2014, 2016; Marchese et al., 2020). The complex calcifying process in CCA takes place during their whole life span and involves the entire organism. For this reason, corallines bear witness to past benthic primary production by macroalgae with an excellent fossil record (Basso et al., 2007; Bracchi et al., 2014, 2016; Ragazzola et al., 2020).

Rhodoliths are unattached nodules formed mostly by CCA. Among them, free-living unattached branches usually characterize maerl beds in the northeastern Atlantic Ocean (Henrich et al., 1995; Birkett et al., 1998; Peña and Bárbara, 2008, 2009; Peña et al., 2014) and in the Mediterranean Sea (Huvé, 1956; Jacquotte, 1962; Gambi et al., 2009; Agnesi et al., 2011; Savini et al., 2012; Basso et al., 2017).

In both geographical settings, the most common species are *Lithothamnion corallioides* (P. Crouan and H. Crouan)

Published by Copernicus Publications on behalf of the European Geosciences Union.

P. Crouan and H. Crouan 1867 and *Phymatolithon calcareum* (Pallas) W. H. Adey and D. L. McKibbin ex Woelkering and L. M. Irvine 1986 (Adey and McKibbin, 1970; Basso et al., 2017; Hernandez-Kantun et al., 2017).

L. corallioides is distributed between the Canary Islands, at roughly 28° N, and Scotland, at about 58° N (Irvine and Chamberlain, 1994; Wilson et al., 2004), and it is considered one of the most suitable species for paleoclimate reconstruction (Foster, 2001). This species usually forms twig-like structures and is brown to pink or purplish and often sterile, with branch diameters typically in the range of 1–2 mm and with knob-like apices (Irvine and Chamberlain, 1994). Primary production, respiration and calcification in *L. corallioides* are strongly influenced by seasonality because of the oscillations of temperature and irradiance levels (Adey and McKibbin, 1970; Potin et al., 1990; Martin et al., 2006). *L. corallioides* shows a favorable response to temperature increase, reaching its maximum primary production during summer (Adey and McKibbin, 1970; Potin et al., 1990). *L. corallioides*' minimum survival temperature is between 2 and 5 °C, while the optimal growth is observed between 13 °C (Adey and McKibbin, 1970) and 14 °C (Blake and Maggs, 2003). In longitudinal sections, the periodical change in growth rate due to the alternation of seasons generates perithallus banding in *Lithothamnion* species, as in the long protuberances of *L. corallioides*. Banding results from an evident alternation of tiers of thick-walled, generally short cells versus thin-walled long cells along the main axis of perithallus growth (Basso, 1995; Basso et al., 1997; Kamenos and Law, 2010, Burdett et al., 2011). Banding has been interpreted as the visible effect of the environment (primarily temperature) on algal growth at different timescales (day, month) (Halfar et al., 2000; Foster, 2001). An alternative explanation would consider banding as the periodical shift between tiers of cells possessing a different wall structure (Nash et al., 2019).

In general, the calcifying process of CCA has been described as the deposition of tangential calcite needles in the outer part of the cell wall (interstitial matrix), followed by the formation of radial needles in the cell wall itself in contact with the plasmalemma. The polysaccharide and fibrillary matrix control both processes (Giraud and Cabioch, 1976; Irvine and Chamberlain, 1994; Adey, 1998; de Carvalho et al., 2017). In *L. corallioides*, calcification has been described as being composed of tangential rod-shaped crystals in the primary wall (PW) and perpendicular fan-like rods in the secondary wall (SW) (Giraud and Cabioch, 1976). Borowitzka (1984, 1989) proposed that coralline algae have semi-organized calcification, suggesting that their calcification is biologically controlled, as also indicated by Cabioch and Giraud (1986), rather than induced, as more recently supported by de Carvalho et al. (2017) and Nash et al. (2019). Cell wall ultrastructures are recognized as a valuable tool to define the phenotypic expression of genotypic information (Auer and Piller, 2020). The compelling evidence of a biological control over calcification in coralline algae was provided by the identification of family-specific cell wall ultrastructures. Epithallial cells in the genus *Lithothamnion* show crystal units as thin rectangular blocks (Auer and Piller, 2020). Seasonality, including seawater temperature oscillations and photoperiod, is considered one of the main factors affecting the growth rate and the biomineralization process (Steller et al., 2007; Kamenos and Law, 2010; Vásquez-Elizondo and Enríquez, 2017), which may influence the ultrastructural pattern.

The identification of CCA in present-day integrative taxonomy is based on genetic methods coupling with the morphological description and measurement of diagnostic features (for example: Basso et al., 2015; Caragnano et al., 2018; Costa et al., 2019). Species identification in the fossil record is, on the contrary, merely based on the preservation of morphological taxonomic characters. Consequently, the identification of valuable morphological characters as a tool for the definition of the paleontological species represents an important challenge. CCA are well represented in the fossil record, and *L. corallioides* has been reported in the Pliocene of Spain (Aguirre et al., 2012) and in the Pleistocene of southern Italy (Bracchi et al., 2014).

This study is aimed at describing the ultrastructural mineralogical features of *L. corallioides* from different geographic settings (northeastern Atlantic Ocean and Mediterranean Sea) and across a wide bathymetric interval (12–66 m) to test if the ultrastructural pattern is preserved under different environmental conditions and therefore can be considered as an evident sign of a biologically controlled mineralization. Moreover, the identification of a specific ultrastructural pattern could be considered as a valuable tool for species identification to be used also in paleobiology. *L. corallioides* has been targeted because of its wide distribution, both geographically and bathymetrically, and its occurrence in the fossil record.

2 Materials and methods

For this study, we considered five collections (Fig. 1, Table 1) from two different geographic settings, the Atlantic Ocean and the western Mediterranean Sea, sampled by scuba diving or grabbing at different depths ranging from 12 m in Morlaix Bay (France) down to 66 m in the Pontine Islands (Italy). All specimens have been collected alive. Table 1 reports locations and dates of sampling.

To highlight possible ultrastructural differences among the same genus, two additional collections, already identified as *Lithothamnion minervae* Basso, 1995, and *Lithothamnion valens* Foslie, 1909, have been considered. These collections have been sampled alive from the Egadi Islands (Italy), during July 2016, at 103 and 86 m water depth respectively.

All samples have been air dried and sheltered from sunlight. Once dried, they were stored in plastic boxes with sil-

Table 1. Location, date of collection and depth of *L. corallioides* samples. In the "basin" column, numbers in brackets correspond to the point in Fig. 1.

Basin	Sample	Location	Date of collection	Depth (m)	No. of branches	Temperature seasonal range (°C)
Atlantic Ocean (1)	France, Morlaix Bay	48°34′42″ N 3°49′36″ W	May 1991	12	23	8.3–17.2
Western Mediterranean (2)	Italy, Egadi Islands	37°58′10″ N 12°03′26″ E	Aug 1991	40	20	13.7–18.8
Western Mediterranean (3)	Italy, Santa Caterina shoal	39°08′32″ N 9°31′14″ E	Jul 2017	40	12	13.2–20
Western Mediterranean (4)	Italy, Elba island	42°44′56.4″ N 10°07′08.4″ E	Dec 1990	45	20	12.9–17.5
Western Mediterranean (5)	Italy, Pontine Islands	40°54′ N 12°45′ E	Jul 2016	66	12	13.9–16.7

ica to avoid any decay and transported to the laboratories of the University of Milano-Bicocca.

The seawater temperature has been extracted from 11 years of monthly reanalysis spanning 1979–2017 from ORAS5 (Ocean Reanalysis System 5), at 0.25° horizontal resolution (Zuo et al., 2019), to indicate the seasonal temperate fluctuation (Table 1).

2.1 Coralline sample preparation

Samples have been prepared for scanning electron microscope (SEM) imaging. Altered, badly preserved or encrusted branches have been discarded. Only the branches showing a shiny surface have been picked from all collections, each controlled under a stereo microscope, and cleaned manually by removing epiphytes and other encrustations. Each sample, composed of multiple branches, has been cleaned in an ultrasonic bath in distilled water for 10 min and air-dried. The branches were then placed in small cylindrical plastic boxes with a base diameter of 1″ (2.54 cm). Branches have been piled up and aligned to obtain multiple layers. The samples were embedded in Epofix resin for SEM analyses, which was stirred for 2 min with a hardener (13 % w/w), and they were left to harden for 1 d at room temperature. Samples have then been cut normal to the multiple layers by using an IsoMet diamond wafering blade 15HC, along the direction of branch growth. The number of branches per sample are indicated in Table 1. Moreover, two additional samples (*L. minervae* and *L. valens*) have been prepared for SEM observations ($n = 10$ branches) by breaking them with a small chisel. Both longitudinal and surface sections have been selected for SEM observations.

2.2 Scanning electron microscope

For SEM imaging, the surfaces of embedded samples have been polished by using different sizes of silicon carbide, cleaned ultrasonically in distilled water for 10 min and air-dried. Samples mounted directly on stub have been simply chrome-coated. SEM images have been taken with a field emission gun scanning electron microscope (SEM-FEG): Zeiss Gemini 500 and a TESCAN VEGA TS 5136XM. Standard magnifications for SEM images were established (~ 2500X, ~ 5000X, ~ 10000X, ~ 20000X and ~ 30000X) to describe comparatively and measure growth bands and cells, the morphology of Mg-calcite crystals, and the main features of perithallial and epithallial cell walls. A rigorous control over cell orientation is required to represent, describe and measure in 2D the main features of a 3D structure such as cell calcification (both PW and SW). Longitudinal axial sections of branches are a standard representation for calcareous red algae, allowing for subsequent visual comparison (Woelkerling, 1988; Quaranta et al., 2007; Burdett et al., 2011). Surface tangential sections are useful to describe the epithallial cells. Transverse or oblique sections are useful to describe qualitatively the 3D aspects and organization of calcite crystals composing both PW and SW. Description of the cell wall structure follows the nomenclature of Flajs (1977), presenting the PW and SW calcifications of the wall. Some authors refer to PW as interstitial calcite (Ragazzola et al., 2016) or interfilament calcite (Nash and Adey, 2017; Nash et al., 2013, 2015). Cell dimensions have been measured as reported in Fig. 2 ($n = 10$ per sample) exclusively on longitudinal sections (Fig. 2). Separation among adjacent filaments was not always obvious (Fig. 2c). In such cases, the PW of adjacent cells has been measured in total (green line in Fig. 2c), and then half of the total was attributed to each cell. In the text we use the term *ultrastructure* to identify the

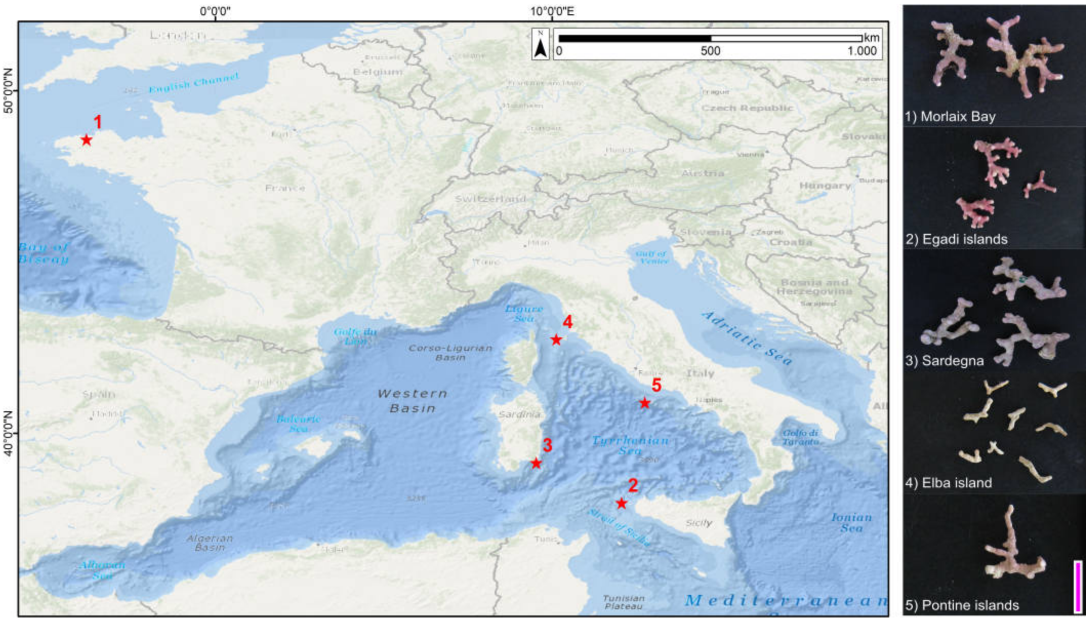

Figure 1. Sampling sites (1–5) and images of selected samples. Service layer credit sources: Esri, GEBCO, NOAA, National Geographic, Garmin, HERE, Geonames.org and other contributors. Scale bar = 1 cm.

singular crystal in one of the layers of the cell wall and *ultrastructural pattern* to indicate the combination and mutual organization of crystals in layers of the cell wall.

2.3 Statistical analyses

Spearman and Pearson correlations were used to test the statistical relationship between the cell measurements in both long and short cells, including morphometry and cell wall thickness. The linear correlation between the mean cell lengths and the sampling depths was measured by Pearson's coefficient as well. One-way ANOVA and the Kruskal–Wallis tests respectively followed by the Tukey's test and the Dunn's test for post hoc analysis were used to compare the cell measurements among sampling sites and to provide evidence of the differences between group means and medians. All statistical analyses were run in R 3.6.3 software.

2.4 Growth rates

Growth rates were estimated under light microscope by measuring a linear transect on the longitudinal section and counting the number of growth bands of fourth order (sensu Foster, 2001) crossed by the transect. The growth rate has been calculated by dividing the length of the transect by the number of growth bands.

3 Results

3.1 Ultrastructures from SEM images

Selected rhodoliths belong to the unattached branches morphotype (Basso, 1998; Basso et al., 2016), never exceeding 3 cm in length (Fig. 1). The diameter of each branch never exceeds 2.5 mm (Fig. 1). The color varies from yellowish white to pink/purplish, with typical knob-like apices (Fig. 1).

Once cut, all samples show the same micromorphology (Fig. 3a–i, Supplement 2), with the constant occurrence of an easily detectable banding due to the alternation of series of short and long cells (Fig. 3a, b) in bands of the fourth order corresponding to 1 year (Foster, 2001). No reproductive structure (conceptacle) was detected.

Along the perithallus, long cells are ovoid to rectangular in shape (Fig. 3c, d, Supplement 2), whereas short cells are more squared (Fig. 3e, f).

Within the long-celled bands, the longest cells were measured in the sample from Morlaix Bay (26.71 ± 1.74 µm), while the less elongated cells were observed in the sample from the Pontine Islands (13.05 ± 0.76 µm) (Table 2, Fig. 4).

Within the short-celled bands, the shortest cells were observed in the sample from Pontine (6.97 ± 0.25 µm), while the longest short cells were from Morlaix Bay (13.90 ± 0.88 µm) (Table 2, Fig. 4). Cell diameter ranges

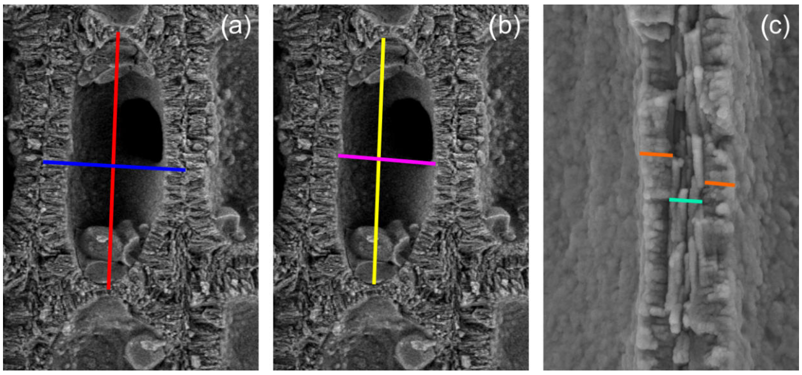

Figure 2. Cell measurements: **(a)** cell wall length (red) and diameter (blue); **(b)** lumen length (yellow) and lumen diameter (purple); **(c)** SW thickness of adjacent cells (orange); PW thickness of adjacent cells (green).

Table 2. Morphometry of short and long cells and lumens and wall thickness measured in longitudinal section (PW = primary wall, SW = secondary wall) with the indication of length (L) and diameter (D) (µm). Standard deviation in brackets.

Sample	Short cell						Long cell					
	Cell		Lumen		Wall		Cell		Lumen		Wall	
	L	D	L	D	SW	PW	L	D	L	D	SW	PW
Morlaix Bay 12 m	13.90 (0.88)	8.31 (1.34)	12.38 (0.93)	6.04 (1.05)	1.61 (0.43)	0.12 (0.03)	26.70 (1.73)	11.11 (1.80)	24.46 (1.73)	9.25 (1.42)	0.57 (0.14)	0.13 (0.06)
Egadi Islands 40 m	13.43 (2.36)	9.22 (0.70)	8.48 (1.189)	4.97 (1.55)	2.08 (0.80)	0.22 (0.07)	18.55 (1.28)	10.27 (0.77)	16.13 (1.16)	8.54 (0.60)	0.74 (0.09)	0.16 (0.05)
Santa Caterina shoal 40 m	10.57 (1.01)	8.29 (0.58)	8.79 (0.72)	4.43 (0.66)	1.87 (0.26)	0.17 (0.16)	16.80 (1.54)	7.69 (1.07)	15.40 (1.51)	5.04 (0.81)	1.25 (0.41)	0.13 (0.03)
Elba island 45 m	12.8 (0.45)	9.4 (0.9)	11.6 (0.54)	5.2 (0.44)	2.2 (0.44)	0.14 (0.05)	17.51 (0.78)	8.64 (0.81)	15.75 (0.89)	6.31 (0.83)	1.08 (0.25)	0.18 (0.06)

between 7.69 ± 1.07 µm (Santa Caterina shoal) and 11.11 ± 1.79 µm (Morlaix) in long cells and between 8.27 ± 0.48 µm (Pontine) and 9.23 ± 0.70 µm (Egadi) in short cells (Table 2, Fig. 4).

Both long and short cells have PWs and SWs, and the style of mineralization shows a consistent ultrastructural pattern. The PW crystallization observed in longitudinal medial sections (cutting the cell lumen) is composed of elongated crystals appearing as rods (Fig. 5a–c, e), but where longitudinal sections are tangential to the PW, crystals are revealed to be flat rectangular tiles (Figs. 5d, f, 6a). The long axis of the PW tiles is parallel to the cell membrane and may form a multi-layered structure which envelops the cell (Fig. 5e). The dimensions of the tiles are 0.61 ± 0.17 µm in length and 0.05 ± 0.01 µm in height (Fig. 6a). Elongated radial crystals (Fig. 7a, b) in longitudinal sections cutting the cell lumen characterize the SW. Small, roundish units, appearing as being fused together, in places showing an apparent multi-layered structure (Fig. 7b) form such crystals. These elongated crystals are radial to the cell lumen (Fig. 7a–c). Where the cell membrane is lost, the SW can be observed from different orientations, and such apparently elongated crystals are revealed to be thin bricks with rounded margins (Figs. 6b, 7d–f). Bricks are squared, and length and width are 0.63 ± 0.15 µm (Fig. 6b). The bricks form a sort of envelope around the cell (Figs. 6b, 7e, f), showing sometimes a zigzag and cross orientation (Fig. 7g, h).

Different thicknesses characterize the PW and SW of short and long cells (Figs. 3, 5, 7; Table 2, Supplement 2) in longitudinal medial sections. Both PW and SW of short cells are generally thicker than in long cells (Table 2) even if the thickness does not show a correlation with sampling bathymetry. The SW thickness ranges between 1.52 ± 0.65 µm (Pontine) and 2.20 ± 0.45 µm (Elba) in short cells and between 0.57 ± 0.14 µm (Morlaix) and 1.26 ± 0.42 µm (Santa Caterina shoal) in long cells (Table 2).

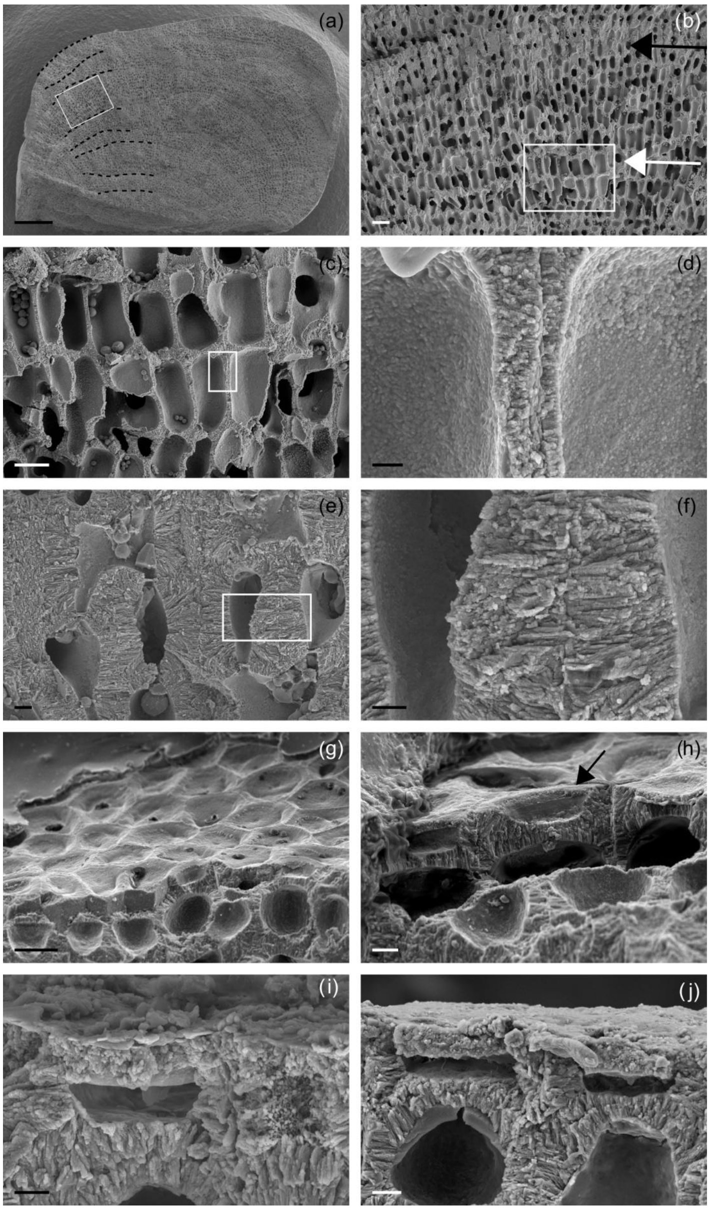

Figure 3. Main features of *Lithothamnion corallioides* under SEM (Morlaix Bay, France). **(a)** Longitudinal section of *L corallioides* with obvious banding (dashed black lines). Scale bar = 100 µm. The inset is magnified in **(b)**; **(b)** alternation of thick-walled (black arrow) and thin-walled (white arrow) cells. Scale bar = 20 µm. The inset is magnified in **(c)**; **(c)** thin-walled long cells. Scale bar = 10 µm. The inset is magnified in **(d)**; **(d)** detail of the thin wall of long cells. Scale bar = 1 µm. **(e)** Thick-walled short cells. Scale bar = 2 µm. The inset is magnified in **(f)**; **(f)** detail of the thick wall of short cells. Scale bar = 1 µm. **(g)** Polygonal shape of epithallial cells in surface view. Scale bar = 10 µm. **(h)** Detail of a flared epithallial cell (arrow). Scale bar = 3 µm. **(i–j)** Longitudinal sections of flared epithallial cells with complete mineralization of the cell walls. Scale bar = 2 µm.

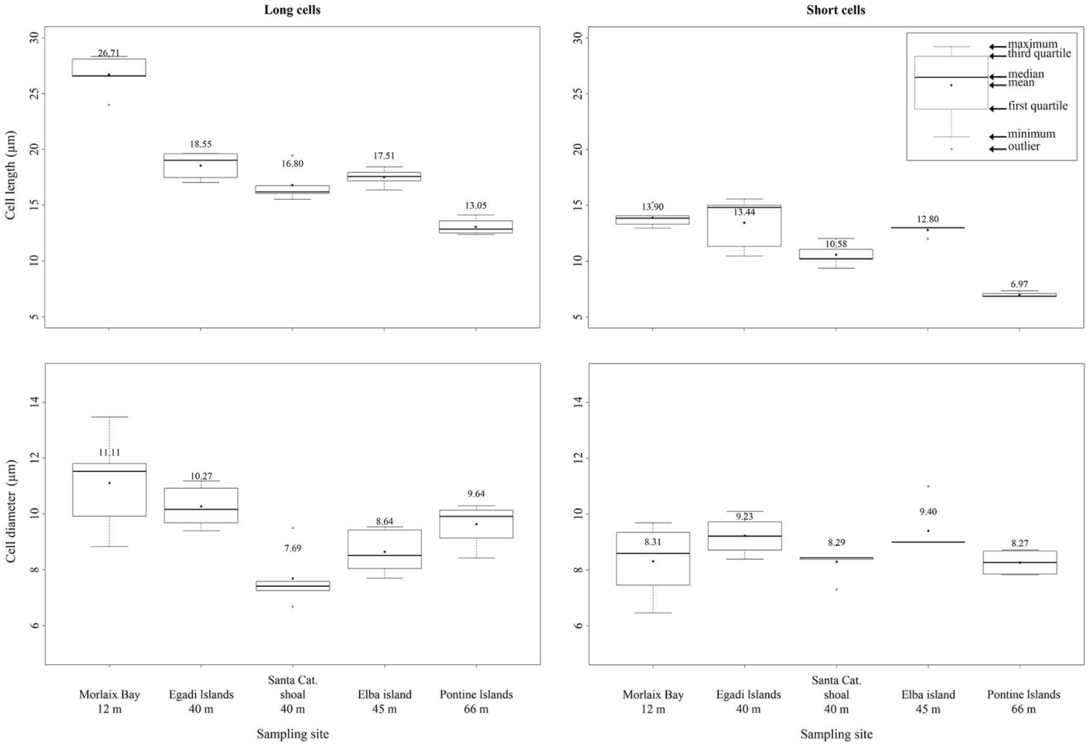

Figure 4. Box plots reporting cell lengths and cell diameters in both long and short cells of *L. corallioides* collected at different sampling sites and ordered along x axis according to the depth.

Both PW and SW show fibrils (Borowitzka, 1982) forming a dense network in support of the mineralization (Fig. 7d).

The epithallus is formed by one to three flared cells in longitudinal sections (Figs. 3g–j, 5f, 7c), always mineralized, with some exceptions in the top distal surface (Fig. 3g–j). The cell wall shows the same ultrastructural features of the perithallial cells, with both PW and SW mineralized (Figs. 3i, j, 5f, 7c).

Based on image analysis and time of collection, the calculated growth rate ranges from 0.10 mm/yr in Pontine to 0.13 mm/yr in both Morlaix and Egadi.

The two additional collections of *L. valens* and *L. minervae* (Fig. 8) are characterized by both PW and SW (Fig. 8a, b, e, f). The SW shows, in both species, an ultrastructural pattern like the one described for *L. corallioides* , with oriented bricks with rounded margins variably orientated, only apparently elongated and radial to the cell lumen in longitudinal sections (Fig. 8b, f). If observed in the cell lumen, where the cell membrane is lost, the SW shows bricks with different orientation and sometimes a zigzag and cross orientation (Fig. 8d, g).

On the contrary, PW shows a different shape and arrangement of crystals which are not characterized by the tiles of *L. corallioides* observed in Figs. 5d and 6a. Calcite crystals are squatter and more granular (Fig. 8a) or with irregular shape (Fig. 8h). One interesting aspect is that both samples show the occurrence of secondary calcite in the form of dogtooth crystals filling the cell lumen (Fig. 8b, c, e).

3.2 Statistical analyses on morphological parameters

The differences in the long cells' morphometry and wall thickness among sampling sites are statistically significant for each measured parameter ($p<0.05$; Supplement 1) (Fig. 9). Interestingly, the long-cell length of the deepest sample from Pontine Islands (66 m depth) is lower than the others ($p<0.001$) (Figs. 4, 9; Supplement), while in the shallowest sample collected in Morlaix (12 m depth) cells are remarkably longer ($p<0.001$) (Figs. 4, 9; Supplement 1).

In short cells, significant differences result only for cell (Fig. 9) and lumen lengths, as well as cell PW ($p<0.05$; Supplement). The shortest cells are observed again in the sam-

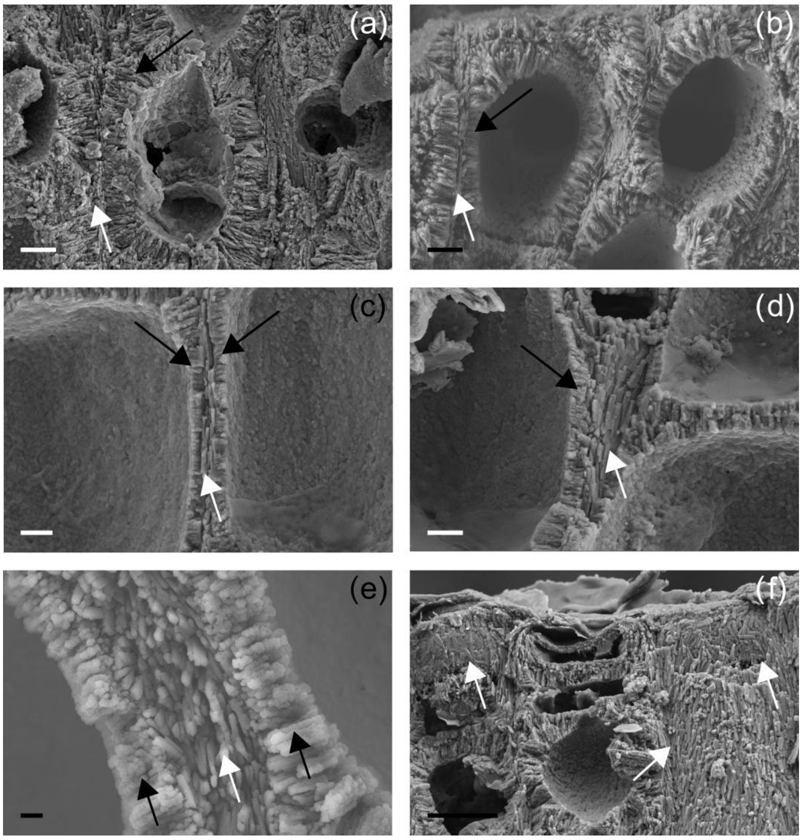

Figure 5. Details on primary wall (PW) in longitudinal section. **(a)** Thick-walled short cell showing both PW (white arrow) and SW (black arrow) for Santa Caterina shoal. Scale bar = 2 µm. **(b)** Thick-walled short cell showing both PW (white arrow) and SW (black arrow) for Pontine Islands. Scale bar = 2 µm. **(c)** Thin-walled long cell showing both PW (white arrow) and SW (black arrows). PW crystals in longitudinal section appear with elongated shape for Santa Caterina shoal. Scale bar = 1 µm. **(d)** Thin-walled long cell showing both PW (white arrow) and SW (black arrow). The fracture shows detail of tiles composing the PW (white arrow) for Santa Caterina shoal. Scale bar = 1 µm. **(e)** Details of multi-layered PW (white arrow) and SW (black arrows). PW crystals in longitudinal section appear as elongated crystals for Pontine Islands. Scale bar = 0.2 µm. **(f)** Perithallial and epithallial cells in which the longitudinal section is locally tangential to the PW (white arrows). Crystals appear as flat rectangular tiles for Santa Caterina shoal. Scale bar = 2 µm.

ple from Pontine Islands, differing from the one collected in Morlaix ($p<0.01$) (Fig. 9; Supplement 1), which stands out for being the highest value. On the contrary, the cell diameter slightly varies among sites, showing significant differences just in long cells ($p<0.01$; Supplement 1) (Fig. 9), with significantly higher values in Morlaix with respect to Elba island and Santa Caterina. The dimensions of the cell lumen change accordingly because of the positive correlation with the cell dimensions (Supplement 1).

Although banding is reported for all samples, elongation decreases with increasing depth, showing a strong inverse correlation in long cells ($p<0.01$; $r = 0.98$) (Fig. 9). The same trend is also observed in short cells, although with non-significant values ($p = 0.09$) (Fig. 9).

4 Discussion

Properly oriented longitudinal and transverse/oblique sections are required to obtain a precise comparative description of the main morphological features of CCA. Multi-scale approaches are also relevant, among which the ultrastructural pattern may represent a new powerful and strategic diagnostic tool (Figs. 3–7).

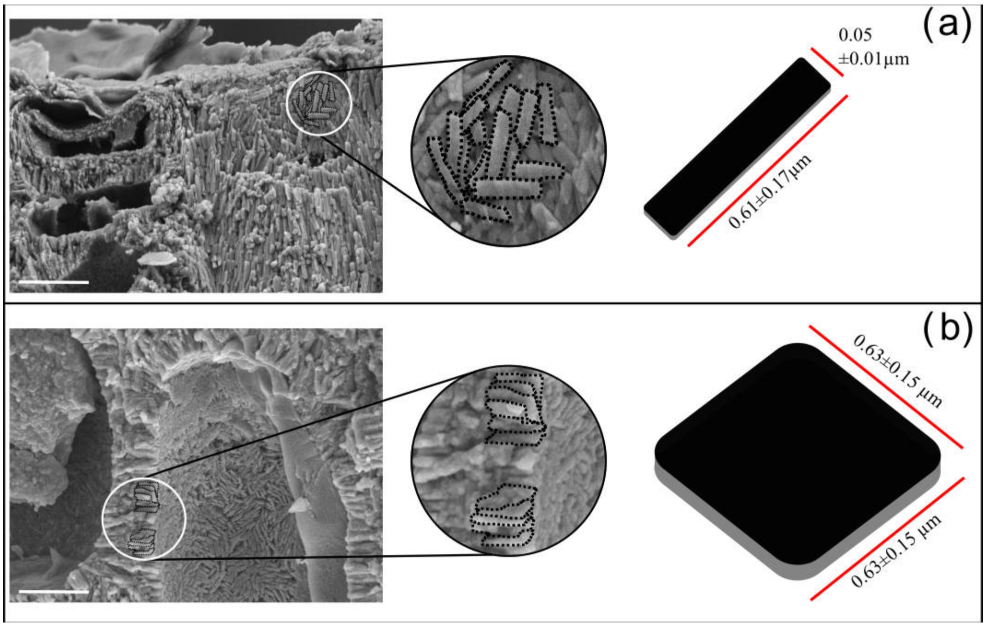

Figure 6. Ultrastructures of *Lithothamnion corallioides*: **(a)** rectangular tiles of the PW; **(b)** squared bricks of SW.

Recent studies based on genetic identification exclude the occurrence of other *Lithothamnion* species in the maerl of Morlaix Bay (Carro et al. 2014; Melbourne et al., 2017). Based on this identification and considering the macroscopic features, the thallus pattern, the microanatomy, the morphology and the morphometry of cell walls (Figs. 3, 5–7, Table 2), we identified the samples from Morlaix Bay as belonging to the species *L. corallioides*.

We compared the Mediterranean specimens with the Atlantic *L. corallioides*, and upon corresponding morphology, anatomy and ultrastructure (Figs. 3, 5–7, Table 2), we considered them as conspecific.

The perithallus of *L. corallioides* clearly shows the alternation of growth bands of third and fourth orders (Fig. 3a, b), in agreement with Foster (2001). Fourth-order bands represent the annual cycling, whereas third-order ones represent seasonal variations and can be firstly distinguished by an evident chromatic change due to the different calcification thickness between long and short cells (Foster, 2001). In our samples, the banding (third and fourth orders) is easily recognizable (Fig. 3), and both long and short cell lengths decrease across depths (Figs. 4, 9), as expected, mirroring a decrease in growth rate, whereas the diameter variation is significantly lower (Fig. 4, Supplement 1).

Giraud and Cabioch (1979) observed that a cell wall fracture in *L. corallioides* shows a layer of radial calcite crystals (SW) separated from its neighbor by a different sheet composed of tangential crystals (PW). A discontinuity that coincides with the fibrillar matrix observed in sections of decalcified material marks the limits of adjacent cellular filaments (Giraud and Cabioch, 1979). Our results match with the observations of these authors in longitudinal sections (Figs. 3, 5, 7), although the discontinuity between adjacent cells is not easily detectable because of the complete mineralization.

Auer and Piller (2020) built a morphological tree based on the observation of different ultrastructural patterns in epithallial cells, which matches with the phylogenetic tree at family level. For Hapalidiaceae, and in the *Lithothamnion*-type epithallial ultrastructure, they observed the occurrence of PWs with primary crystals formed along the middle lamella and the SWs with secondary rod-shaped crystals, also presenting fan-like structures. The samples studied in the present work show the PW and SW in both perithallial and epithallial cell walls (Figs. 3, 5, 7). Both are apparently composed of rod-like crystals in longitudinal sections. However, in longitudinal sections that are locally tangential to the PW, the apparent rods are revealed to be the longest and thinnest side of variably oriented rectangular tiles (Figs. 5, 6a). The tiles that envelop the cell (Fig. 5d, f) are the basic ultrastructural elements forming the PW. Differently, apparent rods of the SW are revealed to be squared and relatively flat bricks with rounded margins, as observed at the cell lumen without membrane or exactly at the contact between the SW longitudinal section and cell lumen (Figs. 6b, 7). Crystals in longitudinal

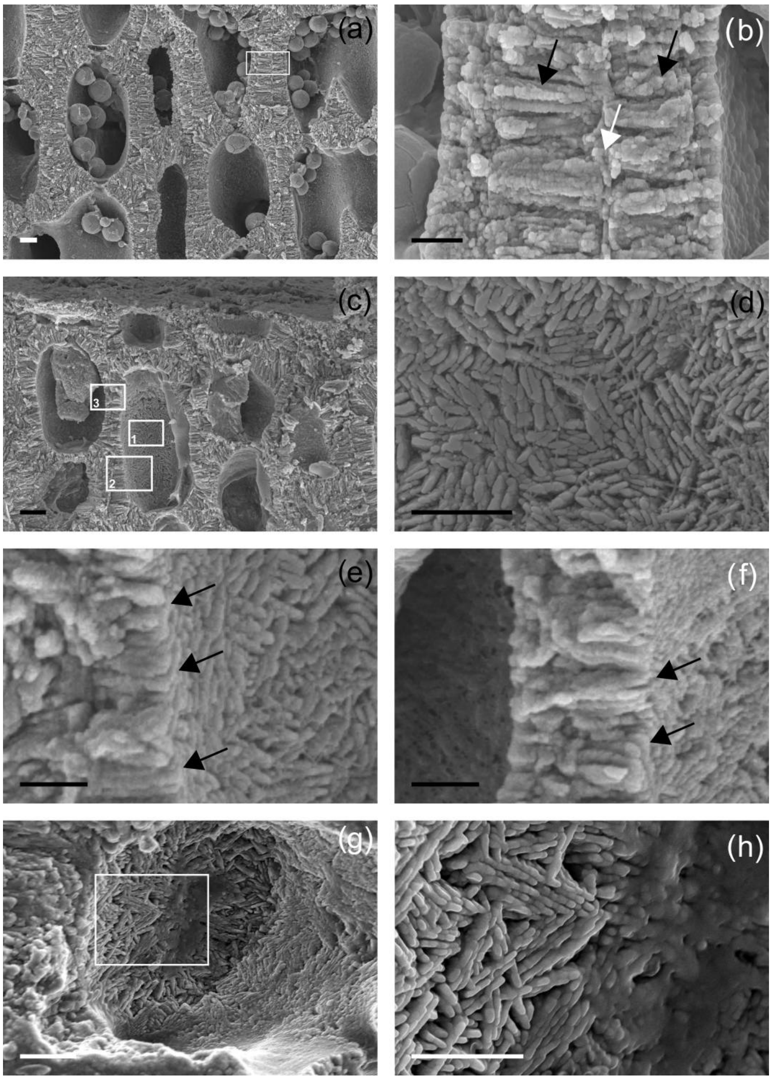

Figure 7. Details of secondary wall (SW) in longitudinal section. **(a)** Thick-walled short cells showing both PW and SW for Morlaix Bay. Scale bar = 2 µm. The inset is magnified in **(b)**; **(b)** very thin PW (white arrow) and SW (black arrows) in cell walls of two adjacent cells. The SW is characterized by elongated radial crystals formed by the fusion of smaller roundish units, in places showing an apparent multi-layered structure, for Morlaix Bay. Scale bar = 1 µm. **(c)** Perithallial thick-walled cells showing both PW and SW, as well as single flattened epithallial cells, for Morlaix Bay. Inset 1 is magnified in **(d)**, inset 2 in **(e)** and inset 3 in **(f)**. Scale bar = 2 µm. **(d)** The SW as visible in lumen cell with no membrane. In this view the crystals appear to be ovoidal to rod-shaped with a complex orientation associated with fibrils for Morlaix Bay. Scale bar = 1 µm. **(e)** The SW as visible in lumen cell with no membrane. A section showing at the same time a longitudinal section of the cell wall (on the left) and the inner surface of the lumen cell (on the right). This perspective provides the actual 3D shape of the SW crystals that are thin bricks (black arrows) for Morlaix Bay. Scale bar = 1 µm. **(f)** The SW as visible in lumen cell with no membrane. A section showing at the same time a longitudinal section of the cell wall (center) and the inner surface of the lumen cell (on the right). This perspective provides the actual 3D shape of the SW crystals that are thin bricks (black arrows) for Morlaix Bay. Scale bar = 1 µm. **(g)** A detail of the SW as visible inside a cell lumen. The crystals are thin bricks with a complex zigzag and cross orientation. The inset is magnified in **(h)** for Egadi Islands. Scale bar = 2 µm. **(h)** A zigzag and cross orientation of bricks in the SW for Egadi Islands. Scale bar = 1 µm.

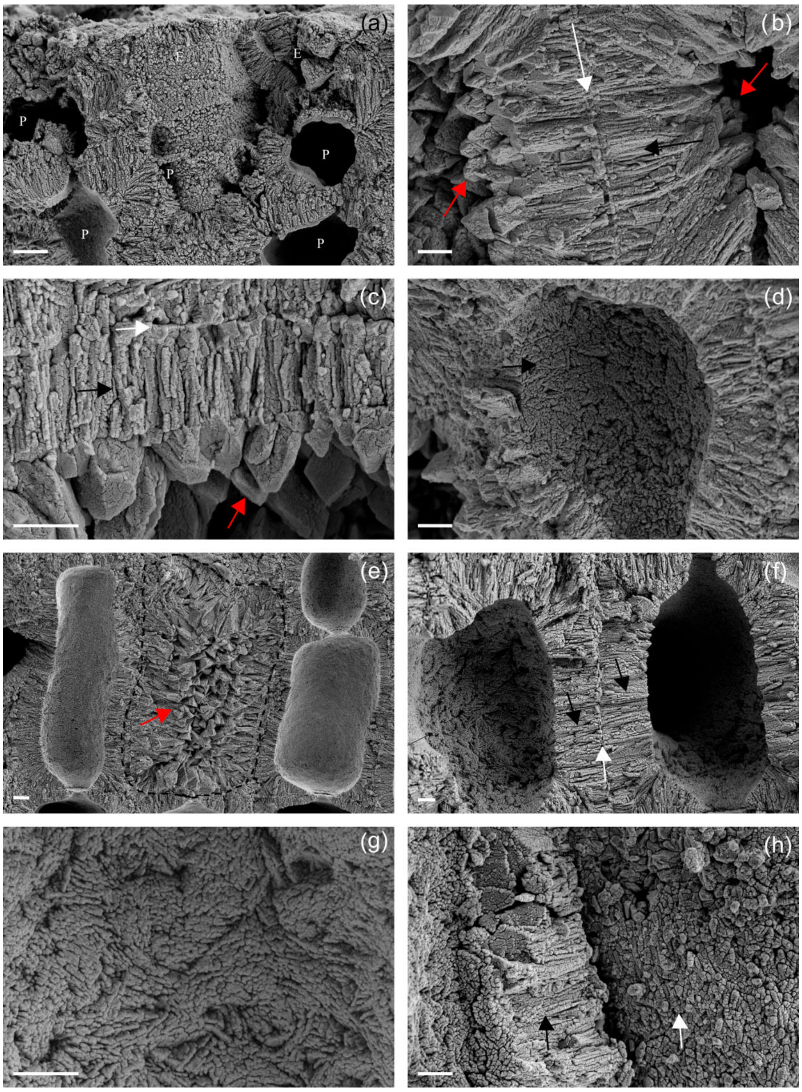

Figure 8. Details of the main ultrastructures of *Lithothamnion valens* **(a–d)** and *Lithothamnion minervae* **(e–h)**. **(a)** Perithallial (P) and epithallial (E) cells showing both PW and SW. Scale bar = 2 µm. **(b)** Details of PW (white arrow) and SW (black arrow) of two adjacent perithallial cells. The secondary wall is characterized by elongated radial crystals, whereas PW crystals are tangential to the cell lumen. The cell lumen is filled by secondary calcite (dogtooth shape, red arrows). Scale bar = 1 µm. **(c)** Detail of a cell wall with evident PW (white arrow) and SW (black arrow), as well as secondary dogtooth calcite filling the cell lumen (red arrow). Scale bar = 2 µm. **(d)** Detail of SW (black arrow) as visible in the cell lumen with no membrane. Note the multi-directional arrangement of calcite crystals. Scale bar = 2 µm. **(e)** Perithallial cells with elongated and rectangular shape. The central cell (dashed) shows a cell lumen filled by secondary calcite with dogtooth shape (red arrow). Scale bar = 2 µm. **(f)** Perithallial cells with both PW (white arrow) and SW (black arrows). Note in the cell lumen that the SW is characterized by elongated crystals showing a multi-directional arrangement. Scale bar = 2 µm. **(g)** Detail of the cell lumen with no membrane, showing multi-directional arrangement of elongated crystals in the SW. Scale bar = 1 µm. **(h)** The fracture shows detail of crystals composing the PW (white arrow) apparently composed of granules. The SW is characterized by elongated crystals in longitudinal section (black arrow). Scale bar = 1 µm.

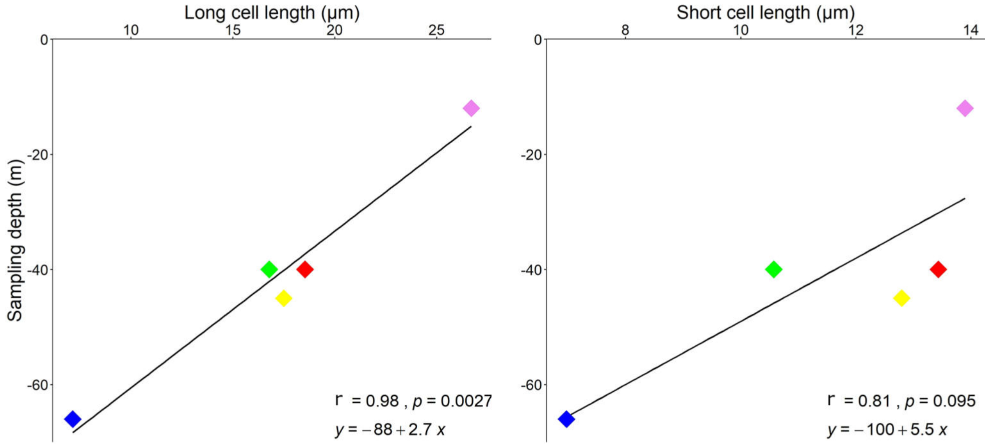

Figure 9. Correlation plots showing the relationship between sampling depth and cell lengths, measured in both long and short cells. Pearson's correlation significance at $p<0.05$. Pink is for Morlaix Bay (France, 12); green is for Egadi Islands (Italy, 40); red is for Santa Caterina shoal (Italy, 40); yellow is for Elba island (Italy, 45); blue is for Pontine Islands (Italy, 66).

sections of the SW are radial to the cell lumen, in agreement with Giraud and Cabioch (1979), and appear formed by small grains fused together (Figs. 3, 7b, f). They can also show a zigzag and cross orientation (Fig. 7g, h) like the fan-delta structure described by Auer and Piller (2020).

Therefore, our findings agree with the results of Auer and Piller (2020), although providing a more detailed description of the ultrastructural pattern of *L. corallioides* (Fig. 6).

Despite the different environmental conditions, likely occurring at the different sampling sites and depths, the ultrastructures of both PW and SW seem conservative and detectable in all samples. Therefore, the ultrastructures and the ultrastructural pattern are not dependent on environmental controls.

However, *L. corallioides* shows variable cell elongations (Table 2) and growth rates, both decreasing according to sampling depth (Fig. 9), and a variation in PW and SW thickness, generally greater in short than in long cells, unrelated to depth (Table 2, Supplement 1). These features possibly represent the effect of the different environmental conditions in which it lives that do not affect the ultrastructural pattern.

As defined by Lowenstam (1981), a biologically controlled biomineralization is recognized in organisms with extensive control over their mineral formation, resulting in well-ordered mineral structures with minor size variations and species-specific crystal habits, as we detected in *L. corallioides*. Despite some analogies with the observations of Nash et al. (2019), our findings demonstrate that the biomineralization process in CCA is biologically controlled (Borowitzka, 1984; Cabioch and Giraud, 1986) rather than induced (de Carvalho et al., 2017; Nash et al., 2019). The two additional samples, *L. minervae* and *L. valens*, show distinct styles of PW calcification, and this is extremely interesting for its application in Paleontology. Ultrastructures and ultrastructural pattern possibly represent a powerful tool for morphological species identification. Further investigation is needed to clarify the validity of this hypothesis in other genera and species.

Finally, the occurrence of calcite in the form of dogtooth crystals filling the cell lumen (Fig. 8b, c, e) is an exceptional finding. The voids of the cell lumens allowed for the development of calcite crystals which in terms of shape, size and pattern are completely different from the original ones forming the cell wall calcification. It represents a form of extremely early alteration, possibly diagenesis, in collections that were alive at the time of sampling. The phenomenon of earliest diagenesis, as already observed in Holocene and live Scleractinia corals (Nothdurft and Webb, 2008; Rashid et al., 2020), has implications in the reliability of climate and paleoclimate studies based on geochemical techniques and also when applied to recent collections. Therefore, the possible occurrence of dog-tooth calcite must be carefully checked when selecting coralline algae samples for geochemical investigations.

5 Conclusions

We define the cell wall ultrastructural pattern of *L. corallioides* as follows:

- perithallus with evident banding as the result of the alternation of series of short-squared and long ovoid/rectangular cells;
- epithallus with one to three flared cells;

- same and consistent ultrastructural pattern of the cell walls both in perithallus and epithallus, with PW and SW calcite walls always present;
- PW characterized by rectangular tiles;
- SW characterized by flattened squared bricks with roundish outlines;
- long and short cells with similar diameter and with different thickness of the PW and SW, resulting mainly in a thicker PW and SW in short cells.

The variable cell elongation, decreasing according to depth and producing an evident banding, never affects the ultrastructural pattern that maintains the same arrangement also under different growth rates. These findings demonstrate that the CCA calcification process seems to be biologically controlled rather than induced. The comparison with other *Lithothamnion* species highlights differences in the mineralization pattern of PW. Therefore, the ultrastructure of the cell wall in CCA results in a promising new diagnostic tool for species identification with important potential applications in paleontology. Lastly, an early alteration phenomenon, at the scale of ultrastructures, has been identified for the first time in living coralline algae.

Data availability. All data of this study are available in this text and in the Supplement.

Supplement. The supplement related to this article is available online at: https://doi.org/10.5194/bg-18-6061-2021-supplement.

Author contributions. VAB conceived the research, conducted SEM observations, interpreted the results, and wrote and revised the manuscript. DB conceived the research, and wrote and revised the manuscript. GP conducted the statistical analyses and prepared Figs. 4 and 9.

Competing interests. The contact author has declared that neither they nor their co-authors have any competing interests.

Acknowledgements. We are grateful to two anonymous reviewers for their fruitful comments on the manuscript. Agostino Meroni is thanked for the extraction of temperature values. For the sample from Pontine Islands, the captain, crew and scientific staff of RV *Minerva Uno* cruise Strategia Marina Ligure-Tirreno are acknowledged for their efficient and skillful cooperation at sea. The sample from Capo Carbonara has been collected in the framework of the agreement between the University of Milano-Bicocca and the Marine Protected Area of Capo Carbonara for the realization of the monitoring activities of the Marine Strategy Framework Directive.

Giulia Piazza is funded by a doctoral fellowship in Environmental Sciences of the Milano-Bicocca University.

This article is a contribution to the Project MIUR-Dipartimenti di Eccellenza 2018–2022 DISAT-UNIMIB.

Review statement. This paper was edited by Hiroshi Kitazato and reviewed by two anonymous referees.

References

Adey, W. H.: Coralline algae as indicators of sea-level, in: Sea-Level Research, edited by: van de Plassche, O., Springer, Dordrecht, https://doi.org/10.1007/978-94-009-4215-8_9, 1986.

Adey, W. H.: Review-coral reefs: algal structured and mediated ecosystems in shallow, turbulent, alkaline waters, J. Phycol., 34, 393–406, https://doi.org/10.1046/j.1529-8817.1998.340393.x, 1998.

Adey, W. H. and McKibbin, D. L.: Studies on the Maerl Species *Phymatolithon calcareum* (Pallas) nov. comb. and *Lithothamnium corallioides* Crouan in the Ria de Vigo, Bot. Mar., 13, 100–106, https://doi.org/10.1515/botm.1970.13.2.100, 1970.

Agnesi, S., Babbini, L., Bressan, G., Cassese, M. L., Mo, G., and Tunesi, L.: Distribuzione della Facies del Maerl e delle associazioni a rodoliti nei mari italiani: attuale stato delle conoscenze, Biol. Mar. Medit., 18, 50–51, 2011.

Aguirre, J., Riding, R., and Braga, J.: Diversity of coralline red algae: Origination and extinction patterns from the Early Cretaceous to the Pleistocene, Paleobiology, 26, 651–667, https://doi.org/10.1666/0094-8373(2000)026<0651:DOCRAO>2.0.CO;2, 2000.

Aguirre, J., Braga, J. C., Martín J. M., and Betzler C.: Paleooenvironmental and stratigraphic significance of Pliocene rhodolith beds and coralline algal bioconstructions from the Carboneras Basin (SE Spain), in: Calcareous algae and global change: from identification to quantification, edited by: Basso, D. and Granier, B., Geodiversitas, 34, 115–136, https://doi.org/10.5252/g2012n1a7, 2012.

Auer, G. and Piller, W. E.: Nanocrystals as phenotypic expression of genotypes – An example in coralline red algae, Sci. Adv., 6, eaay2126, https://doi.org/10.1126/sciadv.aay2126, 2020.

Basso, D.: Living calcareous algae by a paleontological approach: the genus *Lithothamnion* Heydrich nom. cons. from the soft bottoms of the Tyrrhenian Sea (Mediterranean), Riv. It. Pal. Strat., 101, 349–366, doi10.13130/2039-4942/8592, 1995.

Basso, D.: Deep rhodolith distribution in the Pontian Islands, Italy: a model for the paleoecology of a temperate sea, Palaeogeogr. Palaeocl., 137, 173–187, 1998.

Basso, D., Fravega, P., and Vannuci, G.: The taxonomy of *Lithothamnium ramosissimum* (Gümbel non Reuss) Conti and *Lithothamnium operculatum* (Conti) Conti (Rhodophyta, Corallinaceae), Facies, 37, 167–181, https://doi.org/10.1007/BF02537377, 1997.

Basso D., Nalin R., and Massari F.: Genesis and composition of the Pleistocene Coralligène de plateau of the Cutro Terrace (Calabria, southern Italy), Neues Jahrb. Geol. P.-A., 244, 173–182, https://doi.org/10.1127/0077-7749/2007/0244-0173, 2007.

Basso, D., Caragnano, A., Le Gal, L., and Rodondi, G.: The genus Lithophyllum in the north-western Indian Ocean, with description of L. yemenense sp. nov., L. socotraense sp. nov., L. subplicatum comb. et stat. nov., and the resumed L. affine, L. kaiseri, and L. subreduncum (Rhodophyta, Corallinales), Phytotaxa, 208, 183–200, https://doi.org/10.11646/phytotaxa.208.3.1, 2015.

Basso, D., Babbini, L., Kaleb, S., Bracchi, V. A., and Falace, A.: Monitoring deep Mediterranean rhodolith beds, Aquatic Conserv: Mar. Freshw. Ecosyst., 26, 549–561, https://doi.org/10.1002/aqc.2586, 2016.

Basso, D., Babbini, L., Ramos-Esplá, A. A., and Salomidi, M.: Mediterranean rhodolith beds, in: Rhodolith/maërl beds: A global perspective, Springer, Cham, Coas. Res. Lib., 15, 281–298, 2017.

Birkett, D. A., Maggs, C. A., and Dring, M. J.: An Overview of Dynamic and Sensitivity Characteristics for Conservation Management of Marine SACs, Vol. 5, Maerl, Scottish Association for Marine Science, Scotland, 116 pp., 1998.

Blake, C. and Maggs, C. A.: Comparative growth rates and internal banding periodicity of maerl species (Corallinales, Rhodophyta) from northern Europe, Phycologia, 42, 606–612, https://doi.org/10.2216/i0031-8884-42-6-606.1, 2003.

Borowitzka, M. A.: Morphological and Cytological Aspects of Algal Calcification, Int. Rev. Cytol., 74, 127–162, 1982.

Borowitzka, M. A.: Calcification in aquatic plants, Plant Cell Environ., 7, 457–466, https://doi.org/10.1111/j.1365-3040.1984.tb01436.x, 1984.

Borowitzka, M. A.: Carbonate calcification in algae – initiation and control, in: Biomineralization, edited by: Mann, S., Webb, J., and Williams, R. J. P., Chemical and biochemical perspectives, VCH Verlagsgesellschaft, Weinheim, 63–95, 1989.

Bracchi, V. A., Nalin, R., and Basso, D.: Morpho-structural heterogeneity of shallow-water coralligenous in a Pleistocene marine terrace (Le Castella, Italy), Pal. Pal. Pal., 454, 101–112, https://doi.org/10.1016/j.palaeo.2016.04.014, 2014.

Bracchi, V. A., Nalin, R., and Basso, D.: Paleoecology and dynamics of coralline dominated facies during a Pleistocene transgressive–regressive cycle (Capo Colonna marine terrace, Southern Italy), Pal. Pal. Pal., 414, 296–309, https://doi.org/10.1016/j.palaeo.2014.09.016, 2016.

Burdett, H., Kamenos, N. A., and Law, A.: Using coralline algae to understand historic marine cloud cover, Palaeogeogr. Palaeocl., 302, 65–70, https://doi.org/10.1016/j.palaeo.2010.07.027, 2011.

Cabioch, J. and Giraud, G.: Structural aspects of biomineralization in the coralline algae (calcified Rhodophyceae), in: Biomineralization in lower plants and animals, edited by: Leadbeater, B. S. C. and Riding, R., Clarendon Press, Oxford, 141–156, 1986.

Caragnano, A., Colombo, F., Rodondi, G., and Basso, D.: 3-D distribution of nongeniculate corallinales: a case study from a reef crest of South Sinai (Red Sea, Egypt), Coral Reefs, 28, 881–891, https://doi.org/10.1007/s00338-009-0524-6, 2009.

Caragnano, A., Foetisch, A., Maneveldt, G. W., Millet, L., Liu, L. C., Lin, S. M., Rodondi, G., and Payri, C. E.: Revision of Corallinaceae (Corallinales, Rhodophyta): recognizing Dawsoniolithon gen. nov., Parvicellularium gen. nov. and Chamberlainoideae subfam. nov. containing Chamberlainium gen. nov. and Pneophyllum, J. Phycol., 54, 391–409, https://doi.org/10.1111/jpy.12644, 2018.

Carro, B., Lopez, L., Peña, V., Bárbara, I., and Barreiro, R.: DNA barcoding allows the accurate assessment of European maerl diversity: a Proof-of-Concept study, Phytotaxa, 190, 176–189, https://doi.org/10.11646/phytotaxa.190.1.12, 2014.

Costa, I. O., Jesus, P. B. D., de Jesus, T. D. S., Souza, P. D. S., Horta, P. A., and Nunes, J. M. D. C.: Reef-building coralline algae from the Southwest Atlantic: filling gaps with the recognition of Harveylithon (Corallinaceae, Rhodophyta) on the Brazilian coast, J. Phycol., 55, 1370–1385, https://doi.org/10.1111/jpy.12917, 2019.

Crouan, P. L. and Crouan, H. M.: Florule du Finistère, 151, pl. 20, figs 8-10, Paris and Brest, 1867.

de Carvalho, R. T., Salgado, L. T., Amado Filho, G. M., Leal, R. N., Werckmann, J., Linhares Rossi, A., Porto Carreiro Campos, A., Santiago Karez, C., and Farina, M.: Biomineralization of calcium carbonate in the cell wall of *Lithothamnion crispatum* (Hapalidiales, Rhodophyta): correlation between the organic matrix and the mineral phase, J. Phycol., 53, 642–651, https://doi.org/10.1111/jpy.12526, 2017.

Flajs, G.: Skeletal structures of some calcifying algae, edited by: Flügel, E., Fossil Algae: Recent Results and Developments, Springer Berlin Heidelberg, 225–231, 1977.

Foslie, M.: Algologiske notiser VI. Kongelige Norske Videnskabers Selskabs Skrifter, 1909, 1–63, 1909.

Foster, M.: Rhodoliths: between rocks and soft places, J. Phycol., 37, 659–667, https://doi.org/10.1046/j.1529-8817.2001.00195.x, 2001.

Gambi, M. C., Buia, M. C., Massa-Gallucci, A., Cigliano, M., Lattanzi, L., and Patti, F. P.: The "pink mile": benthic assemblages of rhodolith and maërl beds (Corallinales) off the Island of Ischia (Tyrrhenian Sea), in: UNEP-MAP-RAC/SPA, Proceedings of the 1st Mediterranean Symposium on the Conservation of the Coralligenous and Other Calcareous Bio-concretions (Tabarka, 15-16/1/2009), edited by: Pergent-Martini, C. and Brichet, M., 198–201, 2009.

Giraud, G. and Cabioch, J.: Aspects ultrastructuraux de la calcification chez les Corallinacées (Rhodophycées), J. Microscopie, 26, 14a–14a, 1976.

Giraud, G. and Cabioch, J.: Ultrastructure and elaboration of calcified cell-walls in the coralline algae (Rhodophyta, Cryptonemiales), Biologie Cell, 36, 81–86, 1979

Halfar, J., Zack, T., Kronz, A., and Zachos, J.C.: Growth and high-resolution paleoenvironmental signals of rhodoliths (coralline red algae): A new biogenic archive, J. Geophys. Res.-Ocean., 105, 22107–22116, https://doi.org/10.1029/1999jc000128, 2000.

Henrich, R., Freiwald, A., Betzler, C., Bader, B., and Schäfer, P.: Controls on modern carbonate sedimentation on warm-temperate to arctic coasts, shelves, and seamounts in the Northern Hemisphere: Implications for fossil counterparts, Facies, 32, 71–108, https://doi.org/10.1007/BF02536865, 1995.

Hernandez-Kantun, J. J., Hall-Spencer, J. M., Grall, J., Adey, W., Rindi, F., Maggs, C. A., Bárbara, I., and Peña, V.: North Atlantic Rhodolith Beds, in: Rhodolith/Maërl Beds: A Global Perspective, edited by: Riosmena-Rodríguez, R., Nelson, W., and Aguirre, J., Coastal Research Library, Vol. 15, Springer, Cham, https://doi.org/10.1007/978-3-319-29315-8_10, 2017.

Huvé, H.: Contribution à l'étude des fonds à *Lithothamnium* (?) *solutum* Foslie (= *Lithophyllum solutum* (Foslie) Lemoine) de la région de Marseille, Recueil des Travaux de la Station Marine d'Endoume, 18, 105–133, 1956.

Irvine, L. M. and Chamberlain, Y. M.: Seaweeds of the British Isles, Vol. 1, Rhodophyta Part 2B Corallinales, Hildenbrandiales, HMSO, London, 1994.

Jacquotte, R.: Étude des fonds de maërl de Méditerranée, Recueil des Travaux de la Station Marine d'Endoume, Recueil de Travaux de la Station Marine d'Endoume, 26, 141–235, 1962.

Kamenos, N. A. and Law, A.: Temperature controls on coralline algal skeletal growth, J. Phycol., 46, 331–335, https://doi.org/10.1111/j.1529-8817.2009.00780.x, 2010.

Lowenstam, H. A.: Mineral formed by organism, Science, 211, 1126–1131, https://doi.org/10.1126/science.7008198, 1981.

Marchese, F., Bracchi, V.A., Lisi, G., Basso, D., Corselli, C., and Savini, A.: Assessing Fine-Scale Distribution and Volume of Mediterranean Algal Reefs through Terrain Analysis of Multibeam Bathymetric Data. A Case Study in the Southern Adriatic Continental Shelf, Water, 12, 157, https://doi.org/10.3390/w12010157, 2020.

Martin, S., Castets, M. D., and Clavier, J.: Primary production, respiration and calcification of the temperate free-living coralline alga, Aquat. Bot., 85, 121–128, 2006.

Melbourne, L. A., Hernández-Kantún, J. J., Russell, S., and Brodie, J.: There is more to maerl than meets the eye: DNA barcoding reveals a new species in Britain, *Lithothamnion erinaceum* sp. nov. (Hapalidiales, Rhodophyta), Eur. J. Phycol., 52, 166–178, https://doi.org/10.1080/09670262.2016.1269953, 2017.

Nash, M. C. and Adey, W.: Multiple phases of mg-calcite in crustose coralline algae suggest caution for temperature proxy and ocean acidification assessment: lessons from the ultrastructure and biomineralization in *Phymatolithon* (Rhodophyta, Corallinales), J. Phycol., 53, 970–984, https://doi.org/10.1111/jpy.12559, 2017.

Nash, M. C., Opdyke, B. N., Troitzsch, U., Russell, B. D., Adey, W. H., Kato, A., Diaz-Pulido, G., Brent, C., Gardner, M., Prichard, J., and Kline D. I.: Dolomite-rich coralline algae in reefs resist dissolution in acidified conditions, Nat. Clim. Change, 3, 268–272, 2013.

Nash, M. C., Russell, B. D., Dixon, K. R. Liu, M., and Xu, H.: Discovery of the mineral brucite (magnesium hydroxide) in the tropical calcifying alga *Polystrata dura* (Peyssonneliales, Rhodophyta), J. Phycol., 51, 403–4077, https://doi.org/10.1111/jpy.12299, 2015.

Nash, M. C., Diaz-Pulido, G., Harvey, A. S., and Adey, W.: Coralline algal calcification: A morphological and process-based understanding, PLoS ONE, 14, e0221396, https://doi.org/10.1371/journal.pone.0221396, 2019.

Nothdurft, L. K. and Webb, H. E.: Earliest diagenesis in scleractinian coral skeletons: implications for palaeoclimate-sensitive geochemical archives, Facies, 55, 161–201, https://doi.org/10.1007/s10347-008-0167-z, 2008.

Peña, V. and Bárbara, I.: Maerl community in the north-western Iberian Peninsula: a review of floristic studies and long-term changes, Aq. Cons.-Mar. Freshw. Ecos., 18, 339–366, https://doi.org/10.1002/aqc.847, 2008.

Peña, V. and Bárbara, I.: Distribution of the Galician maerl beds and their shape classes (Atlantic Iberian Peninsula): proposal of areas in future conservation actions, Cahier Biol. Mar., 50, 353–368, 2009.

Peña, V., Bárbara, I., Grall, J., Maggs, C. A., and Hall-Spencer, J. M.: The diversity of seaweeds on maerl in the NE Atlantic, Mar. Biodiv., 44, 533–551, https://doi.org/10.1007/s12526-014-0214-7, 2014.

Potin, P., Floch, J. Y., Augris, C., and Cabioch, J.: Annual growth rate of the calcareous red alga *Lithothamnion corallioides* (Corallinales, Rhodophyta) in the Bay of Brest, France, Hydrobiologia, 204, 263–267, https://doi.org/10.1007/BF00040243, 1990.

Quaranta, F., Vannucci, G., and Basso, D.: *Neogoniolithon contii* comb. nov. based on the taxonomic re-assessment of Mastrorilli's original collections from the Oligocene of NW Italy (Tertiary Piedmont Basin), Riv. It. Paleont. Strat., 113, 43–55, https://doi.org/10.13130/2039-4942/6357, 2007.

Ragazzola, F., Foster, L. C., Jones, C. J., Scott, T. B., Fietzke, J., Kilburn, M. R., and Schmidt, D. N.: Impact of high CO_2 on the geochemistry of the coralline algae *Lithothamnion glaciale*, Sci. Rep., 6, 20572, https://doi.org/10.1038/srep20572, 2016.

Ragazzola, F., Caragnano, A., Basso, D., Schmidt, D. N., and Fietzke, J.: Establishing temperate crustose early Holocene coralline algae as archives for paleoenvironmental reconstructions of the shallow water habitats of the Mediterranean Sea, Palaeontology, 63, 155–170, https://doi.org/10.1111/pala.12447, 2020.

Rashid, R., Eisenhauer, A., Liebetrau, V., Fietzke, J., Böhm, F., Wall, M., Krause, S., Rüggeberg, A., Dullo, W.C., Jurikova, H., Samankassou, E., and Lazar, B.: Early Diagenetic Imprint on Temperature Proxies in Holocene Corals: A Case Study from French Polynesia, Front. Earth Sci., 8, 301, https://doi.org/10.3389/feart.2020.00301, 2020.

Ries, J. B.: Mg fractionation in crustose coralline algae: Geochemical, biological, and sedimentological implications of secular variation in the Mg/Ca ratio of seawater, Geoc. Cosmoch. Ac., 70, 891–900, https://doi.org/10.1016/j.gca.2005.10.025, 2006.

Savini, A., Basso, D., Bracchi, V. A., Corselli, C., and Pennetta, M.: Maerl-bed mapping and carbonate quantification on submerged terraces offshores the Cilento peninsula (Tyrrhenian Sea, Italy), Geodiversitas, 34, 77–98, https://doi.org/10.5252/g2012n1a5, 2012.

Steller, D. L., Hernández-Ayón, J. M., Riosmena-Rodríguez, R., and Cabello-Pasini, A.: Effect of temperature on photosynthesis, growth, and calcification rates of the free-living coralline alga *Lithophyllum margaritae*, Cienc. Mar., 33, 441–456, https://doi.org/10.7773/cm.v33i4.1255, 2007.

Vásquez-Elizondo, R. M. and Enríquez, S.: Light Absorption in Coralline Algae (Rhodophyta): A Morphological and Functional Approach to Understanding Species Distribution in a Coral Reef Lagoon, Front. Mar. Sci., 4, 297, https://doi.org/10.3389/fmars.2017.00297, 2017.

Wilson, S., Blake, C., Berges, J. A., and Maggs, C. A.: Environmental tolerances of free-living coralline algae (maerl): implications for European marine conservation, Biol. Cons., 120, 279–289, https://doi.org/10.1016/j.biocon.2004.03.001, 2004.

Woelkerling, W. J. and Irvine, L. M.: The typification and status of Phymatolithon (Corallinaceae, Rhodophyta), British Phycol. J., 21, 55–80, 1886.

Woelkerling, W. J.: The coralline red algae: an analysis of the genera and subfamilies of non-geniculate Corallinaceae, British Museum (Natural History) and Oxford University Press, London, UK, 268 pp., 1988.

Zuo, H., Balmaseda, M. A., Tietsche, S., Mogensen, K., and Mayer, M.: The ECMWF operational ensemble reanalysis–analysis system for ocean and sea ice: a description of the system and assessment, Ocean Sci., 15, 779–808, https://doi.org/10.5194/os-15-779-2019, 2019.

PLOS ONE

RESEARCH ARTICLE

Calcification traits for cryptic species identification: Insights into coralline biomineralization

Daniela Basso[1,2]*, **Giulia Piazza**[1,3], **Valentina Alice Bracchi**[1,2]

1 Department of Earth and Environmental Sciences, University of Milano-Bicocca, Milan, Italy, **2** CoNISMa Research Unit of Milano-Bicocca, Milano, Italy, **3** Department of Earth and Ocean Dynamics, University of Barcelona, Barcelona, Spain

* daniela.basso@unimib.it

Abstract

Calcareous red algae are foundation species and ecosystem engineers with a global distribution. The principles governing their calcification pathways are still debated and the morphological characters are frequently unreliable for species segregation, as shown by molecular genetics. The recent description of the new species *Lithophyllum pseudoracemus*, previously undetected and morphologically confused with *Lithophyllum racemus*, offered a challenging opportunity to test the effectiveness of microanatomy and ultrastructural calcification traits as tools for the identification of these two species, for integrative taxonomy. High resolution SEM images of molecularly identified samples showed that the different size of the perithallial cells and the features of the asexual conceptacle chambers may contribute to the separation of the two species. The two species share the same crystallite morphology in the primary and secondary cell-wall calcification, as previously described in other species belonging to the same clade. However, the perithallial secondary calcification was significantly thicker in *L. racemus* than in *L. pseudoracemus*. We described a granular calcified layer in the innermost part of the cell wall, as a putative precursor phase in the biomineralization and formation of the secondary calcification. The hypothesis of different pathways for the formation of the primary and secondary calcification is supported by the observed cell elongation associated with thicker and higher Mg/Ca primary calcification, the inverse correlation of primary and secondary calcification thickness, and the absence of primary calcification in the newly formed wall cutting off an epithallial cell from the meristem.

Citation: Basso D, Piazza G, Bracchi VA (2022) Calcification traits for cryptic species identification: Insights into coralline biomineralization. PLoS ONE 17(10): e0273505. https://doi.org/10.1371/journal.pone.0273505

Editor: Marcos Rubal García, CIIMAR Interdisciplinary Centre of Marine and Environmental Research of the University of Porto, PORTUGAL

Received: February 11, 2022

Accepted: August 9, 2022

Published: October 3, 2022

Data Availability Statement: All relevant data are within the paper and its Supporting Information files.

Funding: DB and VAB were funded by the national project FISR 2019_04543 CRESCIBLUREEF (https://www.mur.gov.it). GP received a doctoral fellowship in Environmental Sciences from Università di Milano-Bicocca. The funder had no role in study design, data collection and analysis,

Introduction

Non-geniculate "crustose" coralline algae (CCA) have a widely recognized global ecological importance and provide multiple ecosystem services, which include, among others, their role as habitat formers [1–8] and carbonate producers [9–14]. These properties derive from CCA ability to precipitate high-magnesium calcite (containing more than 8–12 mol% $MgCO_3$) in the cell walls, along polysaccharide microfibrils [12, 15–18]. The mineralized thallus offers

decision to publish, or preparation of the manuscript.

Competing interests: The authors have declared that no competing interests exist.

strength and protection to the alga against grazing and other disturbances [19] and can be preserved in the fossil record through geological times [14, 20–24]. During biomineralization, CCA incorporate several major and trace elements that mirror the chemical properties of their growth environment, becoming significant proxy records for paleoecology and palaeoceanography [25–28]. Longitudinal sections of some CCA species show dark and light bands (= thallus zonation), especially obvious in long protuberances, reflecting a rhythmic, seasonal growth pattern [1, 29–32]. Dark bands are formed by thick-walled small cells, while light bands are made of longer, thin-walled cells. Annual growth bands can be used for establishing the age of the CCA and for high-resolution time series analyses [25, 33, 34]. Cell wall calcification is composed of radial high-Mg calcite crystallites, around the cell lumen, and other tangentially arranged crystallites, the latter typically visible at the boundary between two adjacent cell filaments [18, 35–39].

CCA species identification merely based on morphological descriptors can lead to uncertainties, as highlighted by several systematic revisions based on molecular genetics [40–47]. In other calcifying marine organisms such as foraminifera [48–50], coccolithophores [51] and corals [52–55], the pattern of mineralization has been used for taxonomic identification, showing consistency with molecular phylogeny. Recently, Auer and Piller [38] matched the micro- and nanomorphology of CCA cell walls with molecular phylogeny, grouping different genera based on the crystallite shape in the epithallial and meristematic cell walls. Moreover, recent studies on the cell wall ultrastructure of *Lithothamnion corallioides* (P. Crouan & H. Crouan) P. Crouan & H. Crouan revealed a consistent pattern in the crystallite shape and arrangement, apparently unaffected by the environment [39].

CCA are common in Mediterranean benthic communities, where they are distributed from the intertidal zone down to circalittoral depths [56, 57]. Nevertheless, their calcification process is still poorly studied. *Lithophyllum racemus* (Lamarck) Foslie is a Mediterranean endemic non-geniculate CCA, forming unattached globular rhodoliths, showing a typical "praline" morphotype [56, 58–64]. A phylogenetic study [65] revealed the cryptic species *Lithophyllum pseudoracemus* Caragnano, Rodondi & Rindi, that had been previously confounded with the morphologically similar *L. racemus*. The two morphologically similar but genetically distinct species *L. racemus* and *L. pseudoracemus* may occur sympatrically and provide an opportunity to test the suitability of putative descriptors relying on calcification traits as a new taxonomic character for CCA identification at species level. Beside the ultrastructural calcification traits, we considered and measured different classical morphological descriptors that may help in species identification., such as cell and conceptacle microanatomy. Both molecularly classified samples of *L. racemus* and *L. pseudoracemus* [65], and other morphoanatomically similar samples that lack phylogenetic characterization were investigated.

Materials and methods

Sample collection

Samples were collected at different locations across the Western and Eastern Mediterranean Sea (Table 1). They were recovered in the framework of the Italian "Marine Strategy" Programme and by local surveys. The collection of rhodoliths of *Lithophyllum racemus* and *L. pseudoracemus* does not require a permit. Four out of six samples have been targeted for a multi-gene molecular phylogeny at Università Politecnica delle Marche (AN) [65], and identified as *L. racemus* and *L. pseudoracemus* (Table 1). Sample DB661 is the neotype of *L. racemus* [59]. The samples used for phylogenetic analyses are currently stored in the Herbarium Universitatis Florentinae, at the Natural History Museum in Florence (Italy). The last two samples,

Table 1. ***L. racemus*, *L. pseudoracemus*, *L.* cf. *pseudoracemus* and *L.* cf. *racemus* specimens examined under SEM.**

Sample	Herbarium	Sampling site (latitude, longitude)	Depth (m)	Species
DB661	FI058887	Capri, Gulf of Naples (Italy) (40˚34’08”N, 14˚13’32”E)	50	*Lithophyllum racemus*
DB867	FI058894	Pontian Isl. (Italy) (40˚54’47”N, 12˚52’58”E)	64.9	*Lithophyllum racemus*
DB835	FI058891	Villasimius, Sardinia (Italy) (39˚08′32″N, 9˚31′14″E)	40	*Lithophyllum pseudoracemus*
DB768	FI058890	Pontian Isl. (Italy) (40˚11’43”N, 12˚53’07”E)	66.4	*Lithophyllum pseudoracemus*
DB865	-	Sveta Katarina, Rovinj (Croatia) (45˚04’32”N, 13˚37’38”E)	10	*Lithophyllum* cf. *racemus*
DB866	-	Torre dell’Orso, Puglia (Italy) (40˚14’00”N, 18˚28’00”E)	44	*Lithophyllum* cf. *pseudoracemus*

https://doi.org/10.1371/journal.pone.0273505.t001

referred to as *L.* cf. *racemus* (DB865) and *L.* cf. *pseudoracemus* (DB866), were not molecularly classified (Table 1).

SEM image analysis

Specimens were washed and air-dried and then prepared for Scanning Electron Microscopy (SEM) according to [39]. The samples were fragmented along the growth direction, mounted on stubs by mean of graphite paste and finally chrome-coated before analysis under a Field Emission Gun SEM (SEM-FEG) Gemini 500 Zeiss at the University of Milano-Bicocca.

Hereinafter, short cells will be referred to as slow-growing cells constituting dark bands and produced in the cold season; long cells, instead, will be referred to as fast-growing cells constituting light bands and produced in the warm season [1, 30, 33, 37, 39]. Short cells are generally described as smaller, with thicker calcification and with lower Mg/Ca ratio, compared to long cells [33, 37, 39]. Information about biometry and calcification was extracted from 370 SEM images from longitudinal or transverse sections of protuberances. In the descriptions, L denotes the length, H is the height, D is the diameter. Measurements included the size of epithallial and perithallial cell [66] and cell lumen [39], the conceptacle size [67], the pore canal length, the number of cells in the pore canal filament and the number of epithallial cells (Table 2). Other classical descriptors such as the cell, conceptacle and pore canal shapes, pit-connections, conceptacle elevation, and presence and development of a calcified columella were also described. For the description of the columella development, we indicate as H the conceptacle height according to Adey and Adey [67], while the distance between the top of the columella and the conceptacle roof is indicated as h1, as in Basso et al. [59]. Within the calcified cell wall, primary calcification (PC) refers to the outer layer of Mg-calcite, formed by crystallites arranged parallel to the cell membrane (Fig 1) (= PW in [39]). Secondary calcification (SC) refers, instead, to the calcified layer which accounts for most of the cell wall thickness and is constituted of crystallites radial to the cell membrane and normal to the PC crystallites (Fig 1C; SW in [39]). In SEM images of longitudinal sections of algal protuberances, the cell wall area is measured as the calcified surface area surrounding the cell lumen and delimited by the outer borders of the cell (Fig 1D). The boundaries of each cell run at the half of the PC, which may be very thin (Fig 1E). The calcification was analysed mainly in epithallial and perithallial cells. The occurrence of thallus growth over an old conceptacle gave the opportunity to observe the cells of the secondary hypothallus [68], where the PC was particularly evident. The measured calcification traits included the SC maximum thickness, the PC maximum thickness and the cell wall area of epithallial and perithallial cells. Moreover, the shape and size of primary crystallites (= those forming the PC), the shape of secondary crystallites (= forming the SC) were also described. The same information was extracted for short and long cells separately in specimen DB867.

Table 2. Depth of sample collection and mean values (±SD) of biometrical traits from SEM image (μm).

	Lithophyllum racemus		*Lithophyllum pseudoracemus*		*L*. cf. *pseudoracemus*	*L*. cf. *racemus*
	DB661	**DB867**	**DB835**	**DB768**	**DB866**	**DB865**
Depth (m)	50	64.9	40	66.4	44	10
Perithallial cell (LxD)	17.9 ± 4.3 x 11.2 ± 2.4 (N = 39)	27.2 ± 4.6 x 13.2 ± 3.3 (N = 15)	15.4 ± 1.6 x 10.5 ± 1.6 (N = 42)	16.28 ± 2.8 x 10.79 ± 1.2 (N = 22)	21.1 ± 2.5 x 11.8 ± 1.8 (N = 34)	20.5 ± 2.5 x 2.5 ± 2.5 (N = 19)
Perithallial cell lumen (LxD)	13.8 ± 3.2 x 6.3 ± 1.2 (N = 51)	22.1 ± 3.7 x 7.1 ± 1.9 (N = 32)	12.5 ± 2.0 x 4.9 ± 0.9 (N = 63)	14.06 ± 2.6 x 5.43 ± 1.1 (N = 58)	19.4 ± 2.8 x 7.3 ± 1.1 (N = 34)	19.8 ± 2.5 x 7.6 ± 1.2 (N = 23)
Tetra/bisporangial conceptacle chamber (DxH)	275.3 ± 35.5 x 112.5 ± 19.3 (N = 23)	321.9 x 120.8 (N = 1)	261.1 ± 5.9 x 123.7 ± 22.7 (N = 3)	-	318.9 ± 20.3 x 142.0 ± 11.4 (N = 3)	325.1 x 136.9 (N = 1)
Pore canal length	40.9 ± 3.0 (N = 6)	-	41.7 (N = 1)	-	46.8 ± 6.4 (N = 3)	37.5 (N = 1)
Pore canal cells (n)	3–4	-	3	-	2–3	3
Epithallial cell (LxD)	3.7 ± 0.9 x 11.5 ± 0.7 (N = 5)	2.9 ± 0.6 x 12.6 ± 0.6 (N = 3)	3.8 ± 0.5 x 10.1 ± 1.0 (N = 3)	5.21 ± 0.4 x 9.03 ± 0.7 (N = 3)	5.2 x 11.3 (N = 1)	4.8 ± 1.0 x 13.1 ± 1.6 (N = 8)
Epithallial cell lumen (LxD)	2.1 ± 0.4 x 7.5 ± 1.4 (N = 18)	1.3 ± 0.1 x 8.9 ± 0.1 (N = 4)	2.3 ± 0.4 x 7.2 ± 1.1 (N = 7)	2.75 ± 0.5 x 6.16 ± 0.6 (N = 5)	3.0 ± 0.6 x 8.6 ± 2.8 (N = 5)	2.3 ± 0.9 x 8.6 ± 1.4 (N = 9)
Epithallial cells (n)	3, up to 5	3	1 or 2	1 or 2	1 or 2	1 or 2

https://doi.org/10.1371/journal.pone.0273505.t002

Statistical analysis

Principal Component Analysis (PCA) was performed on differently combined datasets. A first dataset included only biometrical data; the second only data on calcification traits and the last dataset included both biometrical and calcification data. Biometrical data comprised epithallial and perithallial cell size. Calcification data, instead, included the SC thickness and the cell wall area in both epithallial and perithallial cells, as well as the PC thickness. The PCA analysis was run in MATLAB R2020a software using the PCA toolbox released by [69]. Moreover, parametric and non-parametric univariate analysis of variance was applied to both biometrical and calcification dataset, in order to evaluate the statistical significance of the differences among group medians and means. Univariate analysis was also applied to compare results from short and long cells. In particular, the Kruskal-Wallis test followed by the Dunn's test for comparisons and the One-way ANOVA followed by the Tukey's test for post-hoc analysis, were performed in R 3.6.3 software.

Results

SEM image analyses

Scanning electron microscope (SEM) imaging of the cell walls showed similar shape of calcite crystallites within *L. racemus* and *L. pseudoracemus* thalli. A detailed description of each sample, including observations on both biometrical parameters and calcification traits, is provided below.

Lithophyllum racemus. Microscopic anatomy: specimens were pink in colour, non-geniculate and fruticose with protuberances up to 1 cm long (up to 5 mm in DB867). A longitudinal section of protuberances showed perithallial filaments with a "fountain" pattern, with rows of cells which ran parallel and then diverge towards the thallus surface following opposite directions (Fig 1A). Dark and light growth bands were also detected (Fig 1A; [65]). Three superposed flattened epithallial cells were frequently observed (up to 5 in DB661; Fig 1B and 1C), L 2.92–3.72 μm and D 11.48–12.59 μm (Table 2). Perithallial cells were connected by primary and secondary pit-connections and lacked cell fusions (Fig 1D and 1E). Perithallial cells were rectangular in longitudinal section, L 17.87–27.20 μm and D 11.16–13.23 μm (Fig 1D and 1E;

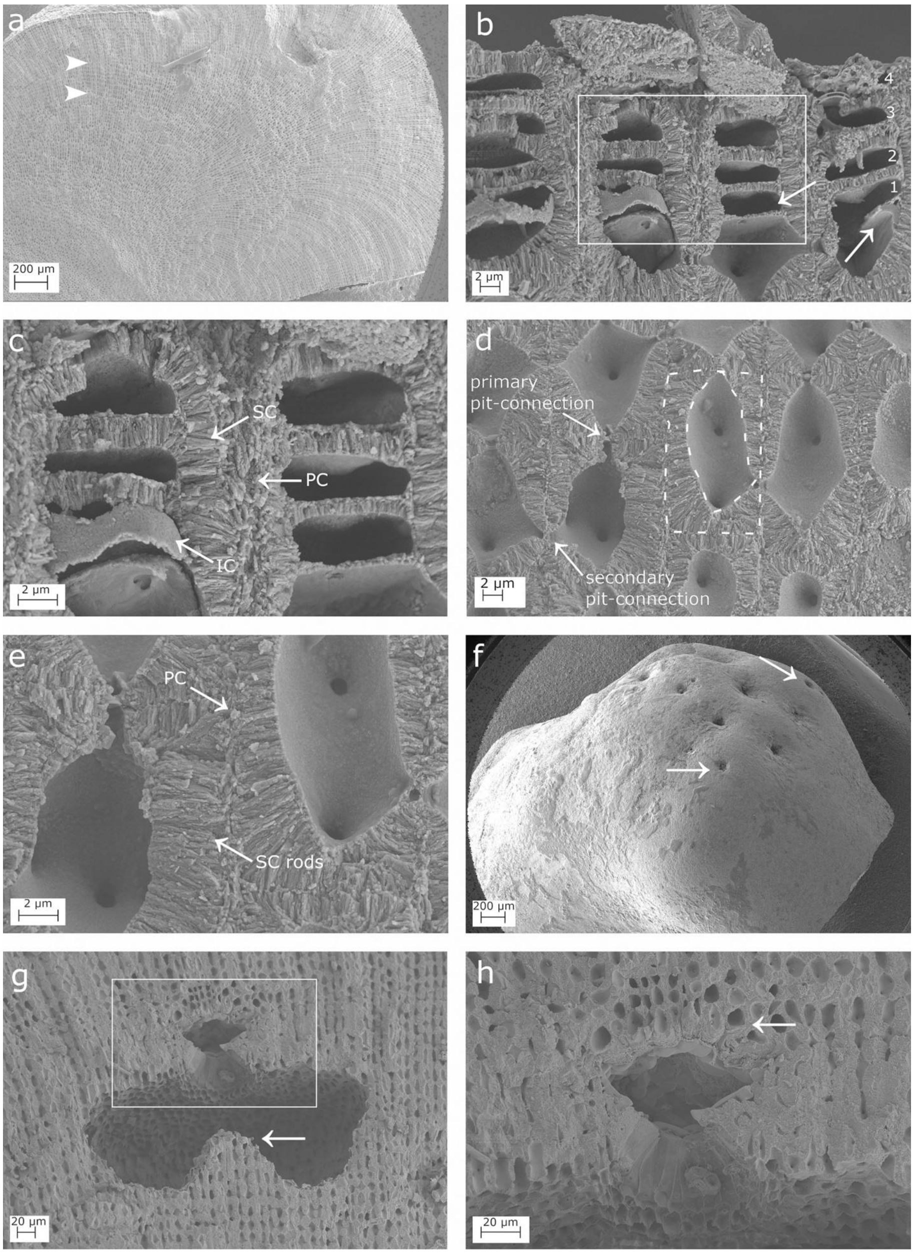

Fig 1. SEM images showing longitudinal sections of *Lithophyllum racemus*. (a) Fountain pattern in the arrangement of perithallial cells; two arrowheads indicate a growth band; (b) Four superimposed epithallial cells (numbered). Note the evidence of meristematic division (white arrows); (c) magnification of the inset in (b) to show: a primary (PC), secondary (SC) and inner calcification (IC); (d)

perithallial cells with primary and secondary pit-connections (arrows); the cell wall area corresponds to the surface included between the two dashed lines; (e) magnification of (d) to show perithallial thin PC and rod-shaped crystallites of the SC; (f) conceptacles weakly protruding from thallus surface (white arrows); (g) a conceptacle chamber showing a well-developed calcified columella (arrow); (h) magnification of the inset in (g) showing the secondary hypothallus (arrow).

https://doi.org/10.1371/journal.pone.0273505.g001

Table 2). Trichocytes were not observed. Many asexual uniporate conceptacles weakly protruded from the surface, with a sunken pore aperture (Fig 1F). The conceptacle chamber was kidney-shaped in longitudinal medial section, D 275.34–321.93 μm and H 112.48–120.82 μm (Fig 1G; Table 2), giving a mean D/H ratio of 2.55. A well-defined calcified columella rose from the conceptacle floor (Fig 1G). The columella had a height exceeding half of the height of the conceptacle chamber (H), therefore the distance between the columella top and the chamber roof (h1 in [59] was < H/2. The pore canal was medially cut and observed only in the neotype DB661. It was conical, appearing triangular in section, about 41 μm long, bordered by filaments composed of 3–4 cells, and showing a rhomboidal enlarged cavity on its top (Fig 1H; Table 2; [70]).

Calcification: the epithallial cells (Fig 1B) were strongly calcified with a cell wall area of 30.17–174.39 μm^2 (Table 3). The PC between different cell filaments was composed of rod-shaped crystallites running more or less parallel to the cell membrane (Fig 1C), while the PC between epithallial cells of the same filament was very thin and hardly visible. The SC consisted of one layer of rods perpendicular to the cell membrane, locally appearing as flattened, loosely packed elements (Fig 1C). They determined an SC maximum thickness of 1.54 ± 0.3 μm (Table 3). We observed an additional, distinct, innermost thin calcified layer (= IC) in contact with the plasma membrane, composed of irregular granules with crenate margins and appearing as a granular surface bordering the cell lumen (Fig 1C). The meristematic cell, showing primary and secondary pit-connections, is superposed by several epithallial cells connected by exclusively primary pit-connections (Fig 1B). The meristem cell and its several generations of superposed epithallial cells shared the same PC and thick SC, as observed at the boundary with the adjacent cell-filament. The cut-off of a new epithallial cell occurs by transversal division of the upper (distal) part of the meristematic cell. The weak calcification of the newly formed horizontal portion of the cell membrane was formed exclusively by the IC (Fig 1B and 1C), with a later formation and then progressive thickening of the SC in older epithallial cells (Fig 1B and 1C).

The perithallial cells in longitudinal section had oblong lumen and strongly calcified cell walls, with an area of 116.57–174.39 μm^2 (Fig 1D and 1E; Table 3). The perithallial PC is composed of packed irregular rhomboids with smooth indented margins, oriented parallel to the cell membrane (Fig 2A and 2B). The PC measured between two adjacent cell filaments was

Table 3. Mean values (±SD) of calcification traits from SEM images (μm, otherwise differently specified).

		Lithophyllum racemus		*Lithophyllum pseudoracemus*		*L.* cf. *pseudoracemus*	*L.* cf. *racemus*
		DB661	**DB867**	**DB835**	**DB768**	**DB866**	**DB865**
Depth (m)		50	64.9	40	66.4	44	10
Perithallial cells	SC thickness	2.7 ± 0.6 (N = 50)	2.9 ± 0.6 (N = 31)	2.5 ± 0.4 (N = 62)	2.3 ± 0.4 (N = 57)	2.4 ± 0.5 (N = 34)	2.9 ± 0.6 (N = 23)
	PC thickness	0.5 ± 0.2 (N = 28)	0.9 ± 0.2 (N = 35)	1.0 ± 0.3 (N = 31)	1.6 ± 0.5 (N = 54)	1.2 ± 0.3 (N = 23)	1.3 ± 0.3 (N = 24)
	Cell wall area (μm^2)	116.6 ± 34.7 (N = 39)	174.4 ± 50.2 (N = 24)	99.7 ± 18.9 (N = 35)	100.5 ± 21.3 (N = 23)	117.7 ± 26.0 (N = 22)	137.8 ± 29.2 (N = 21)
Epithallial cells	SC thickness	1.5 ± 0.3 (N = 18)	1.4 ± 0.2 (N = 3)	1.0 ± 0.3 (N = 3)	0.9 ± 0.2 (N = 5)	1.0 ± 0.4 (N = 4)	1.1 ± 0.2 (N = 9)
	Cell wall area (μm^2)	30.2 ± 8.4 (N = 6)	26.0 ± 8.2 (N = 3)	25.0 ± 9.7 (N = 5)	25.0 ± 8.3 (N = 6)	27.2 ± 8.3 (N = 4)	35.8 ± 12.0 (N = 7)

https://doi.org/10.1371/journal.pone.0273505.t003

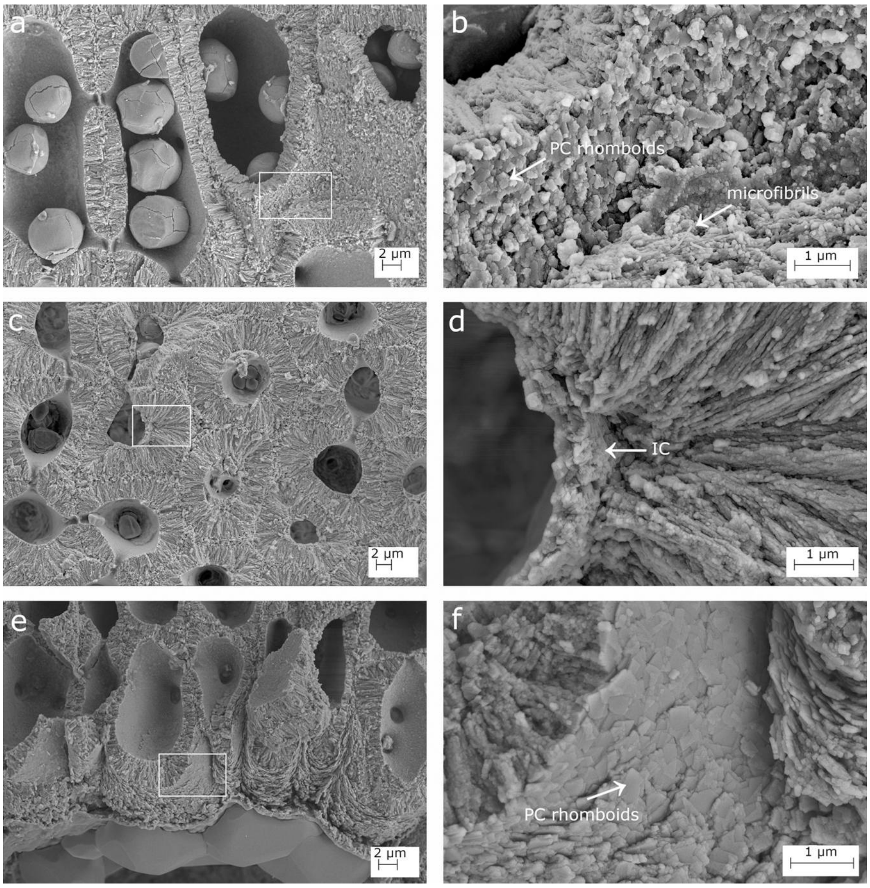

Fig 2. SEM details of the calcification in *Lithophyllum racemus*. (a) Calcified perithallial cells; (b) magnification of the inset in (a): rhomboidal crystallites of the primary calcification (PC, arrow) embedded in organic microfibrils (arrow); (c) transverse section of the perithallus; (d) magnification of the inset in (c) showing the innermost calcified layer (IC, arrow); (e) secondary hypothallus over the conceptacle pore canal in Fig 1H; (f) magnification of the inset in (e): regular rhomboidal crystallites of the hypothallial PC (arrow).

https://doi.org/10.1371/journal.pone.0273505.g002

0.54–0.87 μm thick (Table 3). The perithallial SC was formed by one layer up to 2.94 μm in maximum thickness, composed of rod-shaped crystallites perpendicular to the cell membrane (Fig 1E; Table 3). The internal surface delimiting the cell lumen showed a granular calcification. In transverse section, it was observed an IC composed of irregular, more or less blocky granules (DB867; Fig 2C and 2D).

The primary hypothallus, i.e. the first algal cells growing directly over the substrate, was not detectable in our samples, but some prostrate cells growing over a conceptacle roof were visible, forming a secondary hypothallus. Here, the hypothallial primary crystallites appeared as packed regular and thin rhomboids, 0.4 x 0.4 ± 0.1 μm in size, which clearly progressed between two adjacent cell filaments (Figs 1H, 2E and 2F). Depending on the visual perspective, the same thin rhomboids showed only their thinnest dimension, thus appearing as rod-like structures parallel to the cell lumen, perfectly bordering the rounded shape of the outer cell wall (Fig 2E and 2F).

Lithophyllum pseudoracemus

Microscopic anatomy: specimens were pink in colour, non-geniculate and fruticose with protuberances up to 5 mm long (up to 2 mm in DB768). In sample DB835, it was observed the same "fountain" pattern in the arrangement of perithallial cells, as already observed in *L. racemus* (Fig 3A). The perithallial banding was not detected. One or two epithallial cells were terminating each cell filament (Fig 3B), L 3.84–5.21 μm long and D 9.03–10.07 μm (Table 2). The perithallial cells were rectangular in longitudinal section, with numerous secondary pit-connections, L 15.40–16.28 μm and D 10.55–10.79 μm (Table 2; Fig 3C). The external surface of the asexual conceptacles appeared depressed, with a sunken pore aperture (Fig 3D). The asexual uniporate conceptacles in sample DB835 had a rounded chamber corresponding to a D/H ratio of 2.11 (Fig 3E; Table 2). The triangular pore canal was 42 μm long, counting 3 cells in the pore canal filament (Fig 3F; Table 2). No calcified columella was observed (Fig 3E). Trichocytes were observed exclusively at the periphery of a conceptacle chamber (Fig 3E). Sample DB768 was sterile.

Calcification: the epithallial cells were highly calcified with a cell wall area of 24.96–25.01 μm^2 (Table 3). The PC was not detectable between the epithallial cell and the underlying meristem cell in the same filament, while the PC between two adjacent cell filaments was highly calcified and consisted of irregular granules (Fig 3B). The epithallial SC reached 0.98 μm in maximum thickness and was characterized by 1–2 layers of rods with granular texture laying perpendicular to the cell membrane (Fig 3B; Table 3). The internal surface delimiting the cell lumen showed a granular calcification, forming an IC between the plasma membrane and the perpendicular rods of the SC (Fig 3B).

The perithallus had oblong cells with strongly calcified cell walls (Fig 3C). The perithallial cell walls had an area of 99.71–100.48 μm^2 (Table 3). The perithallial PC was 0.95–1.55 μm in thickness (Table 3), composed of packed irregular rhomboids with smooth indented margins (Fig 3G and 3H). The perithallial SC was 2.31–2.53 μm in maximum thickness, consisting of long perpendicular rods with a granular texture, arranged in 1 to 4 layers (Figs 3H and 4A, 4B; Table 3).

Over a conceptacle roof, in proximity to the pore canal, some prostrate cells of a secondary hypothallus clearly showed their PC (Fig 3F). This consisted of regular packed rhomboids, 0.4 x 0.4 ± 0.1 μm in size (Fig 4C and 4D). The rhomboids appeared as thin slips in some areas. The IC was detectable as a granular layer at the inner boundary of the SC (Fig 4D).

***Lithophyllum* cf. *racemus*.** Microscopic anatomy: specimen DB865 was pink in colour, non-geniculate and fruticose with protuberances up to 3 mm long. At small scale, it was visible the "fountain" pattern of the perithallial growth and in some areas also the banding pattern. One or 2 flattened epithallial cells were observed, L 4.78 ± 1.0 μm and D 13.12 ± 1.6 μm (Fig 5A; Table 2). The perithallial cells were rectangular in longitudinal section L 20.52 ± 2.5 μm and D 12.51 ± 2.5 μm (Table 2). Trichocytes were not observed. The asexual uniporate conceptacle had a kidney-shaped chamber D 325.13 μm and H 136.94 μm (Fig 5B; Table 2), equivalent to a D/H ratio of 2.37. The conceptacle chamber had an evident, calcified columella, reducing the conceptacle chamber height h1 to less than H/2 [59]. The pore canal was triangular in longitudinal section, 37.5 μm long, lined by 3 cells, with a cavity on top (Fig 5B; Table 2).

Calcification: the epithallial cells were strongly calcified and their surface appeared covered by a thick cuticle (Fig 5A). The epithallial cell wall area was 35.80 ± 12.0 μm^2 (Table 3). The PC

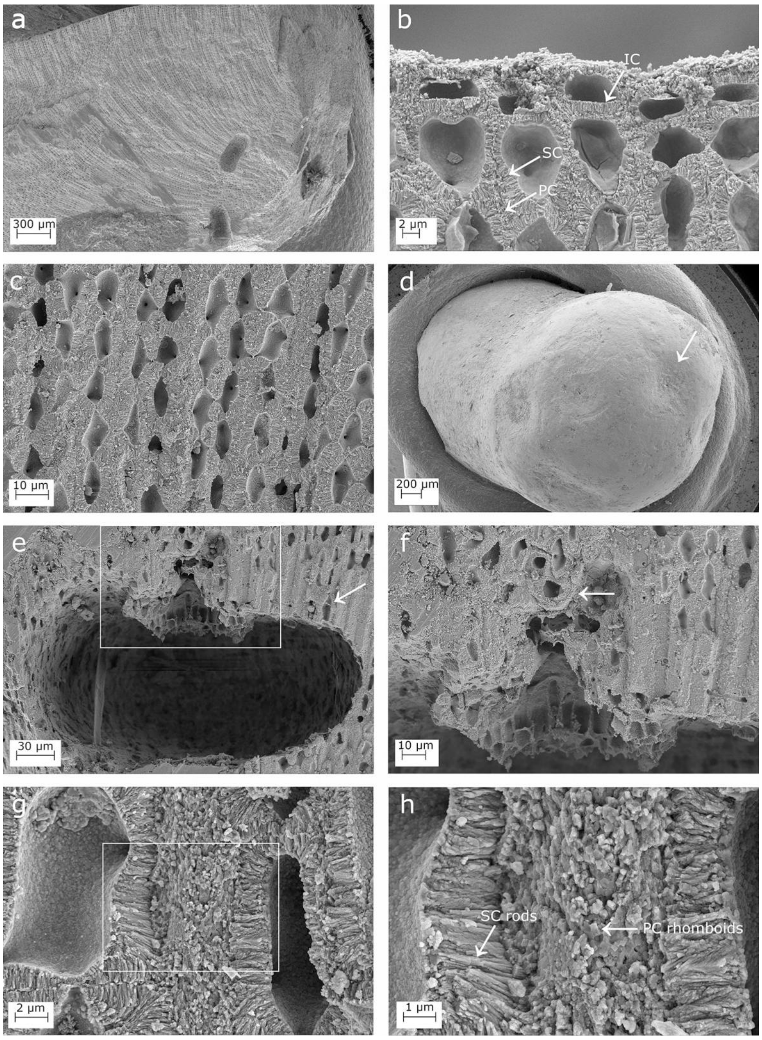

Fig 3. SEM images showing longitudinal sections of *Lithophyllum pseudoracemus*. (a) A protuberance longitudinally cut in half showing the fountain-like arrangement of perithallial cells, due to the diverging cell filaments toward the thallus surface; (b) epithallial cells showing the primary calcification (PC), the secondary calcification (SC), and the innermost calcified layer (IC); (c) the perithallus; (d) depressed conceptacle in surface view (arrow); (e) conceptacle chamber with no calcified columella and a trichocyte on the right (arrow); (f) magnification of the inset in (e) to show secondary hypothallial cells (arrow) over the pore canal; (g) the orientation of the PC crystallites is normal to those of the SC; (h) magnification of the inset in (g) to show the perithallial rhomboidal crystallites of the PC and the rod-shaped crystallites of the SC (arrows).

https://doi.org/10.1371/journal.pone.0273505.g003

between epithallial cells of the same filament was undetectable or absent. The thick epithallial PC between adjacent cell filaments consisted of rhomboidal elements (Fig 5A). The epithallial SC reached a maximum thickness of 1.05 ± 0.2 µm and consisted of perpendicular rods

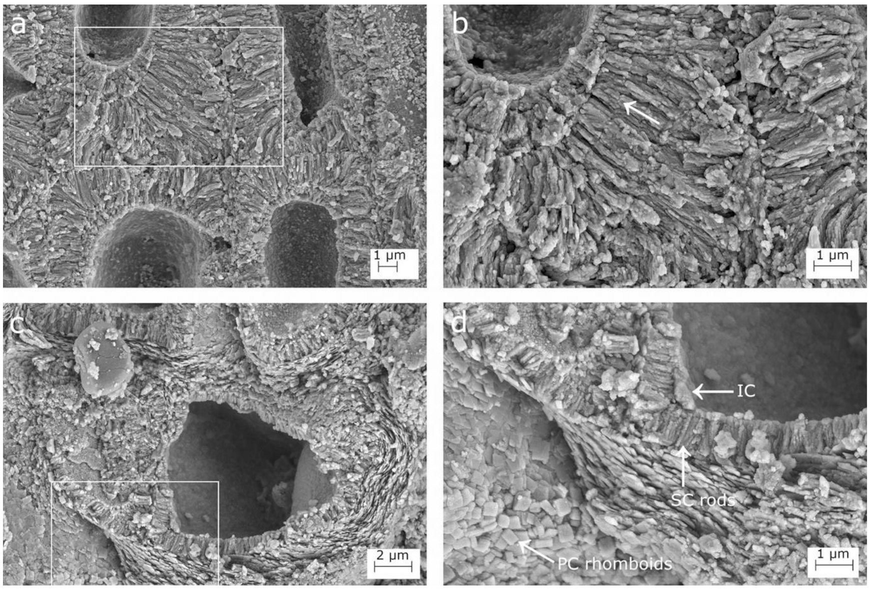

Fig 4. SEM images showing longitudinal sections of the calcified thallus in *Lithophyllum pseudoracemus*. (a) Multiple layers of secondary calcification forming the thick cell walls; (b) magnification of the inset in (a); the arrow points to the contact of two layers of SC; (c), secondary hypothallial cells in the proximity of the pore canal in Fig 3F; (d) magnification of the inset in (c) to show the rhomboidal crystallites in the hypothallial primary calcification (PC); the SC rods and the innermost calcified layer (IC).

https://doi.org/10.1371/journal.pone.0273505.g004

(Fig 5A; Table 3), slightly more regular in shape than those in the perithallial SC. The internal surface delimiting the cell lumen was made of granules which constituted a very thin IC (Fig 5A).

The perithallus had oblong calcified cells with a cell wall area of 137.79 ± 29.2 μm^2 (Table 3). The PC between two adjacent cell filaments, 1.28 ± 0.3 μm thick (Table 3), was composed of small irregular granules. The PC between cells of the same filament was inconspicuous. The SC had a maximum thickness of 2.87 ± 0.6 μm and consisted of a single layer of rods oriented perpendicular to the cell membrane (Table 3).

The secondary hypothallus was detected as prostrate cells growing over a conceptacle roof, close to the pore canal (Fig 5C and 5D). These hypothallial cells had a PC consisting of packed rhomboids, 0.3 x 0.3 ± 0.1 μm in size, running parallel to the cell membrane (Fig 5C and 5D). The hypothallial SC was composed of thin granular rods perpendicular to the cell membrane (Fig 5D). The IC in contact with the SC appeared granular from inside the cell lumen (Fig 5C).

***Lithophyllum* cf. *pseudoracemus*.** Microscopic anatomy: specimen DB866 was dark pink in colour, non-geniculate and fruticose with protuberances up to 4 mm long. One or 2 epithallial cells were flattened, L 5.18 μm and D 11.31 μm (Fig 6A; Table 2). The perithallial cells were L 21.11 ± 2.5 μm long and D 11.82 ± 1.8 μm (Fig 6B; Table 2). The perithallial zonation with the banding pattern was not visible. The asexual uniporate conceptacles had a kidney-shaped chamber D 318.95 ± 20.3 μm, H 141.96 ± 11.4 μm (Fig 6C; Table 2) and 2.25 in D/H. In some conceptacles, a calcified columella was observed rising from the conceptacle floor (Fig 6C). The columella was variably developed, but its height never exceeded half of the height of the

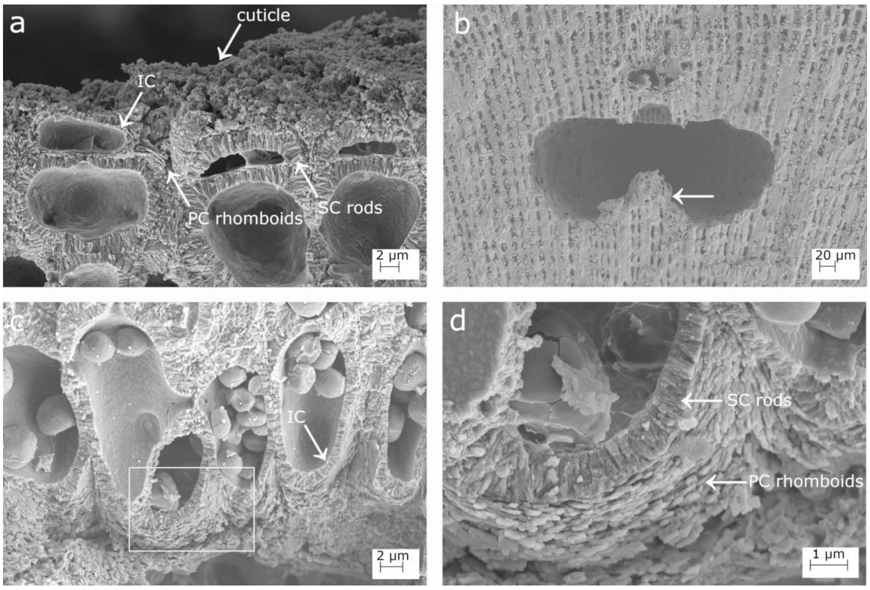

Fig 5. SEM images showing longitudinal sections in *Lithophyllum* cf. *racemus* DB865. (a) Epithallial calcified cells covered by a thick cuticle, and bordered by a primary calcification (PC), a secondary calcification (SC), and an innermost calcified layer (IC); (b) a conceptacle with a well-defined calcified columella (white arrow); (c) secondary hypothallial cells in the proximity of a pore canal and the innermost granular IC; (d) magnification of the inset in (c) showing the SC rhomboidal crystallites, and the PC rhomboids.

https://doi.org/10.1371/journal.pone.0273505.g005

conceptacle chamber, resulting in h1>H/2. The pore canal was triangular, about 47 μm long, composed of 2–3 cells, with a rhomboidal cavity on top (Fig 6C; Table 2).

Calcification: the epithallus was strongly calcified (Fig 6A). The cell wall area was 27.18 ± 8.3 μm^2 (Table 3). The PC between the epithallial and the subtending meristematic cells was undetectable, while the PC between adjacent cell filaments was thick and formed by irregular elements. The epithallial SC consisted of regular rods perpendicular to the cell membrane, reaching 0.99 ± 0.4 μm of maximum thickness (Fig 6A; Table 3). The cell lumina were delimited by the cell membrane which prevented the observation of the calcification (Fig 6A). Nevertheless, there was the evidence of an IC of granular elements in contact with the SC.

The perithallial cells were oblong and regularly arranged in rows. The cell walls had 117.68 ± 26.0 μm^2 of area (Table 3). The PC between cells of the same filament was inconspicuous. The perithallial PC between cells of two adjacent filaments was 1.24 ± 0.3 μm thick and consisted of irregular elements which ran parallel to the cell lumen (Table 3). The perithallial SC consisted of a single layer of rods oriented perpendicular to the cell membrane, 2.43 ± 0.5 μm in maximum thickness (Table 3). The internal surface delimiting the cell lumen was granular, forming a clearly detectable IC layer in contact with the perpendicular rods of the SC. In transverse section, the perithallial cells had a clear hexagonal perimeter (Fig 6D).

The primary hypothallus had a calcification similar to the cells of the secondary hypothallus observed in the samples described above (Fig 6E and 6F). The PC was formed by packed rhomboidal slips bordering the cell (Fig 6F). The SC consisted of perpendicular rods arranged in 1 or 2 rows, very granular in texture.

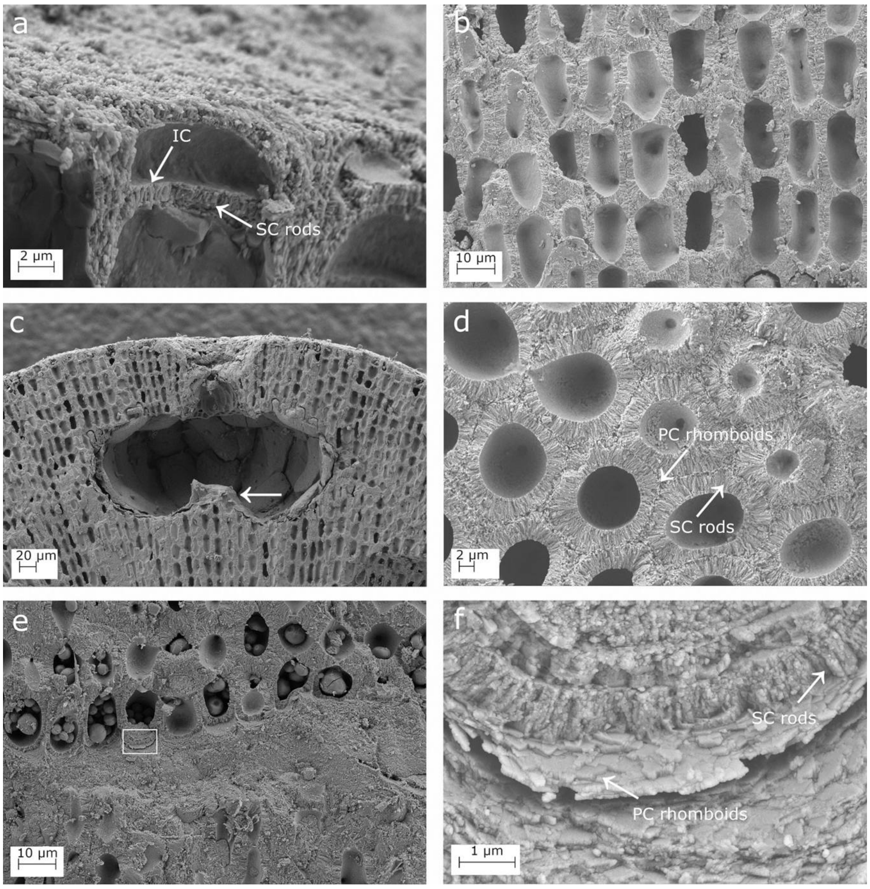

Fig 6. SEM images showing longitudinal sections of *Lithophyllum* cf. *pseudoracemus* DB866. (a) Epithallial cell bordered by the rods of the secondary calcification (SC), and the innermost calcified layer (IC); (b) the calcified perithallus; (c) a conceptacle with a short calcified columella (arrow); (d) transverse section showing the SC and the primary calcification (PC); (e) the primary hypothallus growing over the substrate; (f) magnification of the inset in (e) showing multiple layers of hypothallial PC rhomboids and SC rods.

https://doi.org/10.1371/journal.pone.0273505.g006

Statistics

The statistical analyses ran on biometrical features highlighted significant differences among the perithallial cell sizes ($p<<0.001$; S1 Table, Fig 7). Particularly, the perithallial cells from both samples of *L. pseudoracemus* (DB768, DB835) were significantly smaller than those in *L. racemus* DB867 and the two non-molecularly classified DB865 and DB866 ($p<<0.001$; S1 Table; Fig 7). Instead, the *L. racemus* neotype (DB661) showed intermediate perithallial cell size (Fig 7), differing significantly from the other samples ($p<0.01$), with the exception of *L. pseudoracemus* DB768 ($p = 0.23$) (S1 Table; Fig 7). Other measured biometrical variables did not highlight further distinction between *L. pseudoracemus* and *L. racemus*.

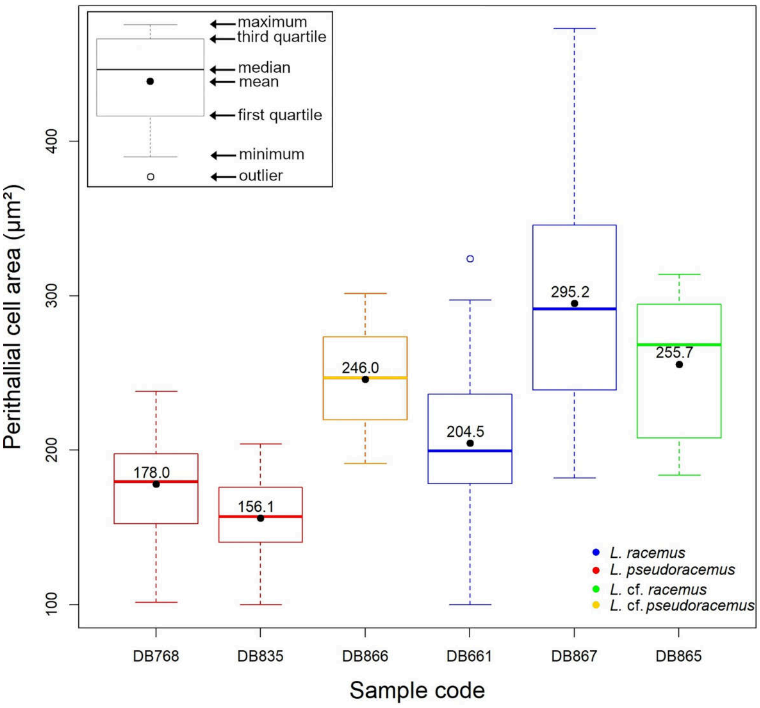

Fig 7. Box plot with the results of the perithallial cell area measurement. The numbers inside the plots indicate the mean values.

https://doi.org/10.1371/journal.pone.0273505.g007

The multivariate analysis on calcification traits was the only statistical test supporting a significant distinction between *L. racemus* and *L. pseudoracemus*. In the PCA model, the first two principal components (*PCs*) resolved the 83% of the total data variance (Fig 8). The main

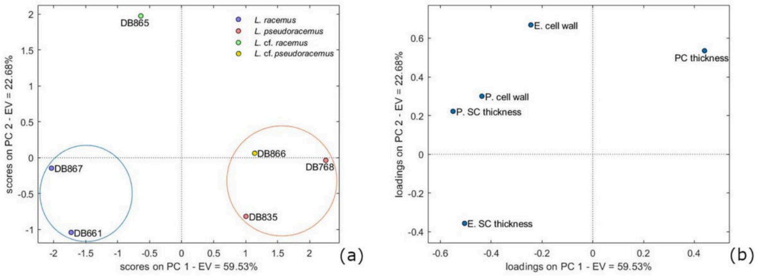

Fig 8. Principal component analysis (PCA). Score plot is shown in (a); loading plot of PCA on calcification data in both perithallial (P.) and epithallial (E.) cells (b). The plots model 83% of the total data variance. Variance proportions are shown along each component axis. Calcification types are evidenced with circles and classified in *L. racemus* type and *L. pseudoracemus* type.

https://doi.org/10.1371/journal.pone.0273505.g008 trend expressed on the *PC-1* axis was the increasing SC thickness with increasing cell wall area, expressed as high negative *PC-1* loadings for the perithallial cell wall area and the SC thickness (Fig 8). At the same time, the PC thickness tended to increase as the SC became thinner, as shown by the high positive *PC-1* loadings. The *PC-2* axis displayed positive loadings of the cell wall area, the perithallial PC thickness and SC thickness, as well as high negative loadings of the epithallial SC thickness (Fig 8). Overall, from the PCA, it was possible to distinguish two main calcification types based on natural groupings in the *PC-2* versus *PC-1* plot (Fig 8). The *L. racemus* type plotted with negative *PC-1* and negative *PC-2* scores (Fig 8) and was characterized by perithallial cells with high values for cell wall area and SC thickness (Fig 8; Table 3). The *L. pseudoracemus* type was characterized by positive *PC-1* and negative or neutral *PC-2* scores corresponding to perithallial cells with low values of cell wall area and thin SC. This category included also *L.* cf. *pseudoracemus* DB866. The sample *L.* cf. *racemus* DB865 differed from the other samples by having highly positive *PC-2* and negative *PC-1* scores (Fig 8). Since the *PC-1* scores explained 60% of the total data variance, they support the inclusion of *L.* cf. *racemus* DB865 in the *L. racemus* type. Most of the difference between sample DB865 and the other samples of the *L. racemus* type relied on the epithallial cell wall area, which was particularly high (Fig 8; Table 3).

Given the results of the PCA, we explored the contribution of the considered variables in supporting the separation of *L. racemus* from *L. pseudoracemus*. The perithallial SC thickness was the only one to separate the two species with significant statistical support (Fig 9; S2 Table). Based on the PCA, *L.* cf. *pseudoracemus* DB866 was attributed to the *L. pseudoracemus* calcification type, while *L.* cf. *racemus* DB865 was attributed to the *L. racemus* calcification type (Figs 8 and 9; Table 2). The mean epithallial SC thickness was also different in *L. racemus* and *L. pseudoracemus* (Table 3), but the ANOVA results did not support a statistical significance of this feature.

In *L. racemus* DB867, it was also possible to clearly distinguish between size of short and long cells within the perithallus (Fig 10). Long cells differed significantly from short cells by length (25.25 μm and 19.58 μm respectively, $p<0.001$). Short and long cells had very similar cell lumen area, but short cells had higher values of cell wall area and thicker SC, while long cells had thicker PC (Fig 10). Nevertheless, none of these differences were statistically significant ($p > 0.05$).

Discussion

Microscopic anatomy

At small scale, both *L. racemus* and *L. pseudoracemus* showed a "fountain" pattern in the arrangement of perithallial cells (Figs 1A and 3A), as already observed by [59] (pl. 63, Figs 5 and 6). In the samples of *L. racemus* DB661, DB867 and in *L.* cf. *pseudoracemus* DB865, the seasonal banding was also appreciable (Fig 1A).

The statistical analyses supported a significant difference between the size of perithallial cells of *L. racemus* and *L. pseudoracemus* (Fig 7; Tables 2, 4 and S1 Table; [65]). However, the molecularly identified samples of *L. racemus* show a very wide range of values of perithallial cell area (Fig 7; Table 2), thus jeopardizing the applicability of this single character for species separation.

The longitudinal medial section of the asexual conceptacle chambers of *L. pseudoracemus* was more rounded than that of *L. racemus*, having a lower D/H ratio (2.11 against 2.55). This pattern was confirmed also in the non-molecularly identified samples (2.25 in *L.* cf. *pseudoracemus* against 2.37 in *L.* cf. *racemus*). A calcified columella rising from the asexual conceptacle floor was observed in most samples but not in *L. pseudoracemus*, in agreement with [65]. The

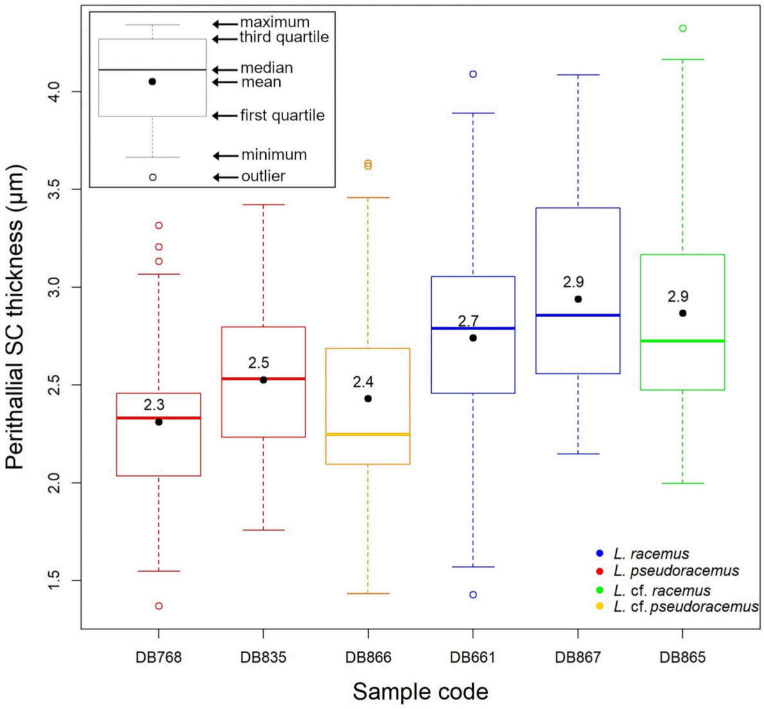

Fig 9. Box plot of the perithallial SC thickness. The numbers inside the plots indicate the mean values.

https://doi.org/10.1371/journal.pone.0273505.g009

calcified columella rising from the conceptacle chamber floor of *L*. cf. *pseudoracemus* DB866 appeared variably developed, but its height was lower than half the height of the conceptacle chamber, consequently, h1 [59] was typically > H/2 (Fig 6C). The low number of observations, however, prevents any attempt of statistical analysis of this feature, that would deserve further investigation aimed at assessing its potential value.

Our biometrical analyses on molecularly characterized samples revealed some differences with the measures reported by [65]. In particular, we observed smaller conceptacles with a depressed surface in *L. pseudoracemus* (mean D 261.08 x H 123.75 μm *vs*. D 321.25 x H 175.00 μm) reported by [65] (Table 2). Moreover, we observed 3–5 layers of superposed epithallial cells in *L. racemus* instead of 1–2 as reported by [65]. These observations demonstrated high variability in microanatomy among samples and even within the same specimen, which would prevent a reliable distinction of the two species solely based on microanatomy and biometrical analysis, in agreement with [65]. Trichocytes have been demonstrated in the genus *Lithophyllum* only recently [71], but their mode of development hampers their identification under SEM and in petrographic thin sections. Nevertheless, no trichocyte was observed even in decalcified histological sections of *L. racemus*, while trichocytes were rarely detected in *L. pseudoracemus* by [65]. Despite the active search for trichocytes in our investigations, we were able to identify one single trichocyte exclusively in proximity of a conceptacle chamber in *L. pseudoracemus* (Fig 3E), thus confirming the published report [65].

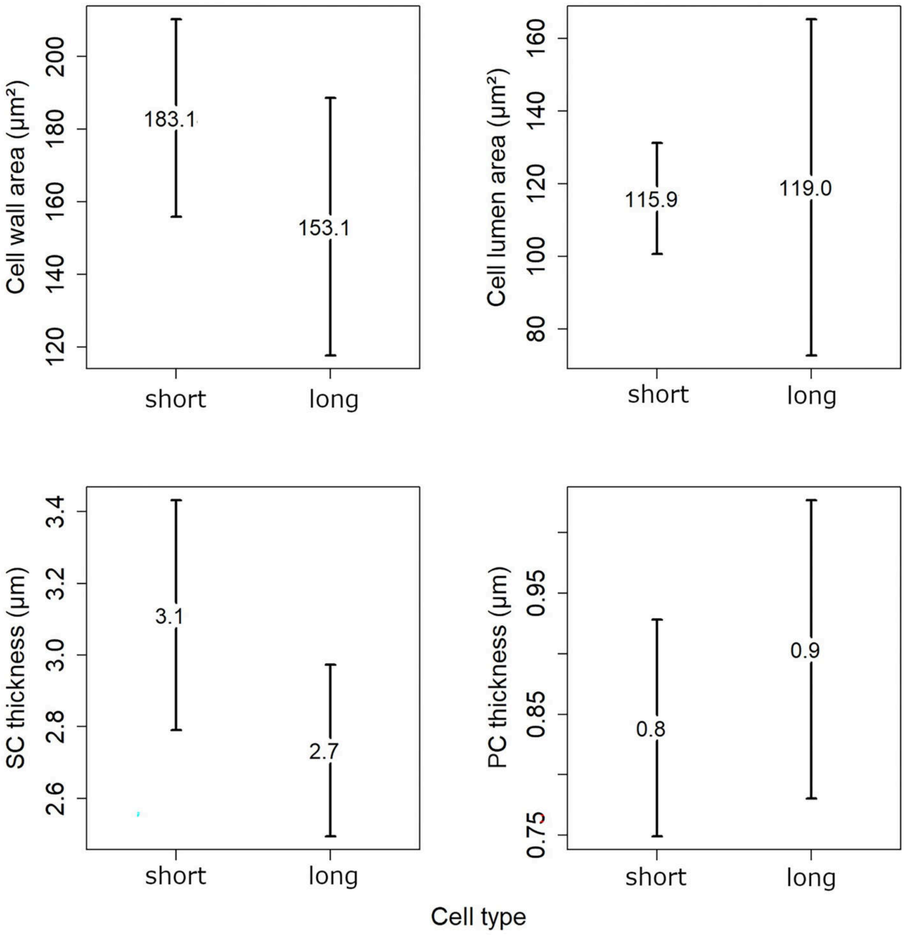

Fig 10. Comparison of mean values for short and long cells in *L. racemus* DB867. The numbers inside the plots indicate the mean values for the cell wall area, cell lumen area, SC thickness and PC thickness.

https://doi.org/10.1371/journal.pone.0273505.g010

Calcification traits

The suitability of skeletal ultrastructure for the taxonomy of calcareous red algae has been proved only recently [38, 39, 70]. Auer and Piller [38] introduced the morphology of crystallites in the PC of epithallial and meristem cells as a new morphological criterion to discriminate among different clades. Among the subfamily Lithophylloideae, *Lithophyllum incrustans*, *L. kotschyanum*, *L. lichenoides*, *L. pygmaeum* and *L. byssoides* (as *Titanoderma byssoides*) were analysed by [38]. According to these authors, the defining traits of Lithophylloideae are rhombic plates as dominant morphotype of epithallial cell wall crystallites and perpendicular rod-shaped crystallites in the SC [38]. Our observations are in substantial agreement, reporting rhomboid-shaped crystallites in the PC and perpendicular rod-shaped crystallites in the SC in both *L*. *racemus* and *L*. *pseudoracemus*, as already concluded by a deep learning approach on SEM images of the two species [70]. However, we found evidence of three different calcified layers in *L*. *racemus* and *L*. *pseudoracemus*: the primary outer calcification formed by parallel rhomboids (PC); the median one with perpendicular rods of the secondary calcification (SC) and the innermost granular layer (IC) (Figs 1C and 4D). The IC appeared composed of granular elements (Fig 1C), was located between the plasma membrane and the SC, and was often covered by organic residue of the plasma membrane. Moreover, we described regular and obvious rhomboids in the hypothallial cells of both primary and secondary hypothallus (Figs 2E, 2F, 4C, 4D, 5C, 5D, 6E and 6F), while they were much less regular in the other cells, regardless of the sample. In fact, within the perithallus, the PC crystallites had irregular shapes and rhomboids became hardly distinguishable, while the crystallites of the SC remained visibly rod-shaped. The particularly regular PC rhomboids observed in the hypothallial cells were apparently absent between epithallial cells of the same filament, and not obvious elsewhere, except in the lateral (= between adjacent filaments) epithallial cell walls of *L*. cf. *racemus* DB865 (Fig 5A). In the meristem, both *L*. *racemus* and *L*. *pseudoracemus* shared a similar pattern of absence of PC and increasing SC thickness, in the newly formed horizontal cell wall that cuts off a new epithallial cell (Fig 1B). At the same time of the new epithallial cut-off, the lateral cell walls (between adjacent filaments) that contain the meristem cell and the epithallial cells issued from it, appeared as a pre-existing calcite "envelope" with well-developed and relatively homogeneous thickness (Fig 1B). In the congeneric species *Lithophyllum kotschyanum* the pattern of calcification of the new epithallial cells differs, since an increasing thickness of the SC toward the lower base of the meristem cell was observed [38]. This observation also supports a species-specific control of calcification traits in CCA. DNA sequencing coupled with the analysis of calcification traits on a broader range of species could elucidate the diagnostic potential of the pattern of calcification of the meristem cutting off the new epithallial cells.

The loss of definition in the primary crystallite shape observed in perithallial cells of *L*. *racemus* and *L*. *pseudoracemus* could be related to solution/precipitation or recrystallization processes and has been already reported in *L*. *kotschyanum* along with progressively increasing calcification [38].

Considering the measured calcification traits, the PCA results (Fig 8) succeeded in allowing the circumscription and separation of two groups of samples which included distinctively the genetically classified *L*. *racemus* (DB661, DB867) and *L*. *pseudoracemus* (DB768, DB835). Overall, *L*. *racemus* was characterized by perithallial cells with large cell wall area (145.48 μm^2 by mean) and thicker SC (2.84 μm); *L*. *pseudoracemus* had instead small perithallial cell wall area (100.09 μm^2 by mean) with thinner SC (2.42 μm) (Fig 8; Table 3). To note is also the direct proportion between the SC thickness and the cell wall area in the perithallus of our corallines (Fig 8). The *L*. *racemus* and *L*. *pseudoracemus* specimens analysed in this work were collected in the Western Mediterranean Basin. The specimens *L*. *racemus* DB867 and *L*. *pseudoracemus* DB768 occurred sympatrically and at a similar depth (Table 1) and nevertheless showed a highly significant distinction in terms of calcification traits (Fig 8). In particular, DB867 had thin PC and high values of SC thickness and cell wall area, while DB768 had thick PC, thin SC and small cell wall area (Fig 8; Table 3).

Samples *L*. cf. *racemus* DB865 and *L*. cf. *pseudoracemus* DB866, non-molecularly identified, were collected in the Eastern Mediterranean, where the presence of both *L*. *racemus* and *L*. *pseudoracemus* was also confirmed by molecular techniques [65]. According to the PCA, sample DB866 fell in the *L*. *pseudoracemus* calcification type (Fig 8). Interestingly, samples with thick perithallial SC had also thick SC in the epithallial cells (Table 3). The epithallial cells in specimen DB865 had the largest diameter (Fig 5A; Table 2), explaining the high cell wall area despite the relatively thin SC. In the perithallus, its cell wall area was large and the SC was thick, in agreement with the major defining traits of *L. racemus* (Fig 8; Table 3) and actually the *PC-1* axis of the PCA, which explained most of the data variance (60%), supports the inclusion of *L.* cf. *racemus* DB865 in the *L. racemus* calcification type (Fig 8). This specimen was collected at the shallowest depth (10 m), while all the other specimens were collected deeper than 40 m, rising a question about the possible response of the epithallial cell size to light availability or other still undefined oceanographic controls.

The distinct zonation (= banding) of *L. racemus* DB867 provided an opportunity to focus on calcification traits in short and long cells separately (Fig 10). In literature, short cells are reported to show thicker cell walls and lower Mg/Ca ratio compared to long cells [33, 37]. Our results showed that *L. racemus* short perithallial cells possess higher SC thickness, and therefore a larger cell wall area, in comparison with long perithallial cells, although keeping an almost stable cell lumen area (Fig 10). The PC observed between two cells of adjacent filaments was thicker in long cells produced in the warm months, while short cells had larger cell wall area due to the thicker SC (Fig 10) [39]. Therefore, we could speculate that warmer temperatures and/or longer light periods would have triggered the production of primary crystallites. The low values of PC thickness in short cells might be explained by a SC that could grow at the expense of the PC during the cold months. This hypothesis is supported by the observation of an inverse correlation between SC and PC thickness, observed in the perithallial cells of most samples (Fig 8; Table 3).

Biomineralization

The calcification in coralline red algae had been traditionally considered a controlled process, by means of cell wall mineralization [72–74]. This view was questioned by the report of different Mg/Ca ratios associated to distinct anatomical structures in CCA [75] and in particular, of higher-Mg calcite detected in wound repairs, in the primary calcification and in hypothallial cells of *Phymatolithon* and *Clathromorphum* [18, 76]. Based on this considerable Mg/Ca ratio variation observed in the Mg-calcite within single specimens, and on the observed relationship of Mg/Ca with ambient temperature, a biologically induced origin of CCA calcification was suggested [76]. The biologically induced mineralization is defined as the secondary precipitation of minerals resulting from interactions between the biological activity and the environment [77].

In contrast with the idea of a biologically-induced calcification in CCA [76] it was recently demonstrated that the ultrastructural shape and arrangement of crystallites in the cell walls is shared by species belonging to the same phylogenetic clade [38, 39]. Moreover, [39] showed the occurrence of species-specific distinct styles of PW calcification within the genus *Lithothamnion*. Despite the variable and quite distinct cell size in *L. racemus* and *L. pseudoracemus*, the ultrastructures observed and analysed in this paper confirm the recently described lithophylloid pattern [38], and the phylogenetic control on the calcification process and on the morphology and orientation of the produced crystallites (Fig 8).

Raz et al. [78] experimentally demonstrated that high-Mg calcite forms via an amorphous precursor phase, composed of spherical particles. Similar findings have been recorded later in corals [79], where amorphous calcium carbonate (ACC) precursors precipitate before being transformed into crystalline calcium carbonate (CCC) after about a day. Similar amorphous-to crystalline pathways were reported in crustaceans, annelids, and mollusk larval shells [80]. From this perspective, the inner layer of calcified grains observed in our corallines (Fig 1C) could represent an intermediate precursor phase preceding the formation of the rod-shaped crystallites. The IC is the only calcification occurring just after the cut off of a new epithallial cell from the meristem, and we frequently observed multiple layers of perpendicular rods within the SC (Fig 4A). Therefore, we suggest that IC would likely be the first step in the formation of SC, with SC multiple-layer thickening deriving from a deposition of a new layer after reactivation of IC. From this point of view, a CCA calcification proceeding from the inner part of the cell wall towards its periphery appears the only plausible explanation [76].

The Mg/Ca ratio in CCA is variable not only among specimens or within a single specimen. At a higher detail, NanoSIMS analysis of the Mg/Ca ratios in *L. glaciale* showed higher values in summer cells, with a pronounced variation within a single cell wall, both in the natural environment and in controlled conditions with constant temperature, although at a lesser extent [37]. This observation would suggest that the Mg/Ca ratio is controlled primarily by the temperature of the environment, as assessed across phyla at a global scale [81], but also that the living CCA cells mediate the calcite Mg/Ca ratio at the ultrastructural scale. In the perithallial cells of *L. glaciale* the highest ratios were recorded in the PC, and at the boundary of the cell lumen, with NanoSIMS evidence of further high Mg/Ca values, localized concentrically in the SC [37] (Fig 2A). This pattern of concentric higher Mg/Ca values supports the hypothesis of successive activations of the IC, possibly driving the formation of additional SC crystallite layers.

Interestingly, we observed the best developed calcite rhomboids in the PC among adjacent cell filaments and in the hypothallial cell walls, both in the primary and secondary hypothallus. We observed also thicker PC in longer cells, which explains the occurrence of higher Mg/Ca ratio in the cell wall of longer perithallial cells produced during the warm season [25, 34, 37, 76]. These observations support the hypothesis that the primary and secondary calcification may be controlled by distinct processes: the calcification of the actively (fast?) developing anatomical parts (hypothallial cells, wound repairs), and in particular the PC and the IC, could be mediated by a higher Mg/Ca phase controlled by distinct physiological activity of CCA cells and their organic templates (e.g.: [15, 18]; on the contrary, the calcification of the SC would develop from the IC and partially at the expenses of the PC, by incremental growth of one or multiple generation of crystallites with relatively lower Mg/Ca ratio.

Conclusions

We used SEM image analyses to compare the classical biometrical descriptors and the calcification traits of two morphologically similar, but genetically distinct sympatric species, *L. racemus* and *L. pseudoracemus*. The perithallial cell area differed significantly between *L. racemus* and *L. pseudoracemus* and the shape of the asexual conceptacles together with the occurrence and shape of the calcified columella could suggest a morphoanatomical criterion for species identification, however, their use would be hampered by a non-negligible degree of variability and values superposition. Therefore, a morphological identification solely based on biometrical measurements of cells and reproductive structures confirmed to be ineffective for species discrimination of *L. racemus* from *L. pseudoracemus*.

The morphology of crystallites in the high-Mg calcite cell walls was coherent with previous studies on other species belonging to the same clade. We observed no distinction of crystallite shape and organization at species level. We rather found differences in the degree of cell calcification, and we could distinguish two *L. racemus* and *L. pseudoracemus* calcification types from a multivariate analysis accounting for the SC thickness, the PC thickness and the cell wall area. Most of the differences were explained by the perithallial SC thickness, higher in *L. racemus* and lower in *L. pseudoracemus*. One corollary is that the exclusive analysis of the cell-wall ultrastructures in epithallial and meristematic cells is a valid diagnostic criterion for higher taxa, but other elements must be taken into account for the identification of congeneric and very similar specimens.

Evidence from SEM images showed the presence of a granular calcified layer in the innermost part of the cell wall (IC), in addition to the SC and PC known in the literature. We suggest that this could represent the precursor phase in the formation of secondary crystallites, becoming an important clue of the biomineralization mechanism in CCA.

A comparative analysis of the calcification of short and long cells, in the framework of published reports about the pattern of variation in the Mg/Ca ratio, suggested that cell elongation both in the perithallus and in the hypothallus is associated with the enhanced production of PC with higher Mg/Ca ratio, possibly triggered by warmer temperatures and/or longer light periods. Moreover, the inverse proportion between perithallial SC and PC thickness, together with the absence of PC in the newly formed wall cutting off an epithallial cell from the meristem, support the existence of two different pathways for the formation of PC and SC.

Our findings suggest the existence of a taxon-dependent hierarchy of ultrastructural patterns and calcification traits, still largely unexplored, consistent with the concept of biologically-controlled calcification in coralline red algae. Classical morphoanatomy should be integrated with new characters such as skeletal ultrastructures, to be assessed in genetically identified specimens, with the aim to improve rather than neglect the information about phylogeny, functions, adaptations and ecology, conveyed by anatomical structures and organization patterns.

Supporting information

S1 Table. Results of statistical tests. Testing the difference of the perithallial cell area of *L. racemus* (DB661, DB867), *L. pseudoracemus* (DB768, DB835), *L.* cf. *racemus* DB865, and *L.* cf. *pseudoracemus* DB866. Statistically significant p-values are given in bold. Kruskal-Wallis test significance at $\alpha = 0.05$; Dunn's test significant at $p \leq \alpha/2$.
(DOCX)

S2 Table. Results of statistical tests. Testing the differences of the perithallial SC thickness in *L. racemus* (DB661, DB867), *L. pseudoracemus* (DB768, DB835), *L.* cf. *racemus* DB865, and *L.* cf. *pseudoracemus* DB866. Statistically significant p-values are given in bold. ANOVA test significance at $\alpha = 0.05$; Tukey's test significant at $p \leq \alpha$.
(DOCX)

Acknowledgments

We are grateful to the Academic Editor Marcos Rubal García and two anonymous reviewers for their constructive comments to an early draft of the manuscript. Samples from Pontian Islands, Villasimius and Torre dell'Orso were collected during the monitoring activities for the Italian "Marine Strategy" Programme. We are grateful to Guido Bressan for providing the sample from Rovinj, and to Luigi Piazzi and the team of the Marine Protected Area "Capo Carbonara" for their support during the field work in Villasimius. The authors are indebted with Tiziano Catelani for his technical support during SEM sessions.

Author Contributions

Conceptualization: Daniela Basso.

Data curation: Giulia Piazza, Valentina Alice Bracchi.

Formal analysis: Giulia Piazza, Valentina Alice Bracchi.

Funding acquisition: Daniela Basso.

Investigation: Daniela Basso, Giulia Piazza, Valentina Alice Bracchi.

Methodology: Daniela Basso, Valentina Alice Bracchi.

Resources: Daniela Basso.

Supervision: Daniela Basso, Valentina Alice Bracchi.

Validation: Daniela Basso.

Visualization: Giulia Piazza.

Writing – original draft: Daniela Basso, Giulia Piazza.

Writing – review & editing: Daniela Basso.

References

1. Freiwald A, Henrich R. Reefal coralline algal build-ups within the Arctic Circle: morphology and sedimentary dynamics under extreme environmental seasonality. Sedimentology. 1994; 41:963–984.
2. Ballesteros E. Mediterranean coralligenous assemblages: a synthesis of present knowledge. Oceanogr Mar Biol. 2006; 44:123–195.
3. Bressan G, Babbini L, Ghirardelli L, Basso D. Bio-costruzione e bio-distruzione di Corallinales nel mar Mediterraneo. Biol Mar Medit. 2001; 8:131–174.
4. Caragnano A, Colombo F, Rodondi G, Basso D. 3-D distribution of nongeniculate Corallinales: a case study from a reef crest of South Sinai (Red Sea, Egypt). Coral Reefs. 2009; 28:881–891.
5. Amado-Filho GM, Moura RL, Bastos AC, Salgado LT, Sumida PY, Guth AZ, et al. Rhodolith beds are major $CaCO_3$ bio-factories in the tropical south west Atlantic. PLoS One. 2012; 7:e35171.
6. Bracchi VA, Basso D, Marchese F, Corselli C, Savini A. Coralligenous morphotypes on subhorizontal substrate: a new categorization. Cont Shelf Res. 2017; 144:10–20.
7. Ingrosso G, Abbiati M, Badalamenti F, Bavestrello G, Belmonte G, Cannas R, et al. Mediterranean bioconstructions along the Italian coast. Adv Mar Biol. 2018; 79:61–136. https://doi.org/10.1016/bs.amb.2018.05.001 PMID: 30012277
8. Marchese F, Bracchi V, Lisi G, Basso D, Corselli C, Savini A. Assessing fine-scale distribution and volume of Mediterranean algal reefs through terrain analysis of multibeam bathymetric data. A case study in the southern Adriatic continental shelf. Water. 2020;12: https://doi.org/10.3390/w12010157
9. Cebrián E, Ballesteros E, Canals M. Shallow rocky bottom benthic assemblages as calcium carbonate producers in the Alboran Sea (southwestern Mediterranean). Oceanol Acta. 2020; 23:311–322.
10. Canals M, Ballesteros E. Production of carbonate particles by phytobenthic communities on the Mallorca-Menorca shelf, northwestern Mediterranean Sea. Deep Sea Res. 2007; 44:611–629.
11. Fortunato H, Schäfer P. Coralline algae as carbonate producers and habitat providers on the Eastern Pacific coast of Panama: preliminary assessment. Neues Jahrb Geol P-A. 2009; 253:145–161.
12. Basso D. Carbonate production by calcareous red algae and global change. In: Basso D, Granier B, editors. Calcareous algae and global change: from identification to quantification. Geodiversitas. 2012; 34:13–33.
13. Bracchi VA, Basso D. The contribution of calcareous algae to the biogenic carbonates of the continental shelf: Pontian Islands, Tyrrhenian Sea, Italy. Geodiversitas. 2012; 34:61–76.
14. Pomar L, Baceta JI, Hallock P, Mateu-Vicens G, Basso D. Reef building and carbonate production modes in the west-central Tethys during the Cenozoic. Mar Petrol Geol. 2017; 83:261–304.
15. Bilan MI, Usov AI. Polysaccharides of calcareous algae and their effect on the calcification process. Russ J Bioorganic Chem. 2001; 27:2–16.
16. Morse JW, Andersson AJ, Mackenzie FT. Initial responses of carbonate-rich shelf sediments to rising atmospheric pCO_2 and "ocean acidification": role of high Mg-calcites, Geochim Cosmochim Ac. 2006; 70:5814–5830.
17. Rahman MA, Halfar J. First evidence of chitin in calcified coralline algae: New insights into the calcification process of *Clathromorphum compactum*. Sci Rep. 2014; 4:6162.

18. Nash MC, Adey W. Multiple phases of Mg-calcite in crustose coralline algae suggest caution for temperature proxy and ocean acidification assessment: lessons from the ultrastructure and biomineralization in *Phymatolithon* (Rhodophyta, Corallinales). J Phycol. 2017; 53:970–984.

19. Smith AM, Sutherland JE, Kregting L, Farr TJ, Winter DJ. Phylomineralogy of the Coralline red algae: Correlation of skeletal mineralogy with molecular phylogeny. Phytochemistry. 2012; 81:97–108. https://doi.org/10.1016/j.phytochem.2012.06.003 PMID: 22795764

20. Aguirre J, Riding R, Braga JC. Diversity of coralline red algae: origination and extinction patterns from the Early Cretaceous to the Pleistocene. Paleobiology. 2000; 26:651–667.

21. Bracchi VA, Nalin R, Basso D. Paleoecology and dynamics of coralline dominated facies during a Pleistocene transgressive–regressive cycle (Capo Colonna marine terrace, Southern Italy). Palaeogeogr Paleoclimatol Palaeoecol. 2014; 414:296–309.

22. Bracchi VA, Nalin R, Basso D. Morpho-structural heterogeneity of shallow-water coralligenous in a Pleistocene marine terrace (Le Castella, Italy). Palaeogeogr Paleoclimatol Palaeoecol. 2016; 454:101–112.

23. Bracchi VA, Basso D, Savini A, Corselli C. Algal reefs (Coralligenous) from glacial stages: origin and nature of a submerged tabular relief (Hyblean Plateau, Italy). Mar Geol. 2019; 411:119–132.

24. Teichert S, Woelkerling WJ, Munnecke A. Coralline red algae from the Silurian of Gotland indicate that the order Corallinales (Corallinophycidae, Rhodophyta) is much older than previously thought. Palaeontology. 2019; 62:599–613.

25. Halfar J, Zack T, Kronz A, Zachos JC. Growth and high-resolution paleoenvironmental signals of rhodoliths (coralline red algae): a new biogenic archive. J Geophys Res-Oceans. 2000; 105:22107–22116.

26. Hetzinger S, Halfar J, Zack T, Gamboa G, Jacob DE, Kunz BE, et al. High-resolution analysis of trace elements in crustose coralline algae from the North Atlantic and North Pacific by laser ablation ICP-MS. Palaeogeogr Palaeoclimatol Palaeoecol. 2011; 302:81–94.

27. Fietzke J, Ragazzola F, Halfar J, Dietze H, Foster LC, Hansteen TH, et al. Century-scale trends and seasonality in pH and temperature for shallow zones of the Bering Sea. P Natl Acad Sci. 2015; 112:2960–2965. https://doi.org/10.1073/pnas.1419216112 PMID: 25713385

28. Ragazzola F, Caragnano A, Basso D, Schmidt DN, Fietzke J. Establishing temperate crustose Early Holocene coralline algae as archive for paleoenvironmental reconstructions of the shallow water habitats of the Mediterranean Sea. Paleontology. 2019; 63:155–170.

29. Cabioch J. Contribution à l'étude morphologique, anatomique et systématique de deux Mélobésiées: *Lithothamnium calcareum* (Pallas) Areschoug et *Lithothamnium corallioides* Crouan. Bot Mar. 1966; 9:33–53.

30. Basso D. Study of living calcareous algae by a paleontological approach: the non-geniculate Corallinaceae (Rhodophyta) of the soft bottoms of the Tyrrhenian Sea (western Mediterranean). The genera *Phymatolithon* Foslie and *Mesophyllum* Lemoine. Riv Ital Paleont Strat. 1995; 100:575–596.

31. Basso D. Living calcareous algae by a paleontological approach: the genus *Lithothamnion* Heydrich nom. cons. from the soft bottoms of the Tyrrhenian Sea (Mediterranean). Riv Ital Paleont Strat. 1995; 101:349–366.

32. Foster MS. Rhodoliths: between rocks and soft places. J Phycol. 2001; 37:659–667.

33. Kamenos NA, Cusack M, Huthwelker T, Lagarde P, Scheibling RE. Mg-lattice associations in red coralline algae. Geochim Cosmochim Ac. 2009; 73:1901–1907.

34. Caragnano A, Basso D, Jacob DE, Storz D, Rodondi G, Benzoni F, et al. The coralline red alga *Lithophyllum kotschyanum* f. *affine* as proxy of climate variability in the Yemen coast, Gulf of Aden (NW Indian Ocean). Geochim Cosmochim Ac. 2014; 124:1–17.

35. Flajs G. Skeletal ultrastructures of calcareous algae. Palaeontogr Abt B. 1977; 160:69–128.

36. Adey WH, Chamberlain YM, Irvine LM. An SEM-based analysis of the morphology, anatomy, and reproduction of *Lithothamnion tophiforme* (Esper) Unger (Corallinales, Rhodophyta), with a comparative study of associated North Atlantic arctic/subarctic Melobesioideae. J Phycol. 2005; 41:1010–1024.

37. Ragazzola F, Foster LC, Jones CJ, Scott TB, Fietzke J, Kilburn MR, et al. Impact of high CO_2 on the geochemistry of the coralline algae *Lithothamnion glaciale*. Sci Rep. 2016; 6:20572.

38. Auer G, Piller WE. Nanocrystals as phenotypic expression of genotypes—An example in coralline red algae. Science Advances. 2020;6 https://doi.org/10.1126/sciadv.aay2126 PMID: 32095524

39. Bracchi VA, Piazza G, Basso D. A stable ultrastructural pattern despite variable cell size in *Lithothamnion corallioides*. Biogeosciences. 2021; 18:6061–6076.

40. Bailey JC, Gabel JE, Freshwater DW. Nuclear 18S rRNA gene sequence analyses indicate that the Mastophoroideae (Corallinaceae, Rhodophyta) is a polyphyletic taxon. Phycologia. 2004; 43:3–12.

41. Kato A, Baba M, Suda S. Revision of the Mastophoroideae (Corallinales, Rhodophyta) and polyphyly in nongeniculate species widely distributed on Pacific coral reefs. J Phycol. 2011; 47:662–72.

42. Pardo C, Lopez L, Peña V, Hernández-Kantún J, Le Gall L, Bárbara I, et al. A multilocus species delimitation reveals a striking number of species of coralline algae forming maerl in the OSPAR maritime area. PLoS One. 2014; 9:e104073. https://doi.org/10.1371/journal.pone.0104073 PMID: 25111057

43. Hernández-Kantún JJ, Riosmena-Rodriguez R, Hall-Spencer JM, Peña V, Maggs CA, et al. Phylogenetic analysis of rhodolith formation in the Corallinales (Rhodophyta). Eur J Phycol. 2015; 50:46–61.

44. Caragnano A, Foetisch A, Maneveldt GW, Millet L, Liu LC, Lin SM, et al. Revision of Corallinaceae (Corallinales, Rhodophyta): recognizing *Dawsoniolithon* gen. nov., *Parvicellularium* gen. nov. and Chamberlainoideae subfam. nov. containing *Chamberlainium* gen. nov. and *Pneophyllum*. J Phycol. 2018; 54:391–409.

45. De Jode A, David R, Haguenauer A, Cahill A, Erga Z, Guillemain D, et al. From seascape ecology to population genomics and back. Spatial and ecological differentiation among cryptic species of the red algae *Lithophyllum stictiforme*/*L. cabiochiae*, main bioconstructors of coralligenous habitats. Mol Phylogenet Evol. 2019; 137:104–113.

46. Pezzolesi L, Peña V, Le Gall L, Gabrielson PW, Kaleb S, Hughey JR, et al. Mediterranean *Lithophyllum stictiforme* is a genetically diverse species complex: implications for species circumscription, biogeography and conservation of coralligenous habitats. J Phycol. 2019; 55:473–492.

47. Coutinho LM, Penelas Gomes F, Nasri Sissini M, Vieira-Pinto T, Muller de Oliveira Henriques MC, Oliveira MC, et al. Cryptic diversity in non-geniculate coralline algae: a new genus *Roseolithon* (Hapalidiales, Rhodophyta) and seven new species from the Western Atlantic. Eur J Phycol. 2021; https://doi.org/10.1080/09670262.2021.1950839

48. Hayward BW, Holzmann M, Grenfell HR, Pawlowski J, Triggs CM. Morphological distinction of molecular types in Ammonia—Towards a taxonomic revision of the world's most commonly misidentified foraminifera. Mar Micropaleontol. 2004; 50:237–271.

49. Pawlowski J, Holzmann M, Tyszka J. New supraordinal classification of Foraminifera: Molecules meet morphology. Mar Micropaleontol. 2013; 100:1–10.

50. Parker JH. Ultrastructure of the test wall in modern porcelaneous foraminifera: implications for the classification of the Miliolida. J Foramin Res. 2017; 47:136–174.

51. Sáez AG, Probert I, Geisen M, Quinn P, Young JR, Medlin LK. Pseudo-cryptic speciation in coccolithophores, P Natl Acad Sci USA. 2003; 100:7163–7168.

52. Cuif J-P, Lecointre G, Perrin C, Tillier A, Tillier S. Patterns of septal biomineralization in Scleractinia compared with their 28S rRNA phylogeny: A dual approach for a new taxonomic framework. Zool Scripta. 2003; 32:459–473.

53. Stolarski J. Three-dimensional micro-and nanostructural characteristics of the scleractinian coral skeleton: A biocalcification proxy. Acta Palaeontol Pol. 2003; 48:497–530.

54. Budd AF, Stolarski J. Searching for new morphological characters in the systematics of scleractinian reef corals: Comparison of septal teeth and granules between Atlantic and Pacific Mussidae. Acta Zool. 2009; 90:142–165.

55. Huang D, Arrigoni R, Benzoni F, Fukami H, Knowlton N, Smith ND, et al. Taxonomic classification of the reef coral family Lobophylliidae (Cnidaria: Anthozoa: Scleractinia). Zool J Linn Soc. 2016; 178:436–481.

56. Basso D. Deep rhodolith distribution in the Pontian Islands, Italy: a model for the paleoecology of a temperate sea. Palaeogeogr Palaeoclimatol Palaeoecol. 1998; 137:173–187.

57. Bressan G, Babbini L. Marine biodiversity of Italian coast: Corallinales of the Mediterranean Sea: guide to the identification. Biol Mar Medit. 2001; 10:235–237.

58. Bosence DWJ. Description and classification of rhodoliths (rhodoids, rhodolites). In: Perit T. editors. Coated Grains. Springer Verlag, 1983. p. 225–42.

59. Basso D, Fravega P, Vannucci G. Fossil and living corallinaceans related to the Mediterranean endemic species *Lithophyllum racemus* (Lamarck) Foslie. Facies. 1996; 35:275–292.

60. Basso D, Babbini L, Kaleb S, Bracchi VA, Falace A. Monitoring deep Mediterranean rhodolith beds. Aquatic Conserv: Mar Freshw Ecosyst. 2016; 26:549–561.

61. Sañé E, Chiocci FL, Basso D, Martorelli E. Environmental factors controlling the distribution of rhodoliths: an integrated study based on seafloor sampling, ROV and side scan sonar data, offshore the W-Pontine Archipelago. Cont Shelf Res. 2016; 129:10–22.

62. Chimienti G, Rizzo L, Kaleb S, Falace A, Fraschetti S, Giosa FD, et al. Rhodolith Beds Heterogeneity along the Apulian Continental Shelf (Mediterranean Sea). J Mar Sci Eng. 2020; 8:813.

63. Rendina F, Kaleb S, Caragnano A, Ferrigno F, Appolloni L, Donnarumma L, et al. Distribution and characterization of deep rhodolith beds off the Campania coast (SW Italy, Mediterranean Sea). Plants. 2020; 9:985.

64. Frezza V, Argenti L, Bonifazi A, Chiocci FL, Di Bella L, Ingrassia M, et al. Benthic foraminiferal assemblages and rhodolith facies evolution in Post-LGM sediments from the Pontine Archipelago Shelf (Central Tyrrhenian Sea, Italy). Geosciences. 2021; 11:179.

65. Caragnano A, Rodondi G, Basso D, Peña V, Le Gall L, Rindi F. Circumscription of *Lithophyllum racemus* (Corallinales, Rhodophyta) from the Western Mediterranean Sea reveals the species *Lithophyllum pseudoracemus* sp. nov. Phycologia. 2020; 59:584–597.

66. Basso D, Rodondi G, Mari M. A comparative study between *Lithothamnion minervae* and the type material of *Millepora fasciculata* (Corallinales, Rhodophyta). Phycologia. 2004; 43:215–223.

67. Adey WH, Adey PJ. Studies on the biosystematics and ecology of the epilithic crustose Corallinaceae of the British Isles. Brit Phycol J. 1973; 8:343–407.

68. Johansen HW. Coralline Algae: A First Synthesis. Boca Raton, USA: CRC Press (Taylor & Francis); 1981.

69. Ballabio D. A MATLAB toolbox for Principal Component Analysis and unsupervised exploration of data structure. Chemometr Intell Lab. 2015; 149(Pt B):1–9, https://doi.org/10.1016/j.chemolab.2015.10.003

70. Piazza G, Valsecchi C, Sottocornola G. Deep learning applied to SEM images for supporting marine coralline algae classification. Diversity. 2021; 13:640. https://doi.org/10.3390/ d13120640.

71. Basso D, Caragnano A, Rodondi G. Trichocytes in *Lithophyllum kotschyanum* and *Lithophyllum* spp. (Corallinales, Rhodophyta) from the NW Indian Ocean. J. Phycol. 2014; 50:711–717.

72. Cabioch J, Giraud G. Structural aspects of biomineralization in the coralline algae (calcified Rhodophyceae). In: Barry SC, Leadbeater BSC, Riding RE, editors. Biomineralization in lower plants and animals, USA, Oxford University Press, 1986. p. 141–56.

73. Borowitzka MA, Larkum AWD, Nockolds CE. A scanning electron microscope study of the structure and organization of the calcium carbonate deposits of algae. Phycologia. 1974; 13:195–203.

74. Borowitzka MA. Morphological and cytological aspects of algal calcification. Intl Rev Cytology. 1982; 74:127–160.

75. Nash MC, Adey W. Anatomical structure overrides temperature controls on magnesium uptake-Calcification in the Arctic/subarctic coralline algae *Leptophytum leave* and *Kvaleya epilaeve* (Rhodophyta; Corallinales). Biogeosciences. 2018; 15:781–795.

76. Nash MC, Diaz-Pulido G, Harvey AS, Adey W. Coralline algal calcification: A morphological and process-based understanding. PLoS One. 2019; 14:e022 1396. https://doi.org/10.1371/journal.pone.0221396 PMID: 31557180

77. Weiner S, Dove PM. An overview of biomineralization processes and the problem of the vital effect. Rev Mineral Geochem. 2003; 54:1–29.

78. Raz S, Weiner S, Addadi L. Formation of high-magnesian calcites via an amorphous precursor phase: possible biological implications. Adv Mater. 2000; 12:38–42.

79. Mass T, Giuffre AJ, Sun C-Y, Stifler CA, Frazier MJ, Neder M, et al. Amorphous calcium carbonate particles form coral skeletons. P Natl Acad Sci. 2017;201707890. https://doi.org/10.1073/pnas.1707890114 PMID: 28847944

80. De Yoreo JJ, Gilbert PU, Sommerdijk NA, Penn RL, Whitelam S, Joester D, et al. Crystallization by particle attachment in synthetic, biogenic, and geologic environments. Science. 2015; 349:6247.

81. Chave KE. Aspects of biochemistry of magnesium.1. Calcareous and marine organisms. J Geol. 1954; 62:266–283.

References

[1] Abdalla A., Cen H., Wan L., Rashid R., Weng H., Zhou W., and He Y. Fine-tuning Convolutional Neural Network with Transfer Learning for semantic segmentation of ground-level oilseed rape images in a field with high weed pressure. *Computers and Electronics in Agriculture*, 167: 105091:158–163, 2019. 6

[2] Caragnano A., Foetisch A., Maneveldt G.W., Millet L., Liu L.C., Lin S.M., Rodondi G., and Payri C.E. Revision of Corallinaceae (Corallinales, Rhodophyta): recognizing *Dawsoniolithon* gen. nov. and *Parvicellularium* gen. nov. and Chamberlainoideae subfam. nov. containing *Chamberlainium* gen. nov. and *Pneophyllum*. *Journal of Phycology*, 54:391–409, 2018. 4

[3] Caragnano A., Basso D., Storz D., Jacob D.E., Ragazzola F., Benzoni F., and Dutrieux E. Elemental variability in the coralline alga *Lithophyllum yemenense* as an archive of past climate in the Gulf of Aden (NW Indian Ocean). *Journal of Phycology*, 53:381–395, 2017. 13

[4] Caragnano A., Basso D., Jacob D.E., Storz D., Rodondi G., Benzoni F., and Dutrieux E. The coralline red alga *Lithophyllum kotschyanum* f. *affine* as proxy of climate variability in the Yemen coast, gulf of aden (nw indian ocean). *Geochimica et Cosmochimica Acta*, 124:1–17, 2014. 9, 13, 25, 107, 111, 112

[5] Caragnano A., Colombo F., Rodondi G., and Basso D. 3-d distribution of nongeniculate Corallinales: a case study from a reef crest of South Sinai (Red Sea, Egypt). *Coral Reefs*, 28:881–891, 2009. 1

[6] Caragnano A., Rodondi G., Basso D., Peña V., Le Gall L., and Rindi F. Circumscription of *Lithophyllum racemus* (Corallinales, Rhodophyta) from the Western Mediterranean Sea reveals the species *Lithophyllum pseudoracemus* sp. nov. *Phycologia*, 59:584–597, 2020. xv, 3, 4, 20, 31, 34, 45, 105, 106

[7] De Jode A., David R., Haguenauer A., Cahill A., Erga Z., Guillemain D., Sartoretto S., Rocher C., Selva M., Le Gall L., Féral J-P., and Chenuil A. From seascape ecology to population genomics and back. spatial and ecological differentiation among cryptic species of the red algae *Lithophyllum stictiforme/L. cabiochiae*, main bioconstructors of coralligenous habitats. *Molecular Phylogenetics and Evolution*, 137:104–113, 2019. 4

[8] Dueñas-Bohórquez A., Raitzsch M., Nooijer L.J., and Reichart G-J. Independent impacts of calcium and carbonate ion concentration on Mg and Sr incorporation in cultured benthic foraminifera. *Marine Micropaleontology*, 81:122–130, 2011. 112

[9] Freiwald A. and Henrich R. Reefal coralline algal build-ups within the Arctic Circle: morphology and sedimentary dynamics under extreme environmental seasonality. *Sedimentology*, 41:963–984, 1994. 1, 8, 9

[10] Hou A., Halfar J., Adey W., Wortmann U. G., Zajacz Z., Tsay A., Williams B., and Chan P. Long-lived coralline alga records multidecadal variability in Labrador Sea carbon isotopes. *Chemical Geology*, 526:93–100, 2018. 13

[11] Kato A., Baba M., and Suda S. Revision of the Mastophoroideae (Corallinales, Rhodophyta) and polyphyly in nongeniculate species widely distributed on Pacific coral reefs. *Journal of Phycology*, 47:662–672, 2011. 4

[12] Marchini A., Ragazzola F., Vasapollo C., Castelli A., Cerrati G., Gazzola F., Jiang C., Langeneck J., Manauzzi M. C., Musco L., , Nannini M., Zekonyte J., and Lombardi C. Intertidal mediterranean coralline algae habitat is expecting a shift toward a reduced growth and a simplified associated fauna under climate change. *Frontiers in Marine Science*, 6: 106, 2019. 1

[13] Peccerillo A. *Plio-Quaternary volcanism in Italy: Petrology, Geochemistry, Geodynamics.* Springer, Italy, 2005. 23

[14] Rösler A., Perfectti F., Peña V., and Braga J.C. Phylogenetic relationships of Corallinaceae (Corallinales, Rhodophyta): Taxonomic implications for reef-building corallines. *Journal of Phycology*, 52:412–431, 2016. 4

[15] Sanyal A., Nugent M., Reeder R.J., and Bijma J. Seawater pH control on the boron isotopic composition of calcite: evidence from inorganic calcite precipitation experiments. *Geochimica et Cosmochimica Acta*, 64(9):1551–1555, 2000. 18, 115

[16] Savini A., Basso D., Bracchi V.A., Corselli C., and Pennetta M. Maerl-bed mapping and carbonate quantification on submerged terraces offshore the Cilento peninsula (Tyrrhenian Sea, Italy). *Geodiversitas*, 34:77–98, 2012. 2, 3

[17] Teruzzi A., Di Biagio V., Feudale L., Bolzon G., Lazzari P., Salon S., Di Biagio V., Coidessa G., and Cossarini G. Mediterranean Sea Biogeochemical Reanalysis (CMEMS MED-Biogeochemistry, MedBFM3 system), Version 1. CMEMS [data set], 2021. available online: `https://doi.org/10.25423/CMCC/MEDSEA_MULTIYEAR_BGC_006_008_MEDBFM3`. 25

[18] Vengosh A., Kolodny Y., Starinsky A., Chivas A.R., and McCulloch M.T. Coprecipitation and isotopic fractionation of boron in modern biogenic carbonates. *Geochimica et Cosmochimica Acta*, 55:2901–2910, 1991. 16, 114

[19] Venn A.A., Tambutté E., Holcomb M., Laurent J., Allemand D., and Tambutté S. Impact of seawater acidification on pH at the tissue–skeleton interface and calcification in reef corals. *Proceedings of the National Academy of Sciences USA*, 110(5):1634–1639, 2013. 115

[20] Gagnon A.C., Gothmann A.M., Branson O., Rae J.W.B., and Stewart J.A. Controls on boron isotopes in a cold-water coral and the cost of resilience to ocean acidification. *Earth and Planetary Science Letters*, 554: 116662, 2021. 112

[21] Agarap A.F. Deep Learning using Rectified Linear Units (ReLU). *arXiv*, page 1803.08375v2, 2018. 30

[22] Budd A.F. and Stolarski J. Searching for new morphological characters in the systematics of scleractinian reef corals: Comparison of septal teeth and granules between Atlantic and Pacific Mussidae. *Acta Zoologica*, 90:142–165, 2009. 9

[23] Sáez A.G., Probert I., Geisen M., Quinn P., Young J.R., and Medlin L.K. Pseudo-cryptic speciation in coccolithophores. *Proceedings of the National Academy of Sciences USA*, 100:7163–7168, 2003. 9

[24] Smith A.M., Sutherland J.E., Kregting L., Farr T.J., and Winter D.J. Phylomineralogy of the Coralline red algae: Correlation of skeletal mineralogy with molecular phylogeny. *Phytochemistry*, 81:97–108, 2012. 8

[25] Fairhall A.W. Accumulation of fossil CO_2 in the atmosphere and the sea. *Nature*, 245:20–23, 1973. 10

[26] Hsiang A.Y., Brombacher A., Rillo M.C., Mleneck-Vautravers M.J., Conn S., Lordsmith S., Jentzen A., Henehan M.J., Metcalfe B., Fenton I.S., Wade B.S., Fox L., Meilland J., Davis C.V., Baranowski U., Groeneveld J., Edgar K.M., Movellan A., Aze T., Dowsett H.J., Miller C.G., Rios N., and Hull P.M. Endless forams: ¿34,000 modern planktonic foraminiferal images for taxonomic training and automated species recognition using Convolutional Neural Networks. *Paleoceanography and Paleoclimatology*, 34:1157–1177, 2019. 34

[27] Carro B., Lopez L., Peña V., Bárbara I., and Barreiro R. DNA barcoding allows the accurate assessment of European maerl diversity: A proof-of-concept study. *Phytotaxa*, 190:176–189, 2014. 2, 3, 20

[28] Hönisch B., Ridgwell A., Schmidt D.N., Thomas E., Gibbs S.J., Sluijs A., Zeebe R., Kump L., Martindale R.C., Greene S.E., Kiessling W., Ries J., Zachos J.C., Royer D.L., Barker S., Marchitto T.M. Jr., Moyer R., Pelejero C., Ziveri P., Foster G.L., and Williams B. The geological record of ocean acidification. *Science*, 335:1058–1063, 2012. 10

[29] Hönisch B. and Hemming N.G. Surface ocean pH response to variations in pCO_2 through two full glacial cycles. *Earth and Planetary Science Letters*, 236:305–314, 2005. 16

[30] Hönisch B., Hemming N.G., Grottoli A.G., Amat A., Hanson G.N., and Bijma J. Assessing scleractinian corals as recorders for paleo-pH: Empirical calibration and vital effects. *Geochimica et Cosmochimica Acta*, 68(18):3675–3685, 2004. 114

[31] Hönisch B., Eggins S., Haynes L., Allen K., Holland K., and Lorbacher K. *Boron proxies in Paleoceanography and Paleoclimatology*. Wiley Blackwell, 2019. xvi, 15, 16

[32] Williams B., Halfar J., Delong K.L., Hetzinger S., Steneck R.S., and Jacob D.E. Multi-specimen and multi-site calibration of Aleutian coralline algal Mg/Ca to sea surface temperature. *Geochimica et Cosmochimica Acta*, 139:190–204, 2014. 25, 112

[33] Frantz B.R., Foster M.S., and Riosmena-Rodríguez R. *Clathromorphum nereostratum* (Corallinales, Rhodophyta): The oldest alga? *Journal of Phycology*, 41:770–773, 2005. 12

[34] Schöne B.R., Fiebig J., Pfeiffer M., Gleb R., Hickson J., Johnson L.A., Dreyer A.W., and Oschmann W. Climate records from a bivalved Methuselah (Arctica islandica, Mollusca; Iceland). *Palaeogeography, Palaeoclimatology, Palaeoecology*, 228:130–148, 2005. 13

[35] Wang B.S., You C.F., Huang K.F., Wu S. F., Aggarwal S.K., Chung C.H., and Lin P.Y. Direct separation of boron from Na- and Ca-rich matrices by sublimation for stable isotope measurement by MC-ICP-MS. *Talanta*, 82:1378–1384, 2010. 6, 37

[36] Hayward B.W., Holzmann M., Grenfell H.R., Pawlowski J., and Triggs C.M. Morphological distinction of molecular types in Ammonia — Towards a taxonomic revision of the world's most commonly misidentified foraminifera. *Marine Micropaleontology*, 50:237–271, 2004. 9

[37] Baggini C., Salomidi M., Voutsinas E., Bray L., Krasakopoulou E., and Hall-Spencer J.M. Seasonality affects macroalgal community response to increases in pCO_2. *PLoS ONE*, 9: e106520, 2014. xi, 12, 23, 24, 25, 44

[38] Lejeusne C, Chevaldonné P, Pergent-Martini C, Boudouresque C.F, and Pérex T. Climate change effects on a miniature ocean: the highly diverse, highly impacted Mediterranean Sea. *Trends in Ecology & Evolution*, 25(4):250–260, 2010. 12

[39] Pardo C., Lopez L., Peña V., Hernández-Kantún J., Le Gall L., Bárbara I., and Barreiro R. A multilocus species delimitation reveals a striking number of species of coralline algae forming maerl in the OSPAR maritime area. *PLoS One*, 9: e104073, 2014. 4

[40] Rollion-Bard C., Blamart D., Trebosc J., Tricot G., Mussi A., and Cuif J-P. Boron isotopes ad pH proxy: A new look at boron speciation in deep-sea corals using ^{11}B MAS NMR and EELS. *Geochimica et Cosmochimica Acta*, 75:1003–1012, 2011. 17, 115, 116

[41] Shorten C. and Khoshgoftaar T.M. A survey on image data augmentation for Deep Learning. *Journal of Big Data*, 6, 2019. 29

[42] Cornwall C.E., Comeau S., and Mcculloch M.T. Coralline algae elevate pH at the site of calcification under ocean acidification. *Global Change Biology*, 23:1–12, 2017. xxii, 4, 12, 13, 18, 39, 89, 90, 91, 92, 104, 114, 115

[43] Cornwall C.E., Comeau S., DeCarlo T.M., Moore B., D'Alexis Q., and McCulloch M.T. Resistance of corals and coralline algae to ocean acidification: physiological control of calcification under natural pH variability. *Proceedings of the Royal Society B: Biological Sciences*, 286: 20181168, 2018. xxii, 12, 18, 39, 89, 90, 92, 114, 115

[44] Payri C.E. Production primaire et calcification des algues benthiques en milieu corallien. *Oceanis*, 26:427–463, 2000. 112

[45] Waters C.N., Zalasiewicz J., Leinfelder R., and Summerhayes C.P. Boron isotopes as a proxy for oceanic pH. In Zalasiewicz J., Waters C., Williams M, and Summerhayes C., editors, *The Anthropocene as a Geological Time Unit. A guide to the scientific evidence and current debate*, pages 165–168. Cambridge University Press, Cambridge, 2019. 10

[46] Ballabio D. A MATLAB toolbox for Principal Component Analysis and unsupervised exploration of data structure. *Chemometrics and Intelligent Laboratory Systems*, 149 (Pt B):1–9, 2015. 41

[47] Basso D. Living calcareous algae by a paleontological approach: the genus *Lithothamnion* Heydrich nom. cons. from the soft bottoms of the Tyrrhenian Sea (Mediterranean). *Rivista Italiana di Paleontologia e Stratigrafia*, 101:349–366, 1995. 2, 3, 8, 12

[48] Basso D. Study of living calcareous algae by a paleontological approach: the non-geniculate Corallinaceae (Rhodophyta) of the soft bottoms of the Tyrrhenian Sea (western Mediterranean). the genera *Phymatolithon* Foslie and *Mesophyllum* Lemoine. *Rivista Italiana di Paleontologia e Stratigrafia*, 100:575–596, 1995. 2, 4, 8, 9, 12

[49] Basso D. Deep rhodolith distribution in the Pontian Islands, Italy: a model for the paleoecology of a temperate sea. *Palaeogeography, Palaeoclimatology, Palaeoecology*, 137:173–187, 1998. 1, 3

[50] Basso D. Carbonate production by calcareous red algae and global change. In Basso D. and Granier B., editors, *Calcareous algae and global change: from identification to quantification*, volume 34, pages 13–33. Geodiversitas, 2012. 1, 8, 10, 11

[51] Basso D., Caragnano A., and Rodondi G. Trichocytes in *Lithophyllum kotschyanum* and *Lithophyllum* spp. (Corallinales, Rhodophyta) from the NW Indian Ocean. *Journal of Phycology*, 50:711–717, 2014. 27

[52] Basso D., Morbioli C., and Corselli C. Rhodolith facies evolution and burial as a response to Holocene transgression at the Pontian Islands shelf break. *Geological Society Special Publication*, 255:23–34, 2006. 4

[53] Basso D. and Brusoni F. The molluscan assemblage of a transitional environment: the Mediterranean maerl from off the Elba Island (Tuscan Archipelago, Tyrrhenian Sea). *Bollettino Malacologico*, 40:37–45, 2004. 22

[54] Basso D., Rodondi G., and Mari M. A comparative study between *Lithothamnion minervae* and the type material of *Millepora fasciculata* (Corallinales, Rhodophyta). *Phycologia*, 43:215–223, 2004. 3, 27

[55] Basso D., Babbini L., Ramos-Esplá A.A., and Salomidi M. Mediterranean rhodolith beds.

In Riosmena-Rodrìguez R., Wendy Nelson W., and Aguirre J., editors, *Rhodolith/maërl beds: A global perspective*, pages 281–298. Springer, Cambridge, 2017. 2, 3

[56] Basso D., Babbini L., Kaleb S., Bracchi V.A., and Falace A. Monitoring deep Mediterranean rhodolith beds. *Aquatic Conservation: Marine and Freshwater Ecosystems*, 26:549–561, 2016. 2, 3

[57] Basso D., Fravega P., and Vannucci G. Fossil and living corallinaceans related to the Mediterranean endemic species *Lithophyllum racemus* (Lamarck) Foslie. *Facies*, 35:275–292, 1996. 3, 20, 27, 34, 53, 105

[58] Basso D., Nalin R., and Massari F. Genesis and composition of the Pleistocene Coralligène de Plateau of the Cutro Terrace (Calabria, Southern Italy). *Neues Jahrbuch fur Geologie und Palaontologie - Abhandlungen*, 244:173–182, 2007. 1

[59] Huang D., Arrigoni R., Benzoni F., Fukami H., Knowlton N., Smith N.D., Stolarski J., Chou L.M., and Budd A.F. Taxonomic classification of the reef coral family Lobophylliidae (Cnidaria: Anthozoa: Scleractinia). *Zoological Journal of the Linnean Society*, 178:436–481, 2016. 9

[60] Massiot D., Fayon F., Capron M., King I., Le Calvé S., Alonso B., Durand J.-O., Bujoli B., Gan Z., and Hoatson G. Modelling one and two-dimensional solid-state NMR spectra. *Magnetic Resonance in Chemistry*, 40:70–76, 2002. 40

[61] Rathi D., Jain S., and Indu S. Underwater fish species classification using Convolutional Neural Network and Deep Learning. In *Proceedings of the 9th International Conference on Advances in Pattern Recognition 2018*, pages 344–349, 2017. 7

[62] Wolf-Gladrow D., Bijma J., and Zeebe R.E. Model simulation of the carbonate chemistry in the microenvironment of symbiont bearing foraminifera. *Marine Chemistry*, 64:181–198, 1999. 114

[63] York D., Evensen N., Martinez M., and Delgado J. Unified equations for the slope, intercept, and standard errors of the best straight line. *American Journal of Physics*, 72(3):367–375, 2004. 16, 39

[64] de Carvalho R.T., Salgado, L.T., Amado Filho G.M., Leal R.N., Werckmann J., Linhares Rossi A., Porto Carreiro Campos A., Santiago Karez C., and Farina M. Biomineralization of calcium carbonate in the cell wall of *Lithothamnion crispatum* (Hapalidiales, Rhodophyta): correlation between the organic matrix and the mineral phase. *Journal of Phycology*, 53:642–651, 2017. 9

[65] Bosence D.W.J. Description and classification of rhodoliths (rhodoids, rhodolites). In Perit T., editor, *Coated Grains*, pages 225–242. Springer Verlag, 1983. 3

[66] Anagnostou E., Williams B., Westfield I., Foster G.L., and Ries J.B. Calibration of the ph-δ^{11}B and temperature-Mg/Li proxies in the long-lived high-latitude crustose coralline red alga *Clathromorphum compactum* via controlled laboratory experiments. *Geochimica et Cosmochimica Acta*, 254:142–155, 2019. xx, 13, 14, 76, 78, 111

[67] Anagnostou E., Huang K.F., You C.F., Sikes E.L., and Sherrell R.M. Evaluation of boron isotope ratio as a pH proxy in the deep sea coral *Desmophyllum dianthus*: evidence of physiological pH adjustment. *Earth and Planetary Science Letters*, 349-350:251–260, 2012. 16

[68] Balan E., Pietrucci F., Gervais C., Blanchard M., Schott J., and Gaillardet J. First-principles study of boron speciation in calcite and aragonite. *Geochimica et Cosmochimica Acta*, 193:119–131, 2016. 17, 115, 116

[69] Balan E., Noireaux J., Mavromatis V., Saldi G.D., Montouillout V., Blanchard M., Pietrucci F., Gervais C., Rustad J.R., Schott J., and Gaillardet J. Theoretical isotopic fractionation between structural boron in carbonates and aqueous boric acid and borate ion. *Geochimica et Cosmochimica Acta*, 222:117–129, 2018. 17, 116

[70] Ballesteros E. Mediterranean coralligenous assemblages: a synthesis of present knowledge. *Oceanography and Marine Biology*, 44:123–195, 2006. 1

[71] Cebrián E., Ballesteros E., and Canals M. Shallow rocky bottom benthic assemblages as calcium carbonate producers in the Alboran sea (southwestern Mediterranean). *Oceanologica Acta*, 23:311–322, 2020. 1

[72] Sañé E., Chiocci F.L., Basso D., and Martorelli E. Environmental factors controlling the distribution of rhodoliths: an integrated study based on seafloor sampling, ROV and side scan sonar data, offshore the W-Pontine Archipelago. *Continental Shelf Research*, 129:10–22, 2016. 3

[73] Howes E.L, Stemmann L, Assailly C, Irisson J-O, Dima M, Bijma J, and Gattuso J-P. Pteropod time series from the North Western Mediterranean (1967-2003): impacts of pH and climate variability. *Marine Ecology Progress Series*, 531:193–206, 2015. 12

[74] Chollet F. Keras. GitHub, 2015. available online: `https://github.com/fchollet/keras`. 33

[75] Marchese F., Bracchi V., Lisi G., Basso D., Corselli C., and Savini A. Assessing fine-scale distribution and volume of Mediterranean algal reefs through terrain analysis of multibeam bathymetric data. a case study in the southern Adriatic continental shelf. *Water*, 12: 10.3390/w12010157, 2020. 1

[76] Noisette F., Egilsdottir H., Davoult D., and Martin S. Physiological responses of three temperate coralline algae from contrasting habitats to near-future ocean acidification. *Journal of Experimental Marine Biology and Ecology*, 448:179–187, 2013. 11

[77] Ragazzola F., Caragnano A., Basso D., Schmidt D.N., and Fietzke J. Establishing temperate crustose Early Holocene coralline algae as archive for paleoenvironmental reconstructions of the shallow water habitats of the Mediterranean Sea. *Palaeontology*, 63:155–170, 2020. 3, 4, 12, 13, 25, 104

[78] Ragazzola F., Foster L.C., Form A., Anderson P.S.L., Hansteen T.H., and Fietzke J. Ocean acidification weakens the structural integrity of coralline algae. *Global Change Biology*, 18:2804–2812, 2012. 2, 10, 11

[79] Ragazzola F., Foster L.C., Jones C.J., Scott T.B., Fietzke J., Kilburn M.R., and Schmidt D.N. Impact of high CO_2 on the geochemistry of the coralline algae *Lithothamnion glaciale*. *Scientific Reports*, 6: 20572, 2016. 9, 12, 110, 111

[80] Rendina F., Kaleb S., Caragnano A., Ferrigno F., Appolloni L., Donnarumma L., Russo G.F., Sandulli R., Roviello V., and Falace A. Distribution and characterization of deep rhodolith beds off the Campania coast (SW Italy, Mediterranean Sea). *Plants*, 9: 985, 2020. 3

[81] Rindi F., Braga J. C., Martin S., Peña V., Le Gall L., Caragnano A., and Aguirre J. Coralline algae in a changing Mediterranean Sea: How can we predict their future, if we do not know their present? *Frontiers in Marine Science*, 6:723, 2019. xv, 2

[82] Al-Horani F.A., Al-Moghrabi S.M., and de Beer D. Microsensor study of photosynthesis and calcification in the scleractinian coral *Galaxea fascicularis*: active internal carbon cycle. *Journal of Experimental Marine Biology and Ecology*, 288(1):1–15, 2003. 115

[83] Mackenzie F.T., Lerman A., and Andersson A.J. Past and present of sediment and carbon biogeochemical cycling models. *Biogeosciences*, 1:11–32, 2004. 1

[84] Auer G. and Piller W.E. Nanocrystals as phenotypic expression of genotypes - an example in coralline red algae. *Science Advances*, 6, 2020. 4, 9, 105, 109, 110, 115

[85] Bressan G. and Babbini L. Marine biodiversity of Italian coast: Corallinales of the Mediterranean Sea: guide to the identification. *Biologia Marina Mediterranea*, 10:235–237, 2001. 1, 20

[86] Bressan G., Babbini L., Ghirardelli L., and Basso D. Bio-costruzione e bio-distruzione di Corallinales nel mar Mediterraneo. *Biologia Marina Mediterranea*, 8:131–174, 2001. 1

[87] Chimienti G., Rizzo L., Kaleb S., Falace A., Fraschetti S., Giosa F.D., Tursi A., Barbone E., Ungaro N., and Mastrototaro F. Rhodolith beds heterogeneity along the Apulian continental shelf (Mediterranean Sea). *Journal of Marine Science and Engineering*, 8: 813, 2020. 3

[88] Coletti G., Basso D., and Corselli C. Coralline algae as depth indicators in the Sommières Basin (Early Miocene, Southern France). *Geobios*, 51:15–30, 2018. 4, 104

[89] Dickson A. G. Standard potential of the reaction: $AgCl(s)+1/2H_2(g) = Ag(s)+HCl(aq)$, and the standard acidity constant of the ion HSO_4^- in synthetic seawater from 273.15 to 318.15K. *The Journal of Chemical Thermodynamics*, 22:113–127, 1990. xvi, 15

[90] Flajs G. Skeletal structures of some calcifying algae. *Fossil Algae*, pages 225–231, 1977. 9, 72

[91] Ingrosso G., Abbiati M., Badalamenti F., Bavestrello G., Belmonte G., Cannas R., Benedetti Cecchi L., Bertolino M., Bevilacqua S., Bianchi C.N., Bo M., Boscari E., Cardone F., Cattaneo-Vietti R., Cau A., Cerrano C., Chemello R., Chimienti G., Congiu L., Corriero G., Costantini F., De Leo F., Donnarumma L., Falace A., Fraschetti S., Giangrande A., Gravina M. F., Guarnieri G., Mastrototaro F., Milazzo M., Morri C., Musco L., Pezzolesi L., Piraino S., Prada F., Ponti M., Rindi F., Russo G.F., Sandulli R., Villamor A., Zane L., and Boero F. Mediterranean bioconstructions along the Italian coast. *Continental Shelf Research*, 79:61–136, 2018. 1

[92] Pecoraino G., Brusca L., D'Alessandro W., Giammanco S., Inguaggiato S., and Longo M. Total CO_2 output from Ischia Island volcano (Italy). *Geochemical Journal*, 39:451–458, 2005. 23

[93] Saldi G.D., Noireaux J., Louvat P., Faure L., Balan E., Schott J., and Gaillardet J. Boron isotopic fractionation during adsorption by calcite – implication for the seawater pH proxy. *Geochimica et Cosmochimica Acta*, 240:255–273, 2018. 17, 116

[94] Foster G.L. Seawater pH, pCO_2 and $[CO_3^{2-}]$ variations in the Caribbean Sea over the last 130 kyr: a boron isotope and B/Ca study of planktic foraminifera. *Earth and Planetary Science Letters*, 271:254–266, 2008. 16

[95] Foster G.L., Pogge von Strandmann P.A. E., and Rae J.W.B. Boron and magnesium isotopic composition of seawater. *Geochemistry, Geophysics, Geosystems*, 11(8): Q08015, 2010. xvi, 15, 16

[96] Amado-Filho G.M., Moura R.L., Bastos A.C., Salgado L.T., Sumida P.Y., Guth A.Z., Francini-Filho R.B., Pereira-Filho G.H., Abrantes D.P., Brasileiro P.S., Bahia R.G., Leal

R.N., Les Kaufman, Kleypas J.A., Farina M., and Thompson F.L. Rhodolith beds are major $CaCO_3$ bio-factories in the tropical south west atlantic. *PLoS One*, 7: e35171, 2012. 1

[97] Callendar G.S. The artificial production of carbon dioxide and its influence on temperature. *Quarterly Journal of The Royal Meteorological Society*, 64:223–240, 1938. 10

[98] Fortunato H. and Schäfer P. Coralline algae as carbonate producers and habitat providers on the Eastern Pacific coast of Panama: preliminary assessment. *Neues Jahrbuch für Geologie und Paläontologie*, 253:145–161, 2009. 1

[99] Kakihana H., Kotaka M., Satoh S., Nomura M., and Okamoto M. Fundamental studies on ion-exchange separation of boron isotopes. *Bulletin of the Chemical Society of Japan*, 50:158–163, 1977. xvi, 15, 18

[100] Rahimpour-Bonab H., Bone Y., Moussavi-Harami R., and Turnbull K. Geochemical comparisons of modern cool-water calcareous biota, Lacepede Shelf, South Australia, with their tropical counterparts. In James N.P. and Clark J., editors, *Cool-Water Carbonates*, volume Special Pubblications 56. SEPM Society for Sedimentary Geology, 1997. 8

[101] Zuo H., Balmaseda M.A., Tietsche S., Mogensen K., and Mayer M. The ECMWF operational ensemble reanalysis–analysis system for ocean and sea ice: a description of the system and assessment. *Ocean Science Journal*, 15:779–808, 2019. 25

[102] Donald H.K., Ries J.B., Stewart J.A., Fowell S.E., and Foster G.L. Boron isotope sensitivity to seawater pH change in a species of *Neogoniolithon* coralline red alga. *Geochimica et Cosmochimica Acta*, 217:240–253, 2017. xxii, 14, 18, 39, 89, 90, 91, 92, 111, 112, 113

[103] Johansen H.W. *Coralline Algae: A First Synthesis*. CRC Press (Taylor & Francis), Boca Raton, USA, 1981. 2

[104] Bladé I. and Castro-Díez Y. Atmospheric trends in the Iberian Peninsula during the instrumental period in the context of natural variability. In Perez F. and Boscolo R., editors, *Climate in Spain: Past, present and future. Regional climate change assessment report*, pages 25–42. CLIVAR, 2010. 10

[105] Goodfellow I., Bengio Y., and Courville A. *Deep Learning*. MIT Press, 2016. 6

[106] Aguirre J., Riding R., and Braga J.C. Diversity of coralline red algae: origination and extinction patterns from the Early Cretaceous to the Pleistocene. *Paleobiology*, 26:651–667, 2000. 8, 12

[107] Andersson A. J. and Mackenzie F. T. Technical comment on Kroeker et al. (2010) meta-analysis reveals negative yet variable effects of ocean acidification on marine organisms. *Ecological Letters*, 13:1419–1434, 2011. 10

[108] Andersson A. J., Mackenzie F. T., and Bates N. R. Life on the margin: implications on Mgcalcite, high latitude and coolwater marine calcifiers. *Marine Ecology Progress Series*, 373:265–273, 2008. 10, 11

[109] Cabioch J. Contribution à l'étude morphologique, anatomique et systématique de deux Mélobésiées: *Lithothamnium calcareum* (Pallas) Areschoug et *Lithothamnium corallioides* Crouan. *Botanica Marina*, 9:33–53, 1966. 8, 12

[110] Cabioch J. and Giraud G. Structural aspects of biomineralization in the coralline algae (calcified Rhodophyceae). In Barry S.C., Leadbeater B.S.C., and Riding R.E., editors, *Biomineralization in lower plants and animals*, pages 141–156. Oxford University Press, 1986. 109

[111] Cabioch J. and Mendoza M.L. *Mesophyllum alternans* (Foslie) comb. nov. (Corallinales, Rhodophyta), a Mediterraneo-Atlantic species, and new considerations on the *Lithothamnion philippii* Foslie complex. *Phycologia*, 37:208–221, 1998. 2, 20, 34

[112] Deng J., Dong W., Socher R., Li L-J., Kai L., and Li F-F. Imagenet: A large-scale hierarchical image database. In *Proceedings of the IEE Conference on Computer Vision and Pattern Recognition*, pages 248–255, 2010. 6, 30

[113] Fietzke J., Heinemann A., Taubner I., Böhm F., Erez J., and Eisenhauer A. Boron isotope ratio determination in carbonates via LA-MC-ICP-MS using soda-lime glass standards as reference material. *Journal of Analytical Atomic Spectrometry*, 25:1953–1957, 2010. 36

[114] Fietzke J., Ragazzola F., Halfar J., Dietze H., Foster L.C., Hansteen T.H., Eisenhauer A., and Steneck R.S. Century-scale trends and seasonality in pH and temperature for shallow zones of the Bering Sea. *Proceedings of the National Academy of Sciences*, 112:2960–2965, 2015. 12, 13

[115] Halfar J., Williams B., Hetzinger S., Steneck R.S., Lebednik P., Winsborough C., Omar A., Chan P., and Wanamaker A.D. 225 years of Bering Sea climate and ecosystem dynamics revealed by coralline algal growth-increment widths. *Geology*, 39:579–582, 2011. 112, 113

[116] Halfar J., Steneck R.S., Joachimski M., Kronz A., and Wanamaker A.D. Jr. Coralline red algae as high-resolution climate recorders. *Geology*, 36:463–466, 2008. 12, 13

[117] Halfar J., Zack T., Kronz A., and Zachos J.C. Growth and high- resolution paleoenvironmental signals of rhodoliths (coralline red algae): a new biogenic archive. *Journal of Geophysical Research - Oceans*, 105:22107–22116, 2000. 8, 9, 12, 13, 111

[118] Hansen J., Ruedy R., Sato M., and Lo K. Global surface temperature change. *Reviews of Geophysics*, 48: RG4004, 2010. 10

[119] Millero F. J. Thermodynamics of the carbon dioxide system in the oceans. *Geochimica et Cosmochimica Acta*, 59(4):661–667, 1995. xvi, 15

[120] Noireaux J., Mavromatis V., Gaillardet J., Schott J., Montouillout V., Louvat P., Rollion-Bard C., and Neuville D.R. Crystallographic control on the boron isotope paleo-pH proxy. *Earth and Planetary Science Letters*, 430:398–407, 2015. 17, 111, 113, 115

[121] Pawlowski J., Holzmann M., and Tyszka J. New supraordinal classification of Foraminifera: Molecules meet morphology. *Marine Micropaleontology*, 100:1–10, 2013. 9

[122] Rodríguez-Carvajal J. Recent advances in magnetic structure determination by neutron powder diffraction. *Journal of Physics: Condensed Matter*, 192:55–69, 1993. 35

[123] Stolarski J. Three-dimensional micro-and nanostructural characteristics of the scleractinian coral skeleton: A biocalcification proxy. *Acta Palaeontologica Polonica*, 48:497–530, 2003. 9

[124] Uchikawa J., Penman D.E., Zachos J.C., and Zeebe R.E. Experimental evidence for kinetic effects on B/Ca in synthetic calcite: Implications for potential $B(OH)_4^-$ and $B(OH)_3$ incorporation. *Geochimica et Cosmochimica Acta*, 150:171–191, 2015. 14, 112, 113

[125] Yu J., Anderson R.F., Jin Z., Rae J.W.B., Opdyke B.N., and Eggins S.M. Responses of the deep ocean carbonate system to carbon reorganization during the last glacial–interglacial cycle. *Quaternary Science Reviews*, 76:39–52, 2013. 16

[126] Park J-H., Hwang K-B., Park H-M., and Choi Y-K. Application of CNN for fish species classification. *Journal of the Korea Institute of Information and Communication Engineering*, 23:39–46, 2019. 7

[127] Cuif J-P., Lecointre G., Perrin C., Tillier A., and Tillier S. Patterns of septal biomineralization in Scleractinia compared with their 28S rRNA phylogeny: A dual approach for a new taxonomic framework. *Zoologica Scripta*, 32:459–473, 2003. 9

[128] Gattuso J-P., Frankignoulle M., and Smith S.V. Measurement of community metabolism and significance in the coral reef CO_2 source-sink debate. *Proceedings of the National Academy of Sciences USA*, 96:13017–13022, 1999. 10

[129] Stewart J.A., Anagnostou E., and Foster G.L. An improved boron isotope pH proxy calibration for the deep-sea coral *Desmophyllum dianthus* through sub-sampling of fibrous aragonite. *Chemical Geology*, 447:148–160, 2016. 17

[130] Stewart J.A., Robinson L.F., Day R.D., Strawson I., Burke A., Rae J.W.B., Spooner P.T., Samperiz A., Etnoyer P.J., Williams B., Paytan A., Leng M.J., Häussermann V., N. Wickes L.N., Bratt R., and Pryer H. Refining trace metal temperature proxies in cold-water scleractinian and stylasterid corals. *Earth and Planetary Science Letters*, 545: 116412, 2020. 13

[131] Stewart J.A., Christopher S.J., Kucklick J.R., Bordier L., Chalk T.B., Dapoigny A., Douville E., Foster G.L., Gray W.R., Greenop R., Gutjahr M., Hemsing F., Henehan M.J., Holdship P., Hsieh Y-T., Kolevica A., Lin Y-P., Mawbey E.M., Rae J.W.B., Robinson L.F., Shuttleworth R., You C-F., Zhang S., and Day R.D. NIST RM 8301 boron isotopes in marine carbonate (simulated coral and foraminifera solutions): inter-laboratory δ^{11}B and trace element ratio value assignment. *Geostandards and Geoanalytical Research*, 45(3):77–96, 2021. 38

[132] Ries J.B., Ghazaleh M.N., Connolly B., Westfield I., and Castillo K.D. Impacts of seawater saturation state (ΩA=0.4–4.6) and temperature (10, 25 °C) on the dissolution kinetics of whole-shell biogenic carbonates. *Geochimica et Cosmochimica Acta*, 192:318–337, 2016. 10

[133] Rae J.B.R., Foster G.L., Schmidt D.N., and Elliott T. Boron isotopes and B/Ca in benthic foraminifera: proxies for the deep ocean carbonate system. *Earth and Planetary Science Letters*, 302:403–413, 2011. 13, 16, 38

[134] Bailey J.C., Gabel J.E., and Freshwater D.W. Nuclear 18S rRNA gene sequence analyses indicate that the Mastophoroideae (Corallinaceae, Rhodophyta) is a polyphyletic taxon. *Phycologia*, 43:3–12, 2004. 4

[135] Garbary J.D. An introduction to the Scanning Electron Microscopy of red algae. In *Modern Approaches to the Taxonomy of Red and Brown Algae*, pages 205–222. Cambridge Academic Press, Cambridge MA USA, 1978. 2

[136] Rimstidt J.D., Balog A., and Webb J. Distribution of trace elements between carbonate minerals and aqueous solutions. *Geochimica et Cosmochimica Acta*, 62:1851–1863, 1998. 111

[137] Parker J.H. Ultrastructure of the test wall in modern porcelaneous foraminifera: implications for the classification of the Miliolida. *Journal of Foraminiferal Research*, 47:136–174, 2017. 9

[138] De Yoreo J.J., Gilbert P.U., Sommerdijk N.A., Penn R.L., Whitelam S., Joester D., Zhang H., Rimer J.D., Navrotsky A., Banfield J.F., Wallace A.F., Michel F.M., Meldrum F.C., Cölfen H., and Dove P.M. Crystallization by particle attachment in synthetic, biogenic, and geologic environments. *Science*, 349: 6247, 2015. 110

[139] Hernández-Kantún J.J., Riosmena-Rodriguez R., Hall-Spencer J.M., Peña V., Maggs C.A., and Rindi F. Phylogenetic analysis of rhodolith formation in the Corallinales (Rhodophyta). *European Journal of Phycology*, 50:46–61, 2015. 4

[140] Hall-Spencer J.M., Rodolfo-Metalpa R., Martin S., Ransome E., Fine M., Turner S.M., Rowley S.J., Tedesco D., and Buia M.C. Volcanic carbon dioxide vents show ecosystem effects of ocean acidification. *Nature*, 454:96–99, 2008. 12, 23, 26

[141] Yu J.M. and Elderfield H. Benthic foraminiferal B/Ca ratios reflect deep water carbonate saturation state. *Earth and Planetary Science Letters*, 258:73–86, 2007. 13, 112

[142] Yu J.M., Elderfield H., and Hönisch B. B/Ca in planktonic foraminifera as a proxy for surface water pH. *Paleoceanography*, 22: 2202, 2007. 13, 14, 113

[143] Harney J.N., Grossman E.E., Richmond B.M., and Fletcher III C.H. Age and composition of carbonate shoreface sediments, Kailua Bar, Ohau, Hawaii. *Coral Reefs*, 2:141–154, 2000. 8

[144] Morse J.W., Andersson A.J., and Mackenzie F.T. Initial responses of carbonate-rich shelf sediments to rising atmospheric pCO_2 and "ocean acidification": role of high Mg-calcites. *Geochimica et Cosmochimica Acta*, 70:5814–5830, 2006. 1, 8, 10, 11

[145] Rae J.W.B. Boron isotopes in foraminifera: systematics, biomineralization, and CO_2 reconstruction. In Marschall H. and Foster G., editors, *Boron isotopes: the fifth element*. Springer International Publishing, Cambridge, 2018. 39

[146] Alverson K., Bradley R., Briffa K., Cole J., Hughes M., Larocque I., Pedersen T., Thompson L., and Tudhope S. A global paleoclimate observing system. *Science*, 293:47–48, 2001. 10

[147] Caldeira K., Akai M., Brewer P., Chen B., Haugan P., Iwama T., Johnston P., Kheshgi H., Li Q., Ohsumi T., Poertner H., Sabine C., Shirayama Y., and Thomson J. Ocean storage. In *Carbon Dioxide Capture and Storage: A Special Report of IPCC Working Group III*. Cambridge University Press, Cambridge UK, 2005. ISBN 10-0-521-68551-6. 10

[148] Cuny-Guirriec K., Douville E., Reynaud S., Allemand D., Bordier L., Canesi M., Mazzoli C., Taviani M., Canese S., Mc-Culloch M., Trotter J., Rico-Esenaro S.D., Sanchez-Cabeza J-A., Ruiz-Fernàndez A.C., Carricart-Ganivet J.P., Scott P.M., Sadekov A., and Montagna P. Coral Li/Mg thermometry: Caveats and constraints. *Chemical Geology*, 523:162–178, 2019. 112

[149] Kaczmarek K., Nehrke G., Misra S., Bijma J., and Elderfield H. Investigating the effects of growth rate and temperature on the B/Ca ratio and δ^{11}B during inorganic calcite formation. *Chemical Geology*, 421:81–92, 2016. 14, 111, 113, 115

[150] Klochko K., Kaufman A.J., Yao W., Byrne R.H., and Tossell J.A. Experimental measurement of boron isotope fractionation in seawater. *Earth and Planetary Science Letters*, 248(1-2):261–270, 2006. xvi, 15, 16

[151] Klochko K., Cody G.D., Tossell J.A., Dera P., and Kaufman A.J. Re-evaluating boron speciation in biogenic calcite and aragonite using ^{11}B MAS NMR. *Geochimica et Cosmochimica Acta*, 73:1890–1900, 2009. 13, 17, 116

[152] Lee K., Kim T-W., Byrne R. H., Millero F. J., Feely R. A., and Liu Y-M. The universal ratio of boron to chlorinity for the North Pacific and North Atlantic oceans. *Geochimica et Cosmochimica Acta*, 74(6):1801–1811, 2010. xvi, 15

[153] Simonyan K., Vedaldi A., and Zisserman A. Deep inside Convolutional Networks: Visualising image classification models and Saliency maps. *arXiv*, page 1312.6034, 2013. 32

[154] Simonyan K. and Zisserman A. Very Deep Convolutional Networks for large-scale image recognition. *arXiv*, pages 1409–1556, 2014. 30

[155] Adey K.A., Hönisch B., Eggins S.M., and Rosenthal Y. Environmental controls on B/Ca in calcite tests of the tropical planktic foraminifer species *Globigerinoides ruber* and *Globigerinoides sacculifer*. *Earth and Planetary Science Letters*, 351:270–280, 2012. 14

[156] Chave K.E. Aspects of biochemistry of magnesium. 1. calcareous and marine organisms. *Journal of Geology*, 62:266–283, 1954. 13, 110, 111

[157] Chave K.E. and Wheeler B.D. Mineralogic changes during growth in the red alga, *Clathromorphum compactum*. *Science*, 147:621, 1965. 13

[158] Kroeker K.J., Micheli F., Gambi M.C., and Martz T.R. Divergent ecosystem responses within a benthic marine community to ocean acidification. *Proceedings of the National Academy of Sciences USA*, 108:14515–14520, 2011. 26

[159] Meier K.J.S., Beaufort L, Heussner S, and Ziveri P. The role of ocean acidification in *Emiliania huxleyi* coccolith thinning in the Mediterranean Sea. *Biogeosciences*, 11:2857–2869, 2014. 12

[160] Pezzolesi L., Peña V., Le Gall L., Gabrielson P.W., Kaleb S., Hughey J.R., Rodondi G., Hernandez-Kantun J.J., Falace A., Basso D., Cerrano C., and Rindi F. Mediterranean *Lithophyllum stictiforme* is a genetically diverse species complex: implications for species circumscription, biogeography and conservation of coralligenous habitats. *Journal of Phycology*, 55:473–492, 2019. 4

[161] Pomar L., Baceta J.I., Hallock P., Mateu-Vicens G., and Basso D. Reef building and carbonate production modes in the west-central Tethys during the Cenozoic. *Marine Petrology and Geology*, 83:261–304, 2017. 1, 8

[162] Melbourne L.A., Hernández-Kantún J., Russell S., and Brodie J. There is more to maerl than meets the eye: DNA barcoding reveals a new species in Britain, *Lithothamnion erinaceum* sp. nov. (Hapalidiales, Rhodophyta). *European Journal of Phycology*, 52:166–178, 2017. 20

[163] Coutinho L.M., Penelas Gomes F., Nasri Sissini M., Vieira-Pinto T., Muller de Oliveira

Henriques M.C., Oliveira M.C., Horta P.A., and Barbosa de Barros Barreto M.B. Cryptic diversity in non-geniculate coralline algae: a new genus *Roseolithon* (Hapalidiales, Rhodophyta) and seven new species from the Western Atlantic. *European Journal of Phycology*, 57:227–250, 2021. 4

[164] Irvine L.M. and Chamberlain Y. *Seaweeds of the British Isles: Volume 1 Rhodophyta. Part 2B Corallinales, Hildenbrandiales.* Pelagic Publishing, London, 1994. 2, 20, 34

[165] Abadi M., Agarwal A., Barham P., Brevdo E., Chen Z., Citro C., Corrado G.S., Davis A., Dean J., Devin M., Ghemawat S., Goodfellow I., Harp A., Irving G., Isard M., Jia Y., Jozefowicz R., Kaiser L., Kudlur M., Levenberg J., Mane D., Monga R., Moore S., Murray D., Olah C., Schuster M., Shlens J., Steiner B., Sutskever I., Talwar K., Tucker P., Vanhoucke V., Vasudevan V., Viegas F., Vinyals O., Warden P., Wattenberg M., Wicke M., Yu Y., and Zheng X. TensorFlow: Large-scale Machine Learning on heterogeneous distributed systems. *arXiv*, page 1603.04467, 2015. 33

[166] Canals M. and Ballesteros E. Production of carbonate particles by phytobenthic communities on the Mallorca-Menorca shelf, northwestern Mediterranean Sea. *Deep Sea Research*, 44:611–629, 2007. 1

[167] Cusack M., Kamenos N.A., Rollion-Bard C., and Tricot G. Red coralline algae assessed as marine pH proxies using ^{11}B MAS NMR. *Scientific Reports*, 5: 8175, 2015. 17, 18, 39

[168] Denizot M. *Les algues floridées encroutantes (à l'éxclusion des Corallinacées)*. Laboratoire de Cryptogamie, Muséum National d'Histoire Naturelle, Paris, 1968. 4, 20

[169] Gutjahr M., Bordier L., Douville E., Farmer J., Foster G.L., Hathorne E.C., Hönisch B., Lemarchand D., Louvat P., McCulloch M., Noireaux J., Pallavicini N., Rae J.W.B., Rodushkin I., Roux P., Stewart J.A., Thil F., and You C-F. Sub-permil interlaboratory consistency for solution-based boron isotope analyses on marine carbonates. *Geostandards and Geoanalytical Research*, 45(1):59–75, 2021. 38

[170] Holcomb M., Venn A. A., Tambutté E., Tambutté S., Allemand D., Trotter J., and

McCulloch M. Coral calcifying fluid pH dictates response to ocean acidification. *Scientific Reports*, 4:1–4, 2014. 115

[171] Holcomb M., DeCarlo T.M., Gaetani G.A., and McCulloch M. Factors affecting B/Ca ratios in synthetic aragonite. *Chemical Geology*, 437:67–76, 2016. 13

[172] McCulloch M., Trotter J., Montagna P., Falter J., Dunbar R., Freiwald A., Försterra G., Correa M.L., Maier C., Rüggeberg A., and Taviani M. Resilience of cold-water scleractinian corals to ocean acidification: boron isotopic systematics of pH and saturation state up-regulation. *Geochimica et Cosmochimica Acta*, 87:21–34, 2012. 12, 18, 115

[173] Pagani M., Lemarchand D., Spivack A., and Gaillardet J. A critical evaluation of the boron isotope-pH proxy: The accuracy of ancient ocean pH estimates. *Geochimica et Cosmochimica Acta*, 69(4):953–961, 2005. 17

[174] Raitzsch M., Bijma J., Benthien A., Richter K.U., Steinhoefel G., and Kucera M. Boron isotope-based seasonal paleo-pH reconstruction for the Southeast Atlantic – a multispecies approach using habitat preference of planktonic foraminifera. *Earth and Planetary Science Letters*, 487:138–150, 2018. 37

[175] Borowitzka M.A. Morphological and cytological aspects of algal calcification. *International Review of Cytology*, 74:127–160, 1982. 109

[176] Borowitzka M.A. Carbonate calcification in algae – initiation and control. In Mann S. andWebb J. and Williams R.J.P., editors, *Biomineralization: chemical and biochemical perspectives*, pages 63–95. VCH Verlagsgesellschaft, Weinheim, 1989. 9, 115

[177] Borowitzka M.A., Larkum A.W.D., and Nockolds C.E. A scanning electron microscope study of the structure and organization of the calcium carbonate deposits of algae. *Phycologia*, 13:195–203, 1974. 109

[178] Rahman M.A. and Halfar J. First evidence of chitin in calcified coralline algae: New insights into the calcification process of *clathromorphum compactum*. *Scientific Reports*, 4: 6162, 2014. 1

[179] Gambi M.C. Emissioni sommerse di CO_2 lungo le coste dell'isola d'Ischia. rilievi su altre aree come possibili laboratori naturali per lo studio dell'acidificazione e cambiamento climatico a mare. *Notiziario S.I.B.M.*, 66:67–79, 2014. xvi, 19, 23

[180] Nash M.C., Diaz-Pulido G., Harvey A.S., and Adey W. Coralline algal calcification: A morphological and process-based understanding. *PLoS One*, 14(9): e0221396, 2019. 9, 109, 110, 111

[181] Nash M.C., Martin S., and Gattuso J-P. Mineralogical response of the Mediterranean crustose coralline alga *Lithophyllum cabiochae* to near-future ocean acidification and warming. *Biogeosciences*, 13:5937–5945, 2016. 11, 13

[182] Nash M.C., Uthicke S., Negri A.P., and Cantin N.E. Ocean acidification does not affect magnesium composition or dolomite formation in living crustose coralline algae. *Biogeosciences*, 12:5247–5260, 2015. 8, 11

[183] Nash M.C. and Adey W. Multiple phases of Mg-calcite in crustose coralline algae suggest caution for temperature proxy and ocean acidification assessment: lessons from the ultrastructure and biomineralization in *Phymatolithon* (Rhodophyta, Corallinales). *Journal of Phycology*, 53:970–984, 2017. 1, 9, 109, 111

[184] Nash M.C. and Adey W. Anatomical structure overrides temperature controls on magnesium uptake - calcification in the Arctic/subarctic coralline algae *Leptophytum leave* and *Kvaleya epilaeve* (Rhodophyta; Corallinales). *Biogeosciences*, 15:781–795, 2018. 109

[185] Modarres M.H., Aversa R., Cozzini S., Ciancio R., Leto A., and Brandino G.P. Neural network for nanoscience Scanning Electron Microscope image recognition. *Scientific Reports*, 7, 2017. 7

[186] Bilan M.I. and Usov A.I. Polysaccharides of calcareous algae and their effect on the calcification process. *Russian Journal of Bioorganic Chemistry*, 27:2–16, 2001. 1, 111

[187] Henehan M.J., Foster G.L., Bostock H.C., Greenop R., Marshall B.J., and Wilson P.A. A new boron isotope-pH calibration for *Orbulina universa*, with implications for understand-

ing and accounting for ‘vital effects. *Earth and Planetary Science Letters*, 454:282–292, 2016. 16

[188] Henehan M.J., Rae J.W.B., Foster G.L., Erez J., Prentice K.C., Kucera M., Bostock H.C., Martınez-Boti M.A., Milton J.A., Wilson P.A., Marshall B.J., and Elliott T. Calibration of the boron isotope proxy in the planktonic foraminifera *Globigerinoides ruber* for use in palaeo-CO_2 reconstruction. *Earth and Planetary Science Letters*, 364:111–122, 2013. 13, 16

[189] Foster M.S. Rhodoliths: between rocks and soft places. *Journal of Phycology*, 37:659–667, 2001. 2, 3, 8, 12

[190] Ribeiro M.T., Singh S., and Guestrin C. ”Why should I trust you?” explaining the predictions of any classifier. In *Proceedings of the ACM SIGKDD International Conference on knowledge discovery and data mining; Association for Computing Machinery*, volume 13-17, pages 1135–1144, 2016. 32, 33

[191] Wara M.W., Delaney M.L., Bullen T.D., and Ravelo A.C. Possible roles of pH, temperature, and partial dissolution in determining boron concentration and isotopic composition in planktonic foraminifera. *Paleoceanography*, 18: 1100, 2003. 14, 113

[192] He M.Y., Xiao Y.K., Jin Z.D., Liu W.G., Ma Y.Q., Zhang Y.L., and Luo C.G. Quantification of boron incorporation into synthetic calcite under controlled pH and temperature conditions using a differential solubility technique. *Chemical Geology*, 337:67–74, 2013. 18

[193] Hobbs M.Y. and Reardon E.J. Effect of pH on boron coprecipitation by calcite: further evidence for nonequilibrium partitioning of trace elements. *Geochimica et Cosmochimica Acta*, 63:1013–1021, 1999. 18

[194] Bianco-Stein N., Polishchuk I., Lang A., Atiya G., Villanova J., Zaslansky P., Katsman A., and Pokroy B. Structural and chemical variations in Mg-calcite skeletal segments of coralline red algae lead to improved crack resistance. *Acta Biomaterialia*, 130:362–373, 2021. 9, 116

[195] Bianco-Stein N., Polishchuk I., Lang A., Portal L., Dejoie C., Katsman A., and Pokroy B. High-Mg calcite nanoparticles within a low-Mg calcite matrix: A widespread phenomenon in biomineralization. *Proceedings of the National Academy of Sciences*, 119(16): e2120177119, 2022. 9, 116

[196] Darrenougue N., de Deckker P., Eggins S., and Payri C. Sea-surface temperature reconstruction from trace elements variations of tropical coralline red algae. *Quaternary Science Reviews*, 93:34–46, 2014. 4, 13, 111

[197] Gussone N., Böhm F., Eisenhauer A., Dietzel M., Heuser A., Teichert B.M.A., Reitner J., Wörheide G., and Dullo W-C. Calcium isotope fractionation in calcite and aragonite. *Geochimica et Cosmochimica Acta*, 69:4485–4494, 2005. 111

[198] Kamenos N., Perna G., Gambi M.C., Micheli F., and Kroeker K. Coralline algae in a naturally acidified ecosystem persist by maintaining control of skeletal mineralogy and size. *Proceedings of the Royal Society B: Biological Sciences*, 283, 2016. 11

[199] Kamenos N.A., Burdett H.L., Aloisio E., Findlay H.S., Martin S., Longbone C., Dunn J., Widdicombe S., and Calosi P. Coralline algal structure is more sensitive to rate, rather than the magnitude, of ocean acidification. *Global Change Biology*, 19:3621–3628, 2013. 11

[200] Kamenos N.A., Cusack M., and Moore P.G. Coralline algae are global paleothermometers with bi-weekly resolution. *Geochimica et Cosmochimica Acta*, 72:771–779, 2008. 12, 13, 111

[201] Kamenos N.A., Cusack M., Huthwelker T., Lagarde P., and Scheibling R.E. Mg-lattice associations in red coralline algae. *Geochimica et Cosmochimica Acta*, 73:1901–1907, 2009. 8, 9, 107

[202] Kamenos N.A., Hoey T., Nienow P., Fallick A.E., and Claverie T. Reconstructing Greenland Ice sheet runoff using coralline algae. *Geology*, 40:1095–1098, 2012. 13

[203] Rayner N.A., Parker D.E., Horton E.B., Folland C.K., Alexander L.V., Rowell D.P., Kent E.C., and Kaplan A. Global analyses of sea surface temperature, sea ice, and

night marine air temperature since the late nineteenth century. *Journal of Geophysical Research*, 108:1–22, 2003. 10

[204] Hemming N.G. and Hönisch B. Boron isotopes in marine carbonate sediments and the pH of the ocean. In Hillaire-Marcel C. and de Vernal A., editors, *Proxies in Late Cenozoic Paleoceanography*, pages 717–734. Elsevier, 2007. 13

[205] Hemming N.G. and Hanson G.N. Boron isotopic composition and concentration in modern marine carbonates. *Geochimica et Cosmochimica Acta*, 56:537–543, 1992. 16, 111, 112, 114

[206] Hemming N.G., Reeder R.J., and Hanson G.N. Mineral-fluid partitioning and isotopic fractionation of boron in synthetic calcium carbonate. *Geochimica et Cosmochimica Acta*, 59:371–379, 1995. 17, 18, 115, 116

[207] Branson O., Kaczmarek K., Redfern S.A.T., Misra S., Langer G., Tyliszczak T., Bijma J., and Ederfield H. The coordination and distribution of B in foraminiferal calcite. *Earth and Planetary Science Letters*, 416:67–72, 2015. 17, 116

[208] Hoegh-Guldberg O., Mumby P.J., Hooten A.J., Steneck R.S., Greenfield P., Gomez E., Harvell C.D., Sale P.F., Edwards A.J., Caldeira K., Knowlton N., Eakin C.M., Iglesias-Prieto R., Muthiga N., Bradbury R.H., Dubi A., and Hatziolos M.E. Coral reefs under rapid climate change and ocean acidification. *Science*, 318:1737–1742, 2007. 10

[209] Nir O., Vengosh A., Harkness J.S., Dwyer G.S., and Lahav O. Direct measurement of the boron isotope fractionation factor: Reducing the uncertainty in reconstructing ocean paleo-pH. *Earth and Planetary Science Letters*, 414:1–5, 2015. xvi, 15, 17

[210] Chan P., Halfar J., Adey W., Hetzinger S., Zack T., Moore G.W.K., Wortmann U. G., Williams B., and Hou A. Multicentennial record of Labrador Sea primary productivity and sea-ice variability archived in coralline algal barium. *Nature Communications*, 8: 15543, 2017. 13

[211] James N. P., Wray J. L., and Ginsburg R. N. Calcification of encrusting aragonitic algae

(Peyssonneliaceae); implications for the origin of late paleozoic reefs and cements. *Journal of Sedimentary Research*, 58:291–303, 1988. 4

[212] Jochum K. P., Scholz D., Stoll B., Weis U., Wilson S.A., Yang Q., Schwalb A., Börner N., Jacob D.E., and Andreae M.O. Accurate trace element analysis of speleothems and biogenic calcium carbonates by LA-ICP-MS. *Chemical Geology*, 318:31–44, 2012. 36

[213] Kerrison P., Hall-Spencer J.M., Suggett D.J., Hepburn L.J., and Steinke M. Assessment of pH variability at a coastal CO_2 vent for ocean acidification studies. *Estuarine, Coastal and Shelf Science*, 94:129–137, 2011. 26

[214] Lionello P, Gacic M, Gomis D, Garcia-Herrera R, Giorgi F, Planton S, Trigo R, Theocharis A, Tsimplis M, Ulbrich U., and Xoplaki E. Program focuses on climate of the Mediterranean region. *Regional Environmental Change*, 14(5):1679–1684, 2010. 12

[215] Montagna P. and Douville E. Geochemical proxies in marine biogenic carbonates: New developments and applications to global change. *Chemical Geology*, 533: 119411, 2020. 13

[216] Potin P., Floc'h J.Y., Augris C., and Cabioch J. Annual growth rate of the calcareous red alga *Lithothamnion corallioides* (Corallinales, Rhodophyta) in the Bay of Brest, France. *Hydrobiologia*, 204:263–267, 1990. 2, 3

[217] Tan P., Steinbach M., Karpatne A., and Kumar V. *Introduction to Data Mining*. Addison-Wesley, 2nd edition, 2018. 32, 33, 34

[218] Brewer P.G. Ocean chemistry of the fossil fuel signal: The haline signature of "Business as Usual". *Geophysical Research Letters*, 24:1367–1369, 1997. 10

[219] Dixon K. R. and Saunders G. W. DNA barcoding and phylo-genetics of *Ramicrusta* and *Incendia* gen. nov., two early diverging lineages of the Peyssonneliaceae (Rhodophyta). *Phycologia*, 52:82–108, 2013. 4

[220] Escudier R., Clementi E., Omar M., Cipollone A., Pistoia J., Aydogdu A., Drudi M., Grandi A., Lyubartsev V., Lecci R., Cretí S., Masina S., Coppini G., and

Pinardi N. Mediterranean Sea Physical Reanalysis (CMEMS MED-Currents), Version 1. CMEMS [data set], 2020. available online: https://doi.org/10.25423/CMCC/MEDSEA_MULTIYEAR_PHY_006_004_E3R1. xi, 26, 44

[221] Hecht-Nielsen R. Theory of the backpropagation Neural Network. In *International 1989 Joint Conference on Neural Networks*, volume 1, pages 593–605, 1989. 6

[222] Henrich R, Reiwald A, Wehrmann A, Schafer P, Samtleben C., and Zankl H. Nordic cold-water carbonates: occurrence and controls. In Reitner J., Neuweiler F., and Gunkel F., editors, *Global and Regional Controls on Biogenic Sedimentation*, pages 35–53. Göttinger Arbeiten zur Geologie und Paläontologie, Gottingen, 1996. 8

[223] Kotikalapudi R. and contributors. Keras-vis. GitHub, 2017. available online: https://github.com/raghakot/keras-vis. 33

[224] Mitra R., Marchitto T.M., Ge Q., Zhong B., Kanakiya B., Cook M.S., Fehrenbacher J.S., Ortiz J.D., Tripati A., and Lobaton E. Automated species-level identification of planktic foraminifera using Convolutional Neural Networks, with comparison to human performance. *Marine Micropaleontology*, 147:16–24, 2019. 34

[225] Moberly R. Composition of magnesian calcites of algae and pelecypods by electron microprobe analysis. *Sedimentology*, 14:113–123, 1970. 13, 25

[226] Lorens R.B. Sr, Cd, Mn and Co distribution coefficients in calcite as a function of calcite precipitation rate. *Geochimica et Cosmochimica Acta*, 45:553–561, 1981. 111

[227] Roberts R.D., Kühl M., Glud R.N., and Rysgaard S. Primary production of crustose coralline algae in a high Arctic Fjord. *Journal of Phycology*, 38:273–283, 2002. 112

[228] Zeebe R.E. and Wolf-Gladrow D. *CO_2 in seawater: equilibrium, kinetics, isotopes*. Elsevier Oceanography Book Series, Amsterdam, 2001. 17

[229] Gabitov R.I., Rollion-Bard C., Tripati A., and Sadekov A. In situ study of boron partitioning between calcite and fluid at different crystal growth rates. *Geochimica et Cosmochimica Acta*, 137:81–92, 2014. 14, 113

[230] Pachauri R.K. and Meyer L.A. IPCC: Climate Change 2014: Synthesis Report. In *Contribution of Working Groups I, II and III to the Fifth Assessment Report of the Intergovernmental Panel on Climate Change*. IPCC, Geneva, Switzerland, 2014. ISBN 978-92-9169-143-2. 12

[231] De Lima R.P., Welch K.F., Barrick J.E., Marfurt K.J., Burkhalter R., Cassel M., and Soreghan G.S. Convolutional Neural Networks as an aid to Biostratigraphy and Micropaleontology: A test on Late Paleozoic microfossils. *Palaios*, 35:391–402, 2020. 7

[232] Selvaraju R.R., Cogswell M., Das A., Vedantam R., Parikh D., and Batra D. Grad-CAM: Visual explanations from Deep Networks via Gradient-Based Localization. *arXiv*, page 1610.02391, 2016. 32, 33

[233] Barker S., Cacho I., Benway H., and Tachikawa K. Planktonic foraminiferal Mg/Ca as a proxy for past oceanic temperatures: a methodological overview and data compilation for the Last Glacial Maximum. *Quaternary Science Reviews*, 24:821–834, 2005. 13

[234] Comeau S., Cornwall C.E., and McCulloch M.T. Decoupling between the response of coral calcifying fluid pH and calcification under ocean acidification. *Scientific Reports*, 7: 7573, 2017. 12, 18

[235] Foo S., Byrne M., Ricevuto E., and Gambi M.C. The carbon dioxide vents of Ischia, Italy, a natural system to assess impacts of ocean acidification on marine ecosystems: An overview of research and comparisons with other vent systems. *Journal of Marine Biology & Oceanography*, 56:237–310, 2018. xi, 26, 28, 44

[236] Hetzinger S., Halfar J., Kronz A., Simon K., Adey W.H., and Steneck R.S. Reproducibility of *Clathromorphum compactum* coralline algal Mg/Ca ratios and comparison to high-resolution sea surface temperature data. *Geochimica et Cosmochimica Acta*, 220:96–109, 2018. 13

[237] Hetzinger S., Halfar J., Zack T., Gamboa ., Jacob D.E., Kunz B.E., Kronz A., Adey W., Lebednik P.A., and Steneck R.S. High-resolution analysis of trace elements in crustose

coralline algae from the North Atlantic and North Pacific by laser ablation ICP-MS. *Palaeogeography Paleoclimatology Palaeoecology*, 302:81–94, 2011. 12, 13, 111

[238] Joher S., Ballesteros E., and Rodrigues-Prieto C. Contribution to the study of deep coastal detritic bottoms: the algal communities of the continental shelf off the Balearic Islands, Western Mediterranean. *Mediterranean Marine Science*, 16(3):573–590, 2015. 4

[239] Kiel S. Assessing bivalve phylogeny using Deep Learning and Computer Vision approaches. *bioRxiv*, 2021. 7

[240] Krief S., Hendy E.J., Fine M., Yam R., Meibom A., Foster G.L., and Shemesh A. Physiological and isotopic responses of scleractinian corals to ocean acidification. *Geochimica et Cosmochimica Acta*, 74(17):4988–5001, 2010. 16

[241] Martin S. and Gattuso J-P. Response of Mediterranean coralline algae to ocean acidification and elevated temperature. *Global Change Biology*, 15:2089–2100, 2009. 10, 11

[242] Martin S., Castets M.D., and Clavier J. Primary production, respiration and calcification of the temperate free-living coralline alga *Lithothamnion corallioides*. *Aquatic Botany*, 85:121–128, 2006. 2, 3, 112

[243] Misra S., Owen R., Kerr J., Greaves M., and Elderfield H. Determination of δ^{11}B by HR-ICP-MS from mass limited samples: Application to natural carbonates and water samples. *Geochimica et Cosmochimica Acta*, 140:531–553, 2014. 37

[244] Pestana E. M. S., Lyra G. M., Santos G. N., Santos C. C., Cassano V., and Nunes J. M. C. Integrative approach reveals underestimated Peyssonneliales diversity in Brazil: registering the first occurrence of *Ramicrusta* and *Incendia*, with the description of three new species. *Phytotaxa*, 439:39–55, 2020. 4

[245] Raz S., Weiner S., and Addadi L. Formation of high-magnesian calcites via an amorphous precursor phase: possible biological implications. *Advanced Materials*, 12:38–42, 2000. 110

[246] Sen S., Stebbins J.F., Hemming N.G., and Gosh B. Coordination environment of b

impurities in calcite and aragonite polymorphs: an ^{11}B MAS NMR study. *American Mineralogist*, 79:819–825, 1994. 17, 18, 116

[247] Teichert S., Woelkerling W.J., and Munnecke A. Coralline red algae from the Silurian of Gotland indicate that the order Corallinales (Corallinophycidae, Rhodophyta) is much older than previously thought. *Palaeontology*, 62:599–613, 2019. 8

[248] Weiner S. and Dove P.M. An overview of biomineralization processes and the problem of the vital effect. *Reviews in Mineralogy and Geochemistry*, 54:1–29, 2003. 109

[249] Wilson S., Blake C., Berges J.A., and Maggs C.A. Environmental tolerances of free-living coralline algae (maerl): implications for European marine conservation. *Biological Conservation*, 120:279–289, 2004. 2

[250] Zhang S., Henehan M.J., Hull P.M., Reid R.P., Hardisty D.S., Hood A.v.S., and Planavsky N.J. Investigating controls on boron isotope ratios in shallow marine carbonates. *Earth and Planetary Science Letters*, 458:380–393, 2017. 17

[251] Fowell S.E., Sandford K., Stewart J.A., Castillo K.D., Ries J.B., and Foster G.L. Intrareef variations in Li/Mg and Sr/Ca sea surface temperature proxies in the Caribbean reef-building coral *Siderastrea sidereal*. *Paleoceanography*, 31:1315–1329, 2016. 112

[252] Alexandersson T. Carbonate cementation in coralline algal nodules in the Skagerrak, North Sea; biochemical precipitation in undersaturated waters. *Journal of Sedimentary Petrology*, 44:7–26, 1974. 8

[253] Corrège T. Sea surface temperature and salinity reconstruction from coral geochemical tracers. *Palaeogeography, Palaeoclimatology, Palaeoecology*, 232:408–428, 2006. 13, 25

[254] Lacoue-Labarthe T, Nunes P.A.L.D, Ziveri P, Cinar M, Gazeau F, Hall-Spencer J.M, Hilmi N, Moschella P, Safa A, Sauzade D, and Turley C. Impacts of ocean acidification in a warming Mediterranean Sea: An overview. *Regional Studies in Marine Science*, 5:1–11, 2016. 12

[255] Mass T., Giuffre A.J., Sun C-Y., Stifler C.A., Frazier M.J., Neder M., Tamura N., Stan C.V., Marcus M.A., and Gilbert P.U.P.A. Amorphous calcium carbonate particles form coral skeletons. *Proceedings of the National Academy of Sciences*, 114(37): E7670-E7678, 2017. 9, 110

[256] Tyrell T. Anthropogenic modification of the oceans. *Philosophical Transactions of the Royal Society A*, 369:887–908, 2011. 10

[257] Riebesell U., Fabry V.J., Hansson L., and Gattuso J-P. Guide to best practices for ocean acidification research and data reporting. *Oceanography*, 22(4):260, 2010. 18

[258] Frezza V., Argenti L., Bonifazi A., Chiocci F.L., Di Bella L., Ingrassia M., and Martorelli E. Benthic foraminiferal assemblages and rhodolith facies evolution in post-LGM sediments from the Pontine archipelago shelf (Central Tyrrhenian Sea, Italy). *Geosciences*, 11: 179, 2021. 3

[259] Masson-Delmotte V., Zhai P., Pirani A., Connors S.L., Péan C., Berger S., Caud N., Chen Y., Gomis M.I. Goldfarb, Huang M., Leitzell K., Lonnoy E., Matthews J.B.R., Maycock T.K., Waterfield T., Telekçi O., Yu R., and Zhou B. IPCC: Climate Change 2021: The Physical Science Basis. In *Contribution of Working Group I to the Sixth Assessment Report of the Intergovernmental Panel on Climate Change*. Cambridge University Press, Cambridge UK, 2021. ISBN 978-92-9169-158-6. 10

[260] Mavromatis V., Montouillout V., Noireaux J., Gaillardet J., and Schott J. Characterization of boron incorporation and speciation in calcite and aragonite from co-precipitation experiments under controlled pH, temperature and precipitation rate. *Geochimica et Cosmochimica Acta*, 150:299–313, 2015. 14, 17, 18, 39, 40, 113, 115, 116

[261] Peña V., Harvey B., Agostini S., Porzio L., Milazzo M., Horta P., Gall L., and Hall-Spencer J. Major loss of coralline algal diversity in response to ocean acidification. *Global Change Biology*, 27, 2021. 11

[262] Peña V., Vieira C., Braga J.C., Aguirre J., Rösler A., Baele G., De Clerck O., and Le Gall L. Radiation of the coralline red algae (Corallinophycidae, Rhodophyta) crown

group as inferred from a multilocus time-calibrated phylogeny. *Molecular Phylogenetics and Evolution*, 150: 106845, 2020. 12

[263] Peña V., de Clerck O., Afonso-Carrillo J., Ballesteros E., Bárbara I., Barreiro R., and le Gall L. An integrative systematic approach to species diversity and distribution in the genus *Mesophyllum* (Corallinales, Rhodophyta) in Atlantic and Mediterranean Europe. *European Journal of Phycology*, 50:20–36, 2015. 3, 4, 20, 34

[264] Bracchi V.A. and Basso D. The contribution of calcareous algae to the biogenic carbonates of the continental shelf: Pontian Islands, Tyrrhenian Sea, Italy. *Geodiversitas*, 34:61–76, 2012. 1

[265] Bracchi V.A., Basso D., Savini A., and Corselli C. Algal reefs (Coralligenous) from glacial stages: origin and nature of a submerged tabular relief (Hyblean Plateau, Italy). *Marine Geology*, 411:119–132, 2019. 8

[266] Bracchi V.A., Basso D., Marchese F., Corselli C., and Savini A. Coralligenous morphotypes on subhorizontal substrate: a new categorization. *Continental Shelf Research*, 144:10–20, 2017. 1

[267] Bracchi V.A., Piazza G., and Basso D. A stable ultrastructural pattern despite variable cell size in *Lithothamnion corallioides*. *Biogeosciences*, 18:6061–6076, 2021. xv, 4, 8, 9, 25, 26, 27, 36, 72, 107, 109, 115

[268] Bracchi V.A., Nalin R., and Basso D. Paleoecology and dynamics of coralline dominated facies during a Pleistocene transgressive–regressive cycle (Capo Colonna marine terrace, Southern Italy). *Palaeogeography Paleoclimatology Palaeoecology*, 414:296–309, 2014. 3, 4, 8

[269] Bracchi V.A., Nalin R., and Basso D. Morpho-structural heterogeneity of shallow-water coralligenous in a Pleistocene marine terrace (Le Castella, Italy). *Palaeogeography Paleoclimatology Palaeoecology*, 454:101–112, 2016. 1, 8

[270] D'Alessandro W., Brusca L., Kyriakopouios K., Michas G., and Papadakis G. Methana, the westernmost active volcanic system of the south Aegean arc (Greece): Insight from

fluids geochemistry. *Journal of Volcanology and Geothermal Research*, 178:818–828, 2008. 23

[271] Adey W.H. and McKibbin D.L. Studies on the maerl species *Phymatolithon calcareum* (Pallas) nov. comb. and *Lithothamnium corallioides* Crouan in the Ria de Vigo. *Botanica Marina*, 13:100–106, 1970. 20, 34

[272] Adey W.H. and Mcintyre I.G. Crustose coralline algae: a re-evaluation in the geological sciences. *Geological Society of America Bulletin*, 84:883–904, 1973. 2

[273] Adey W.H. and Adey P.J. Studies on the biosystematics and ecology of the epilithic crustose Corallinaceae of the British Isles. *British Journal of Phycology*, 8:343–407, 1973. 26, 27

[274] Adey W.H., Chamberlain Y.M., and Irvine L.M. An SEM-based analysis of the morphology, anatomy, and reproduction of *Lithothamnion tophiforme* (Esper) Unger (Corallinales, Rhodophyta), with a comparative study of associated North Atlantic arctic/subarctic Melobesioideae. *Journal of Phycology*, 41:1010–1024, 2005. 9

[275] Liu X. and Song H. Automatic identification of fossils and abiotic grains during carbonate microfacies analysis using Deep Convolutional Neural Networks. *Sedimentary Geology*, 410: 105790, 2020. 6, 7

[276] Rosenthal Y., Lear C.H., Oppo D.W., and Braddock K.L. Temperature and carbonate ion effects on Mg/Ca and Sr/Ca ratios in benthic foraminifera: Aragonitic species *Hoegludina elegans*. *Paleoceanography*, 21: PA1007, 2006. 112

[277] Xiao Y., Li H., Liu W., Wang X., and Jiang S. Boron isotopic fractionation in laboratory inorganic carbonate precipitation: evidence for the incorporation of $B(OH)_3$ into carbonate. *Science In China Series D-Earth Sciences*, 51:1776–1785, 2008. 17

[278] Xiao Y.K., Shirodkar P.V., Zhang C.G., Wei H.Z., Liu W.G., and Zhou W.J. Isotopic fractionation of boron in growing corals and its paleoenvironmental implication. *Current Science*, 90:414–420, 2006. 18

Last bibliographic research: December 2022